NEAR-WALL THERMOMETRY VIA TOTAL INTERNAL REFLECTION FLUORESCENT MICRO-THERMOMETRY (TIR-FMT)

A Thesis
Presented to
The Academic Faculty

by

Keith D. Suda-Cederquist

In Partial Fulfillment
of the Requirements for the Degree
Master of Science in the
Woodruff School of Mechanical Engineering

Georgia Institute of Technology
May 2007

NEAR-WALL THERMOMETRY VIA TOTAL INTERNAL REFLECTION FLUORESCENT MICRO-THERMOMETRY (TIR-FMT)

Approved by:

Professor Minami Yoda, Advisor
Mechanical Engineering
Georgia Institute of Technology

Professor Yogendra Joshi
Mechanical Engineering
Georgia Institute of Technology

Professor Zhuomin Zhang
Mechanical Engineering
Georgia Institute of Technology

Date Approved: 12 March 2007

ACKNOWLEDGEMENTS

I would like to express my gratitude to all of those who have assisted in the completion of this thesis. Foremost, I would like to thank my advisor, Dr. Minami Yoda. Her direction and advice has served as a constant source of support throughout the duration of this project. I would like to thank my additional committee members, Dr. Yogendra Joshi and Dr. Zhuomin Zhang, for their assistance and substantial contributions to this project.

I would like to thank my laboratory colleagues whose support and assistance have been invaluable: Tim Koehler, Carter Dietz, Lorenzo Crosatti, Myeongsub Kim, Charlotte Kotas, and Domenico Lippolis. I would like to especially thank Haifeng Li for always offering great advice in a friendly and patient manner.

Most importantly I wish to express my sincere appreciation of my family and the constant support and love they have given me.

TABLE OF CONTENTS

ACKNOWLEDGEMENTS iii

LIST OF TABLES vii

LIST OF FIGURES viii

SUMMARY xv

I INTRODUCTION 1

1.1 Motivation and Objectives 1

1.2 Literature Review 5

1.2.1 Review of Fluid and Thermal Transport in Microchannels . 5

1.2.2 Microscale Thermometry Techniques 9

1.2.3 Laser-Induced Fluorescent Thermometry 13

1.3 Fluorescence 17

1.3.1 Fluorescent Mechanism 17

1.3.2 Temperature Dependence of Fluorescence 22

1.3.3 Photobleaching 24

1.3.4 Dye Properties 27

1.4 Total Internal Reflection Microscopy 32

1.4.1 Total Internal Reflection 32

1.4.2 Evanescent Wave 34

1.4.3 TIR Fluorescence Microscopy 38

II EXPERIMENTAL APPARATUS AND PROCEDURE 40

2.1 Theoretical Overview 40

2.1.1 Relationship between pH and Fluorescence Intensity 43

2.2 Optical System 46

2.2.1 Illumination System 46

2.2.2 Imaging System 52

2.2.3 Interrogation Region 56

2.3 Fluorophore Solution Preparation 60
2.4 Calibration 63
2.4.1 Experimental Apparatus: Calibration Cell 64
2.4.2 Experimental Apparatus: Calibration Lid 66
2.4.3 Design Considerations 68
2.4.4 Experimental Procedure 70
2.5 Image Processing 73
2.5.1 CCD Camera Corrections 75
2.5.2 Binary Mask Generation 77
2.5.3 Normalization 79
2.5.4 Calibration Data Reduction 80
III EXPERIMENTAL RESULTS AND DISCUSSION 83
3.1 Calibration Results 83
3.1.1 Background Illumination and Out-of-Plane Resolution . . . 83
3.1.2 Average Fluorescence Intensity 84
3.1.3 Normalized Fluorescence Intensity 87
3.2 Calibration Discussion 90
3.2.1 Temporal Variations in Laser Illumination 92
3.2.2 Refractive Index Changes with Temperature 92
3.2.3 Adsorption 104
IV CONCLUSIONS AND RECOMMENDATIONS 108
4.1 Conclusions 108
4.1.1 Extension of TIR-FMT to Microchannels 109
4.2 Recommendations for Future Work 109
4.2.1 Objective-Based Total Internal Reflection Microscopy 110
4.2.2 Two-Color Laser Induced Fluorescence Thermometry 110
APPENDIX A ERROR ANALYSIS 112
APPENDIX B ADSORPTION 127

APPENDIX C TEMPERATURE GRADIENT MEASUREMENTS IN A MICROCHANNEL 142

REFERENCES 177

LIST OF TABLES

1 Properties of rhodamine B and fluorescein 32

2 Components of illumination system 47

3 Specifications of components in imaging system 54

4 Nomenclature of symbols used in image processing 75

5 Estimate of background (B.G.) illumination, interrogation depth and interrogation centroid for calibration measurements. 84

6 Average, r.m.s., and maximum temperature uncertainties (95% confidence) for different spatial resolutions. 90

A.1 Expanded uncertainty for fluorescein solution concentration with greatest uncertainty. Note: uncertainty is based upon instrument resolution uncertainties and expanded uncertainty (95% confidence) are propogated. 113

A.2 Representative uncertainty calculation of temperature measurement based upon entire 715×950 μm viewfield from calibration data. Representative calculation for data point at $T = 55.1$℃($\Theta = 26.3$℃) that has maximum calculated uncertainty. 123

A.3 Representative uncertainty calculation of temperature measurement based upon individual 1.45×1.45 μm pixel from calibration data. Representative calculation for data point at $T = 20.3$℃($\Theta = -8.4$℃) that has maximum calculated uncertainty. 125

B.1 Camera settings for each optical configuration used in charge inversion investigations. 138

C.1 Components of microchannel 143

C.2 Experimental parameters of experimental results shown in Figures C.7 and C.8. All temperatures are in units of [℃] and temperature gradients are in units of [℃/mm]. T_{TC} is the channel thermocouple measurment, and (dT/dr) is the channel temperature gradient predicted by FLUENT model. 159

LIST OF FIGURES

1 Proposed three-dimensional chip architecture via stacked dies [38]. . . 2

2 Basic configuration for single-phase convective cooling of microelectronic package with microchannels 4

3 Tree-diagram of different thermometry techniques 10

4 A simple illustration of fluorescence: excitation light is scattered and absorbed by a fluorophore; subsequent emission of fluorescence; fluorescence is isolated from excitation by an optical filter. 18

5 Example of fluorescent photomicrograph. Image is of pine wood highlighted with fluorescent dye. Reproduced with permission [18] 19

6 Simple Jablonski energy diagram showing: 1) excitation from a ground state to an excited singlet state; 2) relaxation from the excited singlet state to the un-excited singlet state; and 3) emission of fluorescence as electron drops from the un-excited singlet state to a ground state. . . 20

7 Jablonski energy diagram showing different energy levels and different non-fluorescent pathways. Adapted from [18]. 21

8 Chemical structure of rhodamine B 27

9 Chemical structure of fluorescein, disodium salt 27

10 Chemical structure of xanthene nucleus 28

11 Relative absorption and emission spectra for rhodamine B at neutral pH; adapted from [15] 29

12 Relative absorption and emission spectra for fluorescein at neutral pH; adapted from [15] 30

13 Absorption spectrum of rhodamine B at different temperatures [15]. . 31

14 Absorption spectrum of fluorescein at different temperatures [15]. . . 31

15 Application of Snell's Law according to geometric optics. (a) angle of incidence is less than the critical angle; (b) angle of incidence greater than critical angle 33

16 Characteristics of an evanescent wave at an interface between fused silica ($n_1 = 1.463$) and water ($n_2 = 1.33$) for light of wavelength 514 nm at different angles of incidence. The critical angle $\theta_i = 65.38°$ is shown as a dotted line. (a) penetration depth; (b) intensity gain at interface. 35

17 Profiles of the evanescent illumination in x-y plane, assuming an ideal Gaussian laser profile, for four different distances from interface with angle of incidence $\theta_i = 73.9°$, $\lambda = 514nm$, $n_1 = 1.463$, $n_2 = 1.33$ and $G_e = 1.94$. Profiles are color-mapped according to multiples of I_0'. . . 38

18 Intensity of fluorescent emissions from fluorophore located 80 nm away from interface as function of observation angle. Fluorophore molecules are modeled as constant-power, variable amplitude oscillating dipoles with dipole oriented (a) parallel and (b) perpendicular to interface. Adapted from [8]. 39

19 Diagram showing basic procedure for TIR-FMT 41

20 Sensitivity of fluorescence intensity to changes in pH for fluorescein dyes excited at $\lambda_{ex} = 514.5$. Adapted from [17]. 44

21 Diagram of Illumination System 47

22 Spectral power specification for Melles Griot 543-MA-03 overlaid with transmission specifications for two excitation filters. 48

23 Expanded view of illumination system at entrance prism and fused silica substrate showing entrance angle θ_{in}, angle of incidence at entrance θ_1, angle of refraction at entrance θ_2, and angle of incidence for TIR θ_i. 50

24 TIR angle of incidence θ_i, penetration depth d_z, and evanescent gain G_e variation with a $\pm 5°$ variation in entrance angle θ_{in} for the 50

25 Estimated evanescent wave intensity at origin for different e^{-2} beam radii, a, across different entrance angles, θ_{in}. Shown for illumination at $\lambda_{ex} = 514$ nm; illumination at $\lambda_{ex} = 488$ nm demonstrates similar behavior, but all values are approximately 2.5% lower. 52

26 Illustration of imaging system 53

27 Characterization of camera for two combinations of exposure time and multiplication gain settings. Cubic fits are used to correct camera nonlinearities in image processing. 57

28 Illustration of typical illumination and variables used to describe the interrogation region. 59

29 Interrogation depths (blue lines) and centroids (red lines) plotted against SBR ratio for three different penetration depths. 61

30 Illustration of (a) top view and (b) side view of calibration cell. (c) Illustration of scattering when illumination is incident upon adhesive. Figure not drawn to scale. 65

31 Illustration of (a) top view and (b) side view of calibration lid with temperature control loop coil and inlet and outlet of recirculation loop. Figure not drawn to scale. 66

32 Schematic of an experimental series, showing individual image sequences and individual images. Also shown are indexing subscripts i, j, and k. 74

33 The twentieth image (i.e. $k = 20$) from the image sequence $\mathscr{G}_{ijk}$ taken at 25℃. 74

34 Time-averaged image $\mathscr{G}_{ij}$ taken at 25℃. Random noise is reduced in the time-averaged image as compared to the single image from the sequence shown in Figure 33. 76

35 Dark noise subtraction: (a) time-averaged dark noise image; (b) time-averaged image after dark noise subtraction (result of subtracting Figure 35a from Figure 34). 76

36 Corrected image $\mathscr{C}_{ij}$ taken at 25℃. Image is the result of applying equation II.35 to each pixel of Figure 35b. 77

37 Masking: (a) binary mask; (b) product of element-by-element multiplication of binary-mask (Figure 37a) with corrected image (Figure 36). 79

38 Normalizing process: (a) masked, corrected image at 25℃; (b) masked, corrected normalizing image at 30℃; (c) normalized image at 25℃, the quotient of (a) divided by (b). 80

39 Representative images illustrating binning the individual pixels of a normalized image for an image sequence at 55℃: (a) original image of normalized fluorescence intensity at full spatial resolution; (b) image after binning image (a) over 11×11 pixels (corresponding to a spatial resolution of 16 μm); (c) image after binning image (a) over 69 x 69 pixels, corresponding to a spatial resolution of 100 μm. Images are false colored by normalized fluorescence intensity. 82

40 Spatially-averaged total fluorescence intensity vs. temperature for the first experimental run. Data points were generated by spatial-averaging of corrected image values. Error bars are the spatial standard deviation of the corrected images. 85

41 Spatially-averaged total fluorescence intensity vs. temperature for the second experimental run. Data points were generated by spatial-averaging of corrected image values. Error bars are the spatial standard deviation of the corrected images. 86

42 Normalized data points plotted versus Θ with a linear least-squares fit: $F = 1 + 0.0135\Theta$. The error bars are the combined single-pixel precision uncertainty and measurement uncertainty for each data point estimated in appendix A.3.2.4. 88

43 Normalized data points plotted versus Θ with 95% prediction bounds. 91

44 Variations in illumination with respect to time for three different experimental runs. Mean values vary by as much as 2.1%. Error bars are the spatial standard deviations, which typically vary between 1.2% and 2.4%. 93

45 Index of refraction of (a) water and (b) fused silica as a function of temperature. Based upon data from [31] for water and [84] for fused silica. 94

46 Shift in evanescent location for $r = 30$ mm versus temperature difference of entrance prism. Three different entrance angles are shown. . . 96

47 Time-average, corrected images captured at surface temperatures of (a) 20.4℃ and (b) 55.2℃. Direction of illumination propagation is from lower-right to upper-left. Images are in false color. 97

48 Result of normalizing the image of Figure 47a by the image of Figure 47b. (a) The normalized image without filtering; (b) the normalized image after a 15×15 pixel median filter. Images are in false color. . . 98

49 Experimental results with optical path length through fused silica of approximately 4 cm. *(a)* Time-averaged, corrected fluorescence intensity vs. surface temperature; *(b)* normalized fluorescence intensity vs. normalized surface temperature. 100

50 Direct and secondary effect of movement of evanescent-wave illumination. (a) normalizing image at 20.3℃; (b) image captured at 55.1℃: illumination has shifted toward lower right corner and possible diffraction pattern is present in upper left corner; (c) masked normalized fluorescence intensity image for image at 55.1℃ normalized by image at 20.3℃; (d) spatial bias is still present after 15×15 pixel median filter is applied to the image. 101

51 Change in ratio of refractive index n defined as $n = n_{H_2O}/n_{SiO_2}$ with temperature. 102

52 Modeled change in normalized fluorescence intensity due to variation in penetration depth, evanescent gain with temperature. These variations in penetration depth and evanescent gain are due to the variation of θ_i and n with temperature. 103

53 Time-averaged, corrected fluorescence intensity plotted against surface temperature for two experimental runs for 10 μM fluorescein solution in de-ionized water (pH≈5.7) Considerable hysteresis and experimental scatter are present, which can be attributed to adsorption. 106

54 Normalized fluorescence intensity vs. normalized surface temperature for 10 μM fluorescein solution in de-ionized water (pH≈5.7). The fluorescence temperature-sensitivity was determined to be dF/dT = 1.5%/℃, but experimental scatter due to adsorption increased uncertainity to 5.6℃ (95% confidence). 107

A.1 Calibration curves relating corrected pixel value (power incident upon CCD array) to reported grayscale value. 114

A.2 Plot of expanded uncertainty (95% confidence) of corrected pixel values with respect to corrected pixel values. 115

A.3 Expanded resolution uncertainty (95% confidence) of camera after correction for camera non-linearity. 117

A.4 Maximum difference between 68.3% prediction bounds and linear fit of experimental data. 120

A.5 Uncertainty of normalized data points for measurement and precision uncertainties. Precision uncertainties are shown for single-pixel measurements and the mean of an entire image. 122

A.6 Expanded uncertainty (95% confidence) for each data point based upon entire 715 × 950 μm viewfield. 124

A.7 Expanded uncertainty (95% confidence) of a single-pixel temperature measurment for each data point based. Single-pixel resolution is 1.5 × 1.5 μm. 125

A.8 Expanded uncertainty (95% confidence) of a temperature measurement based upon bins of 16 × 16 μm (11 × 11 pixels) and 100 × 100 μm (69 × 69 pixels). 126

B.1 Contribution of fluorophore adsorbed to the surface to fluorescent intensity measurements. 130

B.2 Normalized fluorescence intensity vs. temperature difference for rhodamine B. Arrows in direction of increasing time indicate order of experimental data points. Non-linear relationship indicates that the calibration curve is dependent upon normalizing temperature T_n. The normalizing temperature is T_n = 20 ℃ and the error bars are the spatial standard deviations of the normalized images. 133

B.3 Normalized fluorescence intensity vs. temperature difference of rhodamine B with increasing temperature. The normalizing temperature is $T_n = 20$ ℃ and the error bars are the spatial standard deviations of the normalized images. 134

B.4 Normalized fluorescence intensity vs. temperature difference for rhodamine B solution with charge inversion. 139

B.5 Time-averaged raw grayscale images corresponding to (a) first, (b) penultimate and (c) final data points for 10x objective. Images in left column were under evanescent-wave illumination and in the right column were under epi-illumination. Images are in false color. 141

C.1 Illustration of microchannel dimensions and components. 144

C.2 Illustration of temperature gradient device. 146

C.3 Placement of temperature gradient device relative to microchannel (dotted lines). 149

C.4 Illustration of structures modeled in FLUENT: (a) microscope stage (black) with footprint of fused silica substrate (light gray); (b) fused silica substrate (light gray), water flowing through channel (blue), and footprint of stainless steel structure (green); (c) all structures shown including stainless steel structure (green), hot block (red) and cold block (blue). 153

C.5 Temperature field for simulation with $Q = 1$mL/hr, $T_H = 58$℃ and $T_L = 2$℃: (a) temperature contours across channel at plane of thermocouple; (b) plot of variation in temperature with respect to location. . 155

C.6 Linear relationship between temperature gradient predicted by FLUENT and the external temperature gradient. 156

C.7 Corrected grayscale (left column) and normalized (right column) representative images. Experimental parameters for three image pairs are given in table C.2 Corrected images are false colored according to corrected grayscale value (scale:0-100), while normalized images are false colored according to temperature ([℃]). 158

C.8 Representative images of temperature profile generation: (a) temperature estimates in $x-y$ coordinate system after median pass filter; (b) temperature estimates in $r-s$ coordinate system; (c) average temperature profile with fit. Images are false colored by temperature ([℃]). . 160

C.9 Estimated channel temperature gradients from TIR-FMT measurements plotted against external temperature gradient. 161

C.10 Mid-width channel temperature estimated from TIR-FMT and measured by channel thermocouple plotted against average block temperature. 162

C.11 Example of variations in fluorescence intensity for different normalizing image sequences in same experimental series. Corrected image are shown in left column: (a) first image sequence $\mathscr{C}$ and (b) last image sequence $\mathscr{C}'$ of experimental series. Normalized images are shown in right column: (c) $\mathscr{N} = \mathscr{C}'/\mathscr{C}$ and (d) $\mathscr{N} = \mathscr{C}/\mathscr{C}'$ 164

C.12 Simulation of false temperature gradient generated by displacement of a Gaussian profile. Above: normalizing intensity and normalizing intensity shifted by $0.02a = 6\mu$m; below: false temperature gradient. . 167

C.13 Estimated false temperature gradient generated by real temperature gradient due to displacement of evanescent-wave illumination. Estimations are based upon five different normalizing images. 169

C.14 Images with random variations in fluorescent intensity caused by random fluctuation in illuminating intensity. (a) Averaged and corrected image ($\mathscr{C}^{\phi}$) with abnormal fluorescent intensity; (b) Averaged and corrected normalizing ($\mathscr{C}^{n}$) image used for image (a); (c) normalized image of $\mathscr{C}^{\phi}$ by $\mathscr{C}^{n}$: $\mathscr{N}^{\phi} = \mathscr{C}^{\phi}/\mathscr{C}^{n}$. 171

SUMMARY

The exponential growth in transistor density has created huge thermal management challenges for the microelectronics industry. To address these challenges, forced-convection cooling through microchannels has been proposed as a method of compactly cooling microelectronics. However, to effectively design systems of microchannels it is necessary for scientists and engineers to understand thermal transport characteristics of microchannels, specifically the local convective heat transfer coefficient. Analytical solutions are not available due to the spatially and temporally varying heat fluxes typically generated by microelectronics. To experimentally determine the convective heat transfer coefficient of microchannels it is necessary to measure both the bulk and surface temperature fields.

This investigation aims to develop a technique, named Total Internal Reflection Fluorescent Micro-Thermometry (TIR-FMT), to measure the temperature of water within several hundred nanometers of a wall—effectively, the surface temperature of the wall. Specifically, TIR-FMT is a combination of Total Internal Reflection (TIR) Microscopy and Laser Induced Fluorescence (LIF) Thermometry. In TIR-FMT, Total Internal Reflection is used to generate an evanescent wave in the water near the wall. The intensity of this evanescent wave decays exponentially with distance from the wall, with a e^{-1} lengthscale of the order of 100 nm. A fluorophore (fluorescent species) dissolved in the water can absorb a photon when illuminated by the evanescent wave. An excited fluorophore subsequently emits a red-shifted photon that is called fluorescence. The probability that the fluorophore is excited and emits a fluorescent emission is temperature-dependent. Therefore, by monitoring the intensity

of the fluorescence a correlation can be made to the temperature of the region of illumination.

In this investigation, two major obstacles were encountered—variations in fluorophore concentration and variations in illumination. Spatial and temporal variations in concentration due to adsorption of fluorophore to the wall significantly biased the fluorescence intensity. It was found that adsorption was significantly lower for fluorescein as compared to rhodamine B, the most common fluorophore for LIF Thermometry. Furthermore, the influence of adsorption could be virtually eliminated by using fluorescein buffered to a pH of 9.2.

Variations in illumination were found to be caused by a combination of temporal instabilities in the laser intensity and changes in the location of evanescent-wave illumination due to temperature-induced changes in the refractive index of fused silica. Movement of the location of evanescent-wave illumination induced a spatial bias in the fluorescence intensity and limited the accuracy and spatial resolution of the technique. The error caused by the variations in illumination was reduced, but not eliminated, by decreasing the optical path length through the substrate.

Using the TIR-FMT technique the temperature dependence of the fluorescence intensity from buffered fluorescein (pH=9.2) was determined to be 1.35%/℃. TIR-FMT can be used to measure the temperature of a fluorophore solution within 600 nm of a wall across a temperature range of 12.5-55℃. The r.m.s. uncertainty (95% confidence) of the temperature measured over a single 1.5×1.5 μm pixel was determined to be 2.4℃. Across the entire 715×950 μm microscope viewfield, a r.m.s. uncertainty of 1.5℃ was obtained. By spatial averaging, r.m.s. uncertainties of 2.0℃ and 1.8℃ were attained with spatial resolutions of 16×16 μm and 100×100 μm, respectively.

CHAPTER I

INTRODUCTION

1.1 Motivation and Objectives

According to Gordon Moore's 1965 prediction, the density of transistors on a computer chip doubles every twenty-four months. Despite many technological hurdles, the microelectronics industry has kept pace with Moore's Law for the past four decades and will likely maintain this pace for the near future. The most recent commercial microprocessors from Intel have average feature sizes of 65 nm; the International Technology Roadmap for Semiconductors (ITRS) predicts features sizes of 45 and 32 nm to be available in 2010 and 2013, respectively [38].

The exponential growth in transistor density has created huge thermal management challenges. The average heat flux generated by a single microprocessor will exceed 100 W/cm^2 within the next few years. These challenges are reflected in ITRS projections that the junction to ambient thermal resistance needs to halve from its current value of 0.139℃/W to 0.071℃/W by 2010 for high-performance chip packages [38]. The thermal challenges are further exacerbated by marked spatial and temporal variations in heat flux and further reductions in overall system size. Despite recent advances in heat sinks, forced-air cooling will soon become obsolete and new methods, such as single-phase forced-liquid cooling, two-phase evaporative cooling involving boiling, and structural enhancements, will need to be developed and implemented.

The mass and thermal transport of fluids flowing through individual and arrays of microchannels has been studied for more than two decades with the objective of using this understanding to improve heat transfer in integrated circuits packaging.

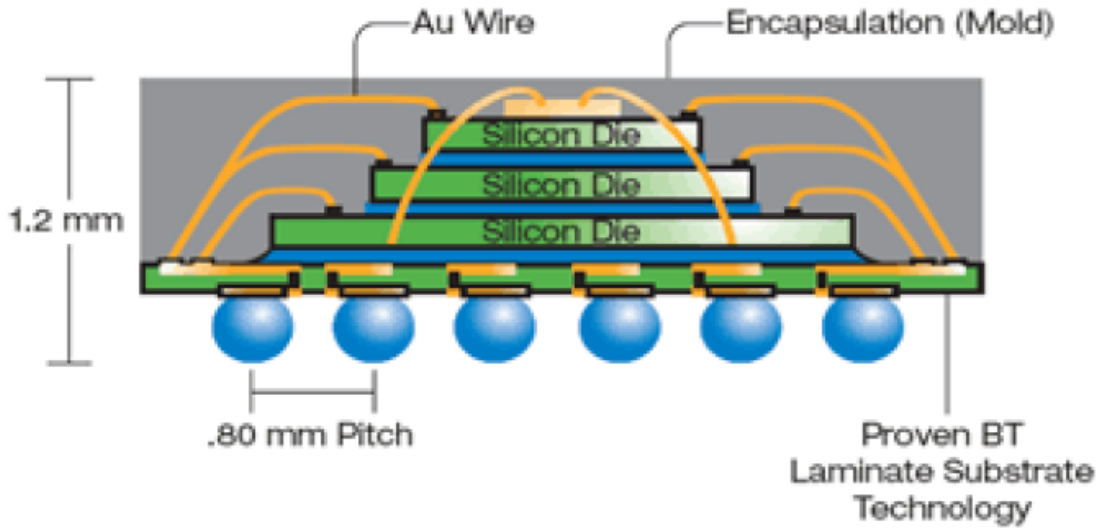

Figure 1: Proposed three-dimensional chip architecture via stacked dies [38].

Tuckerman and Pease demonstrated that the convective heat transfer coefficient, h, should scale inversely with channel width in laminar internal flows [85]. Developing and evaluating effective microfabricated liquid cooling systems integrated within the microprocessors requires more accurate models of fluid and thermal transport for complex microscale geometries. Moreover, as microelectronics evolve from planar to three-dimensional stacked-die architectures (Figure 1), the layout and hence geometry of the microchannel arrays will become even more complex.

The most basic configuration for single-phase cooling of microelectronics with microchannels consists of a single layer of parallel microchannels thermally coupled to the integrated circuit via a high thermal conductivity heat spreader, as illustrated in Figure 2. The rate of conductive heat transfer in solid materials follows Fourier's Law

$$\vec{q} = k\vec{\nabla}T \tag{I.1}$$

where $\vec{q}$ is the heat flux, k is the thermal conductivity, and T is the temperature. Convective heat transfer at the interface between the microchannel wall and the fluid

is assumed to act in the direction normal to the wall and can be described by

$$q = h\,(T_s - T_\infty) \tag{I.2}$$

where h is the local convective coefficient, T_s is the temperature at the interface, and T_∞ is the bulk average fluid temperature. At the interface the temperature and heat flux must be continuous, and hence

$$q = k\frac{dT}{dz} = h(T_s - T_\infty) \tag{I.3}$$

For the ideal case of one-dimensional conduction with hydro-dynamically and thermally fully-developed flow, h can be determined from well-known exact analytical solutions. For example, the Nusselt number

$$Nu = \frac{h_x x}{k} = \frac{48}{11} \qquad \text{and} \qquad Nu = \frac{h_x x}{k} = 3.6568 \tag{I.4}$$

for circular channels with uniform heat flux and uniform wall temperature, respectively.

However, various studies have shown that the heat flux generated by microprocessors has marked spatial and temporal variation [88], [41]. In these cases the Nusselt number can only be determined if the spatially varying surface temperature or heat flux is known at every spatial location [27]. At present, there are few methods for measuring both the surface and bulk fluid temperatures in microchannels with good spatial and temporal resolution. As pointed out in the ITRS report,

> "As the thermal resistances are made smaller and smaller for high power devices, thermal metrology with better resolution and capabilities is required... Efficient accurate thermal sensors to support accurate understanding of Joule heating temperature distribution in the package will be desirable [38]."

The objective of this Master's thesis is to develop a technique that provides spatially well-resolved near-wall temperature measurements, effectively measurements

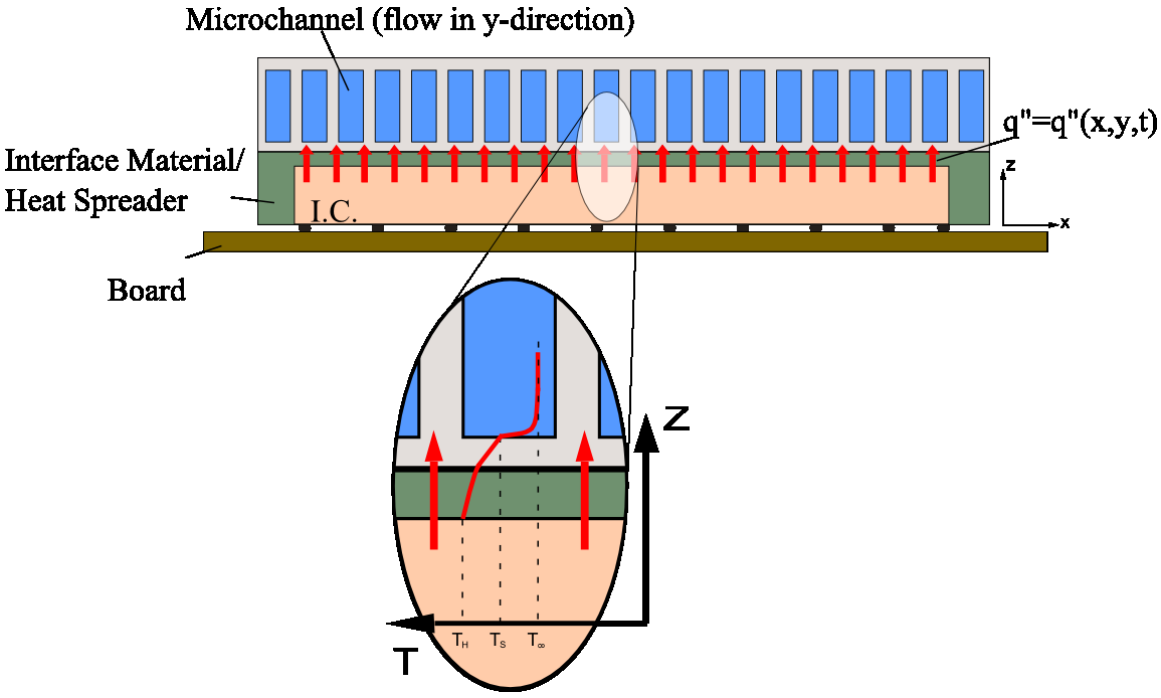

Figure 2: Basic configuration for single-phase convective cooling of microelectronic package with microchannels

of the surface temperature, to address these metrology needs. Specifically the technique is a combination of two established techniques: Laser Induced Fluorescent (LIF) Thermometry and Total Internal Reflection Fluorescent Microscopy (TIRFM). Therefore, the technique is called Total Internal Reflection Fluorescent Micro-Thermometry (TIR-FMT). Strictly speaking, the TIR-FMT technique measures the average temperature of the fluid within 600 nm or less of the wall[1]. This temperature is, however, essentially the temperature at the surface of the microchannel wall. This thesis evaluates the accuracy, temporal resolution and in-plane spatial resolution of the TIR-FMT technique.

[1]see sections 2.2.3 and 3.1.1

1.2 Literature Review

1.2.1 Review of Fluid and Thermal Transport in Microchannels

Over the last decade, the transport of fluids through conduits with overall dimension of 500 microns or less has become a major field of study in fluid mechanics, motivated in part by new microscale biochemical and biomedical sensors. As such,there exists a considerable body of both theoretical and experimental research on fluid and thermal transport in microchannels.

1.2.1.1 Theory

The flow of a fluid through a microchannel can be characterized in terms of a mass, linear momentum and energy balance:

$$0 = \partial_o \rho + \partial_i(\rho v_i) \tag{I.5}$$

$$\rho \frac{Dv_i}{Dt} = \rho F_i - \partial_i p + \mu \partial_k \partial_k v_i \tag{I.6}$$

$$\rho \frac{D}{Dt}\left(e + \frac{v_k v_k}{2}\right) = -\partial_j q_j + \partial_b(T_{ab} v_a) + \rho F_d v_d \tag{I.7}$$

where ρ is the fluid density, e is the thermodynamic internal energy per unit mass, v_i is the velocity, μ is the fluid dynamic viscosity, q_i is the heat flux, T_{ij} is the stress tensor, and F_i is the body force per unit mass. For a Newtonian fluid that follows Fourier's Law, these equations take the form of the well-known Navier-Stokes equations [61]:

$$\frac{D\rho}{Dt} = -\rho \partial_i v_i \tag{I.8}$$

$$\rho \frac{Dv_i}{Dt} = -\partial_i p + \rho g_i - \frac{2}{3}\partial_j\left(\mu \partial_j v_j\right) + 2\partial_j\left(\mu S_{ji}\right) \tag{I.9}$$

$$\rho c_p \frac{De}{Dt} = \partial_j\left(k \partial_j T\right) - \frac{2}{3}\mu\left(\partial_j v_j\right)^2 + 2\mu S_{ij} S_{ji} + \beta T \frac{Dp}{Dt} \tag{I.10}$$

These equations are valid as long the Continuum Hypothesis is valid and thermodynamic quasi-equilibrium is maintained.

Kinetic theory can be used to assess the validity of macroscale continuum-based analysis and determine if the Navier-Stokes equations are valid for flows of gases. The Knudsen number, Kn, is a dimensionless parameter that is defined as

$$Kn = \frac{\lambda}{L_c} \tag{I.11}$$

where λ is the mean free path, and L_c is the characteristic flow length scale. From kinetic theory, we know that for gases, the mean free path is

$$\lambda_{gas} = \frac{k_b T}{\sqrt{2}\pi p d} \tag{I.12}$$

where k_b is Boltzmann's constant, d is the diameter of exclusion around a molecule, p is the pressure, and T is the temperature. At $Kn \leq 10^{-3}$, the gas is in thermodynamic quasi-equilibrium, and the gas can be considered a continuum. For $10^{-3} \leq Kn \leq 0.1$, the Navier-Stokes equations can still be used to model the flow using modified boundary conditions that include a temperature jump and a non-zero slip velocity. At higher $Kn = 0.1 - 10$, we have a transitional regime where continuum-based approaches break down. At very high $Kn > 10$, we have free molecular flow that can be modeled by Monte Carlo methods.

Unfortunately, kinetic theory is not valid for liquids and there is no well-established theory that demarcates the limitations of the Navier-Stokes equations for liquid flows. Molecular-dynamics simulations of liquids have been undertaken to study the interactions between fluid and solid molecules at an interface. In these simulations interactions between molecules are modeled. One such model is the Lennard-Jones 6-12 potential:

$$V_{LJ}(r) = 4\epsilon \left[\left(\frac{\sigma}{r}\right)^{12} - \left(\frac{\sigma}{r}\right)^{6} \right] \tag{I.13}$$

where r is the distance between molecules and ϵ and σ are characteristic energy and length scales. Simulations have shown that the slip length and extent of momentum transfer is strongly influenced by solid lattice structure and strength of wall-fluid interactions [81],[80],[10], [50].

1.2.1.2 Experimental Studies

The incomplete theoretical framework is joined by contradictory and inconclusive experimental studies. Initial studies on fluid dynamics and convective heat transfer inside microchannels suggested deviation from standard correlations; however, further research has indicated that initial deviations were likely due to combinations of experimental problems, not new physics.

Mala and Li [52] observed higher than expected pressure loss across microtubes and suggested the deviation from traditional theory may be caused by early transition from laminar to turbulent flow or surface roughness effects. Adams et al. [2] observed greater than expected Nusselt numbers in microchannels. However, others have suggested exactly the opposite-that Nusselt numbers in microchannels are less than those values suggested by conventional correlations [66].

In laminar flow with optically smooth surfaces with fully degassed and clean fluids, there is relatively good agreement between friction factors and Nusselt numbers for microchannels and conventional channels [27]. This strongly suggests that inadequate knowledge of surface features is responsible for the experimental breakdown of macroscale relationships in microchannels. For microscale devices, the ratio of surface forces to body forces is several orders of magnitude higher than for macroscale devices [24]. As such, surface forces dominate and should be considered more rigorously. Several investigators have used the concept of roughness velocity to characterize the effect of surface roughness on laminar flows in microchannels [66].

The lack of a theoretical basis and contradictory experimental evidence has led to a lively discussion within the scientific community. Gad-el-Hak [23] strives to establish a theoretical basis grounded in molecular dynamics simulations to determine when special treatment is necessary for liquid flows in microchannels. Herwig and Hausner [33], on the other hand, maintain that the data scatter and experimental disagreements are not due to any special microscale phenomena, but can be attributed

to a combination of differences in:

1. surface roughness and other configuration irregularities;
2. cross-sectional geometry;
3. suspended particles;
4. surfaces forces (e.g. electro-kinetic effects);
5. fouling and deposition of particles;
6. compressibility;
7. property variations; and
8. experimental errors and uncertainties.

Further studies have shown that common sources of error include:

1. parallel channel oscillation;
2. non-uniform flow distribution;
3. non-identical channels;
4. neglecting axial heat conduction [83]; and
5. neglecting effects of dissolved gases [1].

Although there are several velocimetry studies of microscale liquid flows, there are far fewer thermometry studies at these scales. This lack is due in part to measurement limitations. Most experimental studies of thermal transport rely upon measurements of bulk inlet and outlet temperatures, and outer-wall heat fluxes and temperatures. While some investigators have used IR thermography to examine surface temperature distributions inside the microchannel, the accuracy and robustness of this technique

remains undetermined. Additional non-intrusive thermometry techniques that can be used in microchannels flows would therefore be valuable in developing and evaluating new microelectronic cooling technologies [25].

1.2.2 Microscale Thermometry Techniques

Temperature is a fundamental thermo-physical quantity that plays a vital role in almost all fields of science. Many physical properties of materials are dependent upon temperature, therefore accounting for temperature variation is a critical, often frustrating, aspect of engineering design. While temperature may be a difficult parameter to control, it's omnipresence provides several avenues for thermometry. Figure 3 gives an overview of various thermometry techniques that have been used at the micro- and nano- scales. This section is intended to provide a brief overview of thermometry techniques, and is not all-inclusive. Those interested in more complete coverage should refer to one of several excellent reviews on the subject [5],[12],[92].

1.2.2.1 Solid State Thermometry

For the past several decades the demands of the microelectronics industry have motivated the development of solid state thermometry techniques with micron and submicron resolution, resulting in a wide variety of scientifically sophisticated techniques. Micro- and nanoscale thermometry techniques can be categorized into electrical, optical far-field, optical near-field and near-field techniques.

Electrical techniques are well-established at the macro-scale in the form of thermocouples, RTDs and thermistors. Such devices have been extended to the microscale via microfabrication techniques and have excellent accuracy. Microscale thermocouples (μTC) based on a thin-film Pt-Cr design have been demonstrated with sub-100 nm resolution [75]. Park and Taya [63] have demonstrated a 10 x 10 μTC array and used it to obtain temperature gradient measurements over a 9 mm square area. However, difficulties in microfabrication make it practically difficult to make large arrays

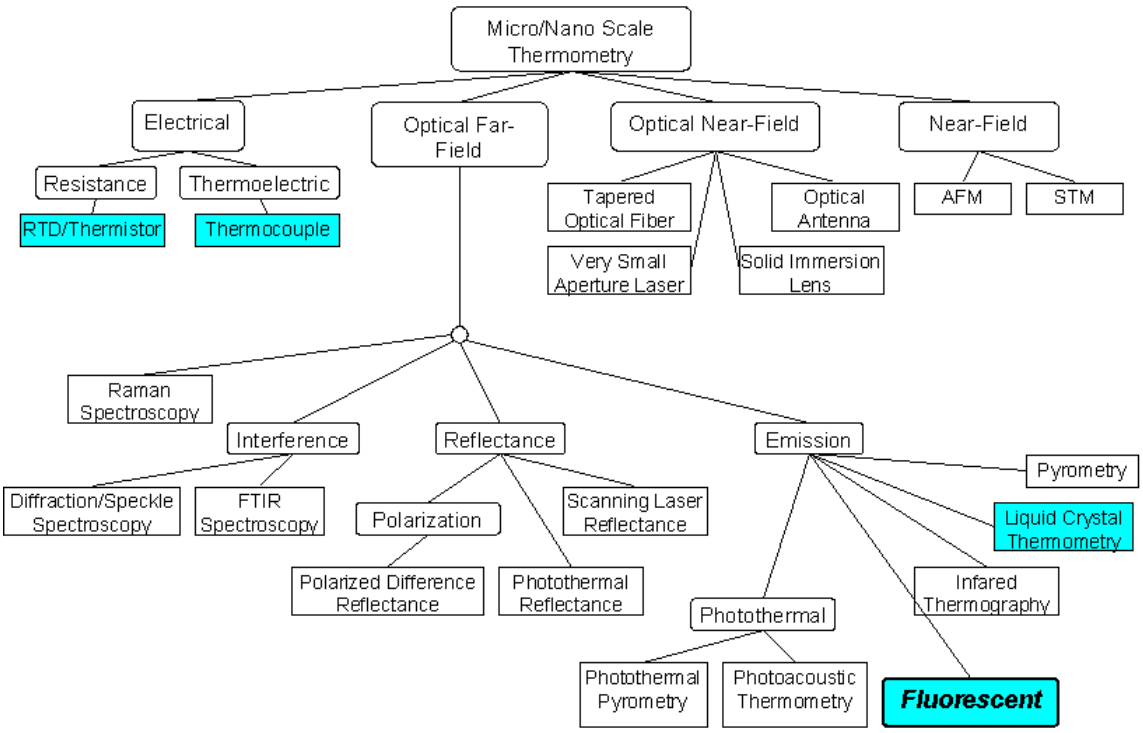

Figure 3: Tree-diagram of different thermometry techniques

of such devices.

Optical far-field techniques are based upon variations in various optical properties of materials. This family of techniques includes interference-, reflectance- and pyrometry-based methods. Interference techniques exploit the changes in the optical path length of a system due to thermal expansion and variations in refractive index with temperature. Reflectance techniques relate temperature to the polarization and intensity of light reflected from a surface. Finally, pyrometry and IR thermography measure the light emitted from a surface in a specific spectral band. The emissivity can be used to relate the intensity of the light to Planck's blackbody distribution and the surface's temperature.

Photothermal Thermometry and FTIR Spectroscopy are both optical far-field techniques that are essentially variations of reflectance and pyrometry techniques, respectively. Photothermal thermometry measures temperature with a high temporal

resolution independent of background radiation by using a high power laser pulse ('pump') to locally heats the test material and a second low power laser pulse ('probe') to measure the modulated reflectance or emission of the heated material. FTIR Spectrometry relates temperature to the inverse Fourier transform of a modulated radiation source.

The spatial resolution of optical far-field techniques is determined by the diffraction limit d, where only features with a separation exceeding a minimum distance can be resolved. This minimum distance

$$d = \frac{\lambda}{2 \cdot NA} \tag{I.14}$$

where λ is the wavelength of the illuminating light, and NA is the numerical aperture of the imaging system. Optical near-field thermometry techniques are able to achieve spatial resolutions below this limit, albeit over a very limited field of view. In most implementations, such techniques measure temperature at a single spatial location, and the temperature probe must be scanned to obtain field data. In these techniques illumination is limited to a very small region of interrogation. This has been accomplished with a tapered optical fiber and with a very small aperture laser (VSAL). An optical antenna structure has been used to measure temperatures with a spot size well below the diffraction limit [29].

Solid immersion lenses achieve high spatial resolution by utilizing lenses fabricated from high refractive index materials that are directly in contact with the measured surface. The numerical aperture, NA of a lens is proportional to the refractive index of the medium between the lens and specimen n and the half angle of the the cone of light that the lens can focus α

$$NA = n \sin \alpha \tag{I.15}$$

Since d is inversely proportional to NA (eq. I.14), increasing n effectively reduces the minimum resolvable spatial dimension.

Non-optical near field thermometry techniques include methods based upon the Scanning Tunneling Microscope (STM) and the Atomic Force Microscope (AFM). Both types of microscopy utilize interatomic forces to maintain a constant force between the medium and the probe tip. STM and AFM were originally developed for surface topography measurements, but they have been equipped with electrically-based temperature probes (i.e., thermocouples or RTDs) and recently extended to local point temperature measurements with sub-nanometer spatial resolution. Temperature profiles can then be obtained using scanning methods.

1.2.2.2 Liquid-Phase Thermometry

Very few of the methods illustrated in Figure 3 (highlighted in blue) are commonly used to measure the temperature of liquids flowing through microchannels. Microthermocouples (μTCs) have been used to provide single-point, bulk temperature measurements [11],[3]. Unfortunately, geometric and fabrication constraints limit the extent and number of μTCs that can be integrated into microchannel walls. Despite continued advances in miniaturization, μTCs are inherently intrusive, disturbing the flow, and are therefore poorly suited for bulk liquid temperature measurements.

Thermochromic liquid crystals have been deposited on surfaces to measure surface temperatures and encapsulated to measure liquid-phase temperatures. When illuminated with white light, encapsulated liquid crystals reflect light based upon the local fluid temperature. While the resulting temperature visualization images are very accurate, liquid crystal thermography is hindered by its limited bandwidth, typically less than 10℃. Park *et al.* reported an accuracy of 2-3% (0.05-0.075℃) over a temperature bandwidth of $\Delta T = 2.5$℃ [62]; Fujisawa *et al.* reported an accuracy of 0.13℃ over a temperature bandwidth of $\Delta T = 5$℃ [22].

Both the intensity and lifetime of the emissions from phosphorescent species,

specifically the phosphorescent supramolecules originally developed for molecular tagging velocimetry applications, have been used to measure temperatures. Thomson and Maynes [82] demonstrated an intensity-based technique to measure temperatures between 20 and 50 ℃ with an accuracy of ± 1 ℃. Recently, Hu *et al.* [35] demonstrated a phosphorescence life-time based technique where a region of interest is marked with a UV laser. After a short delay, t_o, the decaying phosphorescence is integrated over a time period, Δt. Accuracies of ± 0.2 ℃ over a temperature bandwidth of $\Delta T = 4$ ℃ have been reported for this technique. It has been demonstrated that the normalized phosphorescent signal is a function of T, t_o and Δt and suggested that intensity-temperature sensitivity is tunable (by adjusting t_o and Δt) to 8.15-18.2 % per ℃ over a temperature range of 20∼45 ℃. Currently phosphorescence thermometry is limited by the low signal-to-noise ratio of the tracers and the expense and safetey issues associated with UV laseres.

1.2.3 Laser-Induced Fluorescent Thermometry

Fluorescent-based thermometry is at present the leading non-intrusive technique for measuring liquid-phase temperatures [51]. The intensity of fluorescent emissions have been found to be temperature dependent for several fluorophores (fluorescent molecules). In Laser-Induced Fluorescence (LIF) the fluorescence is excited with a laser source, and the emission is imaged in a different spectral bandwidth—thereby isolating the emission signal from illumination. There are three variations of laser induced fluorescent thermometry: 1) Combined Particle Image Velocimetry and Thermometry (PIV/T), 2) Fluorescence Lifetime Thermometry, and 3) Fluorescence Intensity Thermometry.

1.2.3.1 Combined Particle Image Velocimetry and Thermometry

Particle Image Velocimetry (PIV) is a common optical technique that captures sequential images of tracer particles to derive spatially and temporally resolved estimates of velocity. Performing a cross-correlation on regions of the sequential images yields an estimate of the displacement based upon the location of a cross-correlation peak. By dividing the displacement estimate by the time step between images, an estimate of the velocity can be made for each interrogation window. PIV has been used frequently at the macroscale and, more recently, at the microscale (μPIV) [71] and can provide sub-micron out-of-plane spatial resolution (nPIV) [90]. However, smaller length scales require smaller tracer particles; for particle diameters below about 1 micron, Brownian motion becomes an important factor.

Brownian motion refers to the random motion of small particles immersed in fluids. Though the discovery of Brownian motion is attributed to Robert Brown in 1827, it was Albert Einstein who derived a mathematical model for an infinite fluid in 1905 [20]. Einstein theorized that for large time scales, the expected root-mean-square (r.m.s) particle displacement is:

$$\Delta r = \sqrt{2D\Delta t} \tag{I.16}$$

where D is the diffusion coefficient and Δt is the time step between images. The diffusion coefficient is a function of fluid viscosity, μ, particle diameter, d, and temperature, T:

$$D = \frac{k_b T}{6\pi\mu d} \tag{I.17}$$

Though these Brownian fluctuations can be a problem for microscale velocity measurements, increasing the uncertainty in velocity measurements, these temperature-dependent fluctuations can be used to estimate temperatures in microscale flows.

Olsen and Adrian [59] derived relationships for the area under the cross-correlation

peaks and suggested that Brownian fluctuations could be used to measure the temperature inside a fluid. For a given fluid, the tracer particle diameter and fluid viscosity are known, so the width of the cross-correlation peak can be directly related to fluid temperature. Hohreiter *et al.* [34] experimentally verified this technique, obtaining temperature measurements in quiescent liquid with an uncertainty of ±3 ℃. Although PIV/T has the capability to simultaneously measure velocity and temperature, the temperature measurements from the PIV/T appear to have relatively low accuracy and limited spatial and temporal resolutions due to the size of the interrogation region and the large number of images required to generate reliable diffusivity estimates.

1.2.3.2 Fluorescence Lifetime Thermometry

Fluorescent Decay Thermometry has been proven to provide highly accurate temperature measurements based upon the decay over time of fluorescence intensity excited by pulsed excitation. This fluorescence intensity decays exponentially with time, and the $1/e$ time constant , τ, varies with temperature. To measure τ, the fluorescence intensities I_1 and I_2 are measured at two times t_1 and t_2, respectively, after a laser pulse excites a region of interest. The decay constant is then

$$\tau = \frac{t_2 - t_1}{\ln\left(\frac{I_1}{I_2}\right)} \tag{I.18}$$

Allison *et al.* used this technique to measure temperatures between 7 and 77 ℃ and suggested that accuracies of less than 0.1 ℃ were possible [4]. More elaborate, modulation-based methods of measuring the decay time have also been used to measure temperature [28],[91]. Fluorescence decay thermometry has only been used to measure the temperatures of exposed solid surfaces and embedded solid-state structures via fiber optics and has also been demonstrated for *in vitro* biological applications with a solid fluorescent material immersed in a liquid [76]. It has not however been used for liquid-phase studies to our knowledge

1.2.3.3 Fluorescence Intensity Thermometry

The intensity of emitted fluorescence is known to be a function of temperature, pH, viscosity, and solution chemistry for many different fluorescent species. Dual-emission or ratiometric fluorescence thermometry uses two fluorescent species—one temperature-sensitive fluorophore, and one temperature-insensitive fluorophore—with non-overlapping emission bands. The region of interest inside the fluid dyed with both fluorophores is illuminated by a laser, and the resultant fluorescence intensity is measured over both emission bands. The fluorescence intensity of the temperature-sensitive species is then normalized by the fluorescence intensity from the temperature-insensitive species to control for local variations in illumination and provide a direct measurement of the temperature distribution over the region of interest.

Coppeta and Rogers [15] used various fluorophores in aqueous solutions to measure the temperature and pH to an accuracy of ± 3% via a ratiometric technique. In theory, with a carefully selected combination of fluorescent molecules and a sufficient filtering/imaging system, one could simultaneously measure temperature, pH, and any other scalar quantity that influences fluorescent behavior of a molecule. Coolen *et al.* [14] and Seuntiëns *et al.* [74] demonstrated one-color/one-dye LIF thermometry using rhodamine B with over a range of 20-60 ℃ and 20-35 ℃, with accuracies of ±1.7 ℃ and ±0.1 ℃ respectively. Sakakibara and Adrian used two-color LIF thermometry using rhodamine B and rhodamine 110 and reported a random error of ∼1.5 ℃ [69]. With an improved imaging system and post-processing technique they were able to improve random error to ∼0.17 ℃ in their studies of Rayleigh-Benard convection [70]. Lavieille et al. demonstrated two-color LIF with one dye [48] and three-color, again with one fluorescent dye [47], to measure the temperature of evaporating and combusting ethanol droplets with a reported accuracy of 1 ℃ and 0.5-1 ℃, respectively. In these techniques, only a single dye is used, but its emission is monitored over two or three different spectral bands to improve the accuracy of the temperature measurments.

Several investigators have implemented LIF thermometry techniques at the microscale. Ross *et al.* [68] used buffered rhodamine B to measure the temperature field in electrokinetically driven flows inside of microchannels with reported precision of 0.03-3.5 ℃ and spatial and temporal resolutions of 1 μm and 33 ms, respectively. Kim and Kihm [43] used rhodamine B and rhodamine 110 in a ratiometric technique to study microscale free convection in a cuvette, reporting calibration uncertainties of ±2.964 ℃ and ±0.412 ℃ for 47 x 42 and 1200 x 800 μm fields of view. For free convection in the cuvette, r.m.s. deviations from computer predictions ranged from 2.3 ℃ to 0.92 ℃ for 19 x 19 μm and 76 x 76 μm fields of view.

1.3 Fluorescence

Fluorescence is a process whereby a molecule or material absorbs light of a particular wavelength and then emits light of a different and longer wavelength (Figure 4). Fluorescence microscopy, or imaging using fluorescent stains, has been utilized in the chemical and life sciences to selectively highlight or stain portions of a specimen. By selecting a fluorescent molecule with appropriate spectral characteristics that specifically binds to the region of interest in a specimen (e.g. a cell membrane) and illuminating with light at an appropriate wavelength, the stained portions of the specimen emit longer-wavelength fluorescence. When viewed under a microscope with appropriate wavelength filters, only the fluorescence is imaged. (Figure 5).

1.3.1 Fluorescent Mechanism

The basic mechanisms of fluorescence are illustrated by a Jablonski energy diagram showing the energy levels available to the electrons of the fluorescent species (i.e. fluorophore), as shown in Figure 6. Each fluorophore molecule contains a series of quantized energy levels denoted by $S_{n,p}$ and $T_{n,p}$ for singlet and triplet states, respectively. The subscript n denotes the different electron states ($n = 0, 1, 2, 3, \ldots$), while the subscript p denotes the energy levels in each state ($p = 0, 1, 2, 3, \ldots$) due to

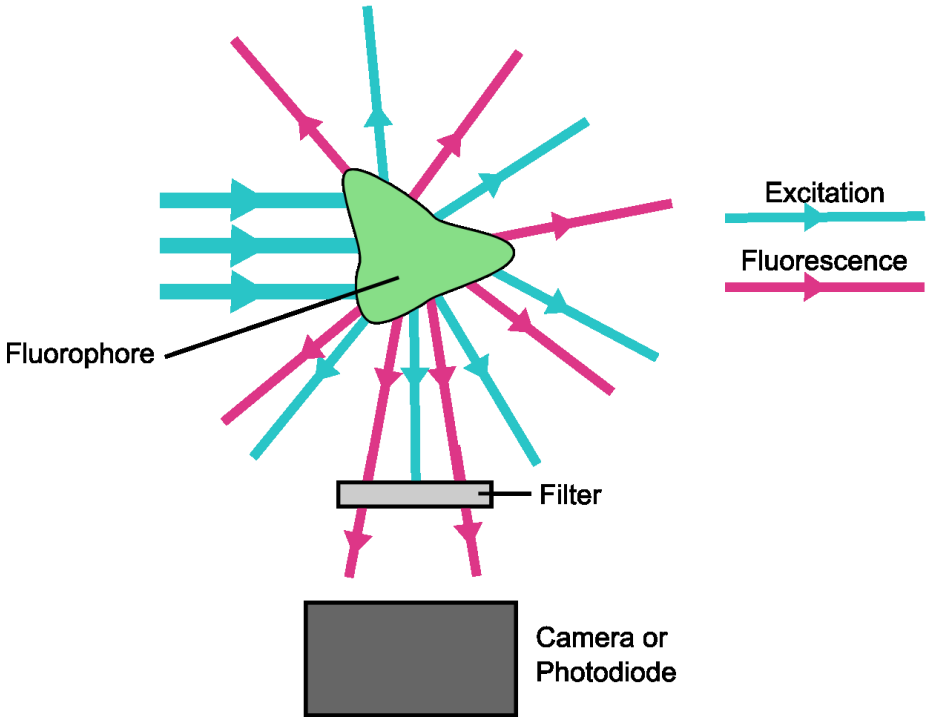

Figure 4: A simple illustration of fluorescence: excitation light is scattered and absorbed by a fluorophore; subsequent emission of fluorescence; fluorescence is isolated from excitation by an optical filter.

vibrational and rotational energy. When energy in the form of photons are incident upon the molecule, an electron moves to a higher energy state, increasing the energy of the molecule from the ground state $S_{0,p}$ to a higher energy state $S_{n,p}$ or $T_{n,p}$ (where $n > 0$) by absorbing a photon.

Fluorescence is basically a three-step process: absorption, relaxation, then emission [32]. The fluorescence process is described here for the energy levels shown in Figure 6. During the absorption step, an incident photon with energy $e_{ex} = h\nu_{ex}$ is absorbed and excites an electron from a ground state $S_{0,2}$ to a higher-energy excited single state $S_{1,3}$. The energy of the incident photon has to be balanced by the increase in energy between $S_{0,2}$ and $S_{1,3}$; hence, $e_{ex} = S_{1,3} - S_{0,2}$. During the relaxation step the electron always returns to the lowest energy level of the first single state, $S_{1,0}$, and the vibrational and rotational energy associated with this transition is dissipated as heat to the surrounding medium. During the final emission step, the electron returns to

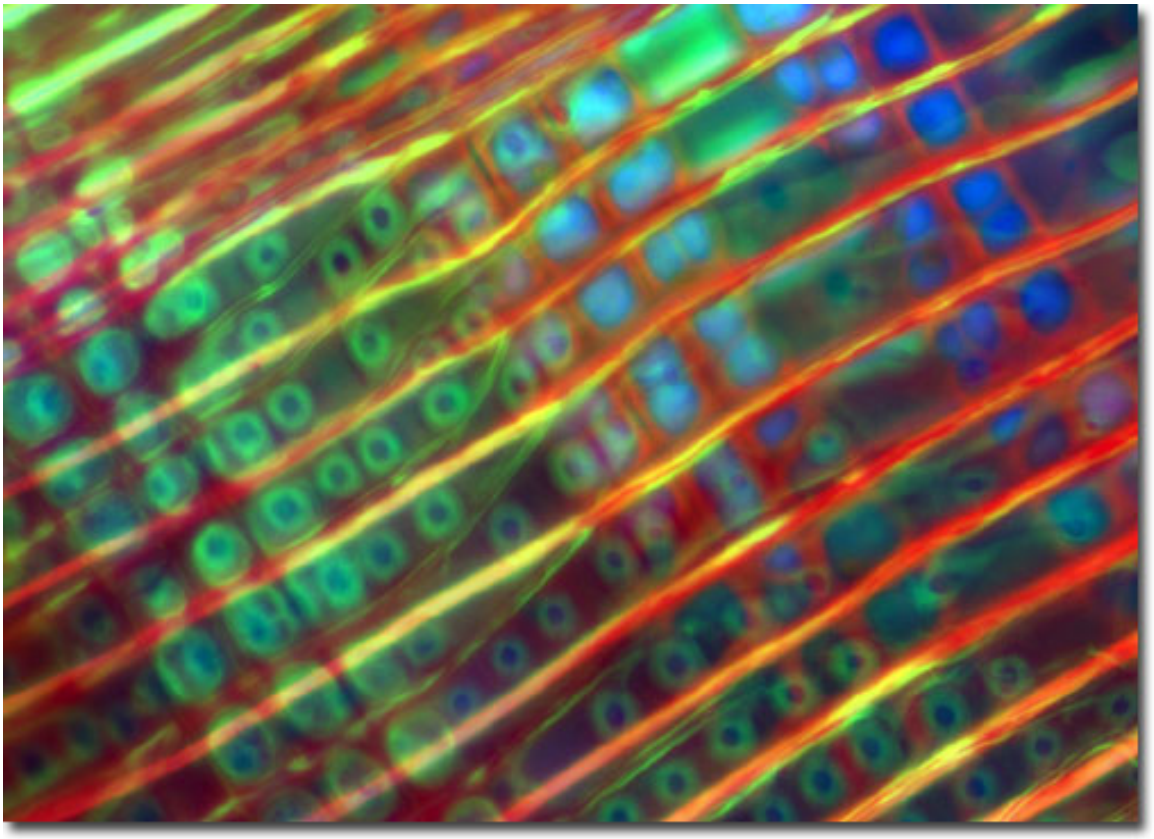

Figure 5: Example of fluorescent photomicrograph. Image is of pine wood highlighted with fluorescent dye. Reproduced with permission [18]

the ground state and a lower-energy photon, of energy $e_{em} = S_{1,0} - S_{0,2} = h\nu_{em} < e_{ex}$ is emitted. This lower-energy, longer-wavelength photon is the fluorescence.

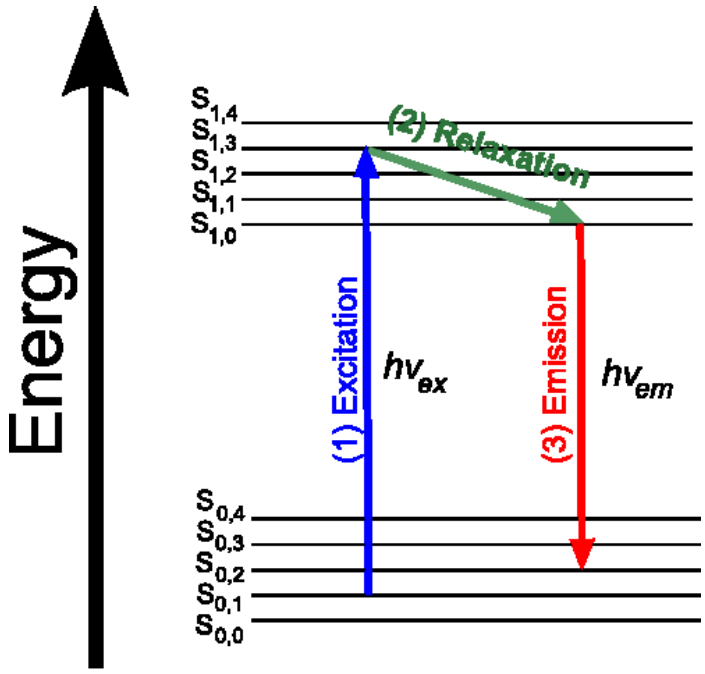

Figure 6: Simple Jablonski energy diagram showing: 1) excitation from a ground state to an excited singlet state; 2) relaxation from the excited singlet state to the un-excited singlet state; and 3) emission of fluorescence as electron drops from the un-excited singlet state to a ground state.

The absorption and emission spectra of fluorescent molecules typically consist of a wide absorption band and a red-shifted, relatively narrow emission band. This behavior can be understood by considering a more complicated version of the Jablonski energy diagram (Figure 7). During absorption an electron is elevated from the ground state to a higher energy state. There are many possible electron states ($n = 1, 2, 3, \ldots$) and energy levels ($p = 0, 1, 2, \ldots$) that correspond to absorption of photons of different wavelengths. During emission the electron travels from the $S_{1,0}$ state to the various levels of the ground state $S_{0,p}$ ($p = 0, 1, 2, \ldots$). The absorption spectrum can be thought of as a plot of the statistical likelihood that a photon with energy hc/λ will find an electron to excite from the ground state $S_{0,p}$ to the many available energy states and levels S_n^m and T_n^m for $n > 0$. The emission spectrum can be thought of as

representing the statistical likelihood that the electron falls from the $S_{1,0}$ level to the $S_{0,p}$ level that will correspond to energy $e = S_{1,0} - S_{0,p} = hc/\lambda$. Therefore there are only as many emission levels as there are energy levels in the ground state, resulting in a relatively narrow emission band. Because of this, the emission spectrum is usually independent of the excitation wavelength [18].

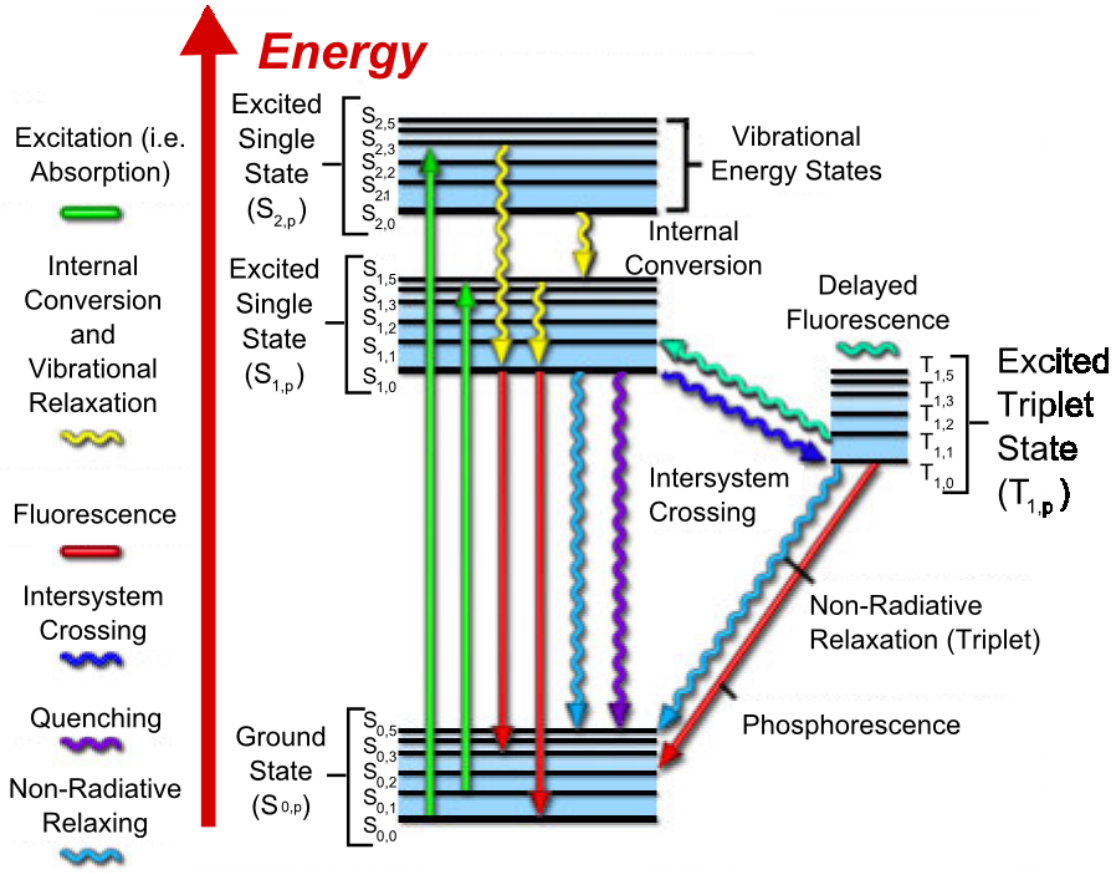

Figure 7: Jablonski energy diagram showing different energy levels and different non-fluorescent pathways. Adapted from [18].

The absorption and emission of fluorescent molecules are frequently quantified by two parameters—the molar extinction coefficient, ε, and the quantum yield, Φ.[2] The molar extinction coefficient is a measure of the amount of light attenuated by a

[2]Also known as the 'molar absorptivity' and 'quantum efficiency', respectively

solution per unit concentration per unit path length

$$\varepsilon = \frac{A}{\ell c} \tag{I.19}$$

where ℓ is the optical path length, c is the solution concentration and A is the absorbance. The quantum yield is defined as

$$\Phi = \frac{\#\text{ photons emitted}}{\#\text{ photons absorbed}} \tag{I.20}$$

For a photon traveling through a solution, ε gives the probability that the photon will be absorbed and Φ gives the probability that an absorbed photon will be emitted as fluorescence.

For a given fluorophore solution, the intensity of the fluorescent emission, $\mathscr{F}$, can be related to the intensity of the illumination, I_o as follows:

$$\mathscr{F} = I_o \Phi \left(1 - e^{-\varepsilon \ell c}\right) \tag{I.21}$$

At low concentrations, the fluorescence intensity is linearly related to concentration, so the fluorescent emission can be simplified to a form analogous to the Beer-Lambert Law:

$$\mathscr{F} = \alpha I_o \Phi \varepsilon \ell c \tag{I.22}$$

where α is a constant of proportionality. According to Guilbault [30], equation I.22 is valid for a range of concentrations between 10^{-5} and 100 μg/ml. In all cases, the fluorescent solutions used in this investigation had concentrations on the order of 1 μg/ml, well within the linear regime where this equation is valid.

1.3.2 Temperature Dependence of Fluorescence

For most fluorophores, the fluorescence intensity is at least slightly temperature-dependent. This temperature dependence is due to three interrelated causes: 1) thermal energy; 2) rates of chemical reactions; and 3) changes in solvent properties.

As temperature increases, the thermal energy of each molecule increases. The increased thermal energy increases the probability that an electron will be elevated to a higher energy state. Hence thermal energy competes with photonic energy to elevate electrons, affecting the probability of absorption. Furthermore, after absorption thermal activation can enhance intersystem crossing between singlet and triplet states. Thermal activation can either increase or decrease the quantum yield, an increasing Φ if thermal activation occurs from a $T_{1,p}$ to a $S_{1,p}$ state, and decreasing Φ if thermal activation occurs from a $S_{1,p}$ state to a $T_{2,p}$state [30].

The complexity of the photochemical and chemical processes that occur in a typical fluorescent event is understated by the simple model presented in section 1.3.1. After absorption of a photon, a fluorescent molecule has a slightly different electron configuration, resulting in different photochemical and chemical reactions for the fluorophore molecule at the excited and ground states. In the simplest case, the reactions can be modeled as first order rate reactions:

$$\frac{d[M]}{dt} = -k_M[M] \tag{I.23}$$

where $[M]$ is the concentration of species M, and k_M is the rate constant. There are usually many reactions associated with fluorescence for each fluorophore. For example, Song *et al.* [78] identified 13 reactions governed by 12 rate constants that are involved in the fluorescence of fluorescein, with all 13 reactions interrelated via shared reactants and products. Photochemical reactions are typically assumed to be independent of temperature because the activation energy is provided by the light source. However the rate constants of the chemical reactions can be influenced by temperature because of their Arrhenius-like behavior:

$$k = Ae^{\frac{-E_a}{RT}} \tag{I.24}$$

where A is the frequency factor constant, E_a is the activation energy, R is the universal gas constant and T is the temperature. Therefore, changes in temperature will change

the rate of the chemical reactions involved in creating fluorescence.

The sensitivity of fluorescence to solvent properties is a key factor in the utility of fluorescence as a measurement technique. Viscosity is typically strongly dependent upon temperature; for instance the viscosity of water varies from 1.79 cP at 0 ℃ to 0.28 cP at 100 ℃. As temperature increases and viscosity decreases, the frequency of molecular collisions increases, leading to collisional quenching. Collisional quenching refers to a decrease in quantum yield due to nonradiative energy transfer from an excited fluorophore to surrounding non-excited molecules. The decrease in viscosity can also effect fluorescence due to a reduction in rigidity of the chemical structure of the fluorophores. Typically as a fluorophore becomes less rigid, its quantum yield decreases [19] and the emission spectrum is red-shifted [30]. It has also been reported that changes in temperature will effect the polarizability of a fluorophore resulting in an increase in dipole moment [51]. The polarization changes affect interactions with the solvent and often result in a so-called thermochromic blue-shift (i.e., longer wavelength shift) of the emission spectrum.

The exact response of a specific fluorophore to changes in temperature is difficult to predict *a priori*. The direction and magnitude of the change in fluorescence will vary with each combination of fluorophore, solvent, and optical filtering. In summary as temperature increases: 1) thermal energy can either increase or decrease and shift the fluorescent absorption and/or emission; 2) changes in chemical reaction rates will not significantly effect absorption but can increase, decrease or shift the emission; and 3) solvent effects will reduce the intensity and possibly shift the fluorescent emission.

1.3.3 Photobleaching

Photobleaching refers to the process in which fluorophores lose their ability to fluoresce due to overexposure to incident light. This loss in fluorescence can often be partially reversed over longer times if the fluorophore is shielded from incident photons.

Photobleaching occurs due to the numerous photochemical and chemical reactions that take place after a photon is absorbed. Some of these chemical reactions convert singlet and triplet states to bleached states that are unable to fluoresce:

$$S_{n,p} \rightarrow B \qquad T_{n,p} \rightarrow B \tag{I.25}$$

where B is a fluorophore in a bleached state. In the case of recoverable photodegredation, there is another reaction that occurs at a lower rate that returns the bleached species to a point in the excitation-emission cycle.

$$B \rightarrow S_{n,p} \qquad B \rightarrow T_{n,p} \tag{I.26}$$

Non-recoverable photobleaching is due to the absence of a chemical reaction that returns a bleached fluorophore to the excitation-emission cycle.

1.3.3.1 Photobleaching Kinetics

Early research into the nature of photobleaching kinetics suggested that the rate of photobleaching is weakly temperature-dependent, with the the rate of photobleaching follows a first-order rate equation [37]:

$$\frac{d[C]}{dt} = -k[C] \tag{I.27}$$

where $[C]$ is the concentration of the unbleached fluorophore and k is the rate constant for photobleaching.

However, some subsequent studies have reported deviations from this first-order rate equation model. Song *et al.* [78],[79] analytically and experimentally investigated photobleaching kinetics in fluorescein and concluded that the first-order rate assumption is only valid in situations where the dominant reaction is between the dye in the triplet state and molecular oxygen. From the excited triplet state, there are two photochemical reactions that suppress dye fluorescence: 1) the dye-to-dye (D-D) mechanism, or reactions between the triplet state and another dye molecule in

either the triplet state or singlet state; and 2) the dye-to-oxygen (D-O) mechanism, or reactions between the triplet state and an oxygen molecule. The D-O mechanism dominates when fluorophores and oxygen are free to diffuse throughout a solution. The D-D mechanism becomes more important in situations such as fluorescence microscopy where the fluorophore is bound to a surface and exposed to sufficiently lower oxygen concentrations.

1.3.3.2 Photobleaching in Laser-Induced Fluorescence

In Laser-Induced Fluorescence studies it is important to understand how photobleaching can affect quantitative measurements. The rate of photobleaching is often quantified by the 'photobleaching quantum yield', which is defined as

$$\Phi_B = \frac{\#\text{ photons bleached}}{\#\text{ photons emitted}} \tag{I.28}$$

Koochesfahani [44] provided a simple model for the concentration of unbleached dye molecules C remaining after continuous illumination from time t_o to time t

$$C(t) = C_o \exp\left[\frac{-\Phi_B \varepsilon I}{N_A h\nu}(t - t_o)\right] \tag{I.29}$$

where C_o is the concentration at time $t = t_o$, I is the intensity, N_A is Avogadro's number, h is Planck's constant, and ν is the frequency of the illumination.

Analytical solutions for $C(t)$ in a uniform flow have been found for optical configurations commonly employed in LIF in terms of a dimensionless photobleaching parameter B defined as:

$$B = \frac{P\Phi_B \varepsilon}{N_A \sqrt{2\pi} a h\nu U} \tag{I.30}$$

where P is the laser power, a is the e^{-2} beam diameter, and U is the average flow velocity. Crimaldi [16] demonstrated that for single-point LIF measurements photobleaching is negligible if $B < 0.02$. Larsen and Crimaldi [46] suggested that photobleaching is negligible if $B < 0.014$ based upon their analysis of photobleaching in planar LIF measurements.

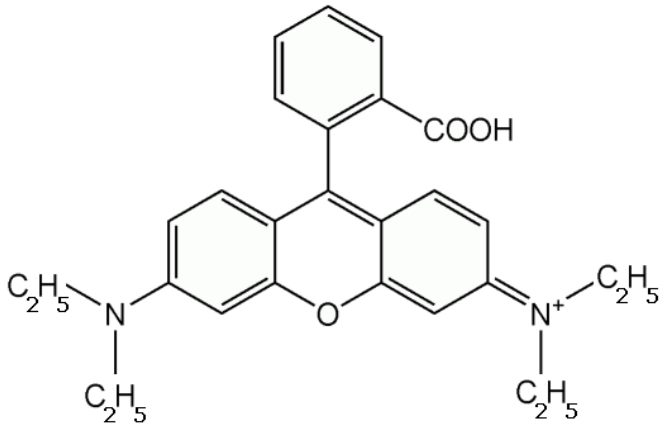

Figure 8: Chemical structure of rhodamine B

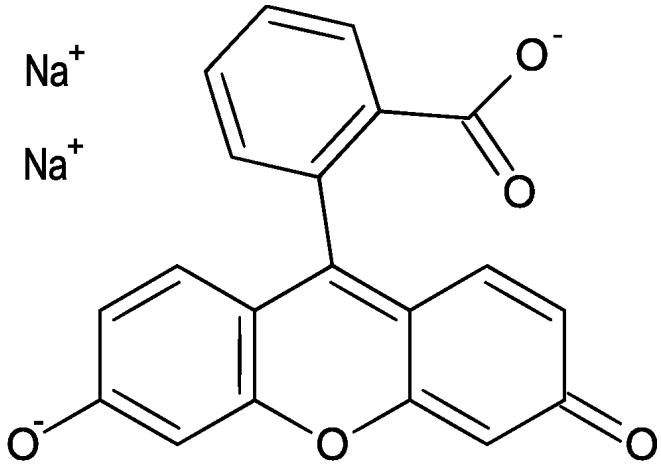

Figure 9: Chemical structure of fluorescein, disodium salt

1.3.4 Dye Properties

The two dyes used in this investigation were rhodamine B and fluorescein (Figures 8 and 9). Both dyes are xanthene dyes, with a chemical structure based on a xanthene nucleus (Figure 10), and are derived from condensation of phthalic anhydride with other chemicals [39]. The chemical, fluorescence and temperature-dependent properties of rhodamine B and fluorescein are reviewed in this section and summarized in table 1.

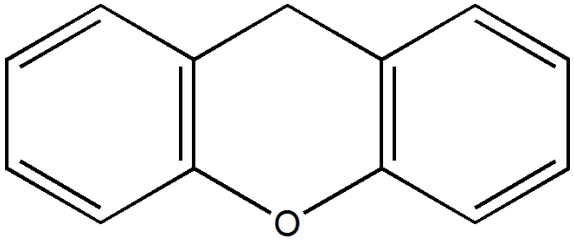

Figure 10: Chemical structure of xanthene nucleus

1.3.4.1 Chemical Properties

Fluorescent dyes are typically large organic molecules that contain ionic functional groups that cause the molecule to be water-soluble and amphoteric (able to act as either an acid or base depending on solution chemistry). Fluorescein has only negatively charged functional groups, while rhodamine B has a permanent positive charge associated with one of its diethylamino groups and negative functional groups [42]. However the charge associated with each dye can change based upon the acidity of each solution. In acidic solutions the dye will protonate and increase in net charge, while in basic solutions the dye will deprotonate and decrease in net charge. Specifically, in a strong acidic solution fluorescein becomes cationic by protonating at one of its double-bonded oxygens and in a strong basic solution becomes di-anionic by deprotonating at the carboxyl and hydroxide groups [73]. Rhodamine B has a permanent positive charge but can deprotonate at its carboxyl group to form a zwitterion (a simultaneously positively and negatively charged molecule) [56].

1.3.4.2 Fluorescent Properties

Rhodamine B has an excitation peak at about 560 nm and an emission peak at about 585 nm, as shown in the absorption and emission spectra of Figure 11. The absorption of rhodamine B has been shown to be independent of pH values above 6 [15]. Fluorescein has an excitation peak at about 488 nm and an emission peak at about 514 nm as shown in Figure 12. Fluorescein absorption is, however, pH

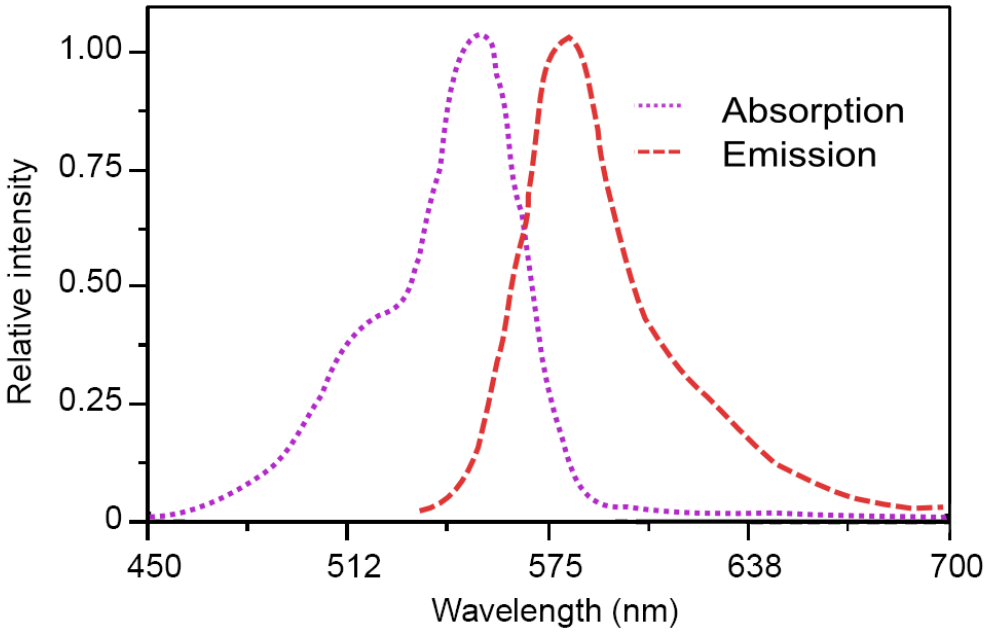

Figure 11: Relative absorption and emission spectra for rhodamine B at neutral pH; adapted from [15]

dependent for pH values between 3-8, and varies strongly with pH for pH values between 6-7.

Photobleaching is a major concern when dealing with fluorescein as can be seen by its relatively high photobleaching quantum yield (given in non-dimensional form in Table 1). Several investigators have reported extensive, partially-recoverable photobleaching of fluorescein in LIF measurements [72]. Although the absorption of rhodamine B is greater than that for fluorescein at their respective absorption peaks, the bleaching quantum yield of fluorescein is an order of magnitude larger than that for rhodamine B.

1.3.4.3 Temperature Dependence

The relationship between fluorescence intensity and temperature for rhodamine B in water has been reported to be in the range of -1.34 to -1.95 %/°C [35]. The differences in reported temperature sensitivities are likely due to different excitation wavelengths, emission filtering and imaging systems. The mobility of the diethylamino groups has

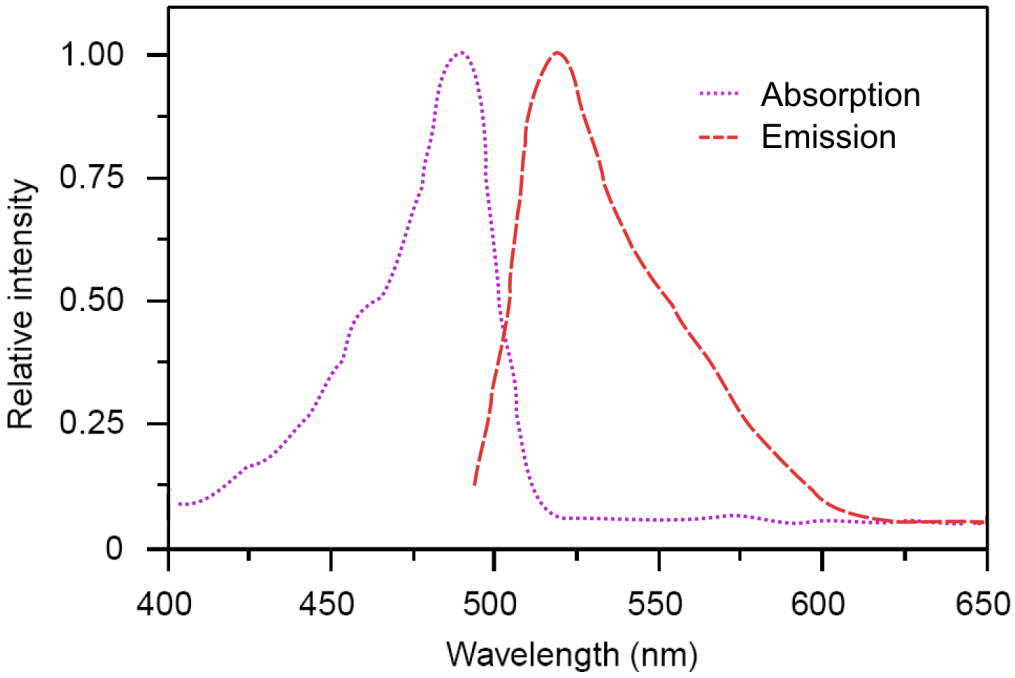

Figure 12: Relative absorption and emission spectra for fluorescein at neutral pH; adapted from [15]

been cited as a primary mechanism in the temperature sensitivity of rhodamine B in ethanol [19]. Rhodamine B contains two diethylamino groups that become more rigid as viscosity increases, resulting in a lower quantum yield at higher temperatures. Such temperature effects on quantum yield would only be seen in the emission spectrum, and indeed, absorption spectra at four different temperatures are nearly identical (Figure 13).

Fluorescein has been reported to have a temperature sensitivity of 2.43 %/℃ when excited at 514 nm and -0.16%/℃ when excited near its peak at 488 nm [15]. The high temperature sensitivity at 514 nm is due to a slight broadening of the absorption peak and a small red-shift in the absorption spectrum with increased temperature (Figure 14). At 514 nm the small red-shift is magnified due to the steep slope of the absorption curve. These observations suggests that illumination at 500-510 nm could potentially give temperature sensitivities for fluorescein up to triple previously reported values.

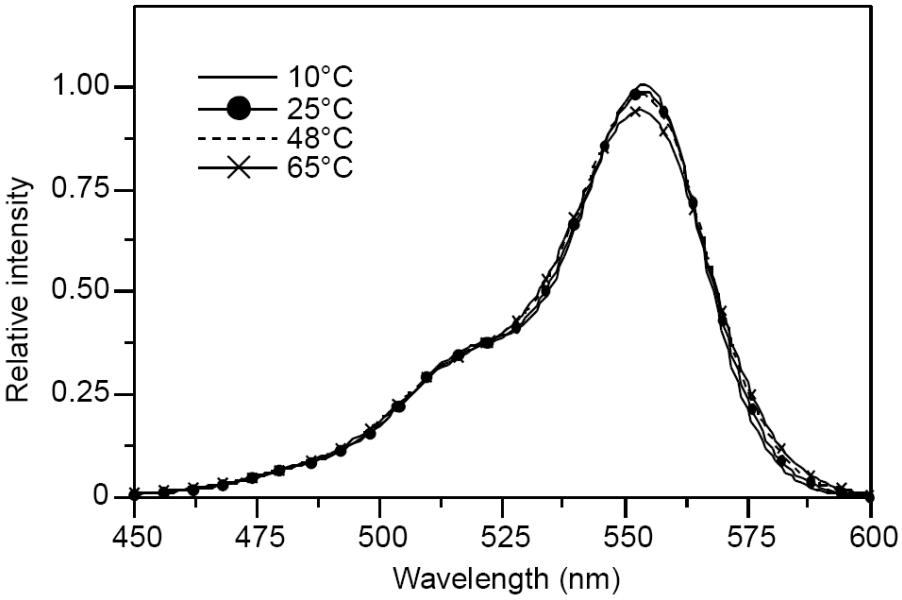

Figure 13: Absorption spectrum of rhodamine B at different temperatures [15].

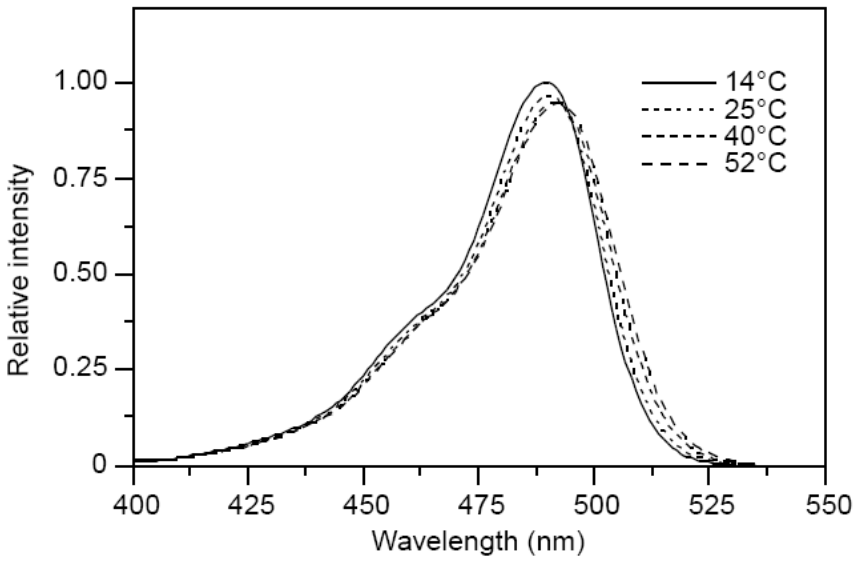

Figure 14: Absorption spectrum of fluorescein at different temperatures [15].

Table 1: Properties of rhodamine B and fluorescein

Property	Rhodamine B	Fluorescein
M.W. [g/mole]	479.01	376.28
Chemical Formula	$C_{28}H_{31}ClN_2O_3$	$C_{20}H_{10}Na_2O_5$
λ_{ex} [nm]	560 [15]	488 [15]
λ_{em} [nm]	585 [15]	514 [15]
Φ_B	0.74×10^{-6} [77]	4.0×10^{-6} [40]
$\varepsilon[\text{cm}^2\text{mole}^{-1}]$	2.1×10^9 [69]	$2.1 \sim 4.2 \times 10^9$
$\Phi_B\varepsilon/N_A[\text{cm}^2]$	2.59×10^{-21}	$1.4 \sim 2.8 \times 10^{-20}$ [16],[46]
$dI/dT[\%/^\circ\text{C}]$	$-(1.34 \sim 1.95)$ [35]	2.43 [15]

1.4 Total Internal Reflection Microscopy

Total Internal Reflection (TIR) Microscopy is a technique used to limit the region of illumination to within the first few hundred nanometers adjacent to an interface. Typically TIR illumination is used to reduce background illumination levels and increase the signal-to-noise ratio. Here TIR illumination is instead used to limit the measurement region to that near the wall.

1.4.1 Total Internal Reflection

In geometric optics, when light propagates through a medium with index of refraction n_1 and is incident upon an interface with a second material with index of refraction n_2 at an angle of incidence θ_i it is refracted according to Snell's Law (Figure 15a):

$$n_1 \sin\theta_i = n_2 \sin\theta_t \tag{I.31}$$

where θ_t is the refracted angle of the transmitted light. When $n_1 > n_2$, total internal reflection occurs if the angle of incidence is greater than or equal to a critical angle θ_c defined by

$$\theta_c = \sin^{-1}\left(\frac{n_2}{n_1}\right) \tag{I.32}$$

According to geometric optics, when θ_i exceeds θ_c, light is completely reflected back into the original medium and no light propagates into the second medium (Figure 15b).

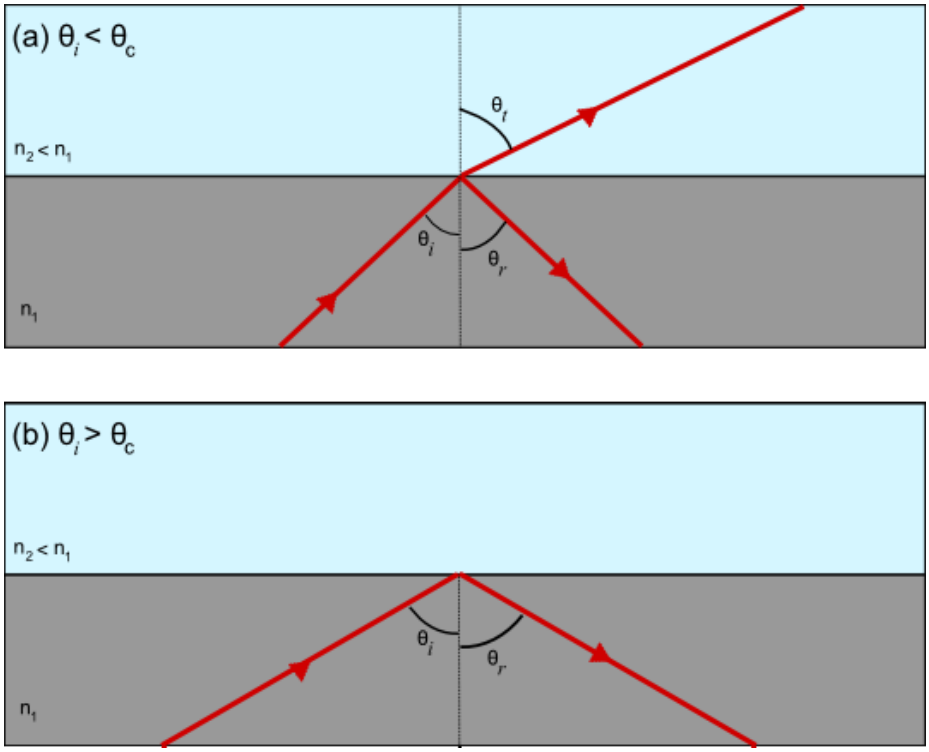

Figure 15: Application of Snell's Law according to geometric optics. (a) angle of incidence is less than the critical angle; (b) angle of incidence greater than critical angle

1.4.2 Evanescent Wave

The Fresnel equations are based upon the continuity of the tangential components of the electric and magnetic fields across an interface for both parallel and perpendicularly polarized light. This boundary condition is violated if no light is transmitted into the second (i.e., lower refractive index) medium. The solution to Maxwell's equations at an interface show that the electromagnetic field does penetrate a short distance into the second medium. This electromagnetic wave is called an "evanescent wave" and can be viewed as a fraction of the energy of the incident beam that propagates parallel to the interface for a short distance (called the Goos-Hänchen shift) before re-entering the first (i.e., higher refractive index) medium [7].

The intensity (defined as the square of the electric field amplitude $I = |E|^2$) of an evanescent wave decays exponentially with distance z normal to the interface:

$$I(z) = I_0 e^{-z/d_z} \tag{I.33}$$

where I_0 is the evanescent intensity at the $z = 0$ interface and d_z is the e^{-1} penetration depth defined as

$$d_z = \frac{\lambda_o}{4\pi}\sqrt{n_1^2 \sin^2\theta_i - n_2^2} \tag{I.34}$$

where λ_o is the free space wavelength (Figure 16a).

The magnitude of the evanescent wave intensity I_0 at the interface varies with θ_i and can be much greater than the incident intensity at the interface. The evanescent wave intensity for parallel $\parallel$ and perpendicularly $\perp$ polarized light in terms of the incident intensity I_i is

$$I_0^{\parallel} = I_i^{\parallel}\frac{4\cos^2\theta_i\left(2\sin^2\theta_i - n^2\right)}{n^4\cos^2\theta_i + \sin^2\theta_i - n^2} \tag{I.35}$$

$$I_0^{\perp} = I_i^{\perp}\frac{4\cos^2\theta_i}{1 - n^2} \tag{I.36}$$

where $n = n_2/n_1 > 1$. The magnitude of the total intensity can the be found by

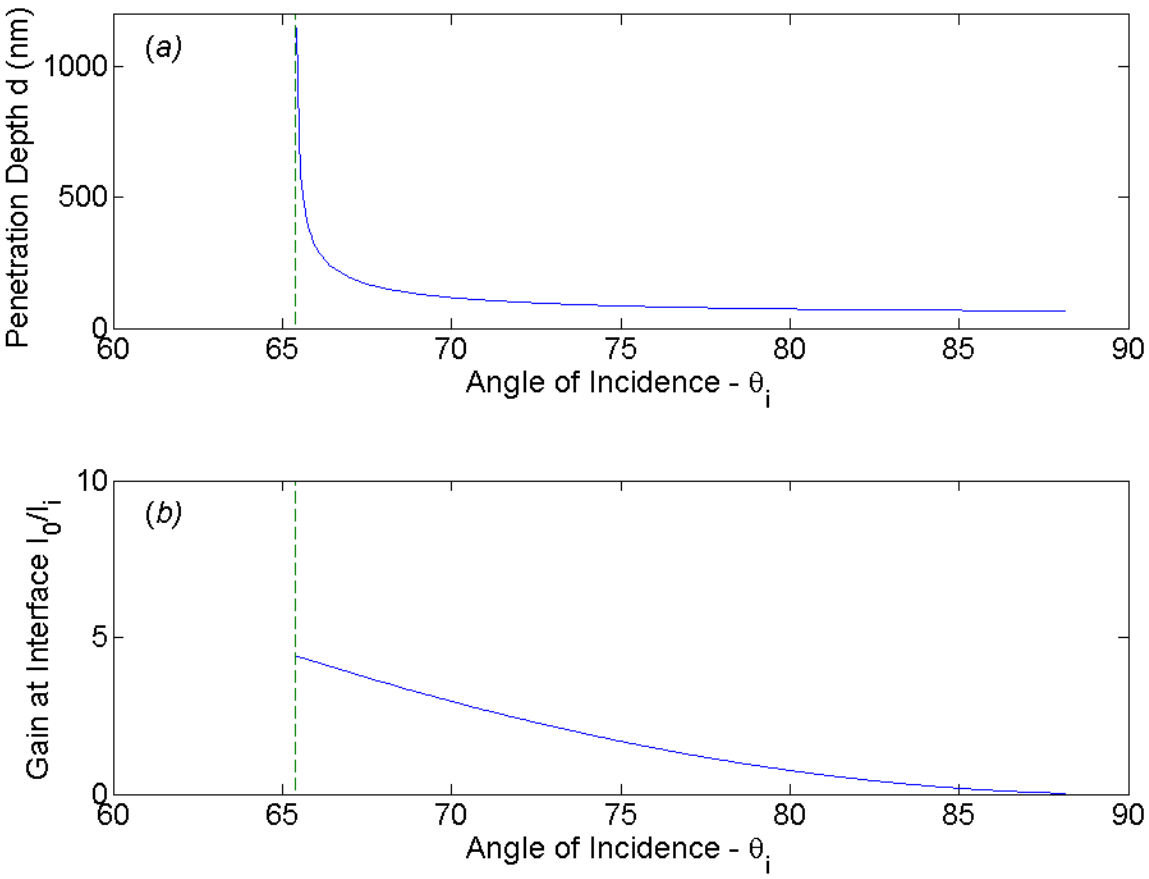

Figure 16: Characteristics of an evanescent wave at an interface between fused silica ($n_1 = 1.463$) and water ($n_2 = 1.33$) for light of wavelength 514 nm at different angles of incidence. The critical angle $\theta_i = 65.38°$ is shown as a dotted line. (a) penetration depth; (b) intensity gain at interface.

summing the parallel and perpendicular components

$$|I_0| = I_0^{\parallel} + I_0^{\perp} \tag{I.37}$$

Even if the incident light is equally polarized between the parallel and perpendicular components, the evanescent intensity will be slightly biased toward the parallel component because $I_0^{\parallel} \geq I_0^{\perp}$ for all θ_i. The gain in magnitude of the total evanescent intensity profile will then be given by

$$G_e = \left|\frac{I_0}{I_i}\right| = 2\cos^2\theta_i \left[\frac{2\sin^2\theta_i - n^2}{n^4\cos^2\theta_i + \sin^2\theta_i - n^2} + \frac{1}{1-n^2}\right] \tag{I.38}$$

The gain in intensity at the interface G_e is independent of position in the x-y plane and is shown in Figure 16b for different angles of incidence.

1.4.2.1 Evanescent field generated by a laser beam

For most experimental conditions, the intensity incident at the interface varies with position in the x-y plane. For laser illumination, the cross-sectional intensity profile is modeled as a symmetrical Gaussian function at the laser aperture and an elliptical Gaussian function at the TIR interface. As such the evanescent field can be modeled as an elliptical Gaussian function in the x-y plane that is exponentially decaying with distance z from the interface. Moreover, for most experimental conditions the polarization and penetration depth can be treated as if the incident field were a plane wave [7].

Defining a coordinate system such that the interface lies in the x-y plane, the plane of incidence lies in the x-z plane, and the origin is defined by the the beam center, in the ideal case of a Gaussian laser profile, the incident intensity profile can be described by

$$I_i(x,y) = I_i' \exp\left\{-2\left(\frac{x}{a}\cos\theta_i\right)^2\right\} \exp\left\{-2\left(\frac{y}{a}\right)^2\right\} \tag{I.39}$$

where a is the e^{-2} beam radius and I_i' is the incident intensity at the origin. Therefore for a given angle of incidence, the evanescent intensity profile at the interface is

$$I_0(x,y) = G_e I_i(x,y) = G_e I_i' \exp\left\{-2\left(\frac{x}{a}\cos\theta_i\right)^2\right\} \exp\left\{-2\left(\frac{y}{a}\right)^2\right\} \tag{I.40}$$

The intensity of the wave will decrease with distance from the interface:

$$I(x,y,z) = I_0(x,y)e^{-z/d_z} \tag{I.41}$$

where d_z is the e^{-1} penetration depth of the evanescent field. Combining the above expressions into a single expression for spatial intensity gives

$$I(x,y,z) = G_e I_i' \exp\left[-2\left(\frac{x}{a}\cos\theta_i\right)^2 - 2\left(\frac{y}{a}\right)^2 - \frac{z}{d_z}\right] \tag{I.42}$$

which in non-dimensional form is then:

$$I(x^\star,y^\star,z^\star) = I_0' \exp\left[-2(x^\star)^2 - 2(y^\star)^2 - z^\star\right] \tag{I.43}$$

Here,

$$x^\star = \frac{x}{a}\cos\theta_i, \qquad y^\star = \frac{y}{a},$$
$$z^\star = \frac{z}{d_z}, \qquad I_0' = G_e I_i'$$

To find I_i' we use the relationship between power and intensity, namely $P = \int_A I dA$, at the interface:

$$P = \iint\limits_{y^\star x^\star} I_i(x,y,z=0)dx^\star dy^\star = I_i' \frac{a^2}{cos\theta} \int_{-\infty}^{\infty} e^{-2y^{\star 2}} dy^\star \int_{-\infty}^{\infty} e^{-2x^{\star 2}} dx^\star = \frac{\pi a^2}{2\cos\theta} I_i' \tag{I.44}$$

Hence, the incident intensity at the origin is $I_i' = (2P\cos\theta_i)\,/\,(\pi a^2)$ and the intensity of the evanescent wave at the origin is

$$I_0' = G_e \frac{2P\cos\theta_i}{\pi a^2} \tag{I.45}$$

Figure 17 shows the evanescent wave intensity field at four different z values.

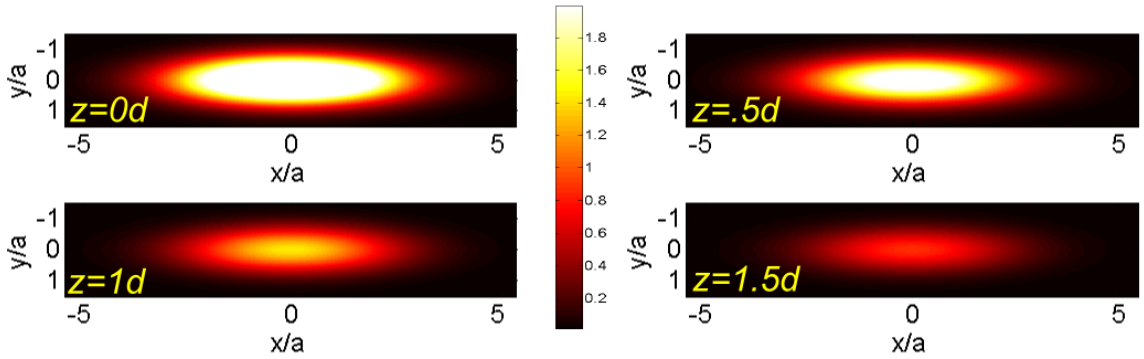

Figure 17: Profiles of the evanescent illumination in x-y plane, assuming an ideal Gaussian laser profile, for four different distances from interface with angle of incidence $\theta_i = 73.9°$, $\lambda = 514nm$, $n_1 = 1.463$, $n_2 = 1.33$ and $G_e = 1.94$. Profiles are color-mapped according to multiples of I_0'.

1.4.3 TIR Fluorescence Microscopy

In TIR fluorescence microscopy, the evanescent wave is used to provide spatially limited illumination where the resultant fluorescence intensity can be used to extract useful quantitative and qualitative information . The interaction between the evanescent wave, fluorophores and the detecting system is often quite complex. Fluorophores in solution illuminated by an evanescent wave are often modeled as a simple constant-amplitude oscillating dipoles. Such models only take into account optical 'far-field' behavior. Axelrod *et al.* [8] presents a more complicated model that takes into account the optical 'near-field' behavior and models a fluorophore as a constant-power, variable-amplitude oscillating dipole. Numerical solutions for the emitted intensity as a function of observation angle for a single fluorophore with parallel and perpendicular dipole orientations relative to the surface are shown in Figure 18.

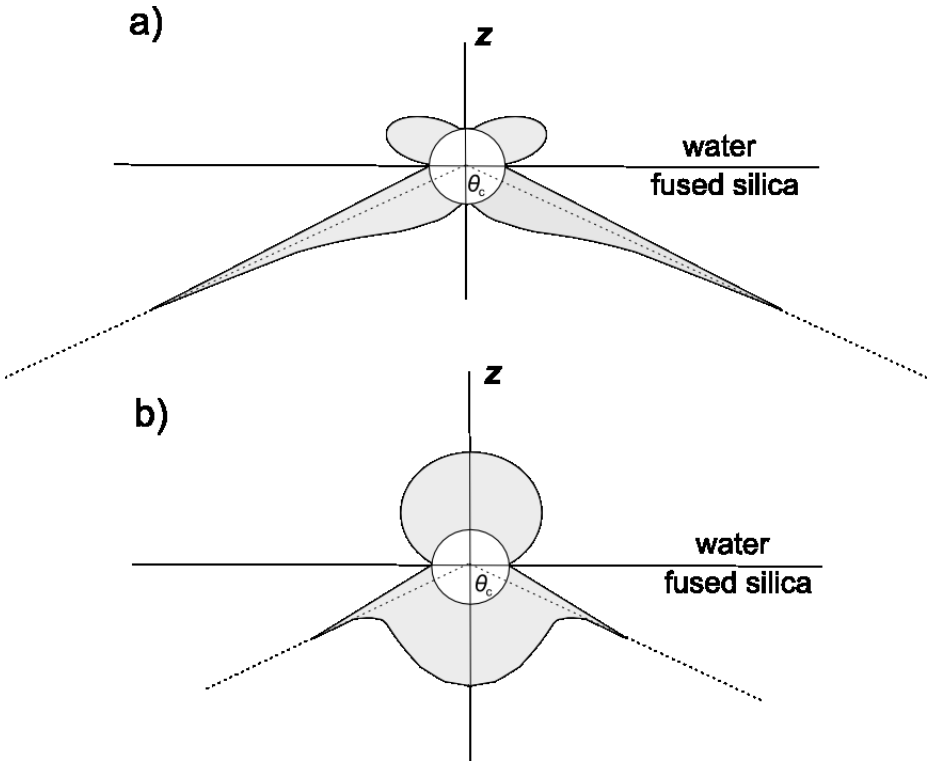

Figure 18: Intensity of fluorescent emissions from fluorophore located 80 nm away from interface as function of observation angle. Fluorophore molecules are modeled as constant-power, variable amplitude oscillating dipoles with dipole oriented (a) parallel and (b) perpendicular to interface. Adapted from [8].

CHAPTER II

EXPERIMENTAL APPARATUS AND PROCEDURE

This chapter describes the experimental apparatus and procedures in five sections. It begins with an overview of the theoretical background and underlying assumptions upon which Total Internal Reflection Fluorescent Micro Thermometry (TIR-FMT) is based. The second section describes and characterizes the optical system used for illumination and image acquisition. The third section outlines the procedure used for solution preparation. The fourth sections describe the experimental apparatus, design considerations, and experimental procedure for the calibration. Finally, the image processing techniques are described.

2.1 Theoretical Overview

This section contains the theoretical background and assumptions upon which Total Internal Reflection Fluorescent Micro-Thermometry is based. Ultimately the accuracy and resolution of this investigation will be largely influenced by the validity of the underlying assumptions.

In TIR-FMT a laser is totally internally reflected at an interface between fused silica and a fluorescent solution (Figure 19). An evanescent wave is generated inside the fluorophore solution and some of the light is absorbed by fluorophores inside the interrogation region. The excited fluorophores emit fluorescence with intensity $\mathscr{F}$ that is collected and focused by the optical system. For dilute solutions $\mathscr{F}$ is given by equation I.22

$$\mathscr{F} = \alpha I_0 \Phi \varepsilon \ell c \tag{I.22}$$

The functional dependencies of the components of equation I.22 can be broadly stated

as

$$\begin{aligned} \alpha &= \text{constant} & I_0 &= I_0(x, y, z, t, \ell) \\ \Phi &= \Phi(pH, T, \lambda, \nu(T)) & \varepsilon &= \varepsilon(pH, T, \lambda, \nu(T)) \\ r\ell &= \ell(n(T), \theta_i) & c &= c(x, y, z, t, T) \end{aligned} \tag{II.1}$$

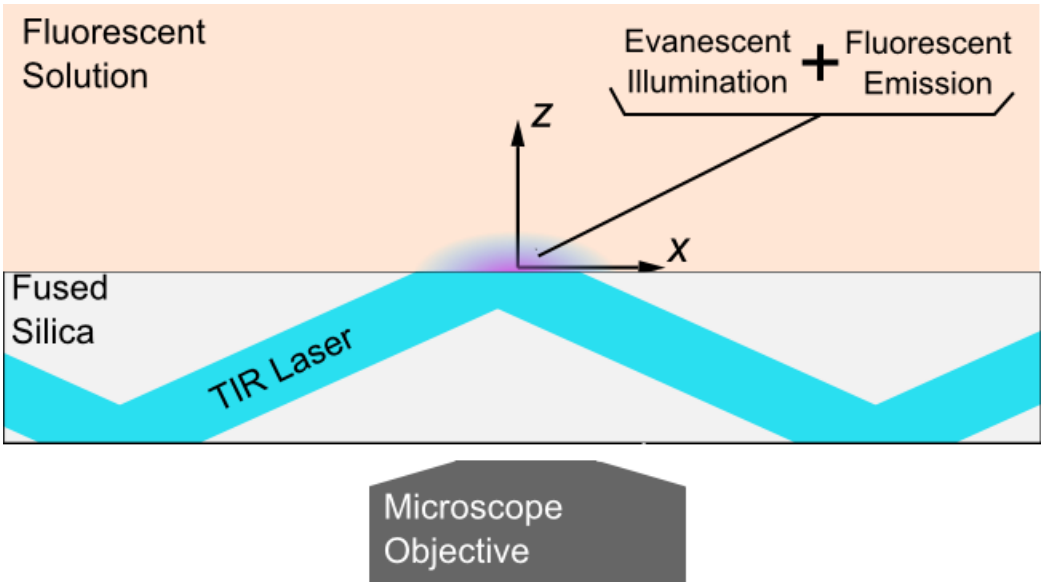

Figure 19: Diagram showing basic procedure for TIR-FMT

The expression for fluorescence intensity can be simplified by utilizing a normalization technique. Each fluorescent data point $\mathscr{F}_\phi$ is normalized by a normalizing fluorescent data point $\mathscr{F}_n$ taken at a known temperature T_n. Here ϕ is used to index different experimental data points. The resulting normalized quantity $\mathscr{F}_\phi^\star$ is

$$\mathscr{F}_\phi^\star = \frac{\mathscr{F}_\phi}{\mathscr{F}_n} = \frac{I_{0,\phi}\Phi_\phi\varepsilon_\phi\ell_\phi c_\phi}{I_{0,n}\Phi_n\varepsilon_n\ell_n c_n} \tag{II.2}$$

The normalized fluorescent signal can be simplified by making several assumptions, which are:

Negligible deviation in optical path length through solution: The optical path length is the product of index of refraction n and physical path length d, $\ell = nd$.

The optical path length of the present investigation can be broken into two components: the path length through the solid fused silica substrate ℓ_s and the path length of the evanescent wave through the liquid solution ℓ_l. The optical path length in equation I.22 is related to the amount of light that is absorbed by fluorophores in solution and so refers to the path length through the liquid solution ℓ_l. The index of refraction of water varies weakly with temperature ($dn/dT = O(-10^{-4})/$℃)and the physical path length is on the order of 10^{-7} m. Therefore, there will be only negligible variation in optical path length through the solution.

Constant Illumination: The illumination will remain constant with respect to time and spatial position. Steady state illumination in the x-y plane relies upon the mechanical stability of optical components and temporal stability of the laser illumination source. Furthermore, changes in temperature will effect the physical path length traveled by the laser beam due to thermal expansion and changes in index of refraction with respect to temperature. For fused silica, the coefficient of thermal expansion is on the order of $10^{-6}/$℃ and dn/dT is on the order of $10^{-5}/$℃.

Constant Concentration: The concentration of the solution will remain spatially and temporally uniform throughout an experiment. It is necessary to ensure that the solution is well mixed and does not significantly interact with any surfaces exposed to the solution. Photobleaching effects and other causes known to cause degradation of the fluorescent dye must be minimized.

With the above assumptions $I_{0,\phi} = I_{0,n}$, $\ell_\phi = \ell_n$ and $c_\phi = c_n$ and the normalized fluorescence intensity becomes

$$\mathscr{F}^\star_\phi = \frac{\Phi_\phi \varepsilon_\phi}{\Phi_n \varepsilon_n} = \frac{\Phi_\phi(pH, T, \lambda_{em}, \nu(T))\varepsilon_\phi(pH, T, \lambda_{ex}, \nu(T))}{\Phi_n(pH, T, \lambda_{em}, \nu(T))\varepsilon_n(pH, T, \lambda_{ex}, \nu(T))} \tag{II.3}$$

Changes in viscosity between data points are due to changes in temperature, and can be incorporated into the temperature dependence. Illumination is monochromatic and constant, so λ_{ex} does not vary. Fluorescence intensity is measured over a fixed bandwidth $\Delta\lambda_{em}$. Integrating Φ over this bandwidth gives

$$\bar{\Phi}(pH, T) = \int_{\Delta\lambda_{em}} \Phi(pH, \lambda_{em}, T) d\lambda_{em} \tag{II.4}$$

Integrating the fluorescence intensity over the emission wavelength interval and normalizing results in a function of pH and temperature

$$\bar{\mathscr{F}}^{\star}_{\phi}(\mathrm{pH}, T) = \frac{\int_{\Delta\lambda_{em}} \varepsilon_{\phi}(\mathrm{pH}, T)\Phi_{\phi}(\mathrm{pH}, T, \lambda_{em}) d\lambda_{em}}{\int_{\Delta\lambda_{em}} \varepsilon_{n}(\mathrm{pH}, T)\Phi_{n}(pH, T, \lambda_{em} d\lambda_{em})} = \frac{\varepsilon_{\phi}(\mathrm{pH}, T)\bar{\Phi}_{\phi}(\mathrm{pH}, T)}{\varepsilon_{n}(\mathrm{pH}, T)\bar{\Phi}_{n}(\mathrm{pH}, T)} \tag{II.5}$$

Ideally, $\bar{\mathscr{F}}^{\star}_{\phi}$ would be only a function of temperature $\bar{\mathscr{F}}^{\star}_{\phi} = \bar{\mathscr{F}}^{\star}_{\phi}(T)$ so it is necessary to consider the relationship between pH and $\mathscr{F}^{\star}_{\phi}$.

2.1.1 Relationship between pH and Fluorescence Intensity

Fluorescence has also been shown to be independent of pH for rhodamine B, but strongly dependent upon pH for fluorescein (Figure 20). In this investigation, many fluorophore solutions were buffered to a fixed pH of 9.2 by inclusion of sodium tetraborate in the solution. For these buffered solutions, the pH is a fixed constant. For the unbuffered solutions, the pH value is a measure of the concentration of hydrogen ions H^+ (protons) present in a solution and is defined as $\mathrm{pH} = -\log_{10}([H^+])$. In a given solution, the concentration of hydrogen ions is at an equilibrium between the disassociation of water and the disassociation of solutes present in the solution. For a single acidic species in water, the concentration of hydrogen ions can be solved for by

$$K_a = \frac{[H^+]\left([H^+] - \frac{K_w}{[H^+]}\right)}{[A] - [H^+] + \frac{K_w}{[H^+]}} \tag{II.6}$$

where K_a is the acid disassociation constant of the acidic species, $[A]$ is the initial concentration of the acidic species and K_w is the disassociation constant of water.

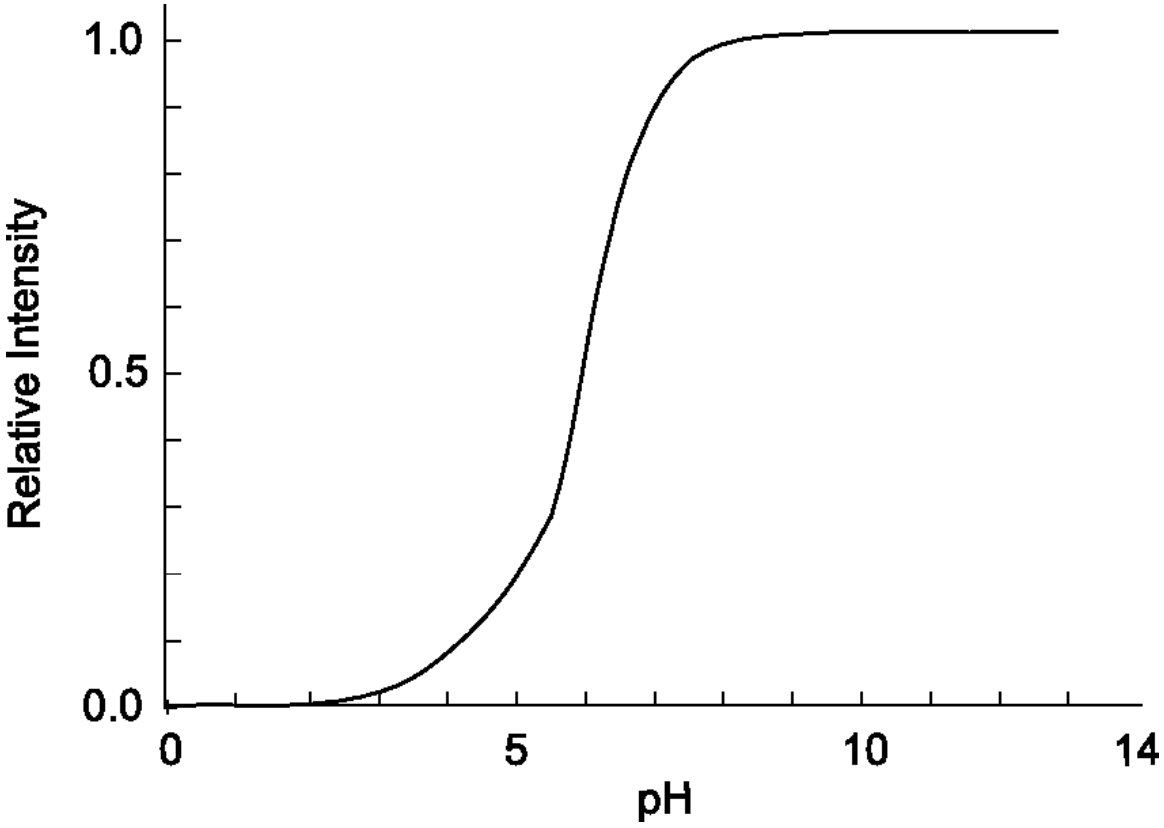

Figure 20: Sensitivity of fluorescence intensity to changes in pH for fluorescein dyes excited at $\lambda_{ex} = 514.5$. Adapted from [17].

Therefore, for a given solution the only variable is the concentration of [A]. The concentration of the fluorophore has been assumed to remain constant, hence by extension we can assume:

Negligible deviations in pH: The pH will remain constant over an experimental run. Further, across several experimental runs there will only be a very small deviation in pH, δ(pH), due to small uncertainty in the concentration of fluorophore is fixed. For example, for fluorescein the acid disassociation constant $K_a = 7.94 \times 10^{-6}$ and for a concentration of fluorescein [Fl]=10 μM the expected pH is 5.24. The sensitivity of pH to concentration in this range is -0.03 per μM. Therefore, a 10% error in fluorescein concentration will only result in a 0.57% change in pH.

Finally, we must assume that over the small range of pH deviations δ(pH) the relationship between $\mathscr{F}$ and temperature will remain nearly constant:

$$\frac{\partial}{\partial \mathrm{pH}} \left(\frac{\partial \mathscr{F}}{\partial T} \right) \approx 0 \tag{II.7}$$

Therefore, the expression for fluorescence intensity is only a function of temperature:

$$\bar{\mathscr{F}}^{\star}_{\phi} = \frac{\bar{\Phi}(T_\phi)\varepsilon(T_\phi)}{\bar{\Phi}(T_n)\varepsilon(T_n)} = \bar{\mathscr{F}}^{\star}_{\phi}(T_\phi, T_n) \tag{II.8}$$

One final assumption is necessary regarding the illumination and image acquisition system.

Random Fluorophore Orientation: The orientations of fluorophore molecules are assumed to be random with respect to incident polarization and observation angle. Therefore, incident illumination is treated as the sum of the parallel and perpendicularly polarized components.

2.2 Optical System

The optical system is made up of two parts: the illumination system and the imaging system. The illumination system is comprised of a laser and a series of optical components that generates a monochromatic totally internally reflecting beam inside of a test cell. The imaging system is comprised of a microscope, optical filters and a camera that images fluorescent emissions.

2.2.1 Illumination System

The illumination system is illustrated in Figure 21 and all components are specified in Table 2. An air-cooled argon-ion laser output a beam at 8 spectral lines with maximum powers shown in Figure 22. Laser excitation filters were placed in the beam path to allow only the 488 nm or 514 nm wavelength to pass. Mirrors were used to steer the beam toward the entrance prism at an angle of approximately 0° to the horizontal corresponding to an angle of incidence of 45°. To monitor laser power, a neutral density filter was placed in the beam path with an optical density of 0.033 ($T = 10^{-O.D.} = 92.7\%$) to reflect a small reference beam to a laser power meter. A focusing lens (f =15 cm) was placed in the beam path with the intent of locating the beam waist approximately at the entrance prism.

As the laser illumination entered the entrance prism it was refracted toward the interface between the entrance prism and the fused silica substrate. Fused silica was chosen as the substrate material due to it's high transmittance in the visible region of the electromagnetic spectrum and it's low level of auto-fluorescence. Auto-fluorescence is the tendency of some materials (including most glasses) to fluoresce, which will contribute to background signal. A fused silica matching immersion liquid was used to optically couple the fused silica prism to the fused silica substrate. The fused silica substrate was a shared component that was part of the test cell and part of the illumination system. As illumination propagated through the fused silica

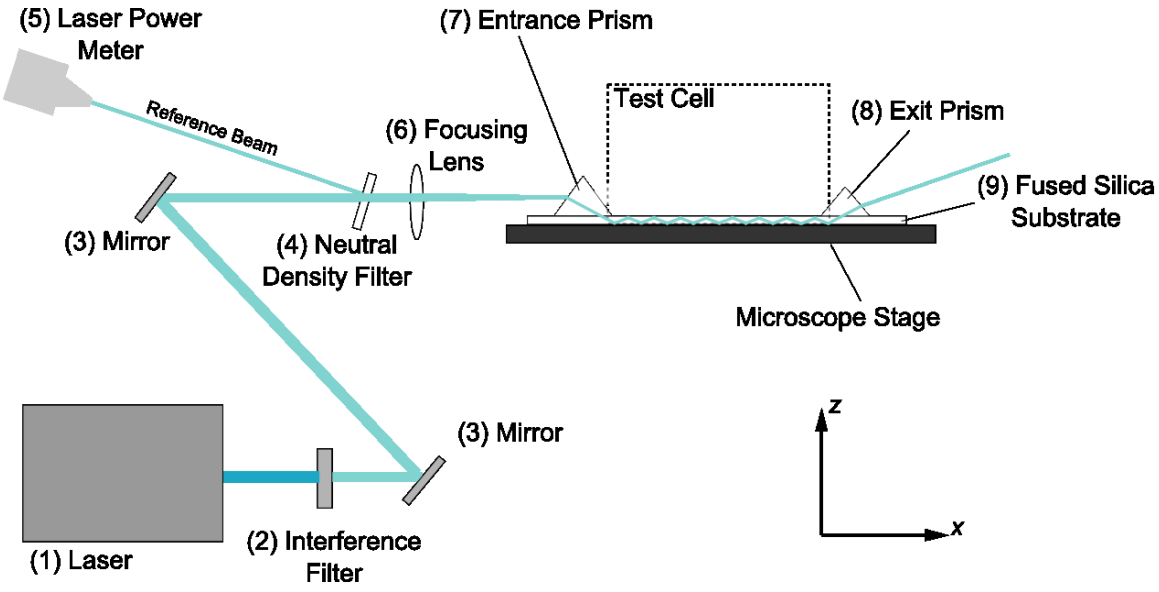

Figure 21: Diagram of Illumination System

Table 2: Components of illumination system

Label	Description	Manufacturer	Model	Notes
1	Argon-Ion Laser	Melles Griot	543-MA-03	Figure 22
2a	Excitation Filter-488 nm	Chroma	z488/10x	Figure 22
2b	Excitation Filter-514 nm	Chroma	z514/5x	Figure 22
3	Optical Mirror	Generic	Generic	
4	Neutral Density Filter	Melles Griot	03 FSG 017	OD=0.033
5	Laser Power Meter	Coherent	Lasermate Q	
6	Convex Lens	Generic	Generic	f=15 cm
7	Fused Silica Entrance Prism	Opto Sigma	055-0190	45°-45°-90°; 10 mm
8	BK-7 Exit Prism	Opto Sigma	055-0115	45°-45°-90°; 6.4mm
9	Fused Silica Substrate	Esco Products	Q325063	Optical Grade
–	Fused Silica Matching Liquid	Cargille Labs	06350	

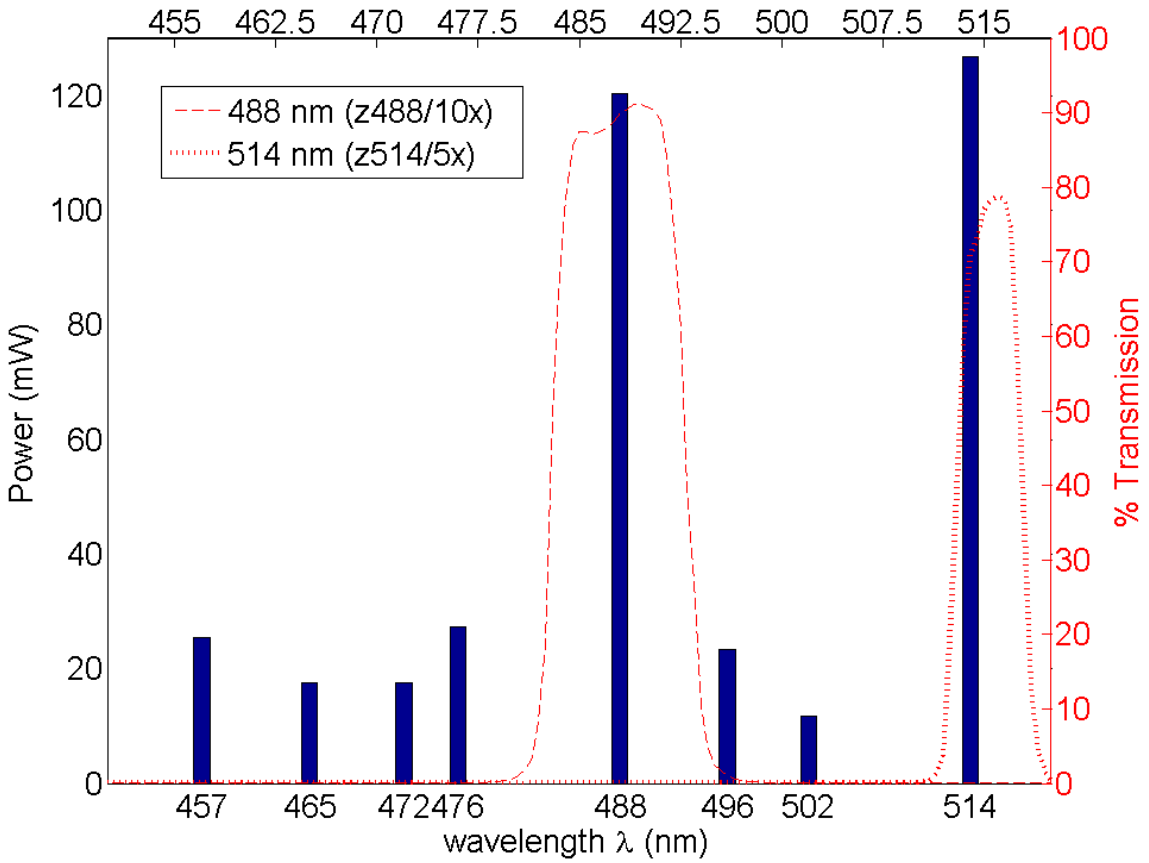

Figure 22: Spectral power specification for Melles Griot 543-MA-03 overlaid with transmission specifications for two excitation filters.

substrate via total internal reflection, an evanescent wave was generated at each reflection. Following several reflections, the illumination was incident at the interface between the fused silica substrate and the exit prism. Again, a fused silica matching immersion liquid was used to optically couple the two materials.

An expanded view of the laser beam incident is shown in Figure 23. The entrance angle θ_{in} was defined as the angle of the laser beam incident upon the entrance prism with respect to the horizontal. The angle of incidence at entrance θ_1 was the angle of the laser beam incident upon the entrance prism with respect to the normal of the prism face and could be related to the entrance angle according to

$$\theta_1 = \theta_{in} + 45^\circ \tag{II.9}$$

The angle of refraction at entrance θ_2 was the result of the beam being refracted at the air-prism interface was determined according to Snell's Law to be:

$$\theta_2 = \sin^{-1}\left(\frac{\sin\theta_1}{n_{SiO_2}}\right) \tag{II.10}$$

here, n_{SiO_2} was the refractive index of the prism. Finally, the angle of incidence of the TIR illumination θ_i was the angle of incidence for the totally internally reflected illumination propagating in the fused silica substrate. It could be related to θ_2 according to

$$\theta_i = \theta_2 + 45^\circ \tag{II.11}$$

The beam was directed such that the entrance angle $\theta_{in} = (0 \pm 5)^\circ$ in order to allow translation of the microscope stage in the x-direction without causing reflection and evanescent wave locations to move significantly. Figure 24 shows the variation of θ_i, penetration depth and evanescent gain with the $\pm 5^\circ$ variation in entrance angle. Although these parameters showed considerable variation with entrance angle, the normalizing procedure mitigated the effect of these variations on the normalized fluorescent signal.

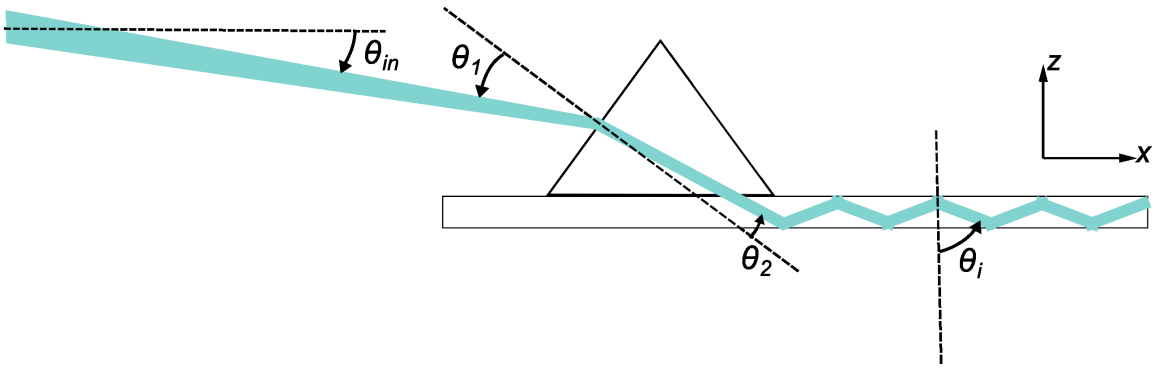

Figure 23: Expanded view of illumination system at entrance prism and fused silica substrate showing entrance angle θ_{in}, angle of incidence at entrance θ_1, angle of refraction at entrance θ_2, and angle of incidence for TIR θ_i.

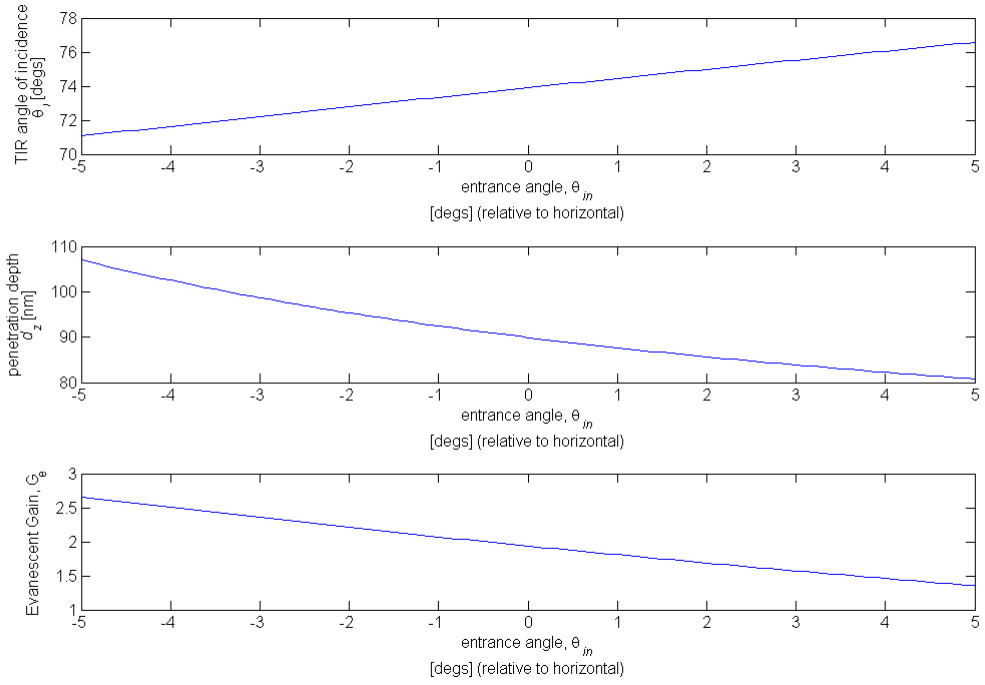

Figure 24: TIR angle of incidence θ_i, penetration depth d_z, and evanescent gain G_e variation with a $\pm 5°$ variation in entrance angle θ_{in} for the

2.2.1.1 Estimated Intensity of Evanescent Wave

The intensity of the evanescent wave generated inside the test cell was estimated based upon measurements of laser power incident at the entrance prism, estimates of transmissions losses based upon the Fresnel Equations, and system geometry. Using a laser power meter (Coherent, Lasermate Q) the maximum power incident at the entrance prism was measured to be 76.3 mW and 78.3 mW at 488 nm and 514 nm, respectively. At the entrance prism, most of the illumination will be transmitted through the prism to the fused silica substrate; however, a small portion of the beam will be reflected. The percentage of the incident power that is reflected can be solved for using the Fresnel equations. For randomly polarized light incident upon an isoeletric medium, the reflected power is described by

$$R = \frac{1}{2}\left(-\frac{\sin(\theta_1-\theta_2)}{\sin(\theta_1+\theta_2)}\right)^2 + \frac{1}{2}\left(-\frac{\tan(\theta_1-\theta_2)}{\tan(\theta_1+\theta_2)}\right)^2 \tag{II.12}$$

where θ_1 is the angle of incidence and θ_2 is the angle of transmittance, as shown in Figure 23. For an entrance angle of 0°, 4.5% of the power will be reflected and the rest transmitted. Combining the measured power at the prism entrance with the losses due to reflection gives estimated powers for the totally internally reflected beam in the fused silica substrate of 72.9 and 74.8 mW at 488 and 514 nm.

The intensity of the evanescent wave at the origin, assuming an ideal Gaussian laser profile, was estimated from equation I.45:

$$I_0' = G_e \frac{2P\cos\theta_i}{\pi a^2} \tag{I.45}$$

The e^{-2} beam radius was estimated from experimental images to be $a = 300\mu$m. The variation of the evanescent wave intensity at the origin as a function of entrance angle for three values of a are shown in Figure 25. The variations in I_0' with entrance angle and beam radius are significant. However, if the geometry of the optical system remains constant between the normalizing data point and the actual data point, then

its influence is mitigated by the normalization. However, the geometry of the optical system will affect penetration depth, signal-to-noise ratio, and the interrogation region. These effects will be addressed in section 2.2.3.

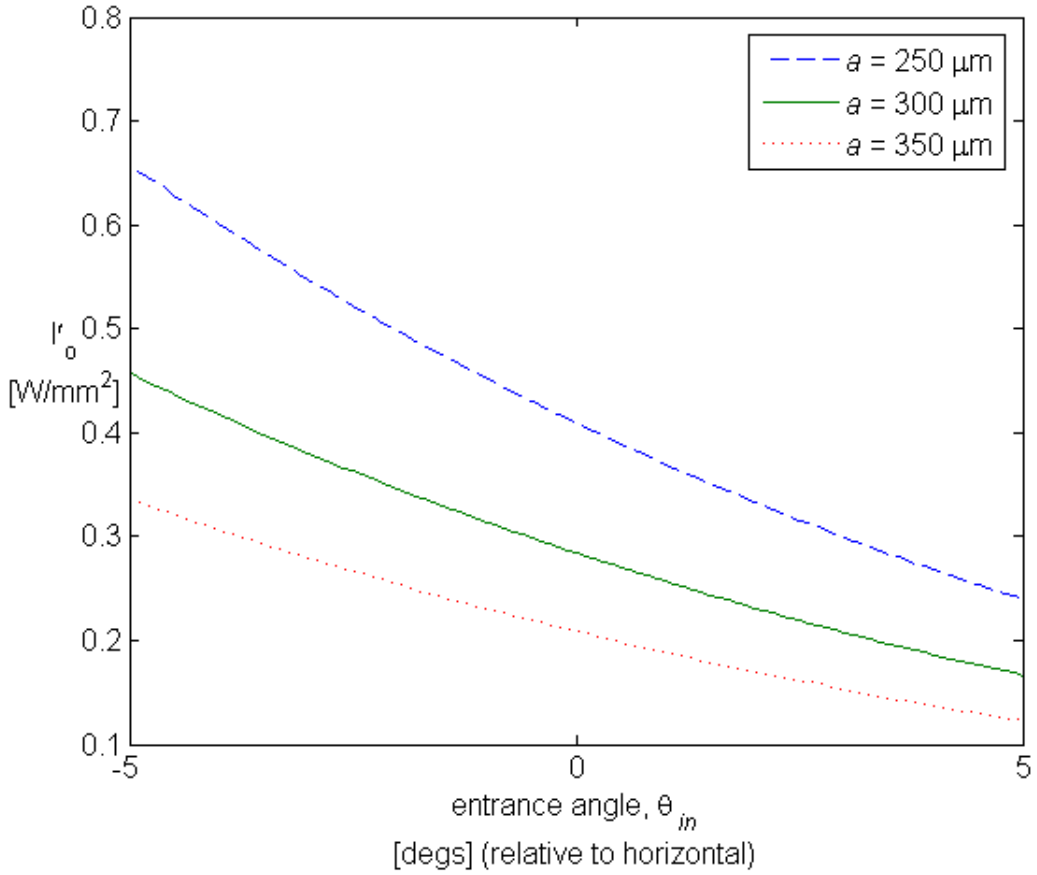

Figure 25: Estimated evanescent wave intensity at origin for different e^{-2} beam radii, a, across different entrance angles, θ_{in}. Shown for illumination at $\lambda_{ex} = 514$ nm; illumination at $\lambda_{ex} = 488$ nm demonstrates similar behavior, but all values are approximately 2.5% lower.

2.2.2 Imaging System

The imaging system is illustrated in Figure 26 and component specifications are listed in Table 3. The imaging system was comprised of a CCD array camera and an inverted epifluorescent microscope equipped with a 10x microscope objective, 0.5x camera eyepiece, and two filter cubes. Combined illumination and fluorescent emissions that

were incident upon the objective aperture were magnified and infinity-focused by the objective. Appropriate filter cubes—a Leica I3 filtercube for illumination of $\lambda_{ex} = 488$ nm or a custom Chroma filtercube for illumination of $\lambda_{ex} = 514$ nm—were placed along the optical path in the microscope tube to act as long-pass filters that attenuated illumination. Fluorescence was focused by the camera eyepiece onto the CCD array and a sequence of images acquired.

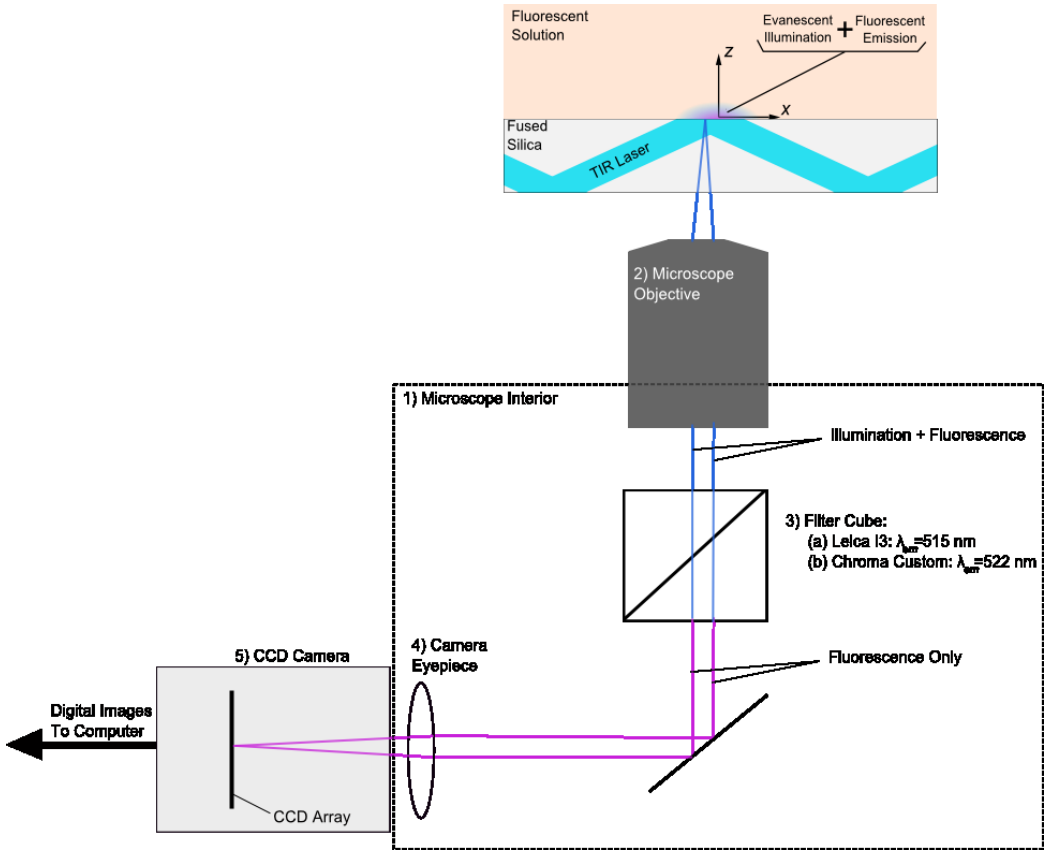

Figure 26: Illustration of imaging system

2.2.2.1 System Magnification

The theoretical system magnification is the product of the objective linear magnification $M_{obj} = 10$x and the camera eyepiece angular magnification $M_{eye} = 0.5$x, giving a system magnification, $M = 5$x. The true magnification of the system was measured by capturing images of a scale with 20 μm increments. Performing a fast Fourier

Table 3: Specifications of components in imaging system

Label	Description	Manufacturer	Model
1	Mircoscope	Leica	DMIRE2
2	Objective	Leica	506075
	Objective Magnification, $M_{obj} = 10$x Numerical Aperture, $N.A. = 0.22$		
3a	Filter Cube	Leica	I3
	Excitation Filter: Bandpass 450-490 nm Dichoromatic Mirror: 510 nm Emission Filter: Longpass 515 nm		
3b	Filter Cube	Chroma	Custom
	Excitation Filter: Bandpass 509-519 nm Dichoromatic Mirror: 520 nm Emission Filter: Longpass 522 nm		
4	Camera Eyepiece	Leica	HC 541511
	Eyepiece magnification, $M_{eye} = 0.5$x		
5	Camera	Ropert Scientific, Inc.	Photometrics Cascade 650
	Pixel size, 7.4 x 7.4 μm Imaging array size, 653 x 492 pixels Minimum achievable gain, 200x Analog-to-digital resolution, 8 bits		
	Combined System Specifications		
	System Magnification, $M = 1.455\,\mu$m/pixel = 5.09x Depth of Field, $\Delta = 7.91\,\mu$m		

transform (FFT) on the images of the scale gives the primary peak of the spatial frequency of the image as 0.07275 [1/pixel]. This primary peak corresponds to the spatial frequency of the scale markings, which occur at a known spatial frequency of $1/(20\mu m)$. Equating the measured spatial frequency in units of [1/pixel] to the known spatial frequency in [1/μm] yields:

$$\frac{.07275}{\text{pixel}} = \frac{1}{20\mu\text{m}} \Rightarrow \frac{(20 \cdot 0.0725)\mu\text{m}}{\text{pixel}} = 1.455\frac{\mu\text{m}}{\text{pixel}} \tag{II.13}$$

The size of each pixel according to manufacturer specifications is approximately 7.4 μm, yielding a true system magnification of $M = 7.4/1.455 = 5.09$x.

2.2.2.2 Depth of Field

Depth of field, Δ, is the distance along the optical axis in object space for which a specimen will remain in focus. For a system it can be calculated from the system magnification M, numerical aperture $N.A.$, and tolerable blur size in the image plane d_Δ according to:

$$\Delta = (1 + |M|)\,\frac{d_\Delta}{M^2 N.A.} \tag{II.14}$$

The tolerable blur size is equal to the size of each pixel in the CCD array $d_\Delta = 7.4\,\mu$m. For the imaging system, the numerical aperture and magnification were known and the depth of field was calculated to be $\Delta = 7.91\,\mu$m.

2.2.2.3 Camera Characterization

The relationship between light incident upon the CCD array and the reported grayscale value was determined experimentally. The Photometrics Cascade 650 has adjustable exposure time, Δt, and multiplication gain, G_C settings, and the relationship between incident light and reported grayscale values varied with each combination of settings. In this investigation, two combinations of settings were utilized and are characterized here:

- Medium Light: $\Delta t = 30$ ms; and $G_C = 3100$

- Low Light: $\Delta t = 50$ ms; and $G_C = 3220$

To characterize the camera, Poiseuille flow of a 10 μM fluorescein solution was driven through a microchannel with cross-section of approximately 469 x 41 μm. A 5 W argon-ion laser (Coherent Innova 90) operating at $\lambda_{ex} = 488$ nm was totally internally reflected to generate evanescent-wave illumination inside of the fluorescein solution. The power of the laser was varied to control the amount of light incident upon the fluorescein solution, and therefore the amount of light incident upon the CCD array. The power P of the laser was measured with a laser power meter (Coherent Lasermate Q) and a series of at least 50 images were recorded at each power level for medium and low light settings. A rectangular region around the center of the elliptical Gaussian of at least 1200 pixels was selected for each image series, and the average reported grayscale value V of the region computed.

The measured power and average reported grayscale values were normalized according to:

$$P_n = 100\frac{P - P_{min}}{P_{max} - P_{min}} \tag{II.15}$$

$$V_n = V - V_d \tag{II.16}$$

Here, P_{min} is the minimum power power measured, P_{max} is the maximum power measured, and V_d is the dark noise of the camera (i.e., the average reported grayscale value with the laser shuttered). The camera response for low and medium light settings, shown in Figure 27, are both non-linear. The cubic fits shown in Figure 27 are used to correct for camera non-linearities during image processing. The uncertainty associated with these corrections are estimated in Appendix A.2.

2.2.3 Interrogation Region

In this investigation, temperature measurements of the near-wall region are possible because evanescent-wave illumination decays with distance from the refractive interface. Ideally, illumination will be negligible for distances more than three penetration

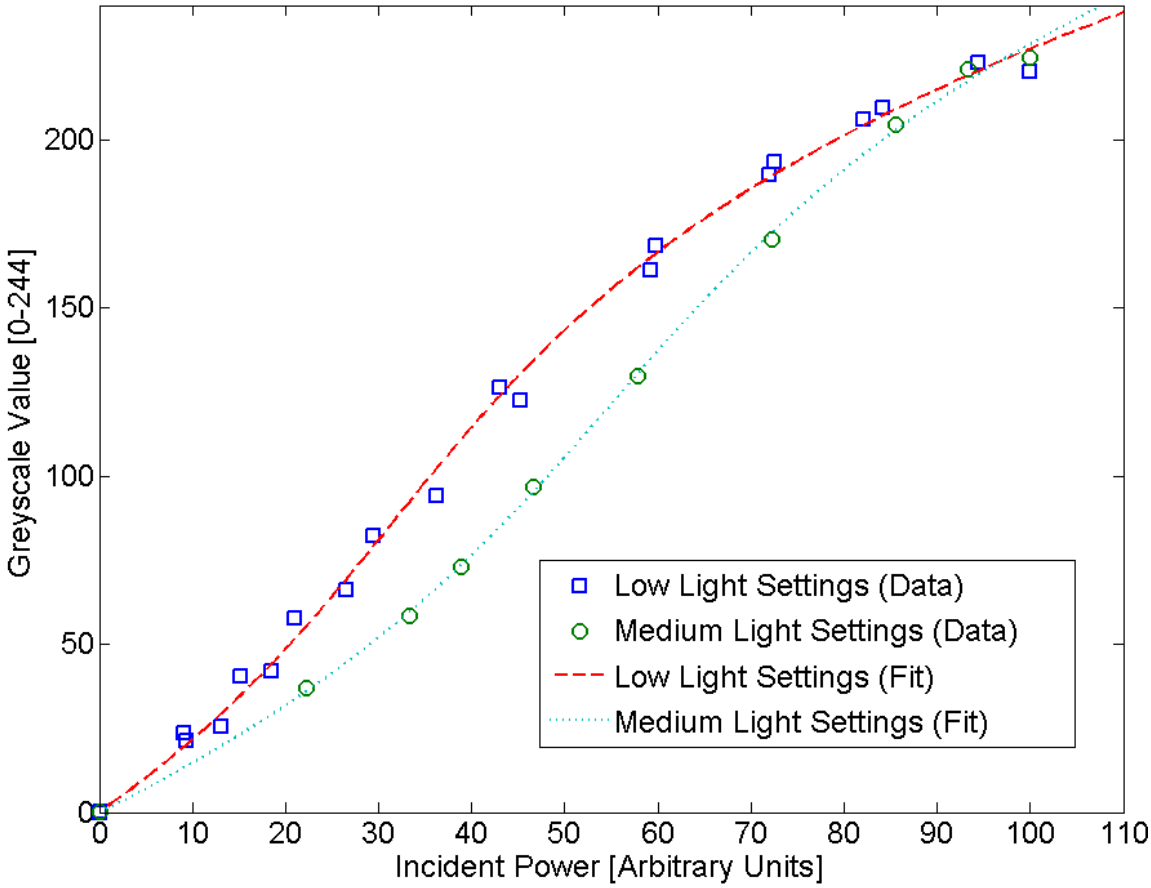

Figure 27: Characterization of camera for two combinations of exposure time and multiplication gain settings. Cubic fits are used to correct camera non-linearities in image processing.

depths from the interface. However, in practice, background illumination is unavoidable due to a combination of partial refraction/reflectance at optical interfaces, scattering, surface imperfections, material defects and other non-idealities. A traditional image processing approach to minimize the effects of background illumination is to simply subtract a background value from every grayscale value. Unfortunately, such an approach would be ineffective for this investigation because background illumination can be absorbed by fluorophores and generate fluorescent emissions. As the fluorescence varies with temperature, the background fluorescence will also be different at each experimental point. Therefore, it is necessary to evaluate the effect of background illumination on the out-of-plane spatial resolution and interrogation region of this measurement technique.

The evanescent-wave illumination will decay with distance from the interface according to equation I.33:

$$I(x, y, z) = I_0(x, y)e^{-z/d_z}$$

If there is a spatially invariant background illumination I_{BG}, then the combined illumination will be

$$I(x, y, z) = I_0(x, y)e^{-z/d_z} + I_{BG} \tag{II.17}$$

For a given pixel (i, j), there is a corresponding 1.455 μm x 1.455 μm area over which the illumination can be considered to be constant with respect to location in the $x-y$ plane. The camera grayscale value $\mathscr{C}_{ij}$ can be approximated as proportional to the integral of the illumination over the depth of focus

$$\mathscr{C}_{ij} \propto \int_0^{\Delta} \left[I_0(x, y)e^{-z/d_z} + I_{BG} \right] dz \tag{II.18}$$

Introducing $\mathscr{C}_E$ and $\mathscr{C}_{BG}$ as the grayscale contributions due to evanescent wave and

background illumination, respectively yields

$$\mathscr{C}_{ij} = \mathscr{C}_E + \mathscr{C}_{BG} \tag{II.19}$$

$$\mathscr{C}_E \propto I_0(x,y) \int_0^{\Delta/2} e^{-z/d_z} dz \approx dI_0(x,y) \tag{II.20}$$

$$\mathscr{C}_{BG} \propto I_{BG} \int_0^{\Delta/2} dz = \frac{\Delta I_{BG}}{2} \tag{II.21}$$

An illustration of typical illumination including contributions to $\mathscr{C}_E$ and $\mathscr{C}_{BG}$ is shown in Figure 28.

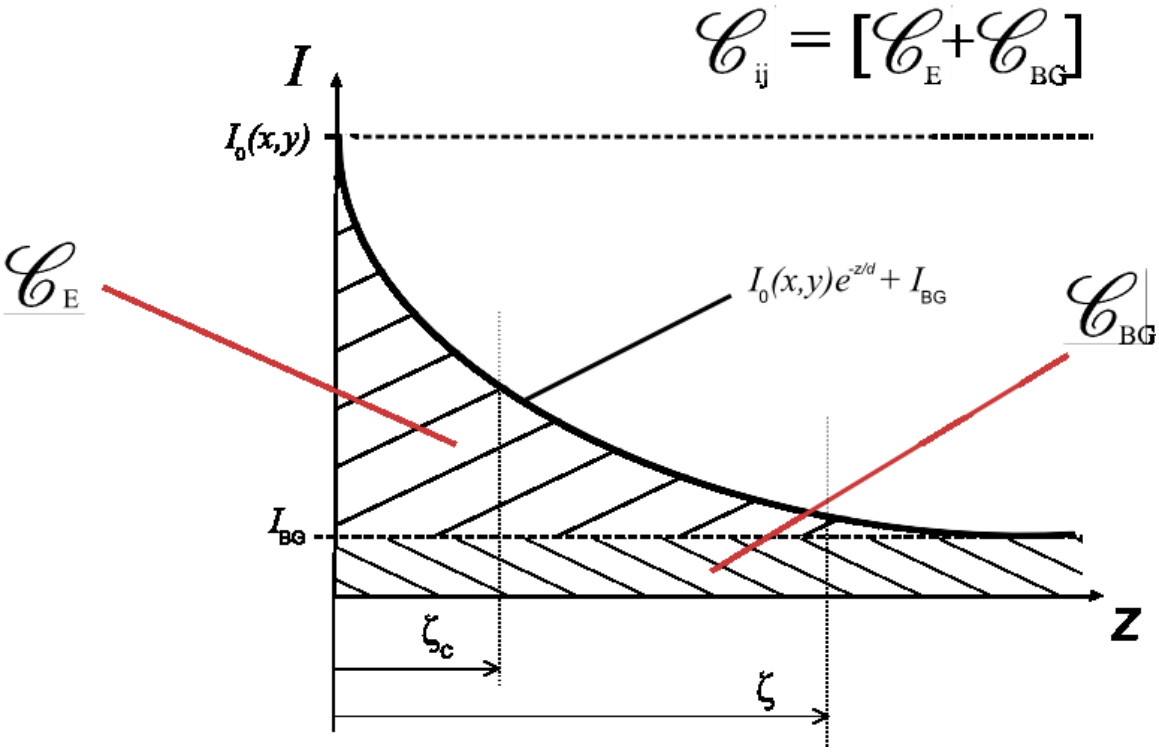

Figure 28: Illustration of typical illumination and variables used to describe the interrogation region.

We define the interrogation depth ζ such that $(1 - e^{-2}) \approx 86\%$ of the illumination lies between $z = 0$ and $z = \zeta$:

$$\frac{\mathscr{C}_{ij}(0 \to \zeta)}{\mathscr{C}_{ij}(0 \to \Delta/2)} = \frac{\int_0^{\zeta} I(x,y,z)dz}{\int_0^{\Delta/2} I(x,y,z)dz} \geq (1 - e^{-2}) \approx 0.86 \tag{II.22}$$

This expression can be simplified to

$$\frac{R_{ij} d_z \left[1 - exp\left(-\zeta/d_z\right)\right] + \zeta}{R_{ij} d_z + \frac{\Delta}{2}} \geq 0.86 \tag{II.23}$$

where R_{ij} is defined as the ratio of evanescent-wave illumination to background illumination

$$R_{ij} = \frac{I_0(x,y)}{I_{BG}} = \frac{\Delta}{2d_z}\left(\frac{\mathscr{C}_{ij}}{\mathscr{C}_{BG}} - 1\right) \tag{II.24}$$

We also define the interrogation centroid ζ_c according to

$$\zeta_c = \frac{\int_0^\zeta zI(x,y,z)dz}{\int_0^\zeta I(x,y,z)dz} \tag{II.25}$$

In terms of R_{ij}, the expression becomes:

$$\zeta_c = \frac{R_{ij}d_z\left[d_z - (d_z+\zeta)\exp\left\{-\zeta/d_z\right\}\right] + \frac{\zeta^2}{2}}{R_{ij}d_z\left[1-\exp\left\{-\zeta/d_z\right\}\right] + \zeta} \tag{II.26}$$

The interrogation depth and interrogation centroid are plotted for three different penetration depths as a function of signal-to-background (SBR) ratio SBR$\equiv \mathscr{C}_{ij}/\mathscr{C}_{BG}$ in Figure 29. Interrogation depth is a strong function of SBR ratio, with an inflection point occurring near SBR = 6. At SBR values below 6, the interrogation depth is independent of the penetration depth. At SBR values above 6, the contribution from background is negligible and the interrogation depth is strongly dependent upon penetration depth. In the limits as SBR approaches one and infinity we see that

$$\text{SBR} \to 1: \qquad \zeta \to \frac{0.86\Delta}{2} \qquad \zeta_c \to \frac{\zeta}{2} = \frac{0.86\Delta}{4} \tag{II.27}$$

$$\text{SBR} \to \infty: \qquad \zeta \to 2d_z \qquad \zeta_c \to 0.69d_z \tag{II.28}$$

It is important to note that the interrogation depth and centroid will be different for each pixel due to differences in SBR ratio. Near the center of the evanescent-wave illumination, the SBR ratio will be higher than at the edge of the illumination.

2.3 Fluorophore Solution Preparation

In this investigation two different fluorophore solutions were used: rhodamine B (Acros Organics, 29657-0250) in de-ionized water with a concentration of [RhB]=1

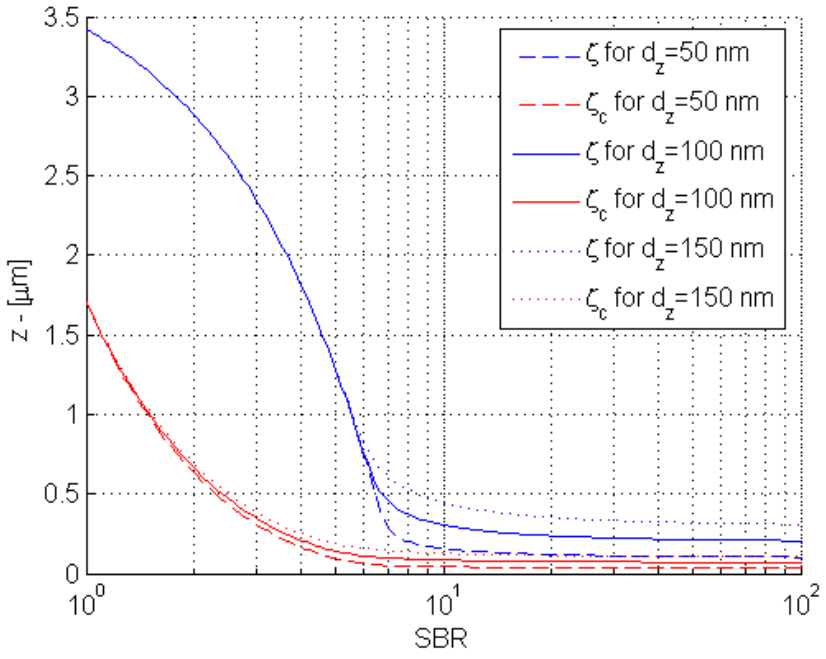

(a)

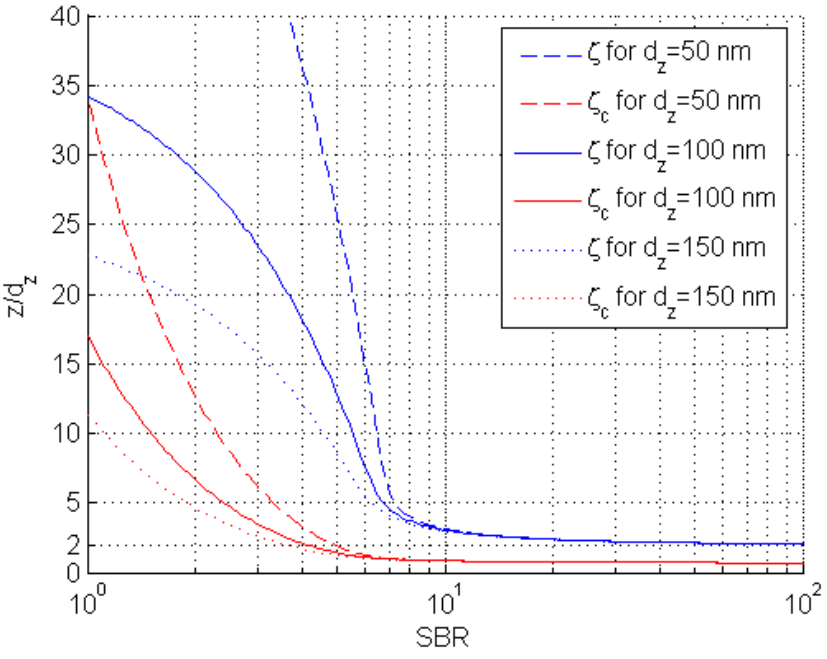

(b)

Figure 29: Interrogation depths (blue lines) and centroids (red lines) plotted against SBR ratio for three different penetration depths.

μM and fluorescein (Spectrum Chemical, FL116) in de-ionized water with a concentration of [Fl]=10 μM. De-ionized water filtered to 0.2 μm from a Barnstead E-Pure system was used with a minimum resistivity of 5.0 MΩ·cm.

The following procedure was used to prepare all fluorescein solutions. A high-concentration intermediate solution was prepared by separating out an amount of fluorescein in the range of 15-50 mg, as measured by a precision scale (Mettler, Type H4) with resolution of 1 mg. The fluorescein of mass m_{fl} was placed into a graduated cylinder and de-ionized water was added to fill the graduated cylinder to the total intermediate solution volume, v_g=100 mL, creating an intermediate solution concentration $[C]_i$ of

$$[C]_i = \frac{m_{fl}}{v_g M.W.} \tag{II.29}$$

where $M.W.$ is the molecular weight of the fluorescein.

To prepare a final fluorescein solution, a small volume v_i of the intermediate fluorescein solution was measured and transfered with a 5 mL polystyrene serological pipet (Fisher Scientific, S68228C) to a laboratory beaker. De-ionized water was added to the laboratory beaker to bring the total solution volume to $v_f = 500$ mL, creating a final solution with concentration $[C]$

$$[C] = \frac{v_i[C]_i}{v_f} = \frac{m_f v_i}{v_g v_f M.W.} \tag{II.30}$$

The amount of intermediate fluorescein solution v_i was calculated according to equation II.30 such that the final solution concentration would be as close to 10 μM as possible. The measurement uncertainty, calculated in Appendix A, remained below 0.4 μM for all 10 μM fluorescein solutions.

The solution was filtered to 1.8 μm using a Buchner funnel (Nalgene, 4280-0700) and a glass fiber filter (Fisher Scientific, Grade G6, 09-804-70A) and degassed by placing under a vacuum for at least 90 minutes.

For some experiments, the fluorescein solution was buffered to a pH of 9.2 by

adding sodium tetraborate decahydrate ($Na_2B_40_7 \cdot 10H_2O$) to the solution. The pH of sodium tetraborate solutions with concentrations across a range from $5 - 50$mM have been shown to have a constant pH of 9.2 at 25℃ [58]. To buffer fluorescein solutions the same experimental procedure was followed, except 50 mL of 100 mM sodium tetraborate in de-ionized water was added to the laboratory beaker prior to adding de-ionized water to bring the total solution volume to $v_f = 500$mL. Therefore, the concentration of sodium tetraborate in the fluorescein solution was 10 mM. The pH of the solution was measured before and after experiments using a pH meter and electrode (Oakton, WD-35614-20) and was found to be 9.2 for all buffered fluorescein solutions.

2.4 Calibration

The purpose of the calibration was to characterize the temperature-dependence of fluorescence intensity from a fluorescein solution illuminated by an evanescent wave. To achieve this end, an experimental apparatus was designed that could heat or cool a fluorescein solution to a temperature over a range of 12.5-55℃. The normalized fluorescence intensity measured by the imaging system was related to the temperature measured by two calibrated thermocouples located near the optical path and attached to the fused silica-solution interface. To improve the accuracy of the calibration it was necessary for the temperature of the solution to be as spatially and temporally uniform as possible. In this section, the experimental apparatus, design considerations and experimental procedure used in the calibration are described.

The experimental apparatus was comprised of two main components: 1) the calibration cell, which contained the fluorescein solution, and provided optical access; and 2) the calibration lid, which reduced evaporative losses and provided support for components of recirculation and temperature control loops.

2.4.1 Experimental Apparatus: Calibration Cell

The calibration cell (Figure 30) was comprised of a fused silica substrate and a hollow fused silica cylinder bonded together by a high strength, epoxy adhesive (Loctite E-60HP). The fused silica substrate also was a component of the optical system and was made from A1-grade optical quality fused silica (Esco Products, Q325063). The hollow fused silica cylinder was made of commercial grade fused silica (Technical Glass Products, CQT47-50-4).

Two T-type thermocouples (Omega, 5TC-TT-T-30-36) were utilized to measure the temperature inside the calibration cell in the vicinity of the fused silica-fluorescein solution interface. The thermocouples were spaced approximately 27 mm apart along the cylinder diameter perpendicular to the beam path. The thermocouples were attached to the fused silica substrate surface using high strength epoxy adhesive (Loctite E-60HP) with an epoxy bead height of 1 mm.

The voltage from each thermocouple was measured and recorded using an Agilent 34970A data acquisition system equipped with a Agilent 34901A multiplexer board and converted to temperature using ITS-90 thermocouple inverse polynomials [60]. To improve the accuracy of the thermocouple measurements, an ice bath was used to provide a 0℃ reference temperature and each thermocouple was calibrated against a Platinum RTD Standard (Burns Engineering, 12001). During calibration the RTD standard and thermocouples were placed inside an Omega CL120 Block Calibrator and the resistance of the RTD was measured using a precision multimeter in a 4Ω configuration. The thermocouples were each calibrated with a first-order polynomial fit:

$$T_c = 1.00041T_r - 0.07160 \qquad \text{for T.C. \#1} \tag{II.31}$$

$$T_c = 0.998624T_r - 0.03877 \qquad \text{for T.C. \#2} \tag{II.32}$$

where T_r is the 'raw' temperature in degrees Celsius from the voltage measurements

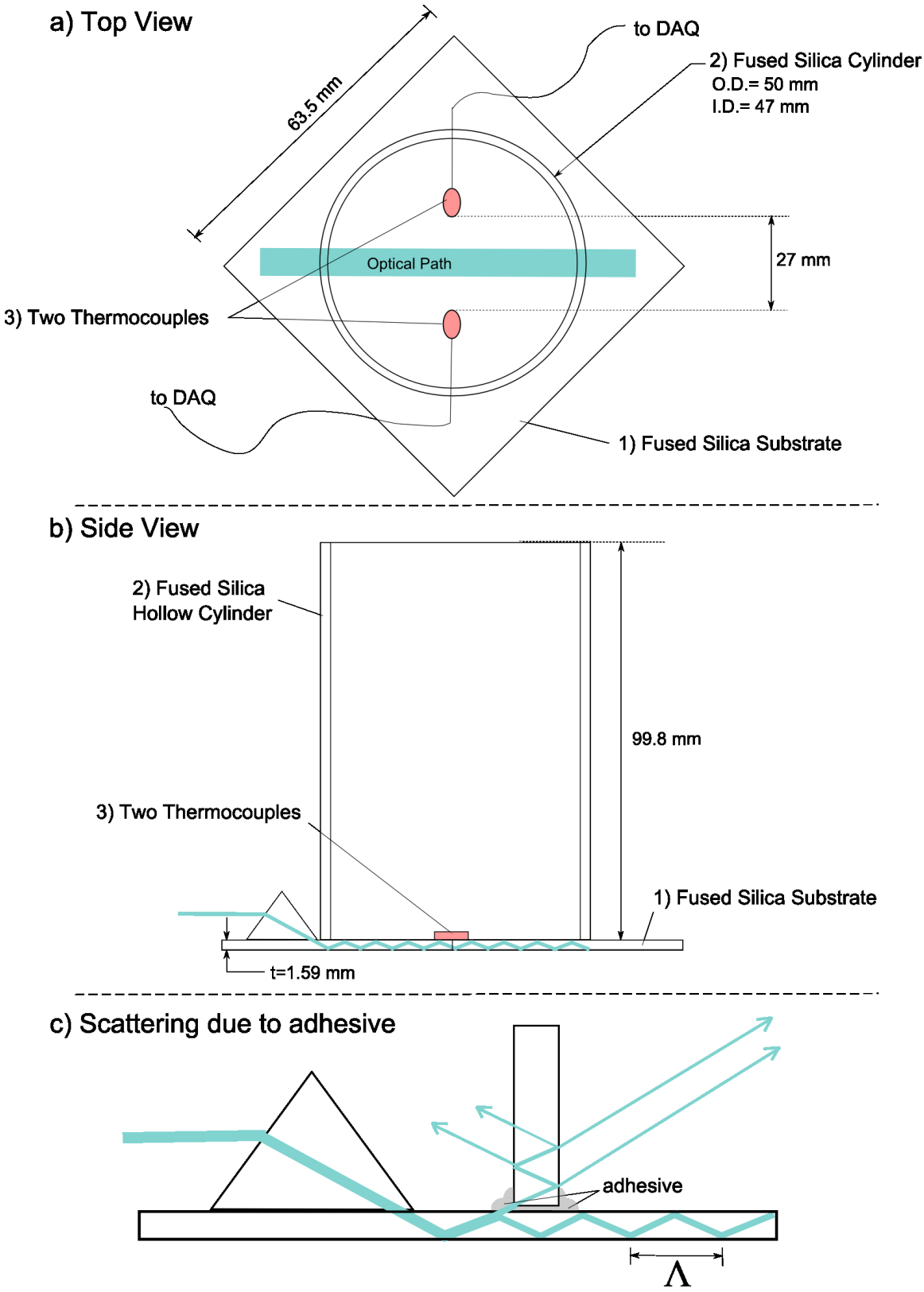

Figure 30: Illustration of (a) top view and (b) side view of calibration cell. (c) Illustration of scattering when illumination is incident upon adhesive. Figure not drawn to scale.

and ITS-90 inverse polynomials, and T_c is the 'corrected' temperature in degrees Celsius. After calibration, r.m.s. deviations from the RTD standard were below 0.05℃ and maximum deviations were below 0.1℃.

2.4.2 Experimental Apparatus: Calibration Lid

The calibration lid (Figure 31) rested on top of the calibration cell and reduced heat and water vapor transfer out of the calibration cell. The calibration lid also provided structural support to components of the recirculation and temperature control flow loops. The recirculation loop mixed the solution to reduce local photobleaching effects and thermal stratification. The temperature control loop controlled the temperature of the fluorophore solution by circulating hot or cold water from a constant temperature bath through a copper coil immersed in the solution.

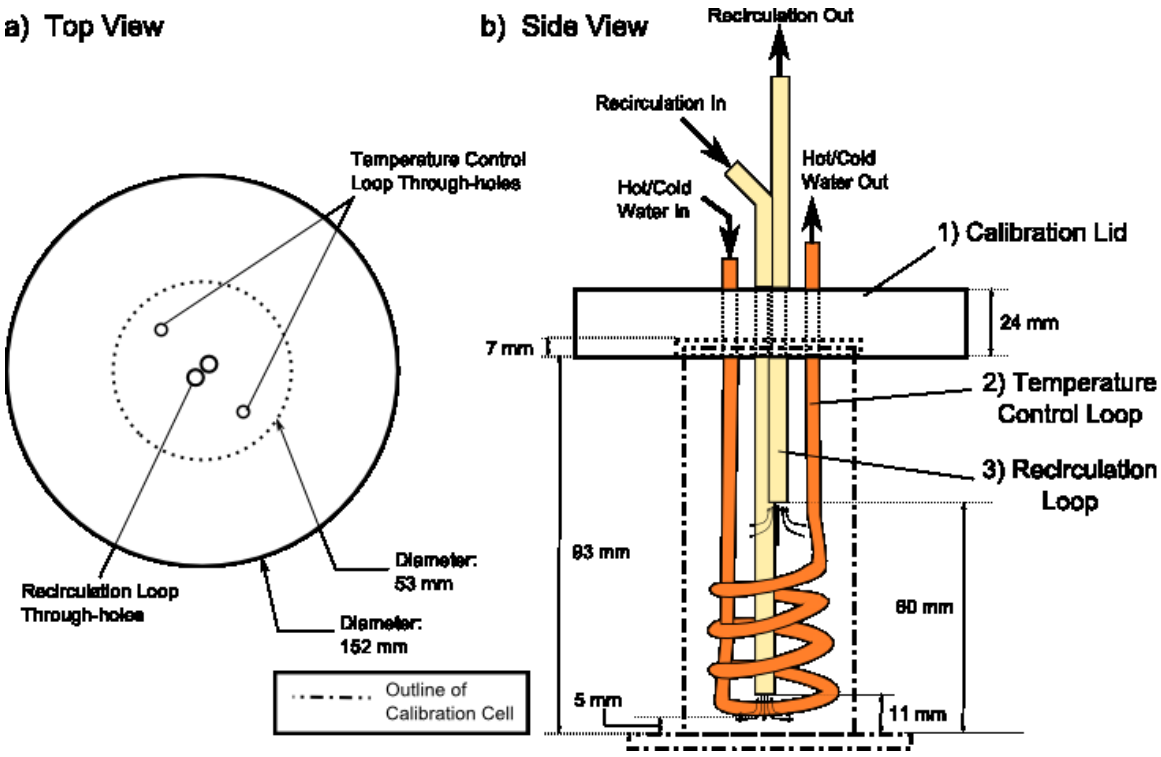

Figure 31: Illustration of (a) top view and (b) side view of calibration lid with temperature control loop coil and inlet and outlet of recirculation loop. Figure not drawn to scale.

The calibration lid was made from a type I PVC (polyvinyl chloride) cylinder with

a height of 24 mm and diameter of 152 mm. A pocket with a diameter of 53 mm and a depth of 7 mm was bored into the bottom of the calibration lid to provide a clearance fit onto the top of the calibration cell. Four through-holes allowed components of the recirculation and temperature control loops to be held in place.

The temperature control loop was comprised of 3/16" (4.8 mm) copper tubing bent into a coil, PVC tubing, and a recirculating constant temperature bath (Haake D8-GH) that formed a closed flow loop. The copper tubing was bent by hand into a coil of approximately four loops with a maximum diameter of 45 mm. Each end of the copper coil was inserted into one of two through-holes in the calibration lid spaced approximately 35.5 mm apart. The copper coil was positioned such that when the calibration lid was rested on the calibration cell, the coil would be centered in the calibration cell with the bottom of the coil suspended 5 mm above the bottom of the fused silica substrate. The copper coil was fixed in this position by epoxy adhesive (Loctite U-05FL). The copper coil was connected to the recirculating constant temperature bath via PVC tubing. By adjusting the temperature of the recirculating constant temperature bath, the temperature of the fluorophore solution could be controlled over a range of 5℃ to 70℃.

The recirculation loop was comprised of a peristaltic pump, plastic tubing, and two copper tubes with O.D.=6.35 mm. The two copper tubes were aligned with the center of the calibration cell in the horizontal plane but vertically staggered by 48.3 mm. Each copper tube was inserted into one of two slightly-off centered through-holes in the calibration lid. The copper tubes were positioned such that the bottom of the recirculation inflow tube was 11 mm from the fused silica substrate and the bottom of the recirculation outflow tube was 60 mm from the fused silica substrate.

Two combinations of peristaltic pump and tubing were used to provide an expanded range of flow rates. A SP200-VO (APT Instruments) with Tygon 3350 sanitary tubing was used to provide flow rates as high as 1.7 mL/sec. For higher flow

rates, a SP300-VO (APT Instruments) with Viton tubing was used to provide flow rates up to 6 mL/sec.

2.4.3 Design Considerations

Because the fluorescence intensity was being calibrated against the temperature measured by two thermocouples, the placement of thermocouples inside of the calibration cell was an important design consideration. It was desired to position the thermocouples so that the locations of the thermocouple beads would have a similar temperature as the interrogation region of the optical system. This could be achieved by placing the thermocouples as close to the interrogation region as possible without being so close as to significantly affect flow or obstruct the optical path.

Attachment of the thermocouples to the fused silica substrate was also an important design consideration. As the interrogation depth is less than one micron, it was desirable to attach the thermocouples to the fused silica surface in such a way that the thermocouple was primarily measuring the fused silica surface temperature. To achieve this aim, a thermally conductive adhesive (Arctic Silver Inc, Silver Thermal Adhesive) was initially used to attach the thermocouples. However, the thermal adhesive was water resistant but not water proof, and with time the thermocouples would detach from the surface. Consequently, high strength adhesive (Loctite E60-HP) was used to attach the thermocouples to the fused silica substrate and no significant deviations in temperature measurements were observed. Axi-symmetric Fluent simulations of the temperature and velocity fields inside of the calibration apparatus indicated that the temperature would be uniform in a cylindrical region with a height of several millimeters and a diameter of 35 mm centered with the calibration cell. The interrogation region and the thermocouple beads were all within this region.

For the recirculation loop, a peristaltic pump was chosen to eliminate contact between the solution and internal pump components, and thereby reduce the chances

of contamination or entrapment of the fluorophore solution. With a peristaltic pump, contact between the solution and the pump is limited to the pump tubing which was identical to the tubing used in the rest of the recirculation loop. Copper tubing was chosen to match the type of tubing used in the temperature control loop. By limiting the variety of materials that the fluorophore solution came into contact with, the opportunity for contamination or entrapment of the fluorophores by corrosion or sorption processes was reduced.

The recirculation inlet was positioned to draw fluorophore solution from the top of the calibration cell; while, the recirculation outlet was positioned to force the fluorophore solution exiting the recirculation loop to impinge upon the fused silica substrate, thereby creating an axi-symmetric stagnation flow. The goal of this orientation was to counter free convection and thermal stratification by removing hotter fluid from the top of the calibration cell and injecting it into the cooler region at the bottom of the calibration cell. It was also intended to decrease local photobleaching effects by increasing fluid velocities near the solution-fused silica interface where evanescent-wave illumination was present.

If the illumination propagating through the fused silica substrate were to be incident at the contact area between the fused silica substrate and the epoxy adhesive, undesired scattering, absorption or refraction (as shown in Figure 30(c)) into the fused silica cylinder or fluorescein solution could cause considerable background illumination and degrade the quality of the evanescent-wave illumination. It was therefore necessary to minimize the size of the bond length of the adhesive along the optical path of the fused silica substrate. The reflection length Λ, defined as the distance between consecutive reflections, can be found from

$$\Lambda = 2t \tan \theta_i \tag{II.33}$$

where t is the thickness of the fused silica substrate. To reduce the likelihood of

illumination being incident upon the adhesive, the thickness of the fused silica substrate was increased to 1.59 mm from an initial design thickness of 1.0 mm. With the 1.59 mm thick fused silica substrate, Λ varied with beam geometry across a range of $8 \sim 12$ mm. It was therefore desirable to limit the adhesive bond length along the optical path to less than 8 mm. The actual bond length was measured to be less than 5 mm along the optical path.

2.4.4 Experimental Procedure

2.4.4.1 Cleaning

Before an experimental run, many components of the experimental apparatus had to be cleaned. The entrance and exit prisms were rinsed twice with methanol and deionized water and blown dry with ultra-high purity Nitrogen gas. Optical components were cleaned by a jet of high-purity, low-moisture compressed gas. The calibration lid was rinsed twice with methanol and deionized water and blown dry with laboratory compressed air.

Of primary importance was the cleanliness of the fused silica substrate because any impurities on the surface could interact with the fluorophore or interfere with the evanescent-wave illumination. Many methods of cleaning were attempted with unsatisfactory results, including ultrasonication, rinsing with methanol, and soaking with sodium hydroxide. Eventually a satisfactorily clean surface was achieved by soaking the calibration cell in a solution of Contrad 70 (Decon Labs) chemical soap diluted to 10%v/v in de-ionized water. For the results presented in this investigation, the calibration cell was soaked in a Contrad 70 for a period of at least 2 hours. The calibration cell was then rinsed with methanol and de-ionized water and blown dry with ultra-high purity Nitrogen gas.

2.4.4.2 Alignment

After cleaning, the calibration cell was placed upon the microscope stage with the center of the calibration cell approximately aligned with the microscope objective. Small drops of fused-silica matching optical liquid were used to optically couple the entrance and exit prisms to the fused silica substrate. The laser illumination location and orientation could be controlled ("steered") by adjusting the mirrors up-beam of the calibration cell. It was necessary to steer the illumination to generate an evanescent wave at a location:

1. aligned with the microscope objective
2. aligned with the approximate center of the calibration cell
3. where the fused silica substrate had few defects
4. where the background signal was minimized.

These four requirements were realized by aligning the evanescent wave with the microscope objective at the center of the calibration cell and then adjusting the mirrors and the microscope stage to reduce background illumination from scattering at the adhesive bond line (Figure 30). The microscope stage was then carefully adjusted to slightly alter the optical path until a region of lesser background signal was observed. Finally, the mirrors were fine-tuned to center the fluorescence signal in the camera viewfield, the image was focused at the solution-fused silica interface, and the laser was shuttered to reduce photobleaching.

2.4.4.3 Experimental Run

Fluorescein solution, prepared as described in section 2.3, was poured into the calibration cell to a height between 70 and 75 mm, corresponding to a volume of approximately 120-130 mL. The calibration lid was placed on top of the calibration cell

and connected to the recirculating constant temperature bath and peristaltic pump. The recirculating constant temperature bath was initially set to 20℃ and the voltage applied to the peristaltic pump remained fixed at 10 VDC, corresponding to a flow rate of 6 mL/sec.

The temperature of the recirculating constant temperature bath was varied in 5℃ increments between 7.5℃ and 60℃ to modify the temperature of the fluorescein solution inside of the calibration cell. The voltages from the two ice-bath-referenced thermocouples attached to the fused silica substrate were monitored to detect when the temperature of the solution reached steady-state, which was typically reached after 10 minutes.

At steady state, the laser was un-shuttered, a sequence of 100 images was captured with the camera at 'medium light' settings (exposure time $\Delta t = 30$ and multiplication gain $G_C = 3100$) and the laser re-shuttered. Simultaneously, the voltage of each thermocouple was sampled by the HP 34970A/34901A data acquisition system at a rate of 1.46 Hz. The time to capture a sequence of 100 images was approximately 12 seconds, the laser was un-shuttered for approximately 20 seconds and the thermocouples were sampled over a period of approximately 30 seconds. The mean, standard deviation and precision uncertainty of voltage measurements from each thermocouple were calculated. Precision uncertainties were on the order of 500 nV, which across the range of 0-60℃ corresponds to a maximum expanded precision uncertainty of 0.026℃.

2.4.4.4 Dark and Background Image Sequences

Dark and background image sequences were also taken to provide a measure of dark and background noise. These image sequences were taken with experimental conditions being as similar to actual data points as practicable. The dark image sequence was taken before an experimental run with the laser shuttered.

Ideally, to measure the background signal it would be possible to capture a sequence of images in a region several millimeters to the side of the evanescent-wave illumination with the illumination path and calibration cell remaining exactly the same as during the experimental run. Unfortunately, this is not possible because it would require movement of the microscope relative to the calibration cell and illumination path. In practice, the microscope objective is fixed in place and the calibration cell and the illumination path are movable. As the calibration cell and illumination path are moved the evanescent-wave illumination and background signal vary. To estimate the background signal during an experimental run, after an experimental run mirrors and microscope stage were adjusted to offset the evanescent-wave illumination from the center of the microscope objective. The mirrors and microscope stage were adjusted (as before the run) while maintaining the offset evanescent-wave illumination until a region of lower background signal was observed. At this location of low background signal, the background image sequence was taken.

2.5 Image Processing

For each experimental point ϕ a sequence of 492 x 653 pixel image exposures were acquired from the CCD camera. Image sequences were 100 images long, resulting in approximately 30 million grayscale values for each data point. In this section the image processing methods used to condense these 30 million grayscale values are described and illustrated with an experimental series taken at 25℃. As shown in Figure 32, an 'experimental series' refers to a series of experimental points taken under different experimental conditions (usually a different temperature) and an 'image sequence' refers to a sequence of images acquired sequentially in time.

The nomenclature used in this section is summarized in Table 4. The subscripts i and j refer to pixel row and pixel length, respectively, and can be mapped into (x, y) coordinates in object space. The subscript k refers to the index of the image

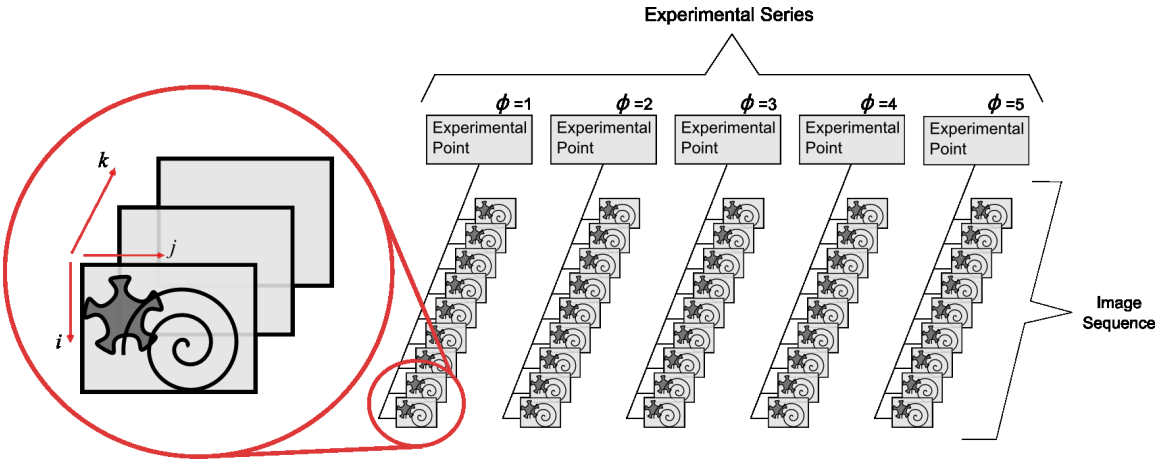

Figure 32: Schematic of an experimental series, showing individual image sequences and individual images. Also shown are indexing subscripts i, j, and k.

in the sequence and can be related to the time of image capture. The absence of a subscript implies that image has been averaged over the entire range of the absent subscript. For instance, while $\mathscr{G}_{ijk}$ refers to the reported grayscale value at a single pixel at a single time, $\mathscr{G}_{ij}$ refers to the time-averaged reported grayscale value at a single pixel and $\mathscr{G}$ refers to the reported grayscale value of an entire image after time- and spatial-averaging. A single image from the image sequence taken at 25℃ is shown in Figure 33.

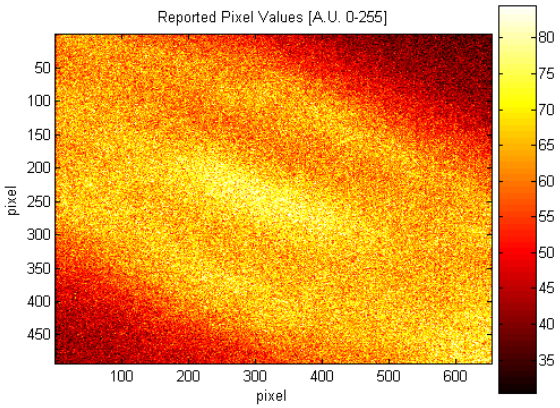

Figure 33: The twentieth image (i.e. $k = 20$) from the image sequence $\mathscr{G}_{ijk}$ taken at 25℃.

Table 4: Nomenclature of symbols used in image processing

Symbol	Description
Superscripts	
ϕ	experimental data point
n	normalizing image
$+$	bright binary image
$-$	dim binary image
Subscripts	
i	pixel row
j	pixel column
k	image number in series
Images	
$\mathscr{G}$	reported greyscale value
$\mathscr{D}$	dark grayscale value
$\mathscr{C}$	corrected pixel value
$\mathscr{N}$	normalized pixel value
$\mathscr{B}$	binarized pixel value
$\mathscr{M}$	mask pixel value

2.5.1 CCD Camera Corrections

There are typically three types of noise present in CCD camera array: background, readout noise, and dark noise. As discussed in section 2.2.3, the background noise, in this case, cannot be subtracted and can strongly affect out-of-plane spatial resolution. Readout noise is introduced into images by chip electronics and analog-to-digital conversion. The Photometrics Cascade 650 has on-chip multiplication gain that is expected to reduce, but not eliminate, the magnitude of read-out noise. To further reduce the influence of read-out noise, each image is time-averaged over 94 images. As seen in Figure 34 , the amount of random noise is lower in the time-averaged image as compared to a single image.

Dark noise is produced in all CCD cameras due to thermal excitation of electrons in the CCD array. To correct for dark noise, a dark image sequence $\mathscr{D}_{ijk}$ was acquired with the laser aperture shuttered for each experimental series. For each experimental point, the image sequence was time-averaged to reduce read-out noise and then the

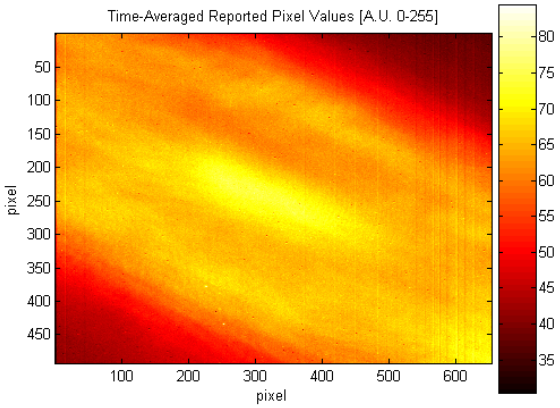

Figure 34: Time-averaged image $\mathscr{G}_{ij}$ taken at 25℃. Random noise is reduced in the time-averaged image as compared to the single image from the sequence shown in Figure 33.

time-averaged dark image (Figure 35a) subtracted:

$$\mathscr{G}_{ij} - \mathscr{D}_{ij} \tag{II.34}$$

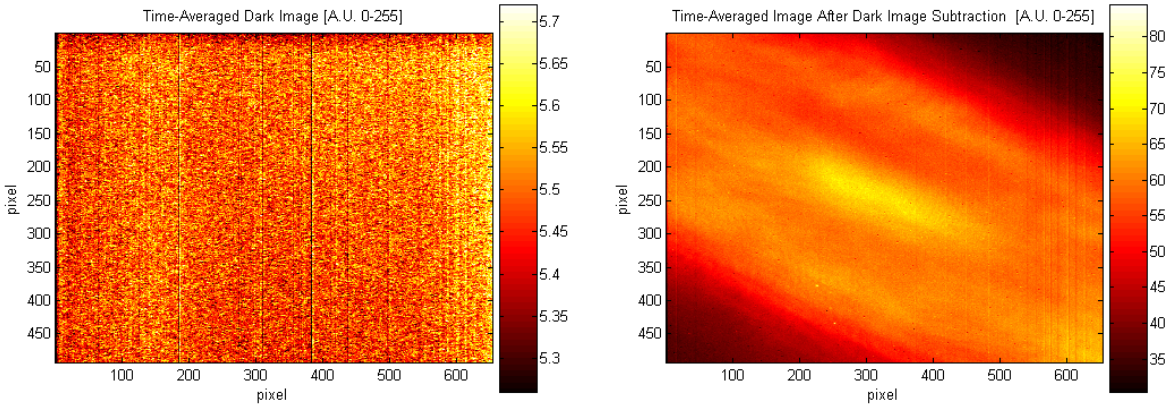

(a) (b)

Figure 35: Dark noise subtraction: (a) time-averaged dark noise image; (b) time-averaged image after dark noise subtraction (result of subtracting Figure 35a from Figure 34).

The non-linearity of the camera, as characterized in section 2.2.2.3 was also corrected for. The equations of the cubic polynomial fits shown in Figure 27, for medium

and low light settings, respectively, are:

$$f_c(g) = 9.3 \times 10^{-6} g^3 - 3.4 \times 10^{-3} g^2 + 0.73g \tag{II.35}$$

$$f_c(g) = 9.9 \times 10^{-6} g^3 - 2.6 \times 10^{-3} g^2 + 0.51g \tag{II.36}$$

Here g is a reported pixel value after subtracting dark noise. Combining corrections for readout noise, dark noise and camera linearity, yields a corrected image $\mathscr{C}_{ij}$:

$$\mathscr{C}_{ij} = f_c\left([\mathscr{G}_{ij} - \mathscr{D}_{ij}]\right) \tag{II.37}$$

The corrected image (Figure 36) is a measure of the total fluorescence intensity (i.e. $\mathscr{C}_{ij} \approx \bar{\mathscr{F}}$) discussed in the Theoretical Overview, section 2.1.

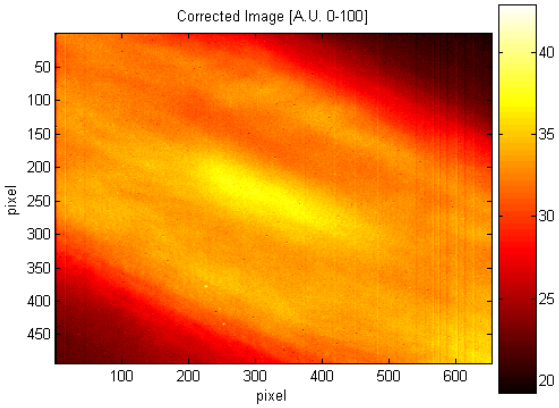

Figure 36: Corrected image $\mathscr{C}_{ij}$ taken at 25℃. Image is the result of applying equation II.35 to each pixel of Figure 35b.

2.5.2 Binary Mask Generation

For each experimental series many pixels were unsuitable for quantitative measurements due to regions of uncharacteristically low or high corrected pixel values. In most cases, low grayscale values corresponded to regions of low illumination toward the edge of the Gaussian illumination. High grayscale values corresponded to regions where defects on the fused silica surface or interior interfered with the propagating beam and/or evanescent-wave illumination.

To identify unsuitable regions in an image, histograms of corrected grayscale values vs. number of occurrences (count) were generated. Histograms typically demonstrated a strong, relatively narrow peak that rapidly declined as intensity increased. As the intensity decreased below the peak there was a relatively gentle decline, corresponding to the low illumination at the edge of the evanescent-wave illumination. For each time-averaged image sequence, a bright i^+ and dim i^- intensity threshold were selected. A binary image was created for each threshold value, with a one or zero assigned to each pixel based upon whether the corrected grayscale value exceeded threshold values. The binary images, represented by $\mathscr{B}_{ij}^{+}$ and $\mathscr{B}_{ij}^{-}$ for i^+ and i^-, respectively were defined as:

$$\mathscr{B}_{ij}^{+} = \begin{cases} 1 & \mathscr{C}_{ij} \leq i^+ \\ 0 & \mathscr{C}_{ij} > i^+ \end{cases} \tag{II.38}$$

$$\mathscr{B}_{ij}^{-} = \begin{cases} 1 & \mathscr{C}_{ij} \geq i^- \\ 0 & \mathscr{C}_{ij} < i^- \end{cases} \tag{II.39}$$

These binary images were used to mask the unsuitable regions in the corrected images by pixel-by-pixel multiplication.

A single binary mask $\mathscr{M}_{ij}$ was created for the each experimental series. This mask was the product of all the bright and dim binary masks for the entire experimental series:

$$\mathscr{M}_{ij} = \prod_{\phi=1}^{N_\phi} \left(\mathscr{B}_{ij}^{\phi+} \cdot \mathscr{B}_{ij}^{\phi-} \right) \tag{II.40}$$

where N_ϕ is the number of experimental points in the experimental series. As a result of this method, if a pixel was unsuitable at any one experimental point, then it was excluded for all data points in that experimental series. The binary mask for the image sequence taken at 25℃ is shown in Figure 37.

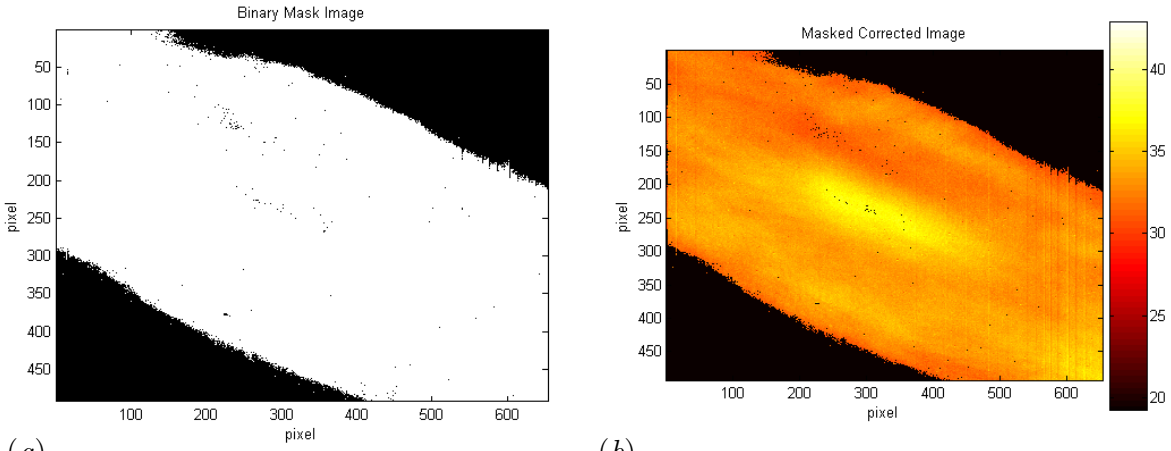

(a) (b)

Figure 37: Masking: (a) binary mask; (b) product of element-by-element multiplication of binary-mask (Figure 37a) with corrected image (Figure 36).

2.5.3 Normalization

Experimental points were normalized to decouple spatial variations in fluorescence intensity due to changing temperature from those due to illumination, optical path length, and concentration, as explained in section 2.1. For each experimental series a single normalization point (designated by the superscript n) was chosen where the temperature of the fluorescein solution was known and spatially uniform. For each data point ϕ, the normalized pixel value $\mathscr{N}_{ij}^{\phi}$ was the result of pixel-by-pixel division of the corrected pixel for that data point $\mathscr{C}_{ij}^{\phi}$ by the corrected pixel value at the normalization point $\mathscr{C}_{ij}^{n}$:

$$\mathscr{N}_{ij}^{\phi} = \frac{\mathscr{C}_{ij}^{\phi}}{\mathscr{C}_{ij}^{n}} \tag{II.41}$$

Figure 38 shows the corrected image, normalizing image, and the normalized image for an image sequence taken at 25℃. The normalized pixel value was a measure of the normalized total fluorescence intensity, that is $\mathscr{N}_{ij} \approx \bar{\mathscr{F}}^{\star}$, discussed in the Theoretical Overview, section 2.1. For the image shown in Figure 38c, there is excellent agreement between spatially-resolved measurements of the normalized fluorescence intensity, with the spatial standard deviation of measurements of only 1%. The

variation appears to be random 'salt-and-pepper' noise, that can be mitigated by spatial-averaging.

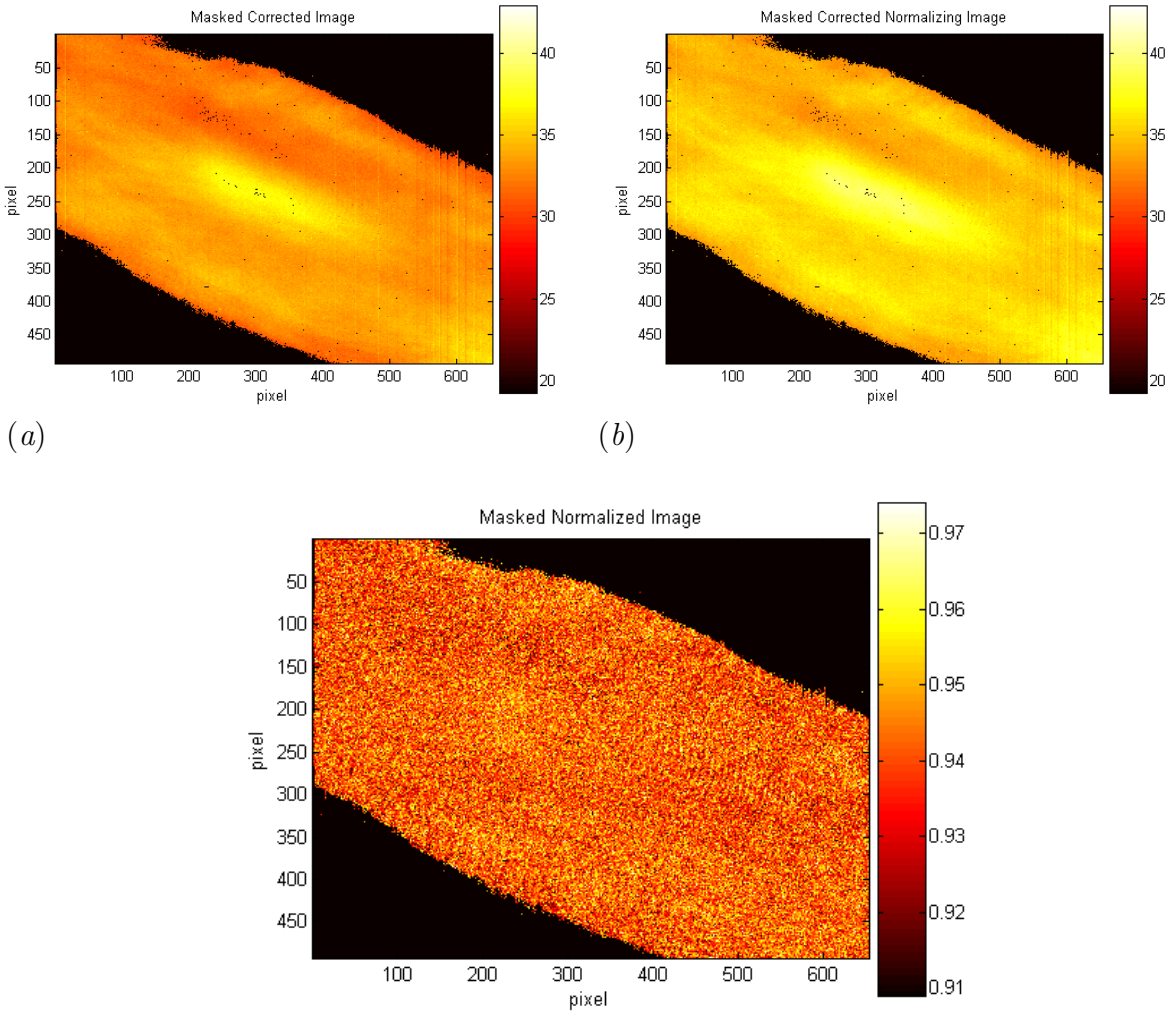

(*a*) (*b*)

(*c*)

Figure 38: Normalizing process: (a) masked, corrected image at 25℃; (b) masked, corrected normalizing image at 30℃; (c) normalized image at 25℃, the quotient of (a) divided by (b).

2.5.4 Calibration Data Reduction

To reduce a normalized image to a single value, the spatial-average of the unmasked pixels of the normalized image was calculated. This average value F^{ϕ} was the final result of image processing that would be plotted against temperature to find a

relationship between fluorescence intensity and temperature:

$$F^{\phi} = \frac{\sum_i \sum_j \mathscr{N}_{ij}^{\phi} \cdot \mathscr{M}_{ij}}{\sum_i \sum_j \mathscr{M}_{ij}} \tag{II.42}$$

The standard deviation of the normalized fluorescence intensity image was estimated from:

$$\sigma_{\mathscr{N}_{ij}^{\phi}} = \sqrt{\frac{\sum_i \sum_j \left[\mathscr{M}_{ij} \cdot \left(\mathscr{N}_{ij}^{\phi} - F^{\phi} \right)^2 \right]}{\sum_i \sum_j \mathscr{M}_{ij}}} \tag{II.43}$$

This standard deviation provided a measure of the spatial variation in the normalized fluorescence intensity.

Each normalized image was also broken into regions to evaluate the uncertainty of the technique at two different spatial resolutions: 16×16 and 100×100 μm. The technique is demonstrated here with an image sequence taken at 55℃ that demonstrated a spatial bias in normalized fluorescence intensity. For 16×16 μm resolution, each normalized image was divided into a total of 2,596 bins of 11×11 pixels (Figure 39b). For 100×100 μm resolution, each normalized image was divided into a total of 63 bins of 69×69 pixels (Figure 39c). The value of each bin was then the average value of the 11^2 or 69^2 constituent pixels.

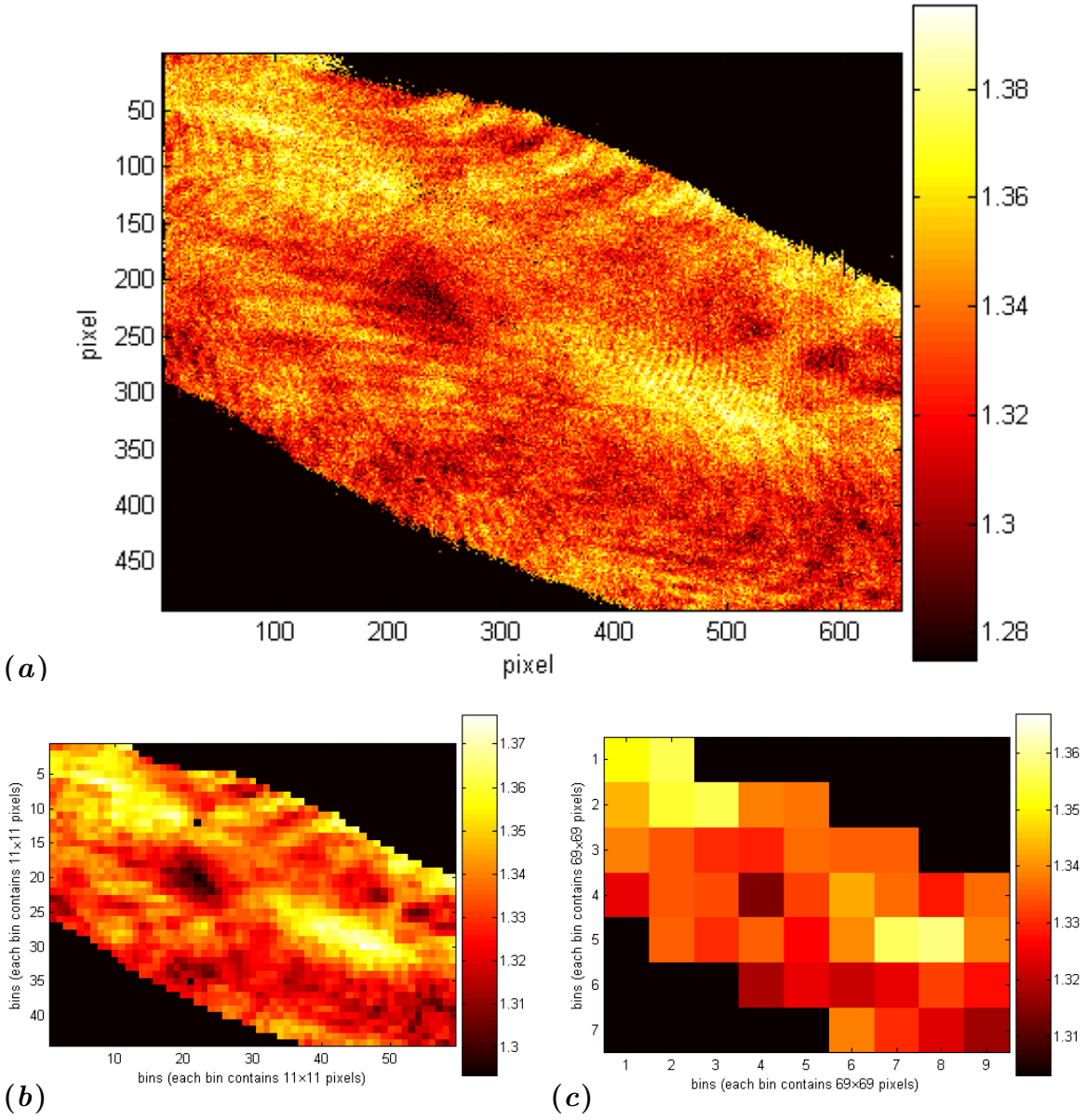

Figure 39: Representative images illustrating binning the individual pixels of a normalized image for an image sequence at 55℃: (a) original image of normalized fluorescence intensity at full spatial resolution; (b) image after binning image (a) over 11×11 pixels (corresponding to a spatial resolution of 16 μm); (c) image after binning image (a) over 69 x 69 pixels, corresponding to a spatial resolution of 100 μm. Images are false colored by normalized fluorescence intensity.

CHAPTER III

EXPERIMENTAL RESULTS AND DISCUSSION

3.1 Calibration Results

Experimental image sequences were taken in two experimental runs producing six experimental series and a total of 44 data points. Each experimental run consisted of an experimental series of increasing set temperature with time, followed by a penultimate experimental series of decreasing set temperature with time, and concluding with a final experimental series of increasing set temperature with time.

The purpose of this experimental procedure was to identify any hysteresis of normalized fluorescence intensity with respect to temperature and to check the repeatability of the calibration. For each experimental run, a new solution was prepared and the optical arrangement that generated the evanescent-wave illumination was different. However, each experimental runs' three experimental series contained the same fluorophore solution and the orientation of the optical system remained constant with one notable exception—the microscope was refocused before each data series. Unless otherwise noted, all results in this chapter are for 10 μM fluorescein solutions in de-ionized water buffered to a pH of 9.2 by 10 mM sodium tetraborate.

3.1.1 Background Illumination and Out-of-Plane Resolution

Image sequences of background illumination were taken for each experimental run at 30℃. These background image sequences were time-averaged and corrected for dark noise and camera non-linearity, yielding corrected images $\mathscr{C}_{ij}$. Histograms of each corrected image with 100 bins were constructed, yielding a normal distribution. The background value should be a constant minimum value upon which evanescent-wave illumination intensity is superimposed. Therefore, the lower edge of each histogram,

determined by a bin count of approximately 200, was taken as the background value. Background values were 5.6 and 9.5 for experimental run one and two, respectively.

Signal-to-background (SBR) ratios were calculated for each experimental run based upon the maximum and minimum values of a masked corrected image of an experimental data point taken at approximately 30℃. The resulting range of corrected values, signal to background ratio (SBR), interrogation depth and interrogation centroid are summarized in Table 5.

Table 5: Estimate of background (B.G.) illumination, interrogation depth and interrogation centroid for calibration measurements.

		Minimum Fluorescence Intensity				Maximum Fluorescence Intensity			
Exp Run	B.G. Signal	Total Signal	SBR	Depth ζ [μm]	Centroid ζ_c [nm]	Total Signal	SBR	Depth ζ [μm]	Centroid ζ_c [nm]
One	5.6	35.6	6.4	0.59	100	46.2	8.3	0.35	90
Two	9.5	32.3	3.4	2.14	280	40.2	4.3	1.65	180

The out-of-plane spatial resolution of the TIR-FMT technique can be determined by the interrogation depth and interrogation centroid, described in section 2.2.3. The best achievable out-of-plane spatial resolution of the TIR-FMT technique across an entire experimental run was achieved in experimental run one. Here, the minimum SBR value corresponds to a interrogation depth of 590 nm. Therefore, the out-of-plane spatial resolution of the technique is conservatively taken as 600 nm.

3.1.2 Average Fluorescence Intensity

Image sequences were time-averaged, corrected for camera non-linearity and averaged to generate corrected images. These corrected images were spatially-averaged to create averaged data points ($\mathscr{C}^{\phi}$) that were a measure of the spatially-averaged total fluorescence intensity. These data points are shown for each experimental run in Figures 40 and 41. A near-linear relationship between fluorescence intensity and temperature is seen, with slight variations in slope for each data series.

There is excellent convergence of data along a straight line for each experimental

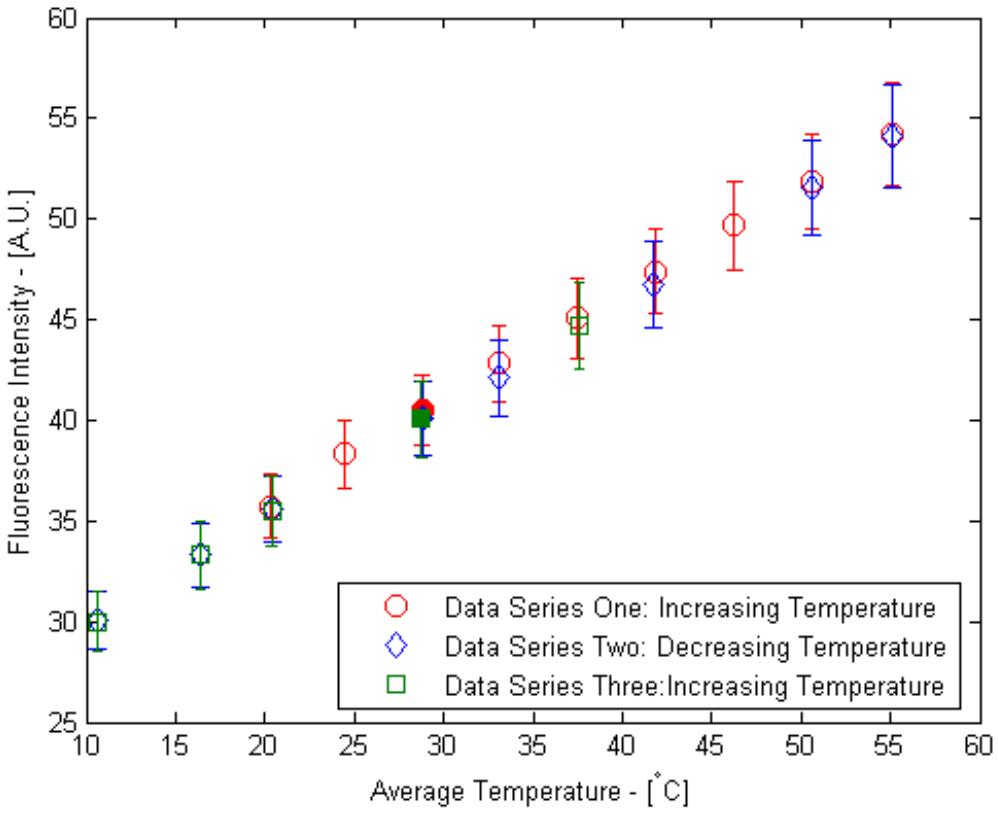

Figure 40: Spatially-averaged total fluorescence intensity vs. temperature for the first experimental run. Data points were generated by spatial-averaging of corrected image values. Error bars are the spatial standard deviation of the corrected images.

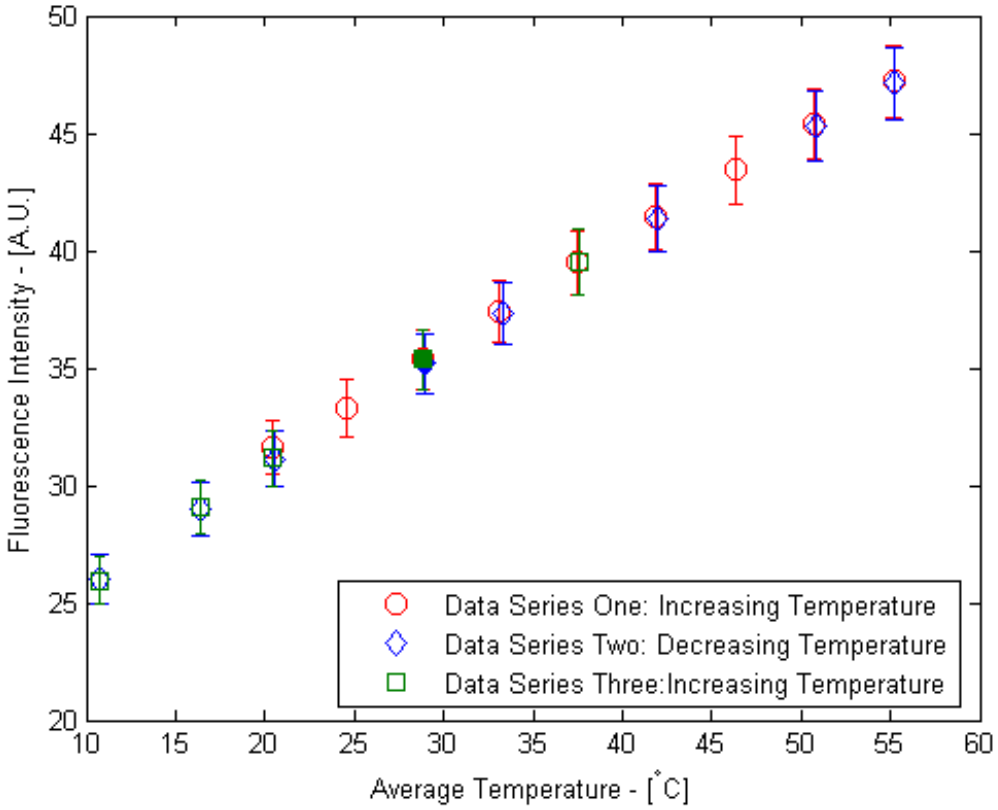

Figure 41: Spatially-averaged total fluorescence intensity vs. temperature for the second experimental run. Data points were generated by spatial-averaging of corrected image values. Error bars are the spatial standard deviation of the corrected images.

run. Significant hysteresis was not present and good repeatability was observed for all experimental results. The linear relationship between averaged fluorescence intensity and temperature allows the normalization point to be different for each data series. The normalizing data points were chosen to be near 30℃ and are shown as filled markers in Figures 40 and 41.

3.1.3 Normalized Fluorescence Intensity

The corrected images were normalized following the procedure described in section 2.5. The normalized images were spatially-averaged and plotted against normalized temperature $\Theta = T - T_n$ (Figure 42). The error bars shown are the standard combined uncertainty of each normalized data point $\sigma_{\mathscr{N},\text{comb}}$ calculated by combining the spatial standard deviation and the resolution uncertainty as described in appendix section A.3.2.4.

The experimental data was fit to a linear polynomial of the form $F = m\Theta + b$, by minimizing a chi-squared merit function weighted according to the uncertainty of each data point [65]. A direct result of the normalization process is that each normalization point ($\phi = n$) results in a data point at $(\Theta, F) = (0, 1)$ with a variance of zero because $F = \text{mean}\,\langle \mathscr{N}_{\phi=n} \rangle = \text{mean}\,\langle \mathscr{C}_n / \mathscr{C}_n = 1 \rangle = 1$ and $\Theta_{\phi=n} = T_n - T_n = 0$. Therefore, the offset parameter b is fixed as 1, while the slope parameter m was found by finding the value for m that minimized the chi-squared merit function:

$$\chi^2 = \sum_{\phi=1}^{N} \left(\frac{F_\phi - 1 - m\Theta_\phi}{\sigma_\phi^2} \right)^2 \tag{III.1}$$

here $\sigma_\phi = \sigma_{\mathscr{N},\text{comb}}$ is the calculated combined uncertainty of each data point. The value of m that minimizes the merit function was found by taking the partial derivative of χ^2 with respect to m and setting equal to zero:

$$\frac{\partial \chi^2}{\partial m} = 0 = -2 \sum_{\phi=1}^{N} \left(\frac{F_\phi - 1 - m\Theta_\phi}{\sigma_\phi^2} \right) \frac{\Theta_\phi}{\sigma_\phi^2} \tag{III.2}$$

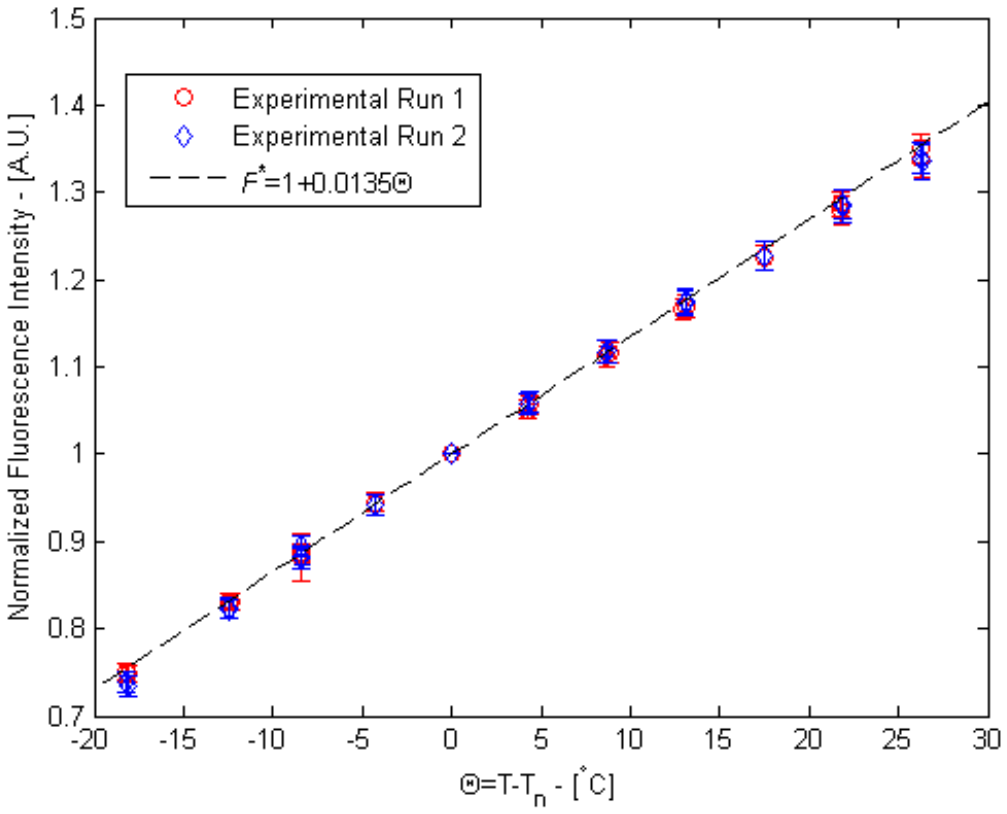

Figure 42: Normalized data points plotted versus Θ with a linear least-squares fit: $F = 1 + 0.0135\Theta$. The error bars are the combined single-pixel precision uncertainty and measurement uncertainty for each data point estimated in appendix A.3.2.4.

defining the following summations:

$$S = \sum_{\phi=1}^{N} \frac{1}{\sigma_\phi^2} \qquad S_x = \sum_{\phi=1}^{N} \frac{\Theta_\phi}{\sigma_\phi^2} \tag{III.3}$$

$$S_{xx} = \sum_{\phi=1}^{N} \frac{\Theta_\phi^2}{\sigma_\phi^2} \qquad S_{xy} = \sum_{\phi=1}^{N} \frac{\Theta_\phi F_\phi}{\sigma_\phi^2} \tag{III.4}$$

and substituting into the above summation yields:

$$m = \frac{S_{xy} - S_x}{S_{xx}} \tag{III.5}$$

Using the above expressions with the calibration data points and the uncertainties as shown in Figure 42, gives a value of $m = 0.0135$. This value of m corresponds to a fluorescence intensity temperature-dependence of $dF/dT = +1.35$ %/℃ for fluorescein. The value of m was well-determined, with the standard uncertainty associated with the parameter m determined to be $u_m = 1.49 \times 10^{-4}$ using the algorithm described in appendix section A.3.3.

In practice, the calibrated relationship $F = 1 + m\Theta$ would be inverted and the normalized fluorescence intensity measured to generate a temperature measurement:

$$T = T_n + \frac{F - 1}{m} \tag{III.6}$$

The accuracy of the such measurements has been estimated in Appendix A.3. The maximum and r.m.s expanded uncertainties of temperature measurements across the 715×950 μm viewfield was found to be 1.94℃ and 1.50℃ with 95% confidence.

The uncertainty of the calibration was dominated by the contribution of the deviation of prediction bounds from the linear-least squares fit. The impact of experimental scatter is illustrated by Figure 43, which shows the experimental data with 95% prediction bounds. Any new individual experimental data point would then have a 95% probability of lying between these two prediction bounds. Prediction bounds deviate from the linear fit by as much as 2.1%, which corresponds to an expanded uncertainity in temperature of $U_T = 1.74$℃.

Table 6: Average, r.m.s., and maximum temperature uncertainties (95% confidence) for different spatial resolutions.

region size (pixels)	spatial res. (μm)	avg. uncertainty (℃)	r.m.s uncertainty (℃)	max. uncertainty (℃)
1×1	1.5×1.5	2.30	2.40	4.16
11×11	16×16	1.95	1.97	2.38
69×69	100×100	1.76	1.78	2.21
492×653	715×950	1.48	1.50	1.94

The expanded uncertainties were estimated for measurements based upon individual 1.5×1.5 μm pixels. The maximum and r.m.s. single-pixel expanded uncertainty were calculated to be 4.16℃and 2.40℃ (95% confidence), respectively. The single-pixel uncertainty was dominated by the precision uncertainty associated with the spatial standard deviation of the normalized image, with a significant contribution from the deviation of prediction bounds from the linear-least squares fit.

Improved accuracy was realized by averaging normalized intensity values across regions of 11×11 and 69×69 pixels, resulting in spatial resolutions of 16×16 μm and 100×100 μm, respectively. These uncertainties were once again dominated by the difference between prediction bounds and the linear-fit. The mean, r.m.s., and maximum temperature uncertainty estimates are summarized in table 6 for four different spatial resolutions. Averaging across regions of 11×11 pixels results in a good combination of uncertainty (r.m.s., 2℃) and spatial resolution (16×16 μm) that compares favorably with the ratiometric LIF results of Kim *et al.* [43]. Kim *et al.* reported average calibration uncertainties (95% confidence) of 2.96℃ across a temperature range of 16-40℃ for a spatial resolution of 47×42 μm using a ratiometric LIF thermometry technique to measure bulk fluid temperatures.

3.2 Calibration Discussion

Two major sources of error were identified in this investigation and will be discussed in this section. The first source of error was variations in illumination due to laser

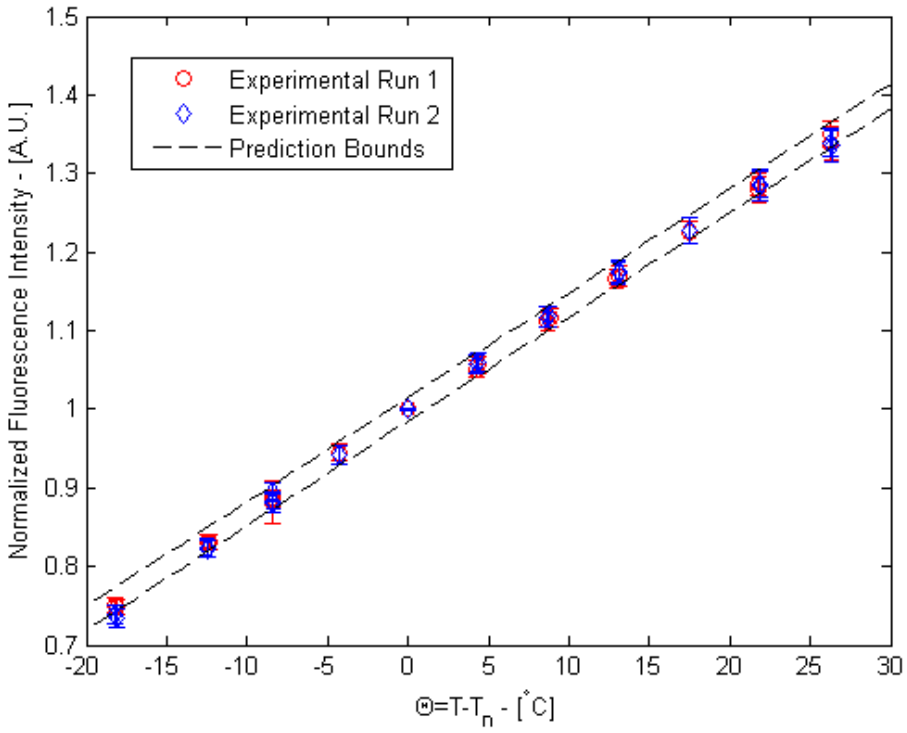

Figure 43: Normalized data points plotted versus Θ with 95% prediction bounds.

instability and temperature-induced changes in refractive index. By reducing the optical path length through the fused silica substrate between the entrance prism and the region of measurement, the influence of variations in illumination can be reduced—but not eliminated. These variations in illumination currently limit the accuracy and in-plane spatial resolution of temperature measurements.

The second source of error was adsorption of fluorophore to the surface of fused silica. Initial investigations with rhodamine B and fluorescein demonstrated spatial distribution of fluorophore concentration at the surface that varied with temperature and generated hysteresis. It was found that this source of error could be eliminated by using a solution of fluorescein buffered to a pH of 9.2.

3.2.1 Temporal Variations in Laser Illumination

Random variations in the laser illumination were investigated by monitoring the fluorescence intensity over a period of 120 minutes at a fixed temperature. The same experimental procedure and image processing techniques were used as during calibration experiments, except the set temperature was kept fixed at 25℃ and image sequences were captured at 5 and 20 minute intervals.

The variations in intensity over three experimental runs are shown in Figure 44. The spatially-averaged normalized intensity was found to vary by as much as 2.1% and the spatial standard deviation of normalized intensity was typically between 1.2-2.4%. These temporal variations in illumination are of the same order of magnitude as the variations in normalized fluorescence intensity observed during calibration.

3.2.2 Refractive Index Changes with Temperature

The refractive index of water and fused silica are both known to vary with temperature. The refractive index of fused silica linearly increases with increasing temperature, while the index of refraction of water decreases with increasing temperature (Figure 45). These variations with temperature introduce two types of non-linearities into the evanescent-wave illumination: 1) movement of evanescent-wave illumination; and 2) variations in the intensity and penetration depth of the evanescent wave. Movement of the evanescent wave causes a significant and consistent spatial bias in the normalized fluorescence intensity. While, variations in the evanescent wave intensity and penetration depth have only a minor impact on calibration linearity.

3.2.2.1 Movement of Evanescent-Wave Illumination

As the temperature of the solution inside the calibration cell changes, the temperature of the fused silica substrate and the fused silica prism will also change. Three-dimensional temperature gradients will develop as heat is conducted through the fused silica interior and convected from the fused silica surface. These temperature

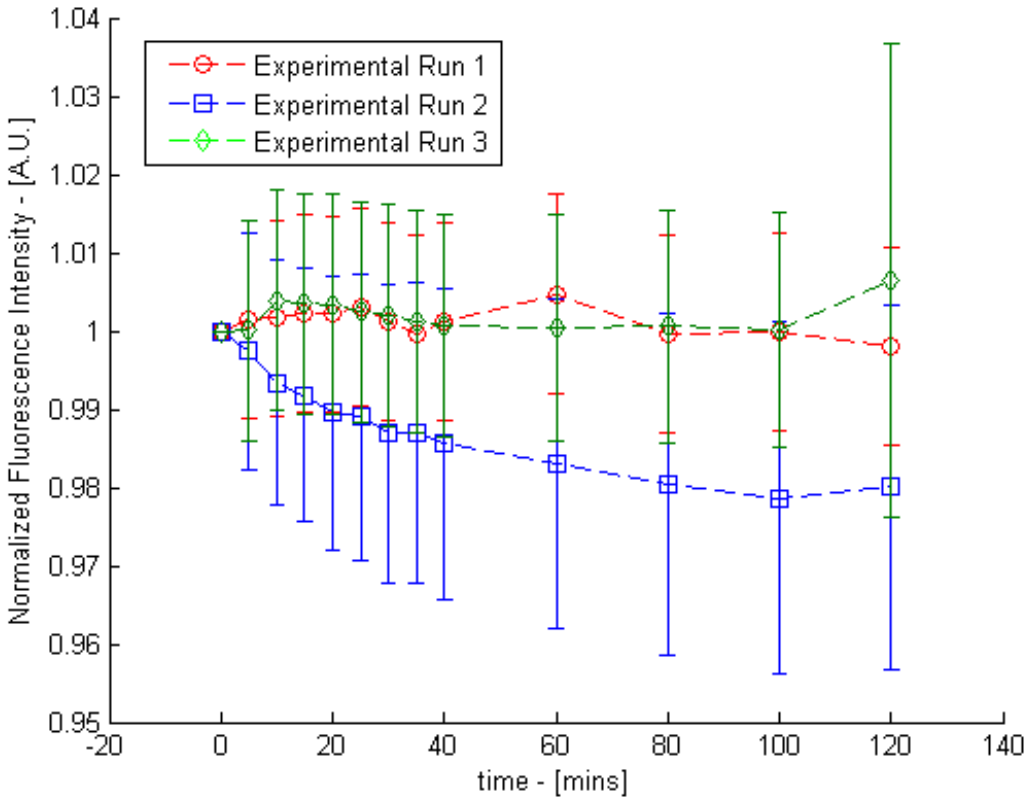

Figure 44: Variations in illumination with respect to time for three different experimental runs. Mean values vary by as much as 2.1%. Error bars are the spatial standard deviations, which typically vary between 1.2% and 2.4%.

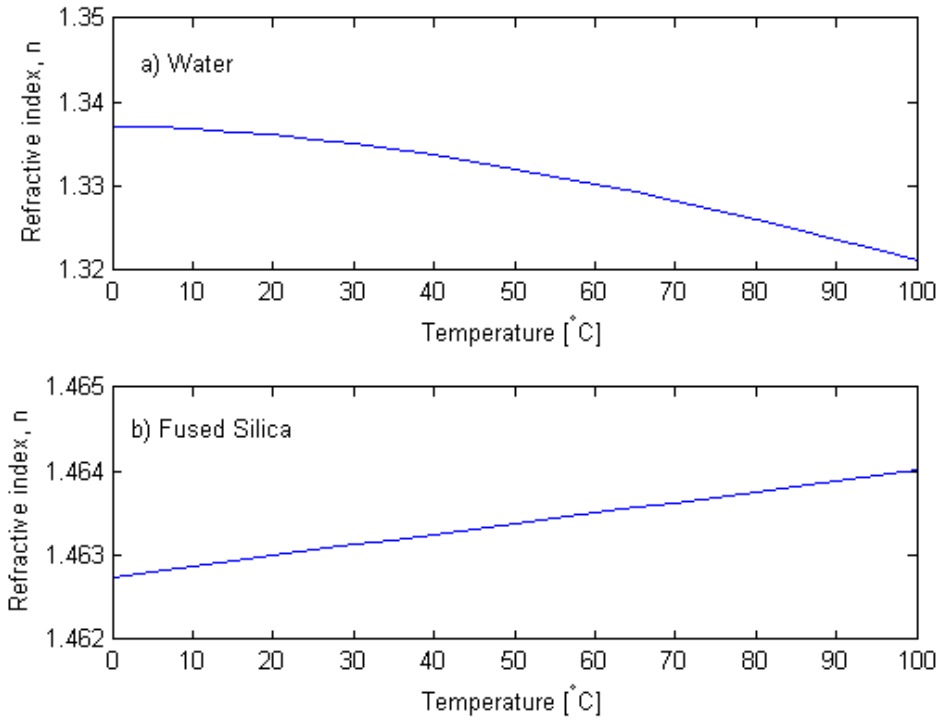

Figure 45: Index of refraction of (a) water and (b) fused silica as a function of temperature. Based upon data from [31] for water and [84] for fused silica.

gradients can cause thermal lensing of the laser illumination propagating through the prism via TIR.

In the simple case where only variations in temperature of the entrance prism are considered, these variations will cause the evanescent-wave illumination to move. As the temperature of the entrance prism varies, the prism refractive index and angle of refraction at the air-prism interface will also vary. The change in angle of refraction will propagate into the angle of incidence of the totally internally reflected light and the location of a total internal reflection will vary according to:

$$\frac{d\theta_i}{dT} = \frac{-1}{n_{SiO_2}} \left(\frac{\tan\theta_i - 1}{\tan\theta_i + 1} \right) \left(\frac{dn_{SiO_2}}{dT} \right) \tag{III.7}$$

$$\frac{dr}{dT} = \frac{-r}{\sin\theta_i \cos\theta_i} \frac{d\theta_i}{dT} = \frac{-r}{n_{SiO_2} \sin\theta_i \cos\theta_i} \left(\frac{\tan\theta_i - 1}{\tan\theta_i + 1} \right) \left(\frac{dn_{SiO_2}}{dT} \right) \tag{III.8}$$

here r is the horizontal distance between the point of refraction at the entrance prism and the center of the evanescent-wave illumination. The net effect of the variation in the index of refraction with respect to temperature at the entrance prism is a shift with a magnitude on the order of 10 μm in the direction of the entrance prism (i.e. up-beam), as shown in Figure 46. The magnitude of the shift per unit temperature is given by the slope of the lines and varies with entrance angle between dr/dT =-0.41 and -0.70 μm per ℃.

Shifts in illumination on the order of 10-100 μm are readily observable in non-normalized images. As the solution temperature gradually increased, illumination gradually shifted up-beam and as the solution temperature gradually decreased, illumination gradually shifted down-beam. Figure 47 shows a 200 x 300 pixel region of two corrected images containing the center of evanescent-wave illumination. These images are from the same data series and were captured at surface temperatures of 20.4 ℃ and 55.2℃. The movement of the evanescent-wave illumination shown in these two images are typical of shifts found in all image sequences.

As a direct effect of the shift in evanescent-wave illumination a spatial bias is

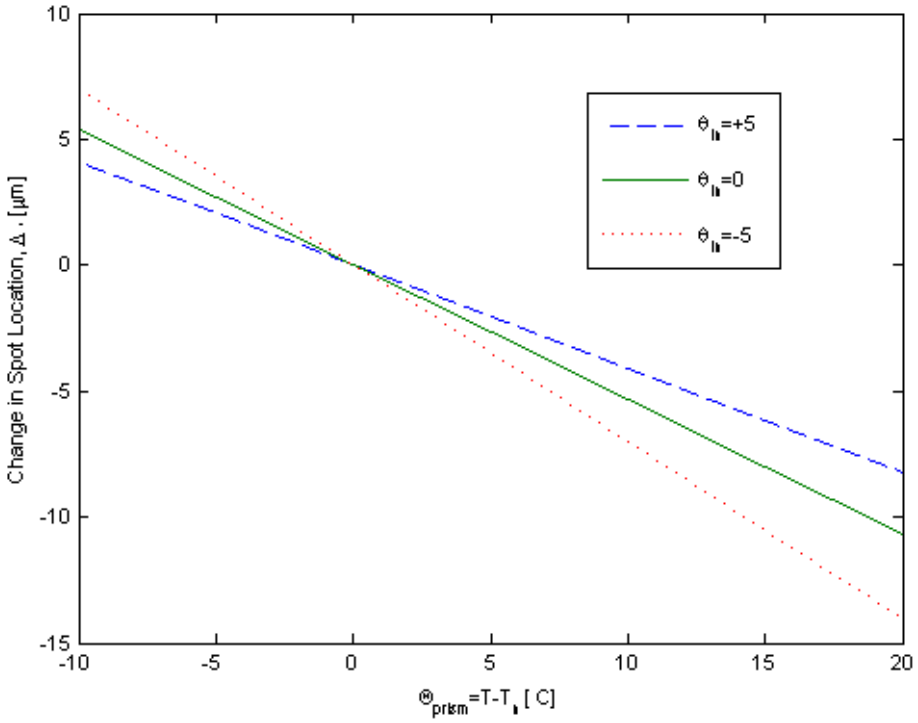

Figure 46: Shift in evanescent location for $r = 30$ mm versus temperature difference of entrance prism. Three different entrance angles are shown.

induced in the normalized images. For instance, if the image taken at 20.4℃ in Figure 47 is used to normalize the image taken at 55.2℃ the resulting image (Figure 48a) shows a clear spatial bias. Unfortunately, this spatial bias cannot be mitigated by mid-range image filtering. For instance, the image after a 15×15 pixel median filter (Figure 48b) retains a significant spatial bias.

After filtering, the normalized image shows a relatively bright region in the lower right corner, and a dark region in the upper left corner. The difference in normalized fluorescent intensity between these spots is approximately 10%, corresponding to a temperature difference of approximately 7.4℃ across a seperation distance of approximately 375 μm. The spatial bias results in an apparent localized temperature gradient of 20 ℃/mm inside the calibration cell, where the temperature is spatially uniform.

The error associated with movement of the evanescent-wave illumination limited

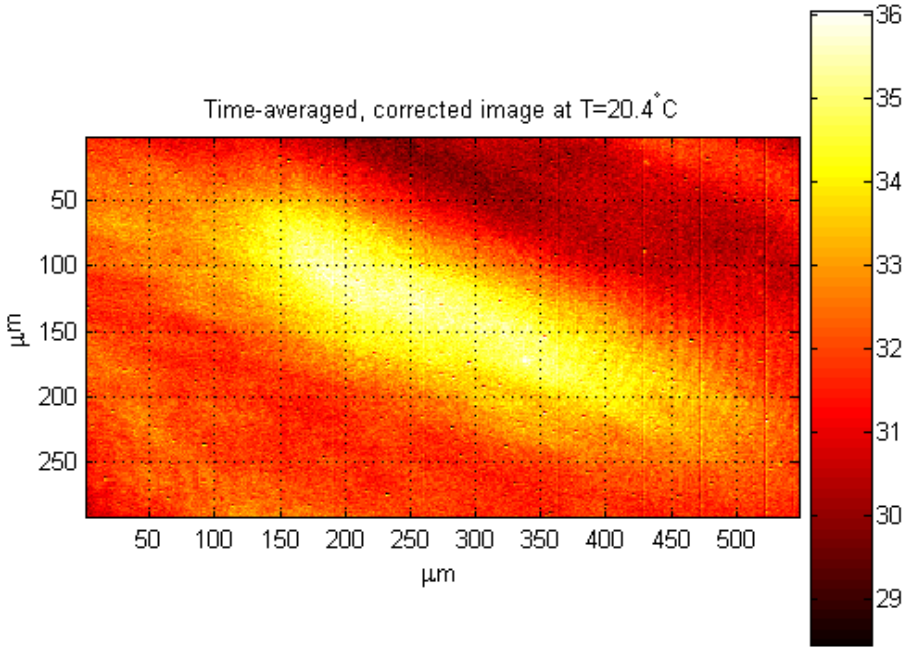

(a)

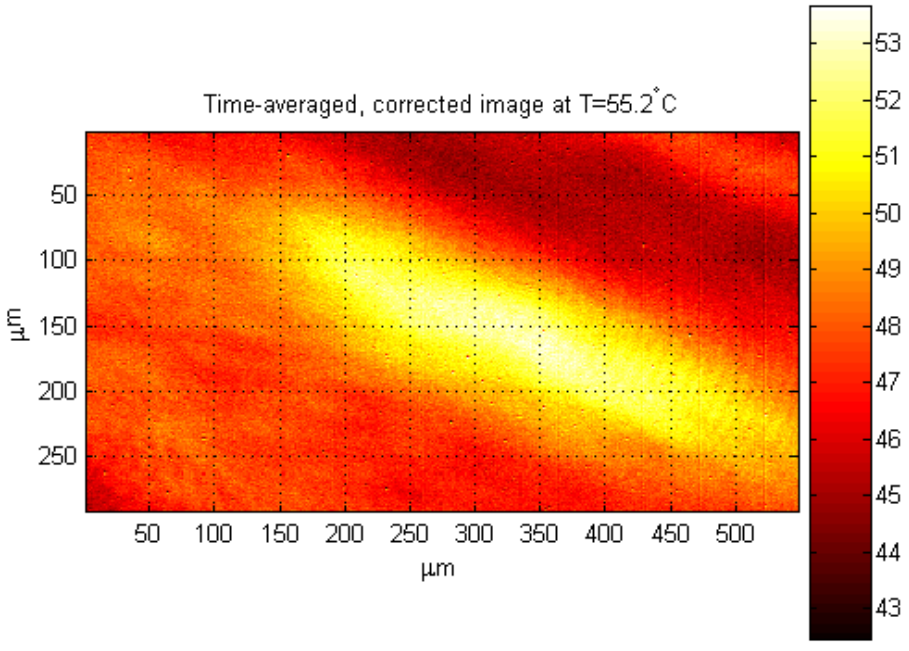

(b)

Figure 47: Time-average, corrected images captured at surface temperatures of (a) 20.4℃ and (b) 55.2℃. Direction of illumination propagation is from lower-right to upper-left. Images are in false color.

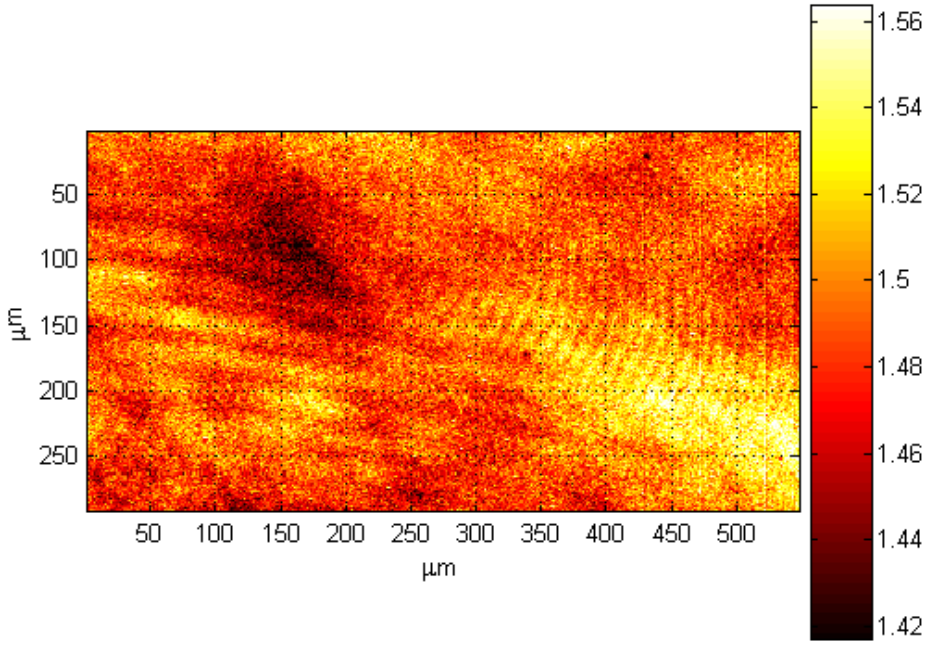

(a)

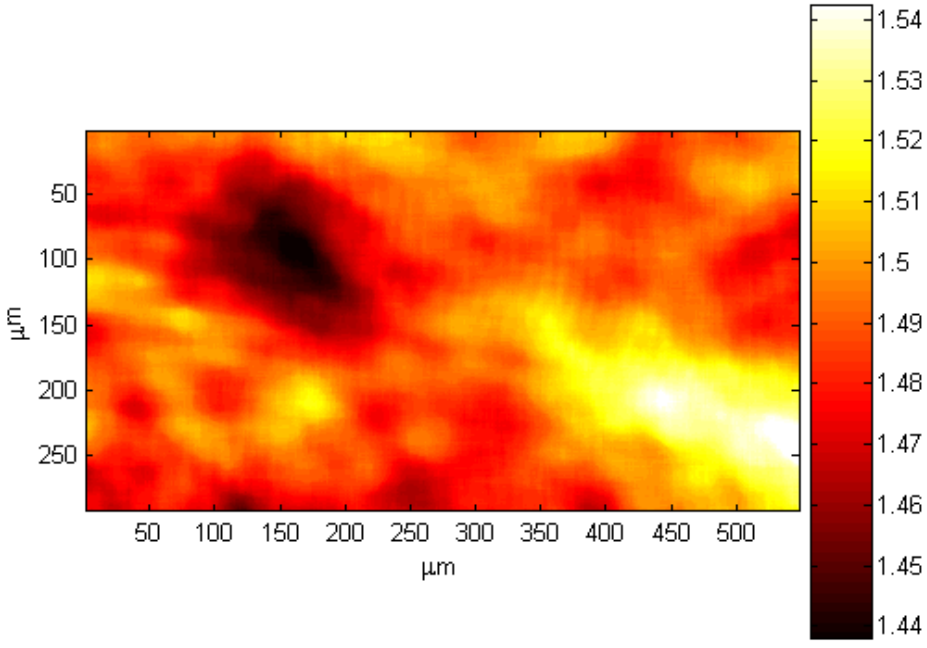

(b)

Figure 48: Result of normalizing the image of Figure 47a by the image of Figure 47b. (a) The normalized image without filtering; (b) the normalized image after a 15×15 pixel median filter. Images are in false color.

the accuracy and spatial resolution of the technique. Attempts were made to measure temperature gradients inside of a microchannel, but movement of the evanescent-wave illumination due to thermally-induced refractive index gradient lensing prevented repeatable and accurate measurement (see Appendix C).

3.2.2.2 Influence of Path Length Through Fused Silica

The optical path length of the propagating TIR wave through the fused silica was observed to influence the degree of variations in normalized fluorescence intensity. Greater variations in normalized fluorescence intensity was observed in experiments with an optical path length through the fused silica of approximately 4 cm (as compared to 2 cm for the results presented above). As shown in Figure 49, hysteresis of approximately 6% was present in the spatially-averaged fluorescence intensity. This hysteresis propogated into the hysteresis in the normalized fluorescence intensity and contributed to greater spatial standard deviations, typically between 1-5%. This can be explained by an increase in the movement distance of evanescent-wave illumination with an increased optical path length.

Examination of fluorescence intensity images, suggests a secondary effect of the temperature-dependence of the refractive index of fused silica that becomes more apparent with increased path length. As the refractive index changes, the path of the propagating TIR beam through the fused silica changes slightly and the interactions with impurities and inclusions in the fused silica also change. The influence of scattering, refraction, absorption, and diffraction events will change with the impurities and inclusions encountered along the optical path.

The images shown in Figure 50(a)-(b) illustrate these random variations in illumination. Anomalous illumination resembling an Airy disc is clearly visible in the upper-left corner of the image sequence taken at 55.1℃, but is absent from the image sequence taken at 20.3℃. Such random variations in illumination strongly bias the

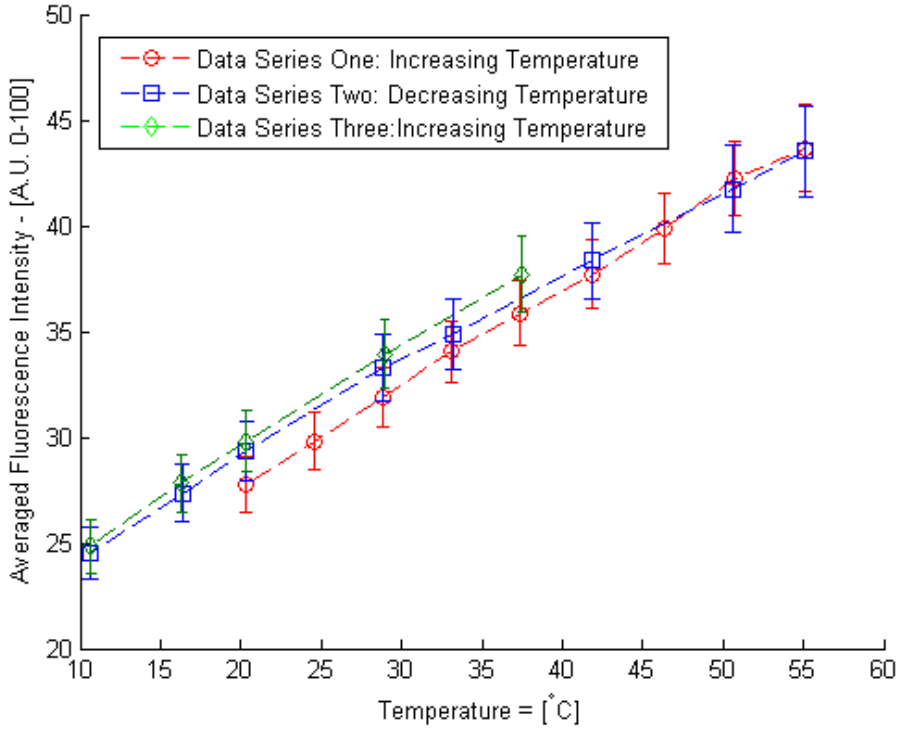

(a)

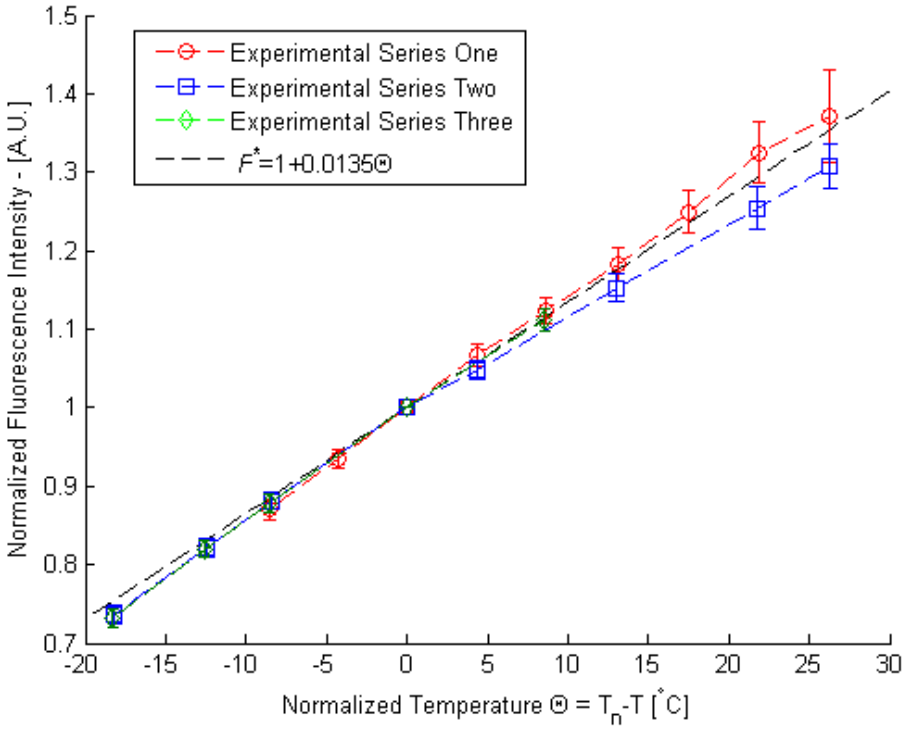

(b)

Figure 49: Experimental results with optical path length through fused silica of approximately 4 cm. *(a)* Time-averaged, corrected fluorescence intensity vs. surface temperature; *(b)* normalized fluorescence intensity vs. normalized surface temperature.

normalized fluorescence intensity image (Figure 50c) and cannot be removed by a 15×15 pixel median filter (Figure 50d). These random variations in the illumination contribute to experimental scatter and deviation from linear behavior. For instance, the image sequence taken at surface temperature of 55.1℃ (Figure 50b) corresponds to the data point with the greatest deviation from the calibration line.

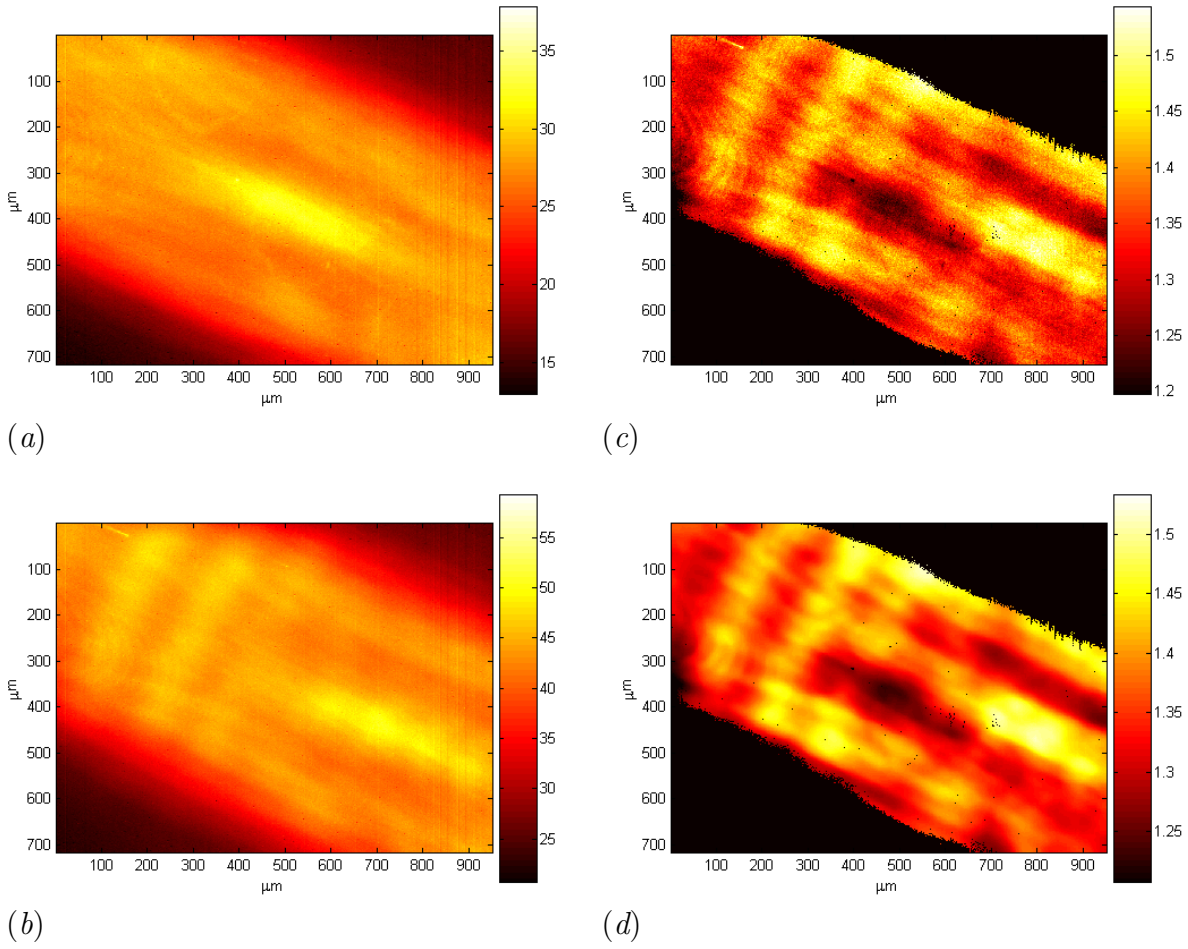

Figure 50: Direct and secondary effect of movement of evanescent-wave illumination. (a) normalizing image at 20.3℃; (b) image captured at 55.1℃: illumination has shifted toward lower right corner and possible diffraction pattern is present in upper left corner; (c) masked normalized fluorescence intensity image for image at 55.1℃ normalized by image at 20.3℃; (d) spatial bias is still present after 15×15 pixel median filter is applied to the image.

3.2.2.3 Intensity and Penetration Depth of the Evanescent Wave

A minor source of uncertainty comes from the relationship between the refractive indices of water and fused silica with the temperature at the TIR interface. This relationship can result in slight changes in the penetration depth and intensity of the evanescent-wave illumination. The opposite signs of dn/dT for water and fused silica indicates that the mismatch in index of refraction between fused silica and water will increase with increasing temperature. The mismatch between fused silica and water was quantified in section 1.4 by the ratio $n = n_{H_2O}/n_{SiO_2} < 1$, which is shown as a function of temperature in Figure 51. As the ratio n varies with temperature, the critical angle θ_c, evanescent gain G_e, and penetration depth d_z of the evanescent-wave illumination vary. Therefore, the magnitude of the volumetric intensity of the evanescent-wave illumination will vary with temperature.

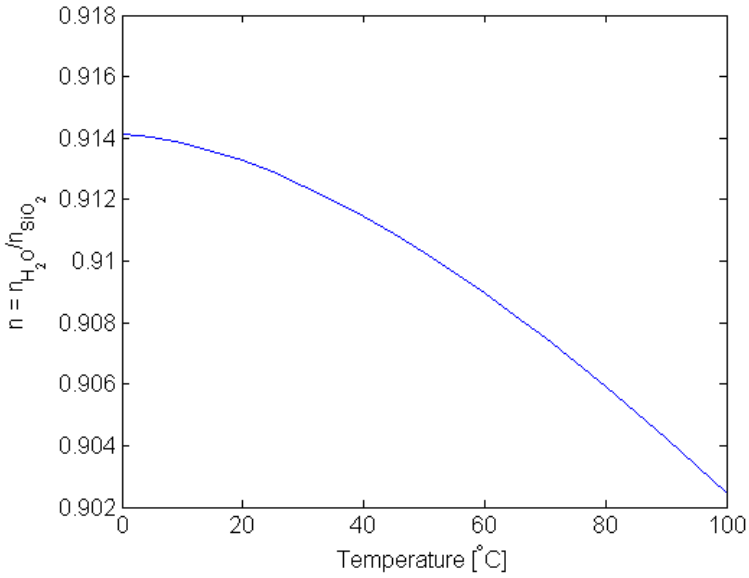

Figure 51: Change in ratio of refractive index n defined as $n = n_{H_2O}/n_{SiO_2}$ with temperature.

The fluorescence intensity reported by the imaging system has been shown to be proportional to the intensity of the evanescent-wave illumination integrated across volume. For an ideal Gaussian laser profile, this relationship can be extended to d_z,

G_e and θ_i that vary with temperature:

$$F \propto \int_V I_0(x,y,z)dV \propto d_z G_e \cos\theta_i \tag{III.9}$$

Figure 52 shows the variation in the product of d_z, G_e and $\cos\theta_i$ with solution temperature for three different entrance angles. The change in normalized fluorescent signal due to the temperature dependence of n is non-linear and dependent upon entrance angle. The magnitude of the change is relatively low with dF/dT due to index mismatch varying between -0.029 to 0.055 %/℃ compared to the calibrated relationship of $dF/dT = 1.346\%/℃$. The thermal mismatch in index of refraction can marginally contribute to experimental scatter and deviations from linear behavior and a 4% variation in the measured thermal response of fluorophores across the investigated temperature range.

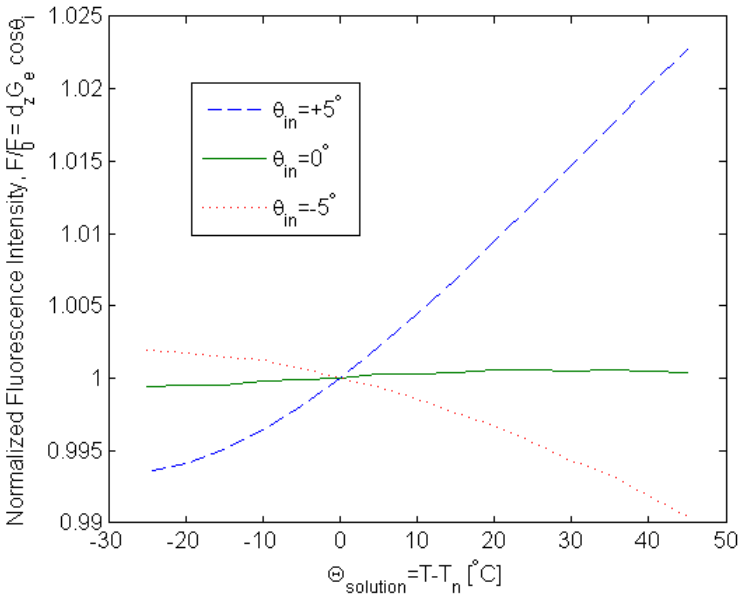

Figure 52: Modeled change in normalized fluorescence intensity due to variation in penetration depth, evanescent gain with temperature. These variations in penetration depth and evanescent gain are due to the variation of θ_i and n with temperature.

3.2.3 Adsorption

In this investigation, adsorption onto the fused silica surface was reduced to insignificant levels by using fluorescein buffered to a pH of 9.2 as the temperature-dependent fluorescent species. Calibration experiments with rhodamine B and fluorescein in un-buffered solutions demonstrated spatially-patterned fluorescence intensity and hysteresis. The cause of the hysteresis and spatial-patterning was attributed to adsorption of fluorophore to the fused silica.

Adsorption of fluorophore molecules onto the fused silica surface is of concern because such adsorption invalidates the assumption that the fluorophore concentration is spatially and temporally invariant in the solution. Furthermore, adsorption is a chemical process that is temperature, concentration and time dependent [67]. Therefore, as the temperature changes the amount of fluorophore adsorbed onto the surface can change irreversibly, causing hysteresis.

The impact of adsorption on calibration results for un-buffered fluorescein is evident in the results presented below. Adsorption is further discussed in Appendix B. Included in this appendix are: a) background information of adsorption mechanism; b) quantitative measurements of the contribution of adsorbed fluorophore to the total fluorescent intensity for fluorescein and rhodamine B; c) calibration results for rhodamine B; and d) description of attempts to reduce adsorption of rhodamine B.

3.2.3.1 Calibration Results for Un-buffered Fluorescein

Hysteresis was observed in experiments with fluorescein in un-buffered solutions. Hysteresis and poor repeatability are evident in plots of time-averaged, corrected fluorescence against surface temperature for two experimental runs of un-buffered 10 μM fluorescein (Figure 53). The normalized fluorescence intensity plotted against normalized surface temperature (Figure 54) exhibits poor convergence along a straight line compared to pH buffered fluorescein solutions. Relative to the buffered fluorescein

solution, un-buffered fluorescein demonstrated a greater fluorescence temperature-sensitivity of $dF/dT = 1.54\%/℃$. However, hystereis and experimental scatter due to adsorption was a major source of error and limited the expanded uncertainity of the calibration to $\pm$ 5.6℃ (95% confidence).

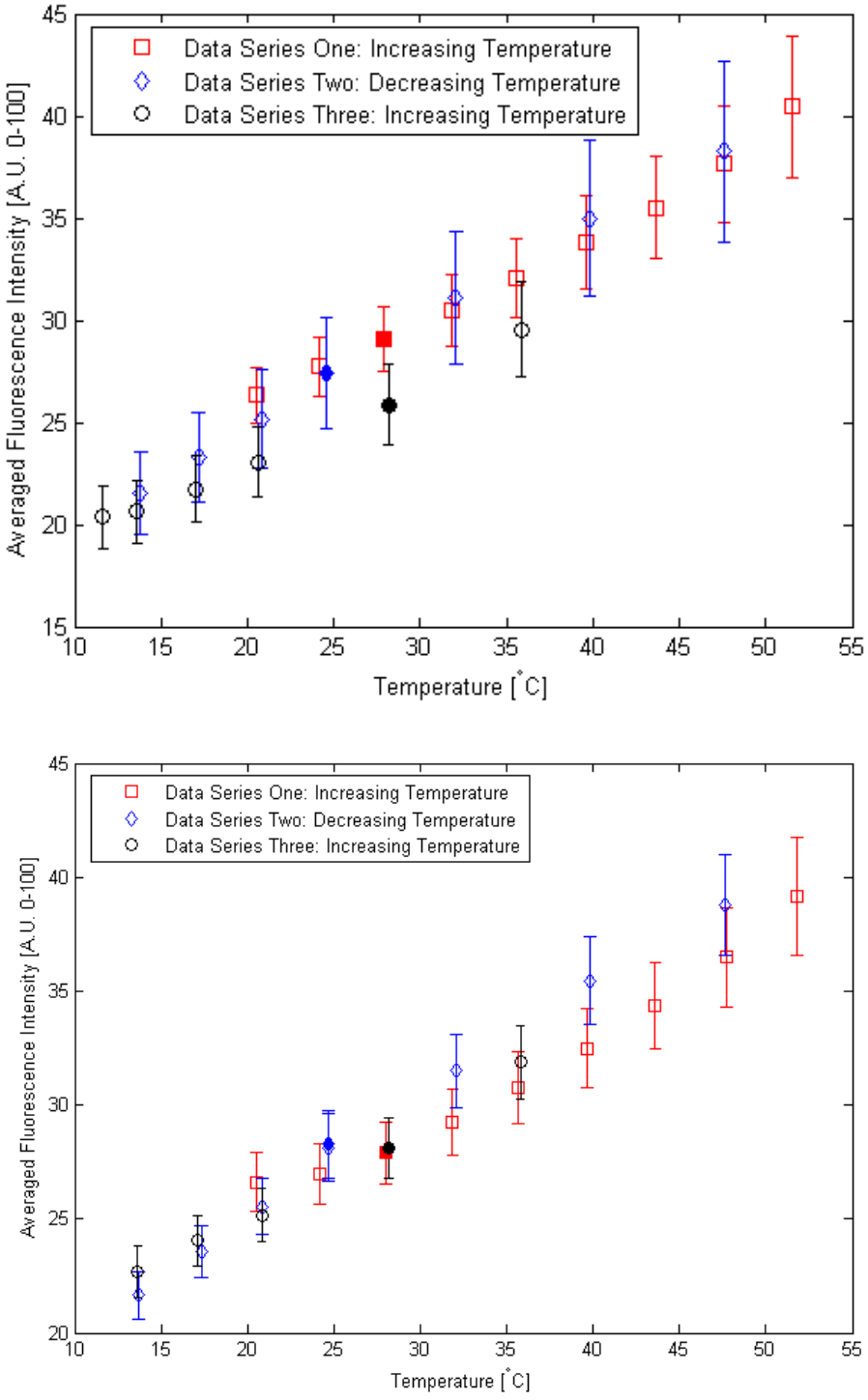

Figure 53: Time-averaged, corrected fluorescence intensity plotted against surface temperature for two experimental runs for 10 μM fluorescein solution in de-ionized water (pH$\approx$5.7) Considerable hysteresis and experimental scatter are present, which can be attributed to adsorption.

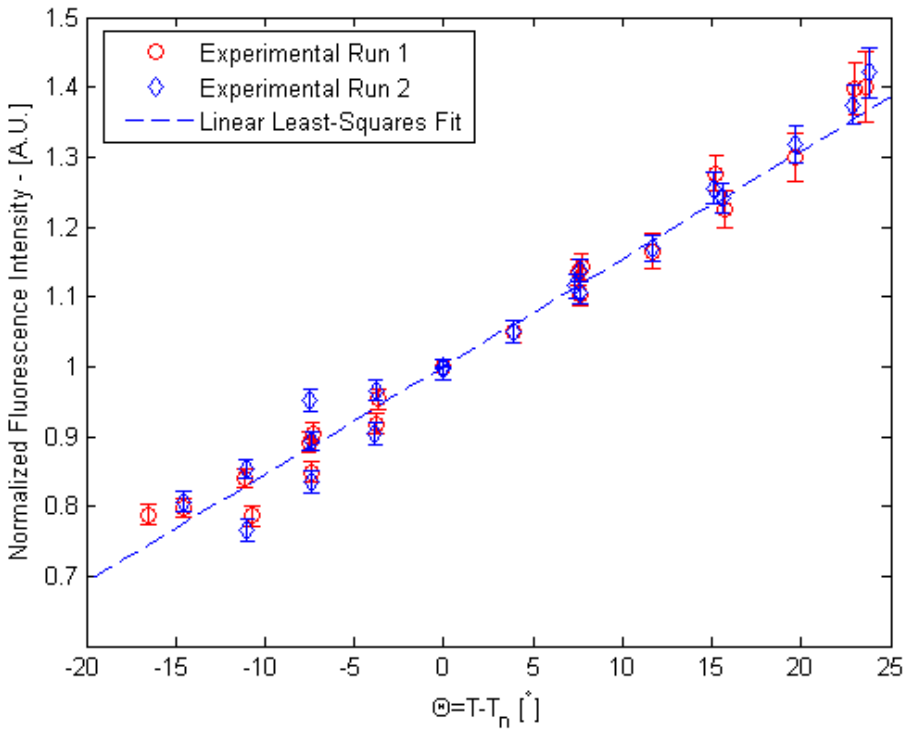

Figure 54: Normalized fluorescence intensity vs. normalized surface temperature for 10 μM fluorescein solution in de-ionized water (pH$\approx$5.7). The fluorescence temperature-sensitivity was determined to be $dF/dT = 1.5\%/$℃, but experimental scatter due to adsorption increased uncertainity to 5.6℃ (95% confidence).

CHAPTER IV

CONCLUSIONS AND RECOMMENDATIONS

4.1 Conclusions

This investigation has shown that the temperature within 600 nm of a wall can be measured by a technique that combined Total Internal Reflection Microscopy and Laser Induced Fluorescence Thermometry. This technique, named Total Internal Reflection Fluorescent Micro-Thermometry (TIR-FMT), can be used to measure temperatures within 600 nm of the wall using a single fluorescent species. The r.m.s. uncertainty of temperature measurements derived from a single 1.5×1.5 μm pixel was determined to be 2.4℃ (95% confidence) across a temperature range of 12.5-55℃. By spatially averaging, r.m.s. uncertainties were reduced to 2.0℃, 1.8℃, and 1.5℃ for spatial resolutions of 16×16, 100×100, and 715×950 μm, respectively. These uncertainties are comparable to average calibration uncertainties for bulk temperature measurements using ratiometric LIF Thermometry reported by Kim *et al.* [43]. For instance, a calibration precision uncertainty of 2.96 ℃ (95% confidence) across a temperature range of 16-40℃ was reported with spatial resolution of 47×42 μm.

Compared to rhodamine B, which has been the preferred fluorophore for bulk temperature measurements using LIF Thermometry, fluorescein was found to be more suitable for near-wall temperature measurements using TIR-FMT. Fluorescein in water demonstrated good temperature-sensitivity of 1.5%/℃, and low levels of adsorption to fused silica. Adsorption is of key importance for TIR-FMT, because variations in flurophore concentrations near the wall strongly bias the fluorescence intensity. By buffering the fluorescein solutions to a pH of 9.2 with sodium tetraborate, adsorption was reduced to negligibly low levels, the signal-to-noise ratio was increased, and good

temperature-sensitivity of 1.35%/℃ was obtained.

The major source of error in the TIR-FMT technique developed in this investigation was variations in illumination. We note, however, that the accuracy obtained with the current implementation was already better than that obtained with a ratiometric approach (which accounts for such variations). The sources of these variations in illumination were determined to be random variations in laser intensity, and changes in the evanescent wave location due to temperature-induced changes in the refractive index of fused silica. Changes in the evanescent-wave illumination were spatially biased and compromised the spatial resolution of the technique.

4.1.1 Extension of TIR-FMT to Microchannels

Eventually it is desired to utilize the TIR-FMT technique to measure the surface temperatures inside of microchannels. Initial investigations to measure a temperature inside of a microchannel (see Appendix C) were hindered by two key challenges: contamination and variations in illumination. The influence of contamination can likely be reduced by controlling fluorophore solution chemistry and careful selection of channel apparatus materials to prevent sorption of fluorophore. Considerable variations in illumination in microchannel experiments can be attributed to thermal gradient lensing by temperature gradients generated in the fused silica substrate and increased scattering and reflection by the channel apparatus. To reduce the error introduced by these variations in illumination, it is necessary to reduce the optical path length through the fused silica and/or control for variations in illumination.

4.2 Recommendations for Future Work

To improve the accuracy and in-plane spatial resolution of the TIR-FMT technique it is necessary to reduce the error introduced by variations in illumination. This can be accomplished by reducing the optical path length through the fused silica substrate, or by controlling for variations in illumination. To bring about these improvements two

methodologies are suggested: Objective-Based Total Internal Reflection Microscopy and Two-Color Laser Induced Fluorescence Thermometry.

4.2.1 Objective-Based Total Internal Reflection Microscopy

Objective-Based Total Internal Reflection Microscopy[1] is a variation of TIR Microscopy that utilizes the microscope objective to guide the illumination to the interface between the substrate (typically a cover-slip) and the specimen. At the interface, the illumination is totally internally reflected, generating a single evanescent wave, and is transmitted back through the microscope objective. This technique requires a high numerical aperture, oil-immersion microscope objective with a short working distance (typically the optical pathlength through a #1 cover slip).

By using objective-based TIR microscopy, the optical path length through the fused silica substrate will be reduced from o(10^4 μm) to o(10^2 μm). By decreasing the optical path length through the substrate by two orders of magnitude, the movement of the evanescent-wave illumination will similarly decrease. This should mitigate the spatial bias and random variations from scattering by inclusions induced by movement of the evanescent wave. Unfortunately, Objective-Based TIR will not reduce the temporal variations in illumination due to laser instabilities. Of further concern is the effect of the thermal pathway created between the sample and the microscope objective by the short working distance and immersion oil. The thermal pathway increases heat transfer to the objective and may influence the optical path of the excitation and the emission light.

4.2.2 Two-Color Laser Induced Fluorescence Thermometry

Two-Color Laser Induced Fluorescence (LIF) Thermometry monitors the intensity of fluorescence emissions in two spectral bands—ideally one temperature-sensitive and one temperature-insensitive spectral band. The fluorescence intensity of the

[1] also known as 'Prismless TIR microscopy'

temperature-insensitive band is used as a direct measure of the intensity-field of the illumination. The fluorescence intensity of the two spectral bands are then ratioed, providing a measure of the temperature fields independent of variations in the intensity of the illumination.

Two-Color/Two-Dye LIF Thermometry has been implemented to successfully measure bulk solution temperatures by using two different fluorophores by several investigators, for example [70], [43]. If a suitable temperature-insensitive fluorophore that does not adsorb onto fused silica is identified, it can be combined with fluorescein to implement Two-Color/Two-Dye LIF Thermometry under evanescent-wave illumination. Such a technique would be sensitive to any variations in concentration of one of the fluorophores due to adsorption or contamination.

Two-Color/One-Dye LIF Thermometry has been implemented to measure bulk solution temperatures in evaporating droplets using a single dye [49]. This technique requires a fluorophore with a temperature-insensitive absorption spectral band and a temperature-sensitive emission spectrum. Specifically, the emission spectrum should posses one temperature-sensitive and one temperature-insensitive spectral band. Unfortunately, fluorescein excited at 514 nm has been shown to posses a temperature-sensitive absorption, so is unsuitable for Two-Color/One-Dye LIF Thermometry [15]. One promising dye-candidate is sulforhodamine B (Kiton Red), that has been shown to have temperature-insensitive absorption, temperature-dependent emissions [15], and undetectable adsorption to silica at a pH=9 [42]. However, it remains to be determined whether an appropriate pair of temperature-sensitive and temperature-insensitive emission spectral bands can be identified for sulforhodamine B.

APPENDIX A

ERROR ANALYSIS

In this appendix the errors associated with experimental parameters and results are addressed, and where possible calculated. For a multi-variable function $f = f(x_1, x_2, x_3, \ldots, x_i)$ the uncertainty of f, u_f can be found from the the uncertainties of the variables $u_{x_1}, u_{x_2}, \ldots, u_{x_i}$ according to the propagation of uncertainty:

$$u_f = \sqrt{\left(\frac{\partial f}{\partial x_1} u_{x_1}\right)^2 + \left(\frac{\partial f}{\partial x_2} u_{x_2}\right)^2 + \ldots + \left(\frac{\partial f}{\partial x_i} u_{x_i}\right)^2} \tag{A.1}$$

The partial derivatives $\frac{\partial f}{\partial x_i}$ in this expression are referred to as influence factors.

A.1 Fluorescein Solutions

The concentration of fluorescein solutions can be calculated by equation II.30:

$$[C] = \frac{v_i [C]_i}{v_f} = \frac{m_{fl} v_i}{v_g v_f M.W.} \tag{II.30}$$

The uncertainty of [C], $U_{[C]}$, can be estimated by propagating the resolution uncertainties (one-half of the instrument resolution) of the instruments used to measure m_f, v_i, v_g, and v_f. Table A.1 shows the uncertainty calculation for the fluorescein solution concentration with the greatest uncertainty, $U_{[C]} = 0.297\mu$M; all other fluorescein solutions in this investigation had lower uncertainties.

A.2 Camera Characterization

In this section, the uncertainty associated with the camera characterization is investigated. The data points and fits are shown graphically in Figure 27 and the equations

Table A.1: Expanded uncertainty for fluorescein solution concentration with greatest uncertainty. Note: uncertainty is based upon instrument resolution uncertainties and expanded uncertainty (95% confidence) are propogated.

x_i	Influence ($\frac{\partial f}{\partial x_i}$)	U_{x_i}	$\left(\frac{\partial f}{\partial x_i}U_{x_i}\right)^2$
$m_f = 0.024$ [g]	$\frac{v_i}{M.W.v_g v_f} = 4.15 \times 10^{-4}$	5×10^{-4}	4.3×10^{-14}
$v_i = 7.8 \times 10^{-3}$ [L]	$\frac{m_f}{M.W.v_g v_f} = 1.28 \times 10^{-3}$	5×10^{-5}	4.1×10^{-15}
v_f=0.50 [L]	$\frac{m_f v_i}{M.W.v_g v_f^2} = 1.99 \times 10^{-5}$	1×10^{-2}	4.0×10^{-14}
$v_g = 0.10$ [L]	$\frac{m_f v_i}{M.W.v_g^2 v_f} = 9.95 \times 10^{-5}$	5×10^{-4}	2.5×10^{-15}
		$\sum \left(\frac{\partial f}{\partial x_i}U_{x_i}\right)^2$	8.8×10^{-14}
		Expanded Uncertainty (95% Confidence), $U_{[C]}$	0.297 μM

of fit are given numerically by equation II.36 as:

$$f_c(g) = 9.3 \times 10^{-6} g^3 - 3.4 \times 10^{-3} g^2 + 0.73g$$

$$f_c(g) = 9.9 \times 10^{-6} g^3 - 2.6 \times 10^{-3} g^2 + 0.51g$$

for medium and low light settings, respectively. These fits have been used as a calibration relating the reported pixel values to the actual amount of light incident upon each pixel, which is called the corrected pixel value.

The bias uncertainty of quantitative measurements taken by the camera depends on the quality of this calibration, while the precision uncertainty is related to the amount of noise present in images captured by the camera.

A.2.1 Bias Uncertainty

Prediction bounds for the calibration functions can be generated for each grayscale pixel value from:

$$u_{f_c} = z\sqrt{gSg'} \tag{A.2}$$

here z is a value that depends on the confidence interval S is the covariance matrix associated with each coefficient of the polynomial fit and u_f is the uncertainty of the correction curve at a pixel grayscale value g. Figure A.1 shows the camera characterization curves with 95% confidence prediction bounds and Figure A.2 shows the

expanded uncertainity U_f vs. corrected pixel value. The uncertainity of the corrected pixel value for all corrected pixel values below 60 remains below 2.0 for both medium and low light level settings. To avoid saturation, images were taken such that valid pixels didn't exceed a corrected pixel value of 60, so the final expanded uncertainity of corrected pixel values was taken as ± 2.0 for medium and low level camera settings.

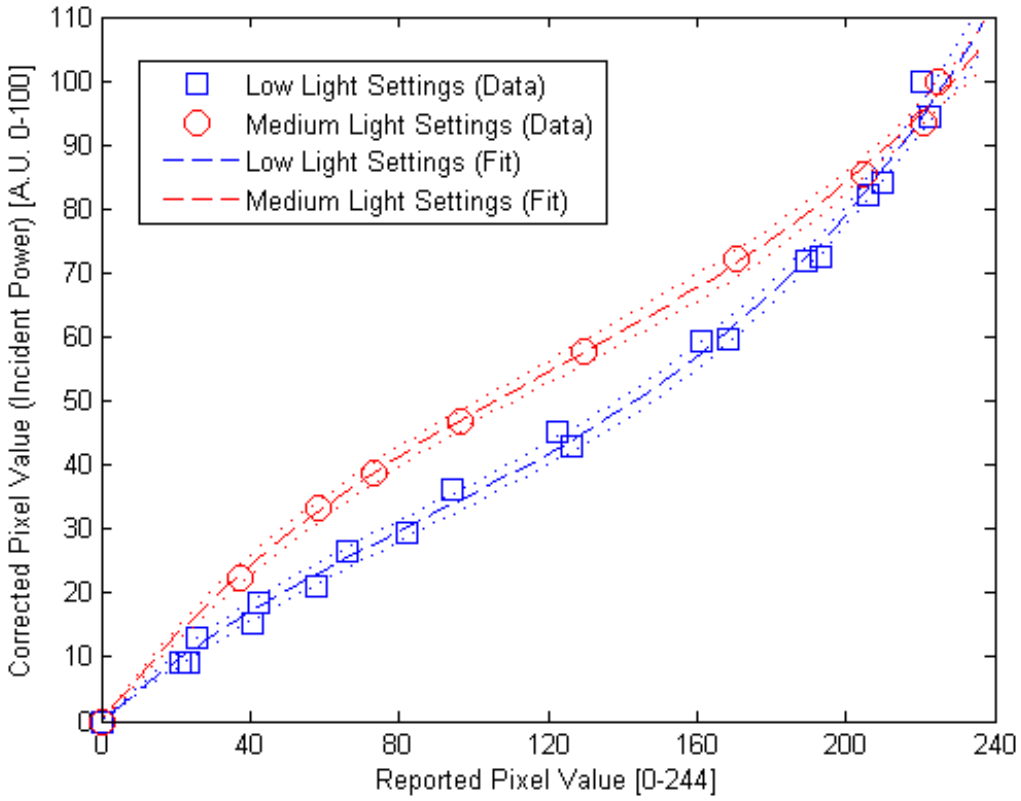

Figure A.1: Calibration curves relating corrected pixel value (power incident upon CCD array) to reported grayscale value.

A.2.2 Precision Uncertainty

The uncertainty arising from camera noise was estimated by capturing a sequence of 100 images under white-light illumination from the microscope lamp with the camera on medium light settings. The image sequence consisted of $492 \times 653 \times 100$ (3.2 million) measurements of intensity. After correcting for camera dark noise and non-linearity,

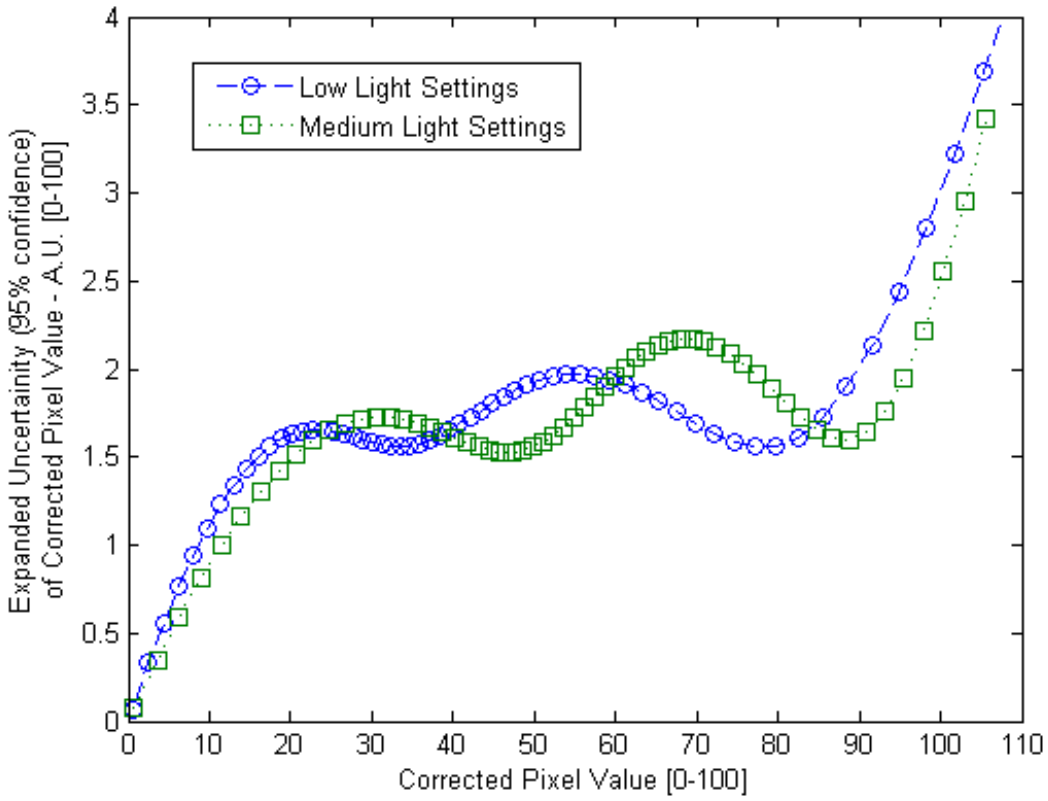

Figure A.2: Plot of expanded uncertainty (95% confidence) of corrected pixel values with respect to corrected pixel values.

three statistical measure of the precision uncertainty associated with the camera were computed: the complete standard deviation σ_{ijk}, the temporal standard deviation $\mu_{xy}[\sigma_t]$, and the spatial standard deviation $\mu_t[\sigma_{xy}]$.

The total standard deviation was found by treating each of the 3.24 million measurements as an independent measurement, and taking the standard deviation of all 3.24 million samples. The temporal standard deviation was found by taking the standard deviation of each pixel location with respect to time, then averaging across all pixel locations. The spatial standard deviation was found by taking the spatial standard deviation of each individual image in the image sequence, then averaging across all 100 images. The resulting values were:

$$\sigma_{xyt} = 3.0$$

$$\mu_{xy}[\sigma_t] = 2.7$$

$$\mu_t[\sigma_{xy}] = 3.0$$

The spatial variation in reported grayscale values is partially due to non-uniformity of the illumination source. The spatial variation in illumination can be estimated by taking the spatial standard deviation of the time-averaged image, yielding a value of $\sigma_{xy}[\mu_t] = 1.3$. We assume the spatial variation is due to non-uniform illumination and is described by $\sigma_{xy} = \sigma_{xy}[\mu_t] = 1.3$ and the temporal variation is due to the camera and is described by $\sigma_t = \mu_{xy}[\sigma_t] = 2.7$. Adding the spatial and temporal variances gives a good agreement to the total standard deviation:

$$\sigma_{xy}^2 + \sigma_t^2 = (1.3)^2 + (2.7)^2 = 8.98 \approx 9 = \sigma_{xyt}^2 \tag{A.3}$$

A.2.3 Resolution Uncertainty

The resolution of the camera is set by the 8-bit analog-to-digital conversion. Output grayscale values vary between 0-245, giving an approximate reported pixel value resolution uncertainty (95% confidence) of $U_g = 0.5$ pixels. The expanded uncertainity

of the corrected pixel value can be found from propogation of uncertainty to be:

$$U_{\mathscr{C}} = \left(\frac{\partial f_c}{\partial g} U_g\right)^2 \tag{A.4}$$

for medium-light settings the partial derivative of the camera correction function is

$$\frac{\partial f_c}{\partial g} = \frac{df_c}{dg} = 2.79 \times 10^{-5} g^2 - 6.8 \times 10^{-3} g + .73 \tag{A.5}$$

The expanded uncertainty of the camera due to resolution uncertainty for medium light settings is shown in Figure A.3

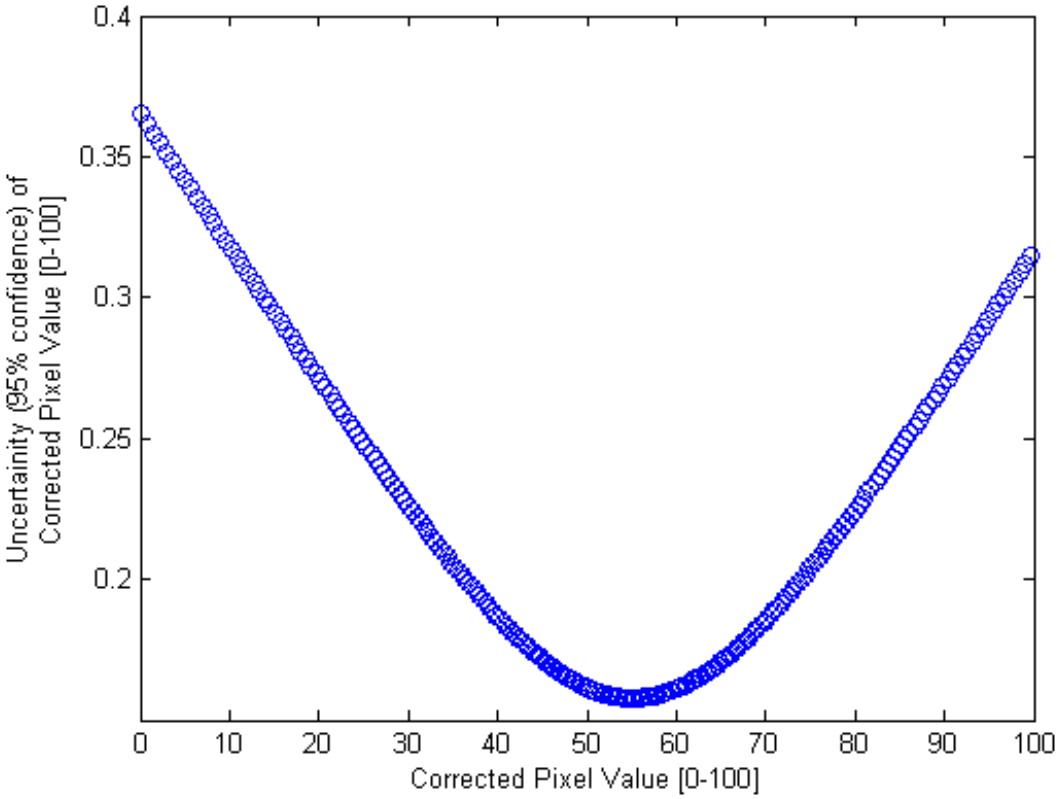

Figure A.3: Expanded resolution uncertainty (95% confidence) of camera after correction for camera non-linearity.

A.3 Calibration

The calibration determined the relationship between the normalized fluorescence intensity and normalized surface temperature to be linear and of the form:

$$F = 1 + m\Theta \tag{A.6}$$

where m was determined to be equal to 1.35%/℃, and $\Theta = T - T_n$ was the normalized surface temperature. To measure temperature, this relationship is inverted:

$$T = T_n + \frac{F-1}{m} \tag{A.7}$$

The uncertainty associated with such temperature measurements can be estimated from propagation of uncertainty:

$$u_T^2 = \left[\frac{\partial T}{\partial T_n} u_{T_N}\right]^2 + \left[\frac{\partial T}{\partial F} u_F\right]^2 + \left[\frac{\partial T}{\partial m} u_m\right]^2 \tag{A.8}$$

In this section, the bias and precision uncertainties associated with T_n, F, and m are estimated and the total uncertainty of temperature measurements computed.

A.3.1 Surface Temperature

The bias uncertainty of the normalizing temperature was conservatively estimated from the calibration of the thermocouples to be ± 0.075 ℃. The maximum precision uncertainty of thermocouple measurements was measured to be 250 nV, which across the range of 5-60℃ corresponds to a maximum precision uncertainty of 0.031℃. Summing the variances gives the combined uncertainty of the thermocouple measurements:

$$u_{T_n} = \sqrt{\sigma_{bias}^2 + \sigma_{prec}^2} = \sqrt{5.6 \times 10^{-3} + 9.6 \times 10^{-4}} = 0.081 \tag{A.9}$$

A.3.2 Normalized Fluorescent Intensity

The uncertainty associated with each normalized fluorescent intensity measurement can be broken into bias and precision uncertainties. The bias uncertainty is due to

experimental scatter and deviation of actual experimental data from the idealized linear fit. The precision uncertainty is due to temporal and spatial variations in the normalized fluorescent intensity measurements. The primary cause of these variations are imperfections in the illumination and imaging systems.

A.3.2.1 Bias Uncertainty

The bias uncertainty can be estimated from prediction bounds of the calibration data. The prediction bounds b_F for a new observation can be computed from:

$$b_F = t\sqrt{s^2 + \Theta S \Theta'} \tag{A.10}$$

here t is the coverage factor, S is the covariance matrix of the estimates of m and s is the root mean squared error[1] defined as:

$$s^2 = \frac{1}{\nu}\sum_{\phi=1}^{N} \sigma_\phi^{-2} \left(\hat{y}_\phi - y_\phi\right)^2 \tag{A.11}$$

where ν is the residual degrees of freedom, and the term $(\hat{y}_\phi - y_\phi)$ is the residual of each data point.

In this case, the prediction bounds give the standard deviation interval in which the mean of a new data point is likely to lie within with 68.3% confidence. The 95% prediction bounds are shown in Figure 43 and the maximum deviations for each temperature from the 68.3% prediction bounds and the linear fit are shown in Figure A.4. The maximum value of $u_{F,\text{fit}} = 0.0127$ was chosen as a conservative estimate of the bias uncertainity of spatially averaged normalized images from the linear fit.

A.3.2.2 Precision Uncertainty

The precision uncertainty was primarily due to variations in the imaging and illumination systems. The precision uncertainty can be estimated as the spatial standard deviation across each normalized image, which are typically in the range of

[1] also known as the 'fit standard error' and the 'standard error of the regression'

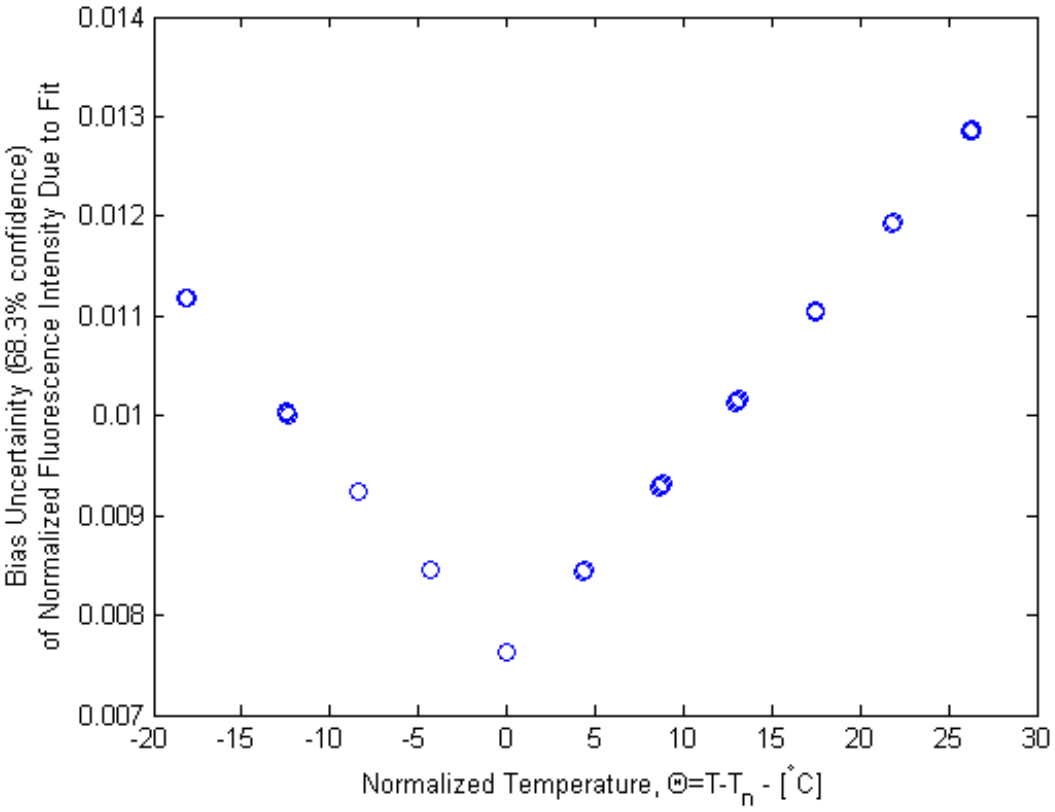

Figure A.4: Maximum difference between 68.3% prediction bounds and linear fit of experimental data.

$\sigma_{N_{ij}} = 1.0 - 2.7\%$. For an individual pixel, the spatial standard deviation implies an expanded precision uncertainties (95% confidence) between ±1.5-3.9℃.

The spatially-averaged corrected pixel value was utilized in the calibration and the precision uncertainty associated with the spatially-averaged corrected pixel value can be determined from the central limit theorem:

$$u_{F,\text{pres}} = \frac{\sigma_{N_{ij}}}{\sqrt{n}} \tag{A.12}$$

here $\sigma_{N_{ij}}$ is the spatial standard deviation of the normalized fluorescence intensity image, and n is the number of samples. For each normalized image, n is on the order of 2×10^5, so the precision uncertainty of the spatially-averaged corrected pixel value for the entire viewfield approaches zero:

$$U_{F,\text{pres}} = 1.96 u_{F,\text{pres}} \to 0 \tag{A.13}$$

A.3.2.3 Resolution Uncertainty

The uncertainty of the camera measurement will propagate into the normalized fluorescence intensity measurement according to:

$$u^2_{F,\text{res}} = \left(\frac{1}{\mathscr{C}^n}\right)^2 \left[u^2_{\mathscr{C}} + F^2 u^2_{\mathscr{C}^n}\right] \tag{A.14}$$

From the camera characterization, the expanded uncertainty was taken as $U_{\mathscr{C}} = 2$ and was approximately constant across the range of measurement. Therefore, the standard uncertainty of the normalizing image $\mathscr{C}^n$ is approximately equal to the uncertainty of the temperature specific image $\mathscr{C}$ (i.e. $u_{\mathscr{C}^n} \approx u_{\mathscr{C}} \approx 1$) then the expression simplifies to:

$$u^2_{F,\text{res}} = \left(\frac{1}{\mathscr{C}_n}\right)^2 \left[1 + F^2\right] \tag{A.15}$$

these values can be computed for each image based upon the average corrected pixel values of the normalizing image, $\mathscr{C}^n$, and the average normalized pixel value F.

A.3.2.4 Combined Precision and Resolution Uncertainties

The resolution and precision uncertainties for individual pixels, and the precision uncertainties for entire images are shown in Figure A.5. The error bars shown in Figure 42 are the combined resolution uncertainty and precision uncertainty for individual pixels:

$$u_{F,\text{comb}} = \sqrt{u_{F,\text{res}}^2 + u_{F,\text{pres}}^2} \tag{A.16}$$

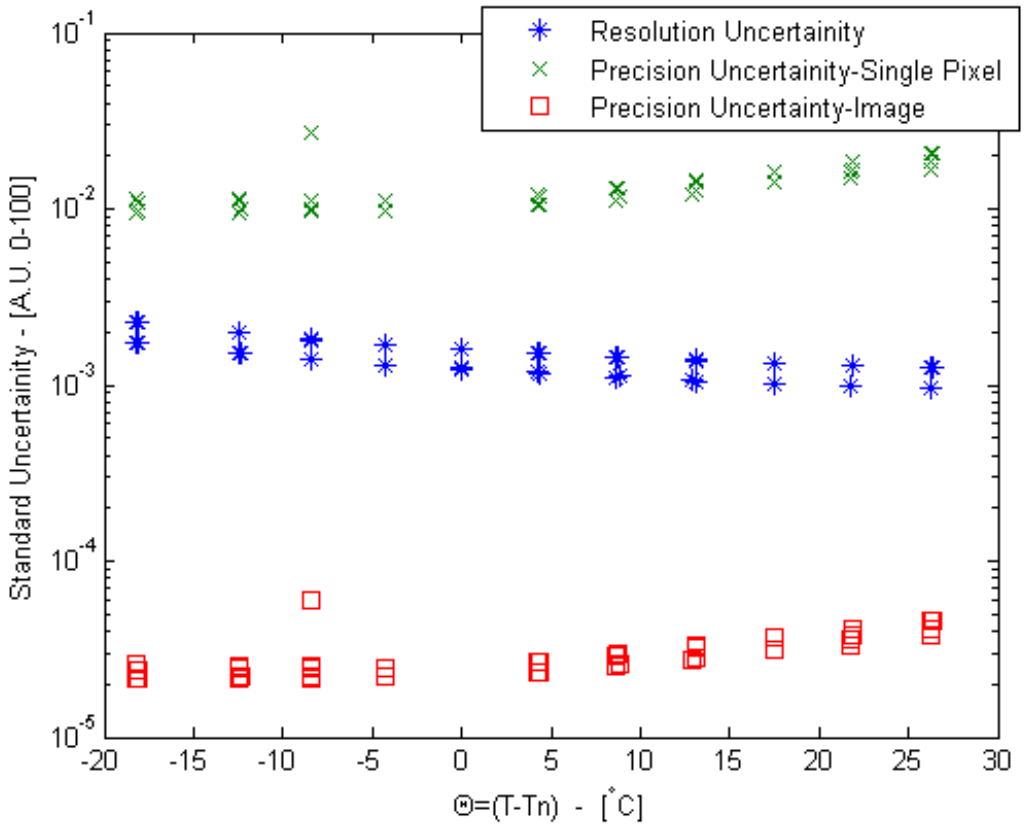

Figure A.5: Uncertainty of normalized data points for measurement and precision uncertainties. Precision uncertainties are shown for single-pixel measurements and the mean of an entire image.

A.3.3 Calibration Curve

The uncertainty of the slope of the calibration curve is related to the uncertainty of the underlying data points and the quality of fit of the data points. In this case, the

data point were fit to a linear fit with offset fixed at 1 and minimizing a χ^2-merit function, as described in section 3.1.3. The uncertainty of the parameter m can be found by performing a propagation of uncertainty calculation upon the data set:

$$\sigma_m^2 = \sum_{\phi=1}^{N} \left(\frac{\partial m}{\partial F_\phi} \sigma_\phi \right)^2 = \sum_{\phi=1}^{N} \left(\frac{\theta_\phi}{\sigma_\phi^2 S_{xx}} \sigma_\phi \right)^2 = \frac{1}{S_{xx}} \tag{A.17}$$

For the calibration data, this expression yields a variance of $\sigma_m^2 = 2.23 \times 10^{-8}$ which is equivalent to an expanded uncertainty of $U_m = 2.93 \times 10^{-4}$ with 95% confidence.

A.3.4 Combined Uncertainty

The combined expanded uncertainty (95% confidence) for temperature measurments based upon the average across the entire 715 × 950 μm viewfield was computed for each data point and is shown in Figure A.6. The bias uncertainty due to the difference between prediction intervals and the linear fit dominates the uncertainty. For the data point with maximum error (corresponding to a surface temperature of 55.1℃), the components of equation A.8 have been estimated and are summarized in table A.2. The maximum expanded calibration uncertainity was found to be ±1.94℃ with 95% confidence across a range 12.5-55℃.

Table A.2: Representative uncertainty calculation of temperature measurement based upon entire 715 × 950 μm viewfield from calibration data. Representative calculation for data point at $T = 55.1$℃($\Theta = 26.3$℃) that has maximum calculated uncertainty.

Note	x_i	Influence ($\frac{\partial f}{\partial x_i}$)	u_{x_i}	$\left(\frac{\partial f}{\partial x_i} u_{x_i}\right)^2$
Bias+Precision	$T_n = 28.8$ [℃]	1	0.081	0.0066
Bias (Fit)	$F = 1.35$	$\frac{1}{m}$	0.0127	0.885
Precision	$F = 1.35$	$\frac{1}{m}$	$0.0169/\sqrt{2 \times 10^5}$	7.9×10^{-6}
Measurement	$F = 1.35$	$\frac{1}{m}$	9.63×10^{-4}	0.0051
Bias	$m = 0.01346$[1/℃]	$\frac{1-F}{m^2}$	1.5×10^{-4}	0.083
			$\sum \left(\frac{\partial f}{\partial x_i} u_{x_i}\right)^2$	0.98
			u_T	0.99
		Expanded Uncertainty (95% Confidence), $U_T = 1.96 u_T$		1.94 ℃

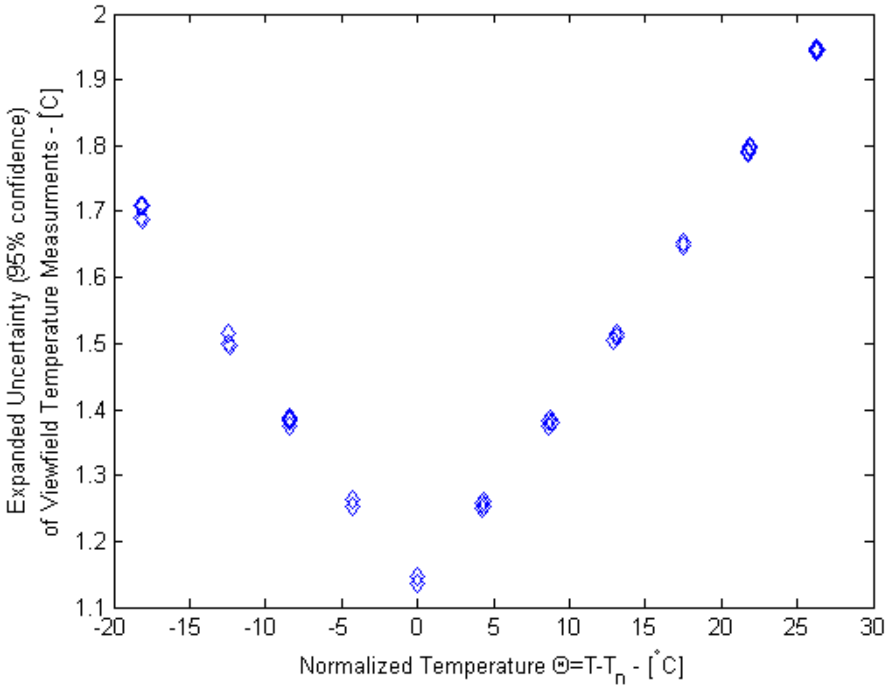

Figure A.6: Expanded uncertainty (95% confidence) for each data point based upon entire 715 × 950 μm viewfield.

The combined expanded uncertainty (95% confidence) for an individual 1.45 × 1.45 μm pixels was computed for each data point and is shown in Figure A.7. The uncertainty calculation is dominated by two terms: the bias uncertainty from the fit and precision uncertainty due to the spatial variation of each pixel's reported fluorescence intensity, $\sigma_{\mathcal{N}_{ij}}$. The precision uncertainty due to the spatial variation are in the range of 1.0-2.7%. For the data point with maximum error (corresponding to a surface temperature of 20.3℃), the components of equation A.8 have been estimated and are summarized in table A.3. The single-pixel uncertainty for this data point has been estimated to be $U_T = 4.2$℃ with 95% confidence.

The combined expanded uncertainty (95% confidence) was calculated for 16 × 16 μm and 100×100 μm regions. Each normalized image was broken into bins containing either 11 × 11 or 69 × 69 pixels, as described in section 2.5.4. The average value of each bin was plotted against the normalized surface temperature and the uncertainty

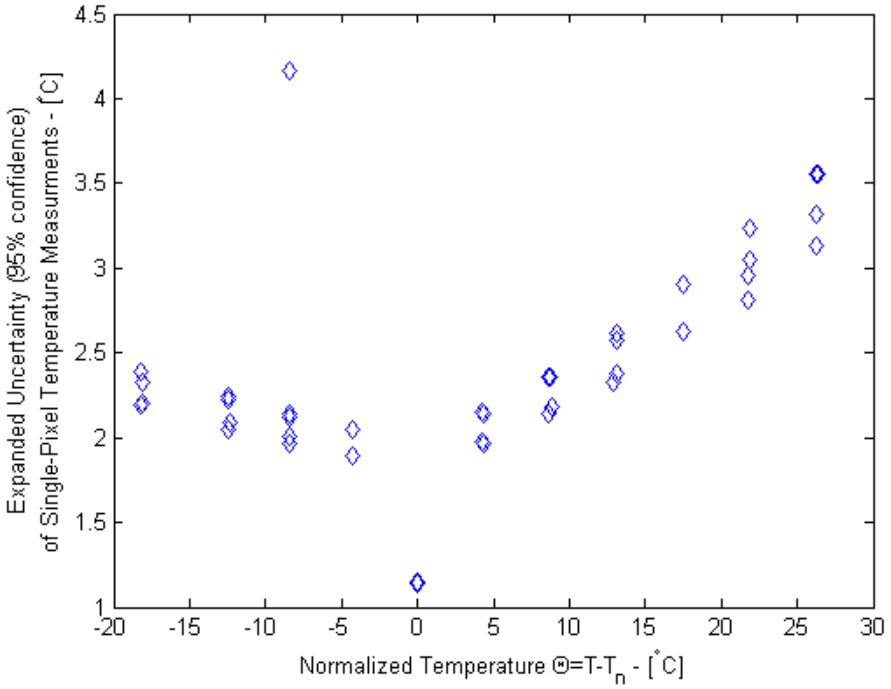

Figure A.7: Expanded uncertainty (95% confidence) of a single-pixel temperature measurment for each data point based. Single-pixel resolution is 1.5×1.5 μm.

Table A.3: Representative uncertainty calculation of temperature measurement based upon individual 1.45×1.45 μm pixel from calibration data. Representative calculation for data point at $T = 20.3$℃$(\Theta = -8.4$℃$)$ that has maximum calculated uncertainty.

Note	x_i	Influence $(\frac{\partial f}{\partial x_i})$	u_{x_i}	$\left(\frac{\partial f}{\partial x_i} u_{x_i}\right)^2$
Bias+Precision	$T_n = 28.8$ [℃]	1	0.081	0.0066
Bias (Fit)	$F = 0.88$	$\frac{1}{m}$	9.2×10^{-3}	0.47
Precision	$F = 0.88$	$\frac{1}{m}$	0.027	4.0
Measurement	$F = 0.88$	$\frac{1}{m}$	1.4×10^{-3}	0.011
Bias	$m = 0.01346$ [1/℃]	$\frac{1-F}{m^2}$	1.5×10^{-4}	0.0099
			$\sum \left(\frac{\partial f}{\partial x_i} u_{x_i}\right)^2$	4.50
			u_T	2.12
			Expanded Uncertainty (95% Confidence), $U_T = 1.96 u_T$	4.16 ℃

calculated using the same methods used to the determine the uncertainty of single-pixel and whole-viewfield temperature measurments. The uncertainties calculated at each normalized surface temperature for 16×16 and 100×100 μm regions are shown in Figure A.8. The maximum uncertainties are 2.4℃ and 2.2℃ for the 16×16 and 100×100 μm regions, respectively.

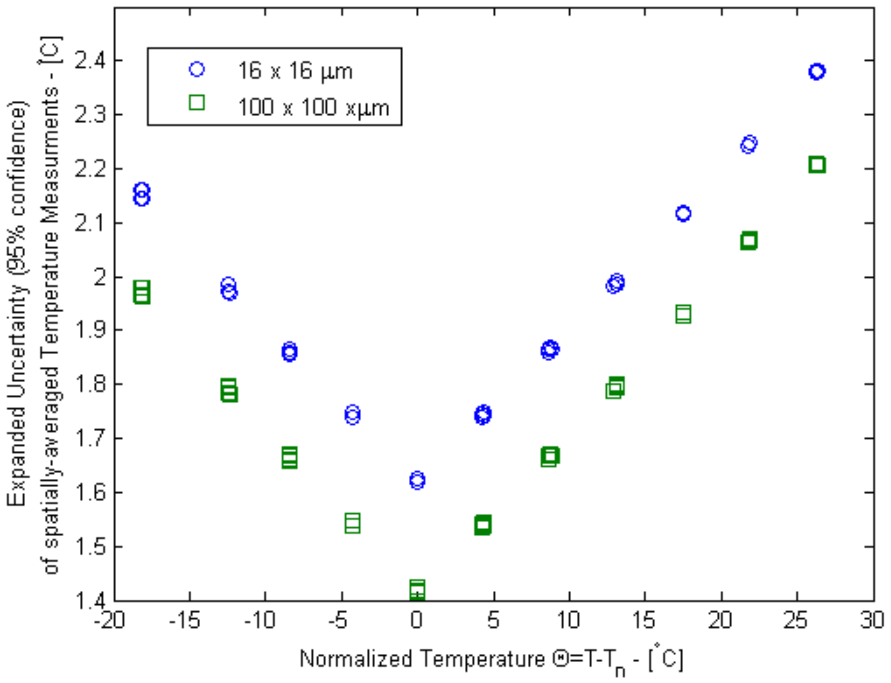

Figure A.8: Expanded uncertainty (95% confidence) of a temperature measurement based upon bins of 16×16 μm (11×11 pixels) and 100×100 μm (69×69 pixels).

APPENDIX B

ADSORPTION

Adsorption of fluorophore at the fused silica substrate was observed in experiments with both rhodamine B and fluorescein. This adsorption results in a variation in fluorophore concentration at the interface between the fused silica and fluorophore solution. This variation in concentration is particularly problematic for this investigation because it occurs in the measurement region and is temperature dependent.

B.1 Adsorption Background

Adsorption refers to the process by which solute (adsorbate) accumulates on the surface of another material (adsorbant). The adsorption of fluorescein and rhodamine B to silica surfaces has been attributed to electrostatic interactions [42]. When silica is in contact with a solution of pH $\geq$ 3, surface hydroxyl groups act as a weak acid and deprotonate, leaving the surface with a net negative surface charge [45],[36]. The magnitude of the surface charge has been shown to be temperature dependent [45]. This surface charge results in an electrical potential ψ that influences the concentration of ions in the solution near the interface. The electrical potential can be described by the Gouy-Chapman model:

$$\psi = \psi_o \exp\left(-\frac{z}{\lambda_D}\right) \tag{B.1}$$

here ψ_o is the potential at the interface, z is the distance from the interface, and λ_D is the Debye length [9]. The Debye length is the length scale of the electrostatic interactions, and is defined as

$$\lambda_D = \sqrt{\frac{\epsilon kT}{2e^2 N_A \check{I}}} \tag{B.2}$$

where ϵ is the permittivity of the solution, k is Boltzman's constant, T is the absolute temperature, e is the elementary charge, N_A is Avogadro's number, and $\check{I}$ is the ionic strength of the solution.

The presence of the negative electric field will attract positively charged ions and repulse negatively charged ions. Rhodamine B has both positive and negative charged functional groups at pH above 3.1 so it is adsorbed onto both positively and negatively charged surfaces. Fluorescein can exist in a di-anionic (-2), mono-anionic (-1), neutral, or cationic (+1) form, depending on the pH of the solution. By increasing pH, fluorescein will tend to exist in the more negatively charged forms and so will be less likely to adsorb to silica surfaces[32]. At pH$>$ 9 fluorescein will exist in the di-anionic form, with a higher quantum efficiency resulting in a greater fluorescence intensity. Therefore, buffering fluorescein to a pH of 9.2 has two benefits: reduces adsorption to fused silica, and increases the fluorescence intensity resulting in higher signal-to-noise ratios.

B.2 Adsorption Measurement

To measure the typical contribution of adsorbed species to the total fluorescence intensity measurement, two measurements were undertaken. First the combined fluorescence intensity under evanescent-wave illumination from fluorophores adsorbed to the surface and those in the bulk of the solution was measured. Second the fluorescence intensity under evanescent-wave illumination was measured only from fluorophores adsorbed to the surface.

B.2.1 Procedure

Three fluorophore solutions were prepared:

1. 5 μM rhodamine B in de-ionized water (pH=4.8)

2. 10 μM fluorescein in de-ionized water (pH=5.7)

3. 10 μM fluorescein with 10 mM sodium tetraborate in de-ionized water (pH=9.2)

The calibration cell was cleaned and evanescent-wave illumination was generated via prism-based TIR following typical procedures. Approximately 100 mL of solution was added to the calibration cell, and the microscope objective was aligned with an area of evanescent-wave illumination. A sequence of 100 images was captured, and image processing undertaken to correct for dark noise and camera non-linearity to generate a time-averaged, corrected image $\mathscr{C}_{ij}$. This image provided a measure of the fluorescence intensity under evanescent-wave illumination from fluorophores both adsorbed to the surface and in the bulk of the solution.

To measure the fluorescence intensity from only fluorophores adsorbed to the surface, the bulk fluorophore solution was removed from the calibration cell using a peristaltic pump and a vacuum generated by an aspirator. Approximately 100 mL of buffer solution was added (de-ionized water for solutions (1) and (2), and 10 mM sodium tetraborate for solution (3)) to the calibration cell to dilute any remaining bulk fluorophore solution and to maintain a similar experimental environment. During these steps, care was taken to not physically alter the orientation of the calibration cell, to ensure that the evanescent-wave illumination did not vary significantly. A sequence of 100 images was captured, and image processing undertaken to correct for dark noise and camera non-linearity to generate a time-averaged, corrected image $\mathscr{C}_{ij}^{ads}$. This image provided a measure of the fluorescence intensity under evanescent-wave illumination only from fluorophores adsorbed to the surface.

B.2.2 Results

The contribution of fluorophore adsorbed onto the fused silica surface was estimated by dividing the average value of $\mathscr{C}_{ij}^{ads}$ by the average value of $\mathscr{C}_{ij}$. The percent contribution of adsorbed species is shown for each solution in Figure B.1. Adsorption

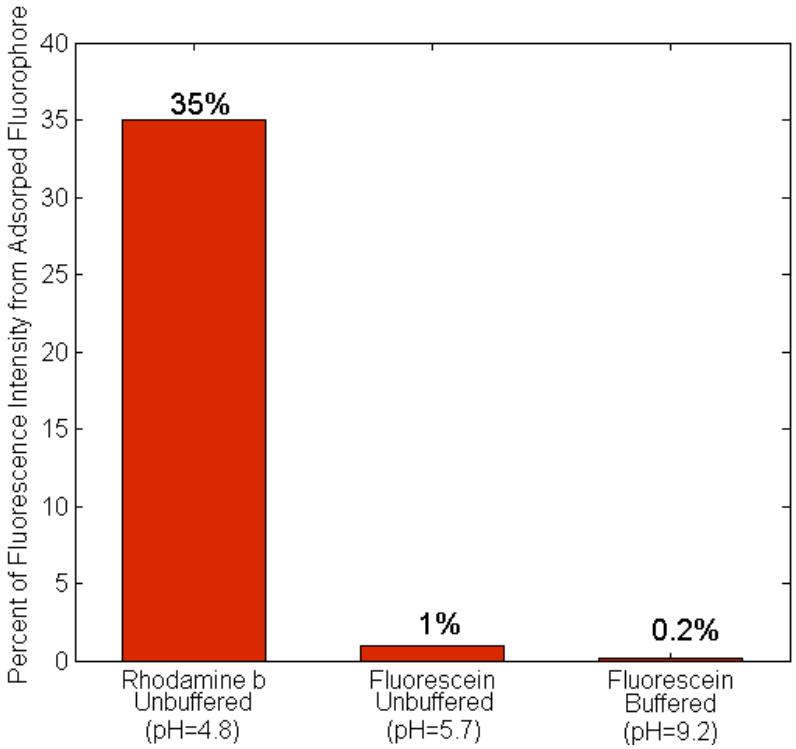

Figure B.1: Contribution of fluorophore adsorbed to the surface to fluorescent intensity measurements.

levels are an order of magnitude lower for fluorescein in de-ionized water, as compared to rhodamine B in de-ionized water. A further order of magnitude decrease in adsorption is realized by buffering the fluorescein solution with sodium tetraborate to a pH of 9.2. These results are similar to the findings of Kasnavia *et al.* [42] who found that fluorescein demonstrated lower levels of adsorption to silica particles than three other fluorescent dyes: rhodamine B, rhodamine WT, and sulforrhodamine B. Kasnavia *et al.* also found that adsorption of fluorescein to silica was undetectable when the solution pH=9.

B.3 Calibration with Rhodamine B

Calibrations were performed to determine the relationship between temperature and fluorescence intensity of rhodamine B ([RhB]=1.0 μM) under evanescent-wave illumination at 488 nm. The experimental apparatus and procedure were similar to those

of fluorescein calibrations with several differences:

Optical Filters An interference bandpass filter (Edmund Optics, 30907) with center wavelength of 488.1 nm and peak transmission of 47% was used to attenuate illumination at wavelengths other than 488 nm. The maximum illumination power at a location just before the entrance prism was measured to be 40 mW. A Leica I3 filter cube was used to isolate fluorescence emissions from laser illumination.

Recirculating Constant Temperature Bath A recirculating constant temperature bath (Haake C1-B3) was used that did not have any chilling capabilities. Any temperatures below room temperature ($\approx$ 20°C) were achieved by adding ice to the constant temperature bath.

Objective Magnification A 40x objective (Leica) was used in the imaging system.

Camera Correction The non-linearity of the camera was not corrected for. Image sequences were taken at a multiplication gain of 3475 and an exposure time of 100 ms, which corresponds to a much lower light level than for the fluorescein calibrations. It is believed that at higher gain settings, the camera shows greater deviation from linear behavior.

Thermocouple Attachment The thermocouples in the calibration cell were attached to the fused silica surface by a combination of thermal adhesive (Arctic Silver, Thermal Adhesive) and epoxy adhesive (Loctite U-05FL).

Cleaning To reduce adsorption of rhodamineB, after adding the fluorophore solution the fused silica substrate was swabbed with a foam swab (Fisher Scientific, 14-960-3H).

The experimental apparatus and procedure used for calibrations improved with time. These rhodamine B calibrations pre-dated fluorescein calibrations; therefore, the experimental techniques used for fluorescein calibrations reflected improved equipment and methods.

The normalized fluorescence intensity variations with temperature of two experimental runs are shown in Figure B.2. A non-linear, inverse relationship between temperature and fluorescence intensity was observed. The non-linear relationship indicates that the calibration curve is dependent upon normalizing temperature T_n, which was chosen as $T_n = 20$℃. The fluorescence intensity demonstrated strong hysteresis with normalized intensities returning to only approximately 50% of their initial values after heating. Further investigations demonstrated that the hysteresis did not recover with time or a subsequent increase in temperature (i.e. the hysteresis loop did not close). The hysteresis can be attributed to irreversible desorption of rhodamine B from the fused silica surface with increasing temperature.

If the experimental data points of decreasing temperature (i.e. $dT/dt < 0$) that exhibited hysteresis were ignored, the remaining data points demonstrated good repeatability and were in good agreement with a second-order polynomial fit. As during fluorescein calibrations, the offset was fixed at one because $(\Theta, F) = (0, 1)$, and the resulting second-order polynomial fit was:

$$F = 5.34 \times 10^{-5}\Theta^2 - 0.0381\Theta + 1 \tag{B.3}$$

The increasing temperature (i.e. $dT/dt > 0$) data points and resulting second-order polynomial fit are shown in Figure B.3.

B.4 Attempts to Block Adsorption of Rhodamine B

Many procedural changes were implemented to attempt to reduce the level of adsorption of rhodamine B to fused silica with only limited success. Although these investigations were not successful, further investigations may yield better results. These

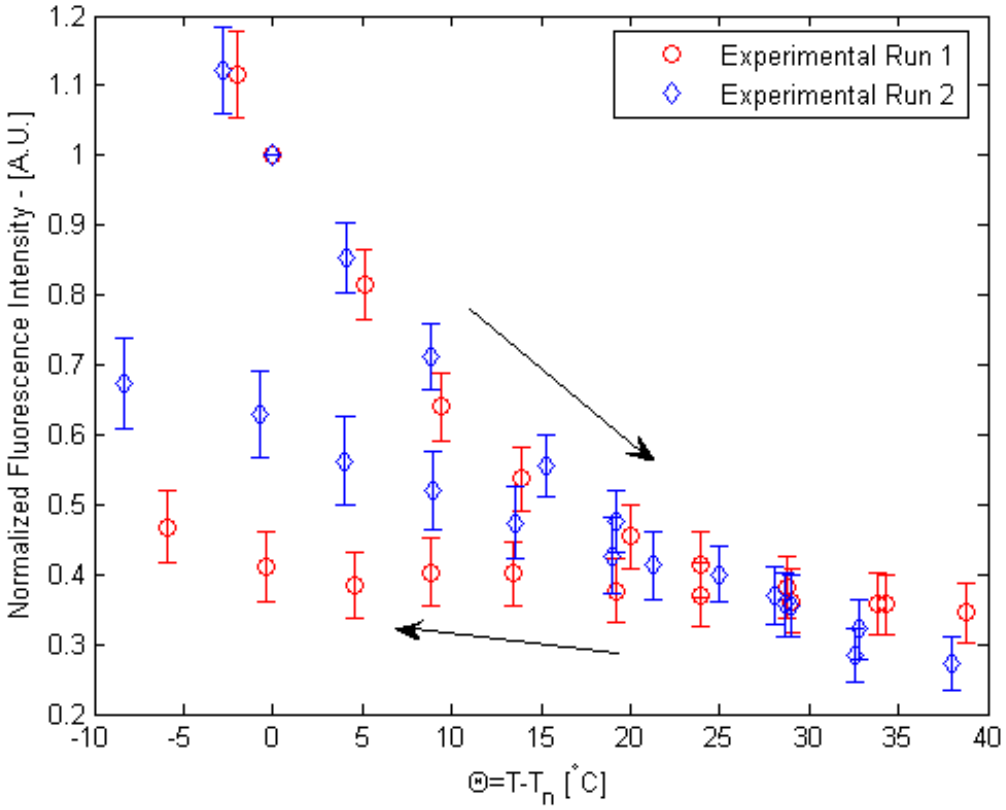

Figure B.2: Normalized fluorescence intensity vs. temperature difference for rhodamine B. Arrows in direction of increasing time indicate order of experimental data points. Non-linear relationship indicates that the calibration curve is dependent upon normalizing temperature T_n. The normalizing temperature is $T_n = 20\,℃$ and the error bars are the spatial standard deviations of the normalized images.

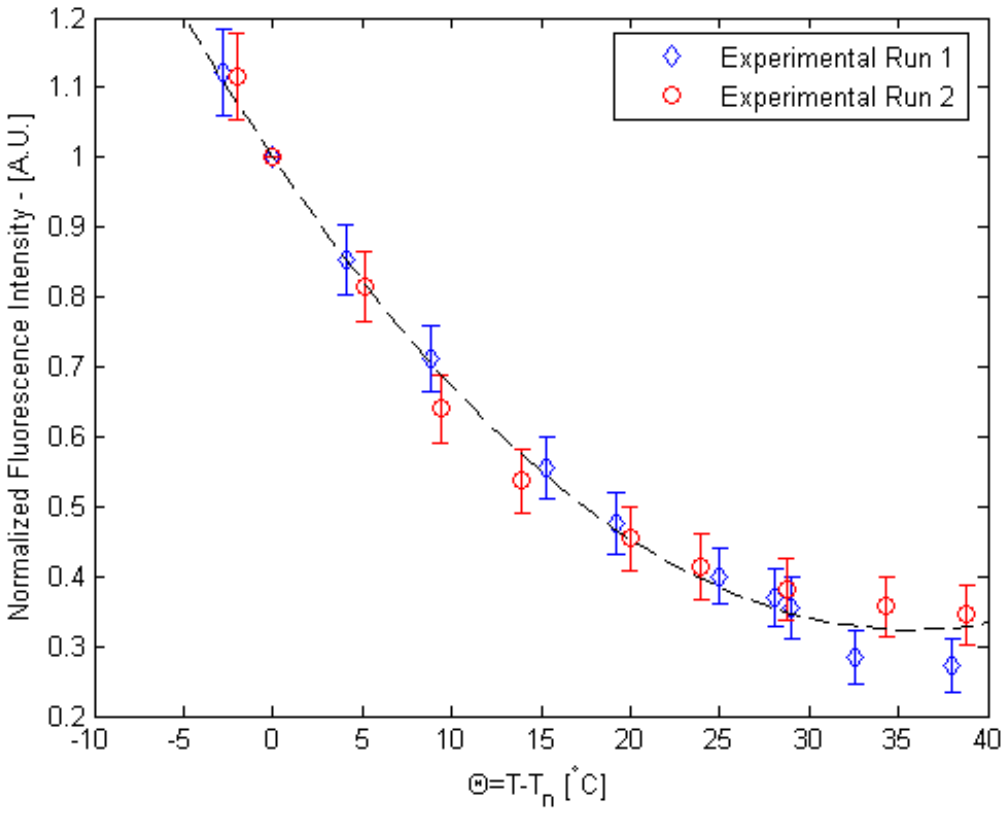

Figure B.3: Normalized fluorescence intensity vs. temperature difference of rhodamine B with increasing temperature. The normalizing temperature is $T_n = 20$ ℃ and the error bars are the spatial standard deviations of the normalized images.

methods can be grouped into four categories: cleaning, protein blocker, surfactant and charge inversion.

B.4.1 Cleaning

Initially, the spatial variation of fluorescence intensity on the surface was believed to be due to attraction of rhodamine B to debris on the fused silica surface. It was felt that the the debris could have originated from environmental dust, dissolved adhesive, or residue left from previous experiments. During the rhodamine B calibrations previously described, the fused silica surface was swabbed to reduce adsorption of rhodamine B. Qualitatively, swabbing reduced the magnitude of fluorescence intensity and provided a more spatially uniform fluorescence intensity measurement. However, strong hysteresis was still present suggesting that adsorption was sill present. Furthermore, swabbing would not be possible in the confined geometry of a microchannel that would later be studied. Therefore, chemical methods of cleaning the fused silica surface and reducing adsorption were desired.

Solutions of methanol, acetone, 1 M sodium hydroxide and chemical soap were utilized to to clean the fused silica surface. The best cleaning was achieved with an overnight soak in a chemical soap solution (Contrad 70); however, cleaning did not significantly reduce adsorption.

B.4.2 Protein Blocker

Protein-based blockers are used in immunoassay to selectively prevent false-signal by blocking binding between tracer molecules and non-target molecules. For instance, if a tracer molecule R is known to bind to target molecule T and substrate molecule S, then the binding of R to S will produce a false-signal. Therefore, a blocker molecule B is added to the solution to prevent binding of R to S; by, for instance, binding to the substrate and blocking any R from coming into contact with S.

Two different commonly used protein-based blockers were investigated: Bovine

Serum Albumin (BSA) in a 1x PBS (Phosphate Buffered) solution and dry skim milk (DSM) in water. The test cell was soaked with BSA of 1% (g/ml) or DSM of 5% (g/ml) for approximately one hour, then flushed with either PBS or water. A rhodamine B solution with a concentration of $\approx$ 1 μM was added to the test cell and the qualitative fluoresence intensity was observed. Compared to control experiments with no protein blocker, the fluorescence intensity with both blockers still demonstrated spatial non-uniformities. However, for BSA the total fluorescence intensity was noticeably dimmer. This suggests that BSA was able to block some, but not all adsorption of rhodamine B to the fused silica surface.

B.4.3 Surfactant

NaDDBS (sodium dodecylbenzenesulfonate) is an anionic surfactant that has been used to increase the solubility of single-walled carbon nano-tubes in water and other organic solvents [55]. When dissolved in water, NaDDBS disassociates into a positively charged Na^+ ion and a negatively charged $DDBS^-$. The negative charge on the $DDBS^-$ ion is localized on the hydrophilic 'head', while the hydrophobic 'tail' has no net charge. In theory, the anionic hydrophilic 'head' should be attracted to the positively charged hydrophilic portion of the rhodamine B molecule. In theory, the combined rhodamine B-DDBS pair would exhibit a reduced net charge and hydrophobicity. The neutrally charged, hydrophobic pair should not be attracted to the negatively charged hydrophilic fused silica substrate.

A solution with concentrations of [RhB]= 1 μM and [NaDDBS]= 0.8 mM in water was prepared and poured into he test cell. Compared to a control solution of 1μM rhodamine B, the NaDDBS-rhodamine B solution exhibited fluorescence intensity measurements consistent with greater levels of adsorption. Greater spatial patterning and an increase in surface fluorescence relative to bulk fluorescence was observed.

B.4.4 Charge Inversion

Charge inversion is a technique that has been used in electrosmotic flows in microchannels to invert the charge of fused silica channel walls [87],[86]. By adding ionic salts to the solution, positively charged ions form a positively charged layer near the negatively fused silica surface. This effect can be enhanced by a salt whose positive ion has valence greater than one, e.g. $CaCl_2 \rightarrow Ca^{2+} + 2Cl^{-1}$. The higher valence positive ion will be more strongly attracted to the fused silica surface.

Solutions with rhodamine B concentration of [RhB]=1μM and calcium ion concentrations ranging between [Ca^{2+}]=0.005-.25 M were prepared. Qualitative observations showed that charge inversion greatly reduced surface adsorption of rhodamine B to the fused silica surface, with best results being achieved with a concentration of [Ca^{2+}] = 0.05 M.

A calibration of the relationship between fluorescence intensity and temperature for rhodamine B was performed using both epi-illumination and evanescent-wave illumination. The calibration cell was soaked with a solution of [Ca^{2+}] = 0.5 M for approximately 5 minutes, then drained. A solution with concentrations of [Ca^{2+}] = 0.05 M and [RhB]=1.0 μM was added to the calibration cell. The experimental procedure was similar to the previous rhodamine B calibration, with two exceptions: a higher quality 488 nm laser excitation filter (Chroma) was utilized, and epi-illumination was provided via the microscopes mercury arc lamp. The higher quality laser excitation filter had a higher transmittance at 488 nm, and also reduced laser power instabilities. Image sequences were taken sequentially for epi-illumination and evanescent-wave illumination at each data point.

Initially, the fluorescence intensity was spatially variant, indicating adsorption of rhodamine B to the fused silica surface. However, over a period of approximately ten minutes the fluorescence intensity magnitude significantly decreased and became spatially uniform, indicating that adsorption of rhodamine B to the fused silica surface

had decreased.

A series of data points were acquired under increasing temperature ($dT/dt > 0$), for three different optical configurations: 1) evanescent-wave illumination with 10x objective, 2) evanescent-wave illumination with 40x objective, and 3) epi-illumination with 10x objective. The different magnitudes of illumination intensity and objective collection efficiencies resulted in drastically different levels of intensity incident upon the CCD array. The multiplication gain setting was kept fixed at 3300 and the camera exposure varied for each optical configuration as summarized in table B.1. By fixing the multiplication gain, the camera non-linearities should be consistent for each of the three optical configurations.

Table B.1: Camera settings for each optical configuration used in charge inversion investigations.

	Illumination	Objective	Multip. Gain	Exposure (ms)
1	Evanescent	10x	3300	70
2	Evanescent	40x	3300	200
3	Epi-	10x	3300	6

The resulting normalized fluorescence intensities as a function of temperature are shown in Figure B.4. For all three optical configurations, the relationship between temperature and fluorescence intensity is approximately linear. This linear relationship is in agreement with previous studies of the temperature dependence of rhodamine B under epi-illumination [35].

Significant hysteresis was observed under evanescent-wave illumination for the final data points for both the 10x and 40x objective. Examination of the raw grayscale images (Figure B.5) shows the presence of aggregates that settle on the fused silica surface with time. These aggregates are more readily visible under epi-illumination. The spatial density of aggregates increases with time, and greatly increases between the penultimate and final data points. These aggregates contain fluorophores so

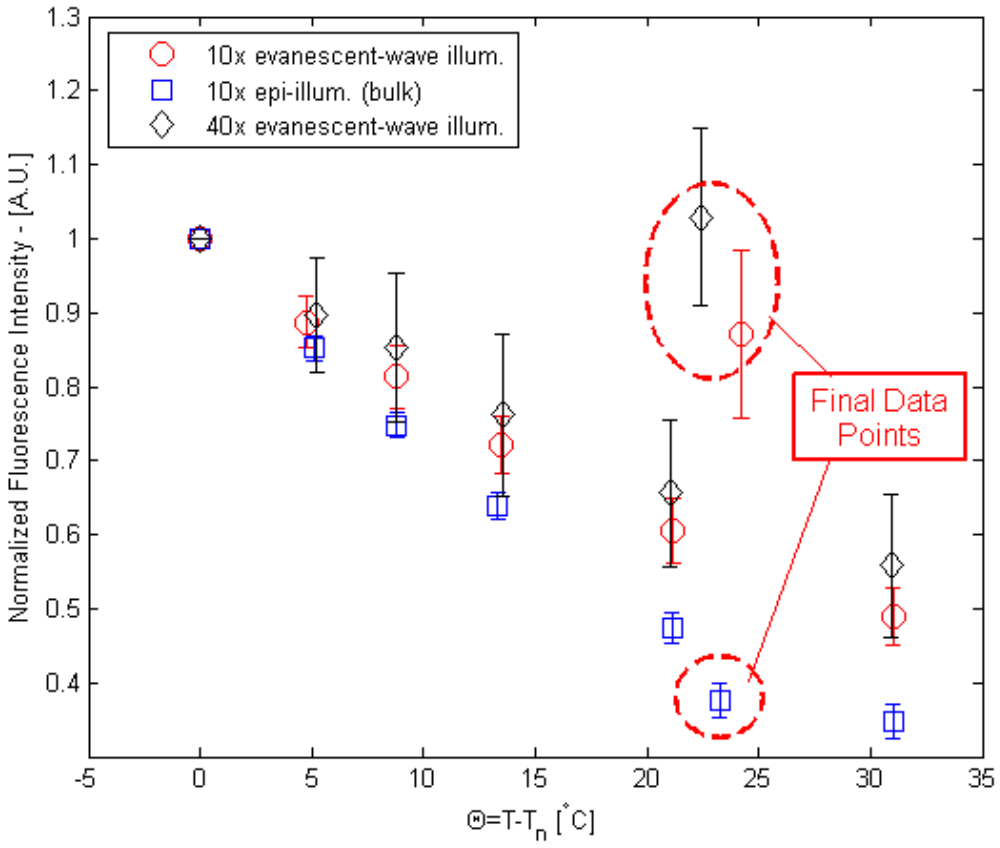

Figure B.4: Normalized fluorescence intensity vs. temperature difference for rhodamine B solution with charge inversion.

they greatly increase the concentration of rhodamine B near the fused silica surface and therefore bias the normalized fluorescence intensity upward under evanescent-wave illumination. Under epi-illumination, the aggregates appear to interfere with fluorescence from the bulk of the fluid and therefore slightly bias the normalized fluorescence intensity downward.

Fluorophore aggregates settling on the surface likely affected all evanescent wave illuminated measurements. The aggregation of rhodamine B in solution with Ca^{2+} and Cl^{-} ions is not a well understood process. It is conceivable that such a process could be time and temperature-dependent. Without a better understanding of the chemistry involved in charge inversion, compensating for or mitigating the bias introduced into fluorescence intensity by aggregation during charge inversion will be difficult.

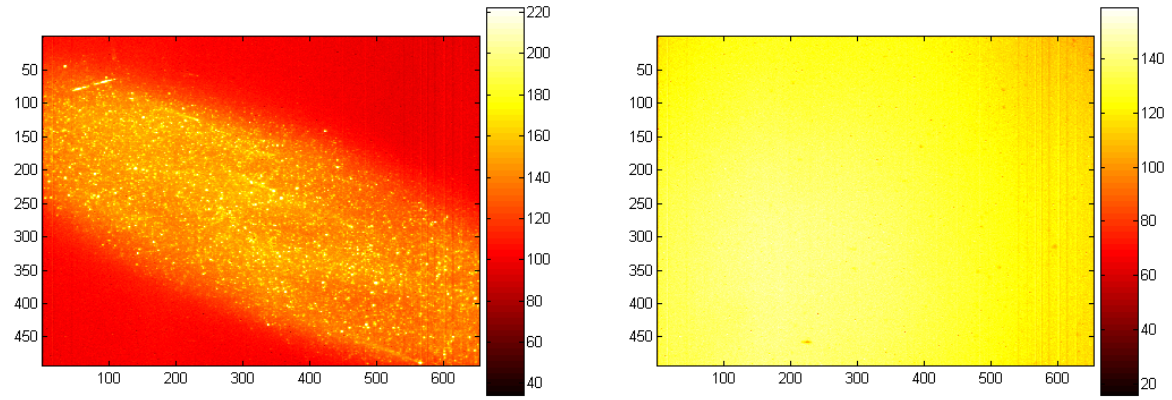

(a) $\Theta = 0$℃

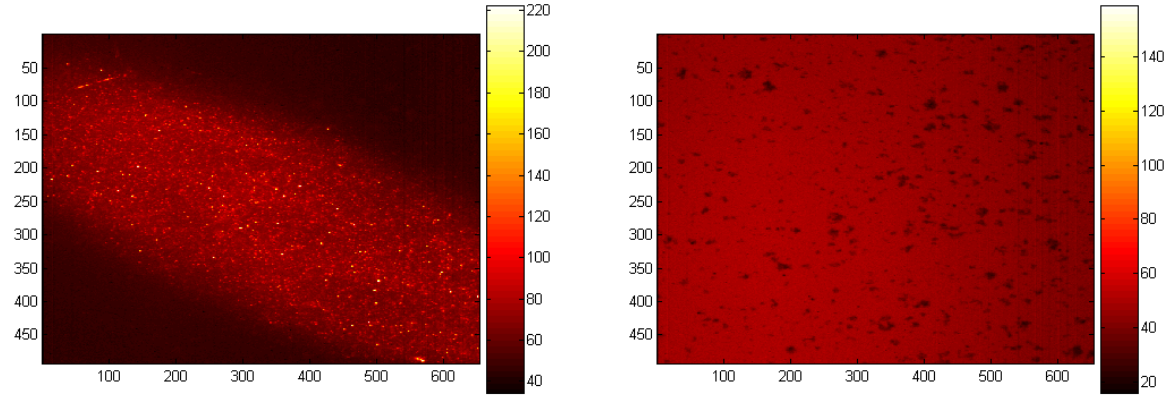

(b) $\Theta = 31$℃

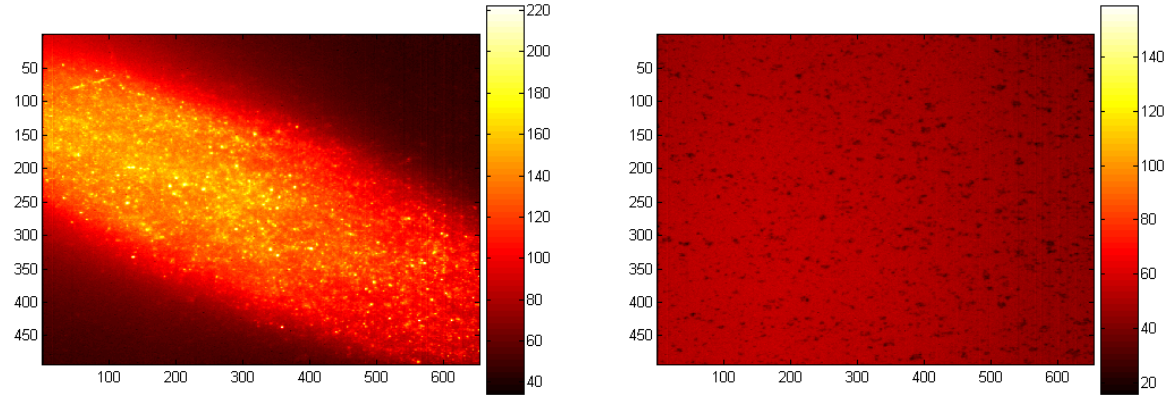

(c) $\Theta = 24$℃

Figure B.5: Time-averaged raw grayscale images corresponding to (a) first, (b) penultimate and (c) final data points for 10x objective. Images in left column were under evanescent-wave illumination and in the right column were under epi-illumination. Images are in false color.

APPENDIX C

TEMPERATURE GRADIENT MEASUREMENTS IN A MICROCHANNEL

A proof-of-concept experiment was undertaken to evaluate the capabilities of the Total Internal Reflection Fluorescence Micro-Thermometry technique. The objectives of this experiment were to generate a known spatially variant temperature field, and to compare the known temperature field to measurements obtained with the TIR-FMT technique.

Due to variations in illumination and adsorption there was a large variability in results and poor convergence between measured and expected values. The results are presented here as a starting point for future investigators.

C.1 Temperature Gradient Procedure

A linear temperature gradient across the width of a microchannel was chosen as the known spatially variant temperature field. The microchannel was fabricated from stainless steel and fused silica using traditional machining methods. A temperature gradient was established across the microchannel using a device similar to those developed by Mao *et al.* [54],[53].

C.1.1 Experimental Apparatus: Microchannel

An illustration of the microchannel is shown in Figure C.1 and channel components are summarized in Table C.1.1. The microchannel was fabricated by milling a channel with dimensions of $0.794 \times 1.59 \times 54$ mm (depth x width x length) into a piece of 316 stainless steel plate with overall dimensions of $1.59 \times 44 \times 56$ mm (depth x width x length). A 63.5 x 63.5 mm square fused silica optical window with thickness of

Table C.1: Components of microchannel

	Description	Manufacturer	Model	Dimensions (mm) ($d \times w \times l$) ($h \times i.d. \times o.d.$)
1	Stainless Steel Plate	–	316 S.S.	$1.59 \times 44 \times 56$
2	Fused Silica Window	Esco Products	Q325063	$1.59 \times 63.5 \times 63.5$
3a/b	Inlet/Outlet Tube	McMaster-Carr	89875K38	$12.7 \times 3.0 \times 3.76$
4	Thermocouple	Omega	TMQSS-020G-6	O.D = 0.5
5a	Comp.-Lock Fitting	Parker Inst.	1-1 HBZ	1/16" O.D. tubing
5b	Ferrule	Small Parts Inc	Fp-1/26-01	0.18-0.20" O.D. tubing
5c	Comp.-Lock Nut	Parker Inst.	1 BZ	–

1.59 mm was used as a coverplate and was bonded to the stainless steel channel with epoxy adhesive. The resulting microchannel has an approximate cross sectional area of $A_c = 1.26$ mm^2, wetted perimeter of $P_w = 4.768$ mm and a hydraulic diameter D_h of:

$$D_h = \frac{4A_c}{P_w} = 1.06\text{mm} \tag{C.1}$$

Channel inlets and outlets were fabricated by drilling two holes with diameter 1.59 mm through the stainless steel a distance 3 mm from the edge of the stainless steel plate. Centered above each through-hole was a 316 stainless steel tube of dimensions 12.7 x 3.0 x 3.76 mm (height x I.D. x O.D.) held in place by epoxy adhesive. The stainless steel inlet tube was connected to a syringe pump (Harvard Apparatus, 55-2111) by approximately 100 cm of 3.18 x 6.35 mm (I.D. x O.D.) PVC chemical tubing. The stainless steel outlet tube was connected to approximately 75 cm of 3.15 x 6.35 (I.D. x O.D.) PVC chemical tubing that led to a waste container.

The temperature inside the microchannel was measured by a T-type thermocouple inside a stainless steel sheath (Omega, TMQSS-020G-6) with an outer diameter of 0.5 mm. The thermocouple was referenced to an ice bath cold junction and the thermocouple's voltage was measured and recorded by a data acquisition system (Agilent 34970A/34901A). The thermocouple was calibrated using the same procedure as

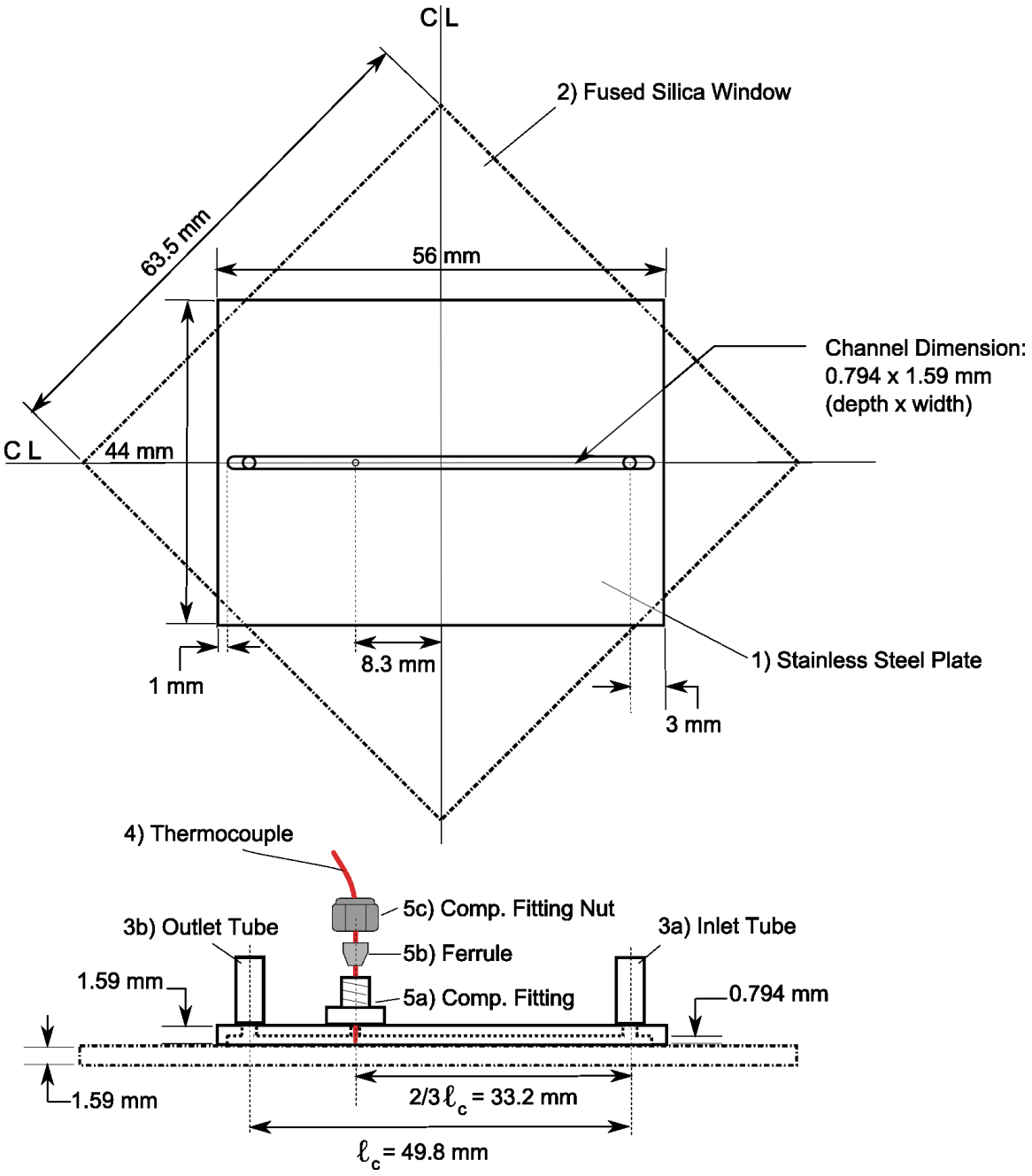

Figure C.1: Illustration of microchannel dimensions and components.

described in section 2.4.1, with the relationship between the measured temperature T_r and true corrected temperature T_c described by a first-order polynomial:

$$T_c = 1.0098T_r - 0.185 \tag{C.2}$$

The thermocouple was inserted into the microchannel through a 0.794 mm diameter through-hole located $2/3\,\ell_c$ from the inlet, where $\ell_c = 49.8$ mm is the channel length defined as the distance between the centerlines of the inlet and outlet. Centered with the through-hole was a 316 stainless steel 1/16" compression-lock fitting that was held in place by high-strength epoxy adhesive. The thermocouple was inserted through the compression-lock fitting and sealed by a compression-lock nut with a graphite/polyimide ferrule that is used for hypodermic tubing.

C.1.2 Experimental Apparatus: Temperature Gradient Device

The temperature gradient device (Figure C.2) consisted of two aluminum blocks that were maintained at different temperatures. One aluminum block (the 'hot' block) was heated by a cartridge heater, and the other (the 'cold' block) was cooled by water from a recirculating constant temperature bath. Both blocks had exterior dimensions of 12.7 x 12.7 x 50.8 mm (width x height x length). The two blocks were were bonded to a piece of polycarbonate sheet that held the blocks in place at a fixed separation distance of 10 mm.

A 100 W cartridge heater (McMaster-Carr, 4877K12) was inserted into a 7.1 mm diameter hole bored to a depth of 43 mm into one end of the hot block. Thermally conductive silicone-filled paste (Omega, Omegatherm 201) was used to fill the gap between the outer diameter of the cartridge heater and the aluminum block to ensure good thermal contact. Power was supplied to the cartridge heater by a 60 Volt power supply (Agilent E3612A).

For the cold block, a hole of diameter 10.29 mm was bored through the piece lengthwise and both ends were threaded with female 1/8" NPT threading. An adapter

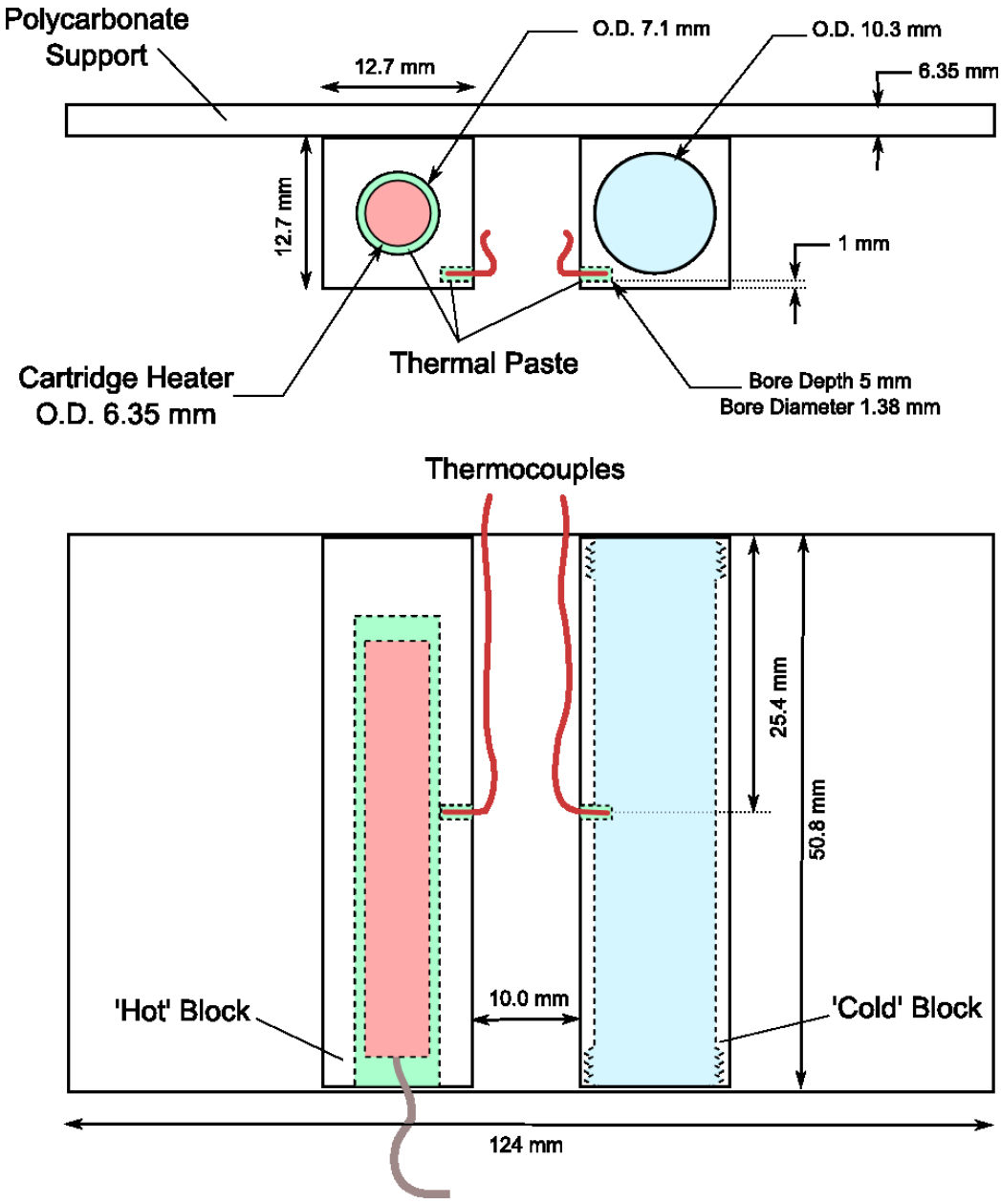

Figure C.2: Illustration of temperature gradient device.

(McMaster-Carr, 2808K51) that created a union between 1/8" NPT female fitting and a barbed 1/4" I.D tube fitting was inserted into each end of the block with Teflon tape to form a water-tight seal. Each adapter was connected to the recirculating constant temperature bath (Haake D8-GH) by PVC tubing with dimensions 6.35 x 9.53 mm (I.D. x O.D).

A T-type thermocouple (Omega, 5TC-TT-T-30-36) was inserted into a 1.38 mm diameter hole that was bored to a depth of 5 mm. The hole was located approximately 1 mm above the bottom surface at midlength of each block. The gap between the thermocouple and the aluminum block was filled with thermally conductive silicone-filled paste (Omega, Omegatherm 201) to ensure good thermal contact. The thermocouple voltages were measured and converted to temperature using the cold-junction software compensation capabilities of the Agilent 34970A/34901A.

C.1.3 Design Considerations

C.1.3.1 Material Selection

The channel was made from 316 stainless steel because of its machinability, high thermal conductivity, ability to be bonded to fused silica and excellent chemical compatibilities. Initial channel prototypes made out of aluminum corroded and were incompatible with sodium hydroxide and chemical soap (Contrad 70) used in cleaning. Several high-performance plastics were considered as a channel material, but were unsuitable due to poor machinability, low thermal conductivity, poor chemical resistance, high cost, or difficulty in bonding.

C.1.3.2 Thermal and Mass Transport

The relative locations and orientations of the channel, channel thermocouple, temperature gradient device, direction of solution flow, and direction of beam propagation are shown in Figure C.3. Thermocouple and TIR-FMT temperature measurements were taken closer to the channel outlet than the channel inlet to increase the likelihood

of thermally fully-developed flow.

Thermocouple measurements inside the microchannel were to be taken at steady state at a location where the flow was hydro-dynamically and thermally fully-developed. Therefore, the thermocouple was located two-thirds of the channel length downstream from the entrance. Furthermore, fully-developed behavior was encouraged by maintaining a low flow rate through the channel. The syringe pump (Harvard Apparatus, 55-2111) was equipped with a 10 mL syringe (B.D., 301604) and set to deliver fluid at a volume flow rate between $Q = 1 - 2\,\mathrm{mL/hr} = 0.2778 - .5556\,\mathrm{mm^3/sec}$. For the channel cross-section of $A_c = 1.26\,\mathrm{mm^2}$, the average velocity of the solution through the channel was between $\bar{v} = 0.22 - .44\,\mathrm{mm/sec}$. Therefore, on average a fluid particle would be in the channel for a period of 1.25-2.5 and 1.9-3.8 minutes before arriving at the location of the thermocouple and channel outlet, respectively.

The region of interest for temperature measurements using TIR-FMT was selected to be in close proximity to the thermocouple. Taking thermocouple and TIR-FMT measurements in close proximity, would decrease divergence in measurements due to local variations in temperature. However, scattering would occur if the evanescent-wave illumination was incident upon the thermocouple sheath. Therefore, TIR-FMT measurements were taken within one reflection length (≈ 11 mm) of the thermocouple but far enough away to prevent scattering.

C.1.3.3 Device Dimensions

The overall height of the channel apparatus was selected as 1.59 mm to generate a steep temperature gradient in the channel. Decreasing the channel apparatus height caused a greater proportion of the heat transfered between the hot and cold block to flow through the measurement region, resulting in a steeper temperature gradient in the measurement region.

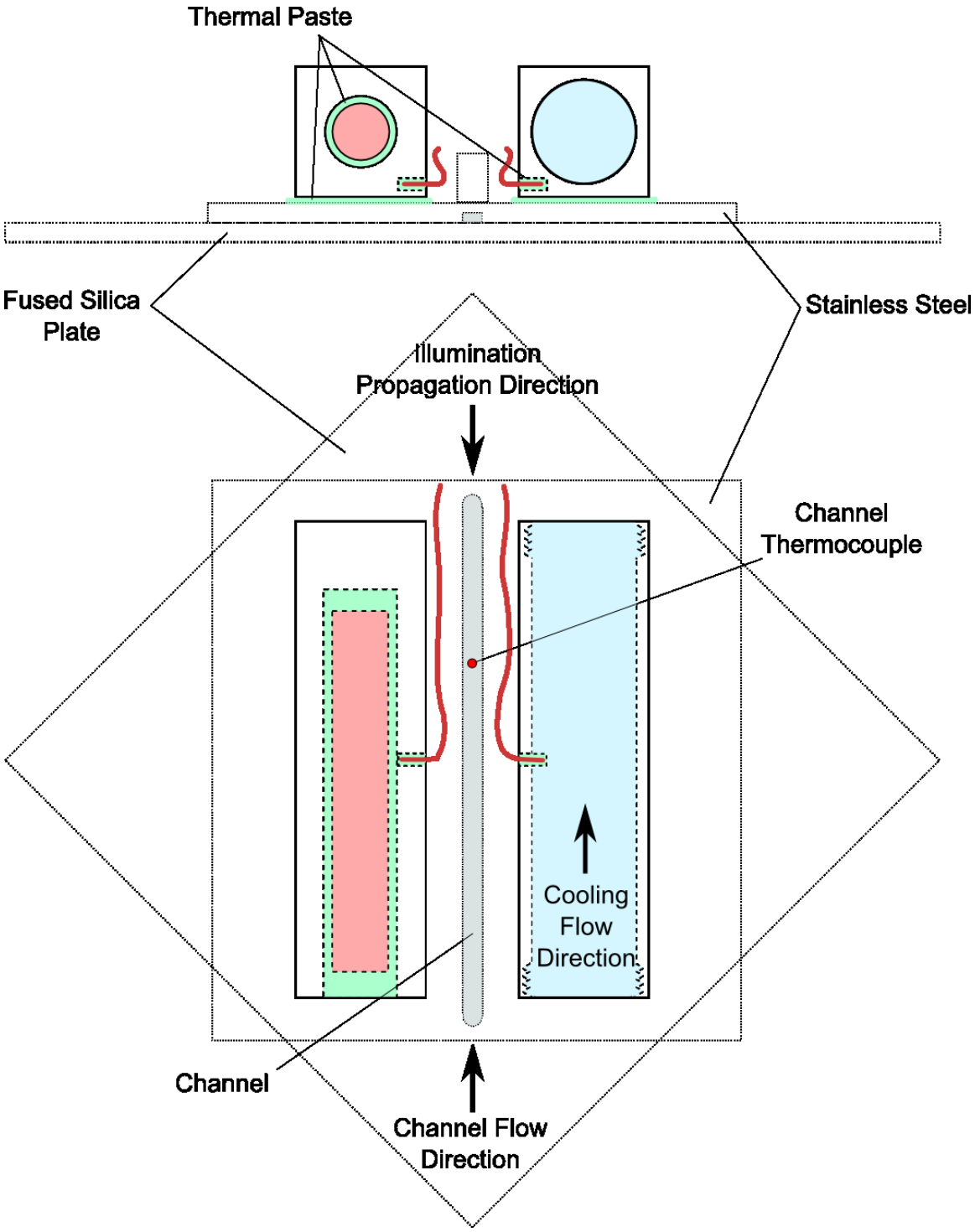

Figure C.3: Placement of temperature gradient device relative to microchannel (dotted lines).

C.1.4 Experimental Procedure

C.1.4.1 Cleaning

The cleaning methods described in section 2.4.4.1 were used to clean all optical components. The channel apparatus was soaked for between 2-15 hours in a solution of Contrad 70 (Decon Labs) chemical soap diluted to 10%v/v in deionized water. After soaking, the channel apparatus exterior was rinsed with deionized water and methanol and blown dry with ultra-high purity nitrogen gas.

The channel interior was flushed at least twice with deionized water that was removed via suction generated by a venturi pump. Fluorophore solution, prepared as described in section 2.3, was used to flush the channel interior, syringe and inlet and outlet tubing. For these experiments, un-buffered 10 μM fluorescein solution in de-ionized water was used. It is anticipated that using fluorescein buffered to a pH of 9.2 would produce better results by reducing adsorption, but these experiments were not undertaken. The fluorophore flow path was flushed at least 4 times with fluorophore solution to clear any small amounts of deionized water that may have remained inside the channel interior.

C.1.4.2 Alignment

The cleaned channel apparatus was placed upon the microscope stage, and the stage translated so that the laser beam grazed the upper surface of the channel apparatus. The channel apparatus was then rotated so that the channel was aligned with the laser beam. The channel was fixed in place with label tape (Fisher Sci, 15-939) and the stage translated so the objective was centered with the channel.

The entrance and exit prisms were optically coupled to the fused silica substrate with fused-silica matching immersion liquid at the ends of the channel. Mirrors in the optical system were slightly adjusted to generate a totally internally reflected beam propagating through the fused silica. The mirrors were further adjusted to center a

beam reflection, and therefore generate an evanescent wave, at a location between 500-1500 μm downstream/upbeam of the channel thermocouple.

The temperature gradient device was placed on top of the channel apparatus with thermal paste (Omega, Omegatherm 201) used to thermally couple the two surfaces. The temperature gradient device was approximately centered on the channel apparatus so the channel was equally spaced between the hot and cold block. A small weight was placed on top of the temperature gradient device to improve the thermal contact between the hot and cold block and the top of the channel apparatus.

C.1.4.3 Experimental Run

The syringe, tubing, and channel were filled with fluorophore solution and the syringe pump set to deliver fluid at a rate of either 1 or 2 mL/hr. The temperature of the hot and cold blocks could be controlled by varying the power supplied to the cartridge heater and adjusting the set temperature of the recirculating constant temperature bath.

A dark and normalizing image sequence were taken with the temperature of the hot block, cold block and solution in the channel all were approximately equal. The normalizing temperature differed between experimental runs: in early experiments room temperature (varied between 20-30 ℃) was used, while in later experiments the cartridge heater power and recirculating constant temperature bath were adjusted to a normalizing temperature 30 ℃.

For non-normalizing data points, the temperature of the hot and cold block were varied to generate a temperature gradient across the channel width. The temperature of the blocks and inside the channel were monitored to determine when the system approached thermal steady-state. At near steady-state an image sequence was acquired and the reference laser power and thermocouple readings were recorded.

At each data point, the laser was un-shuttered and image sequences of 100 images

were captured. The camera was configured to 'low light' settings (exposure time $\Delta t = 50$ ms and multiplication gain $G_C = 3220$). Simultaneously, the voltage of the channel thermocouple and the software-compensated temperature measured by the hot and cold block thermocouples were sampled by the HP 34970A/34901A data acquisition system at a rate of 1.46 Hz. The time to capture a sequence of 100 images was approximately 12 seconds, the laser was un-shuttered for approximately 20 seconds and the thermocouples were sampled over a period of approximately 30 seconds.

C.2 Model of Channel with Temperature Gradient

A 3-dimensional FLUENT model of the thermal and mass transport through the channel experimental apparatus was developed. The structures included in the model (figure C.4) were the stainless steel channel apparatus, fused silica substrate, the bottom 2 mm of both temperature blocks and part of the microscope stage. The fluorophore solution was modeled as liquid water flowing through the channel apparatus at rates of $Q = 1 - 2$ mL/hr.

C.2.1 Simulation Results

For all simulations hydrodynamically and thermally fully-developed flow was achieved by the mid-length of the channel $\ell_c/2$. Velocity and temperature fields at the plane of the thermocouple, defined as $\ell_{TC} = 2\ell_c/3$, were examined. Velocity fields demonstrated parabolic behavior that was qualitatively consistent with flow through a rectangular duct.

The temperature of the fluid showed very little variation with height (i.e. $dT/dz \rightarrow 0$). The temperature of the near-wall region only showed notable deviation from bulk fluid temperature at the lower corners of the channel. Figure C.5 shows filled contours of temperature and a plot of temperature variation across the channel at the plane

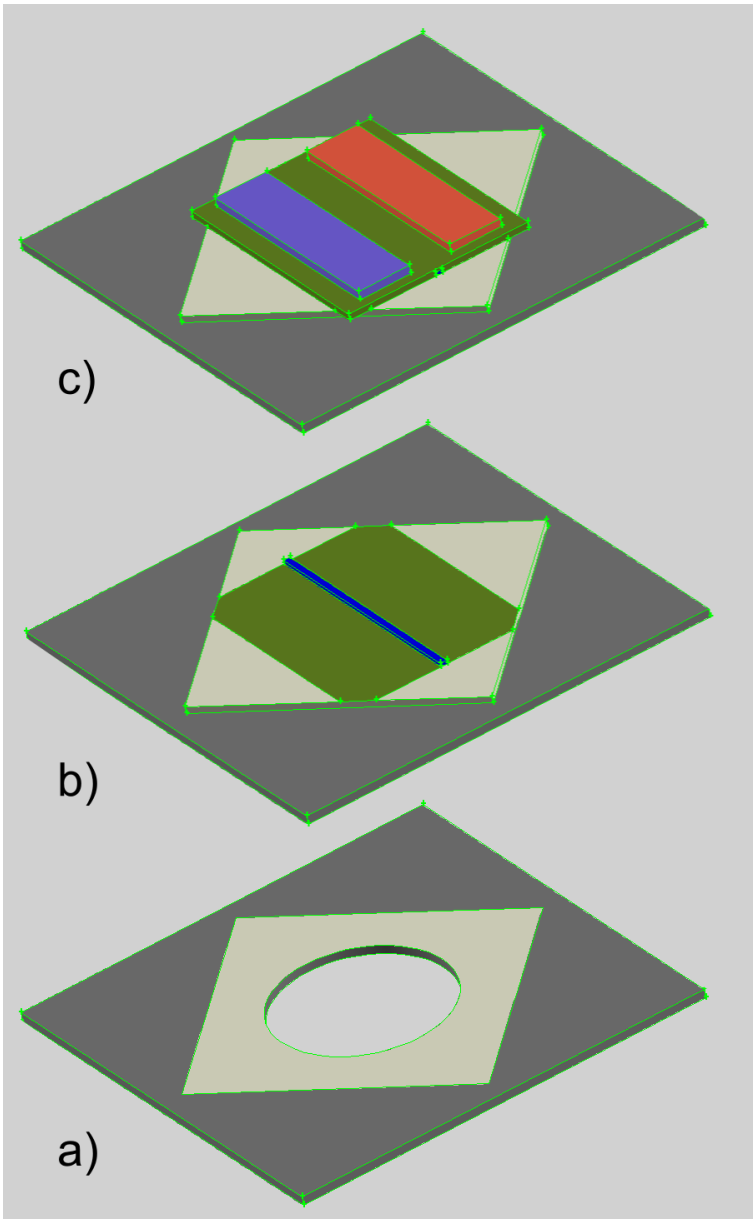

Figure C.4: Illustration of structures modeled in FLUENT: (a) microscope stage (black) with footprint of fused silica substrate (light gray); (b) fused silica substrate (light gray), water flowing through channel (blue), and footprint of stainless steel structure (green); (c) all structures shown including stainless steel structure (green), hot block (red) and cold block (blue).

of the thermocouple.

The temperature gradient in the channel predicted by FLUENT simulations was compared to simple estimates based upon experimental variables T_H and T_L, which are the temperatures of the hot and cold blocks, respectively. The temperature gradient was estimated by the 'external' temperature gradient $\Delta T/\Delta r$, defined as:

$$\Delta T/\Delta r = \frac{T_H - T_L}{10\text{mm}} \tag{C.3}$$

These estimates are based upon what the temperature gradient would be if the temperature gradient device were to create a temperature gradient through a single thermally isotropic medium. The relationship between the temperature gradient predicted by FLUENT simulations and the external temperature gradient was well-approximated by a linear model, as shown in Figure C.6.

According to FLUENT predictions, the temperature gradient in the channel will be approximately 150% of the 'external' applied temperature gradient. This increase in temperature gradient inside the channel is due to the lower thermal conductivity of water compared to stainless steel ($k_{H_2O} \approx 0.6\text{W/m·K}$, $k_{SS} \approx 15\text{W/m·K}$). Fourier's law of conduction indicates:

$$q = k\frac{dT}{dx} \Rightarrow \frac{dT}{dx} = \frac{q}{k} \tag{C.4}$$

here q is the heat flux. The primary form of heat transfer between the hot and cold blocks will occur horizontally through the stainless steel apparatus. The heat being transfered through the stainless steel adjacent to the channel will remain nearly constant as the heat enters the water. As q is approximately constant, the lower thermal conductivity of the water, implies that the temperature gradient will increase. Importantly, the linear relationship between predicted temperature gradient and 'external' temperature gradient is independent of flow rate and the magnitude of T_H and T_L for the range of values studied.

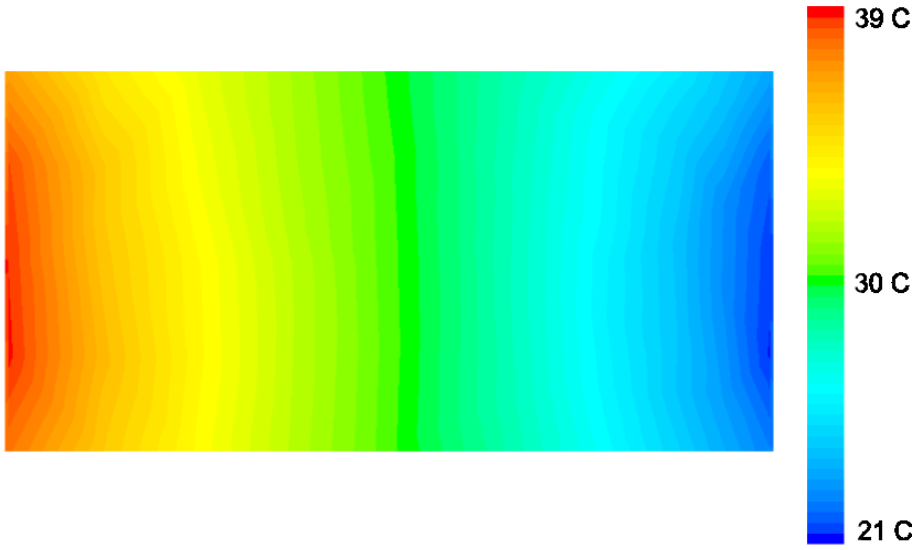

(a)

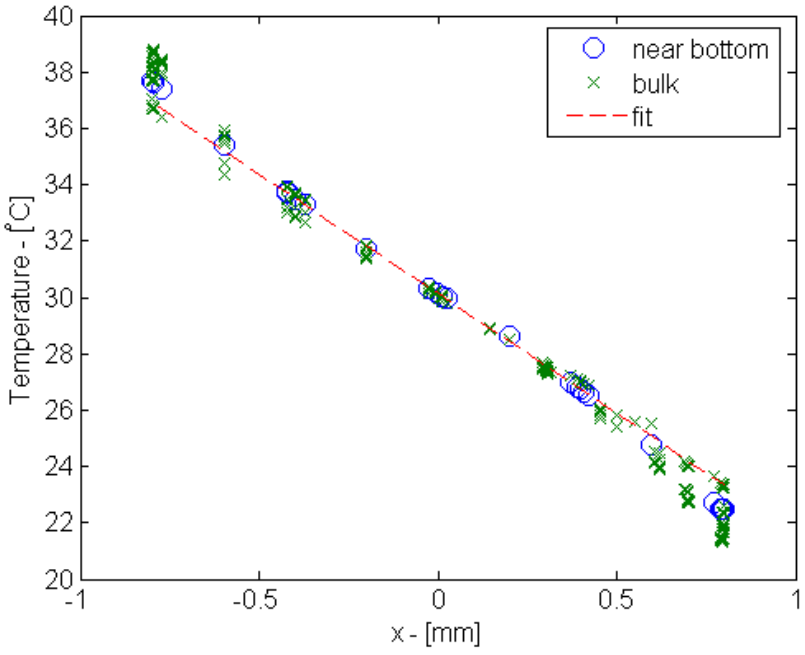

(b)

Figure C.5: Temperature field for simulation with Q = 1mL/hr, T_H =58℃ and T_L = 2℃: (a) temperature contours across channel at plane of thermocouple; (b) plot of variation in temperature with respect to location.

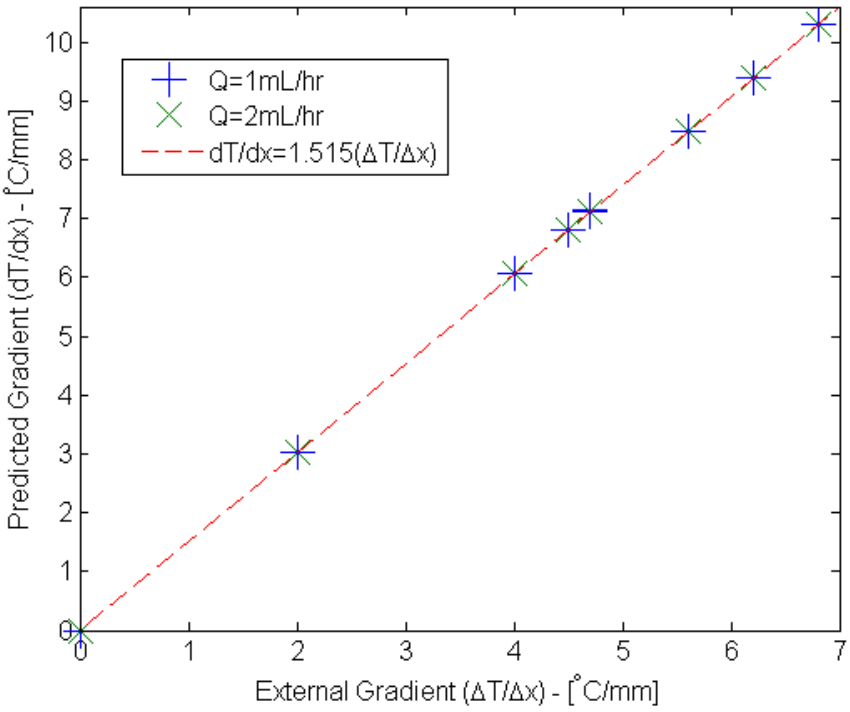

Figure C.6: Linear relationship between temperature gradient predicted by FLUENT and the external temperature gradient.

C.3 Temperature Gradient Results

A total of thirty-one image sequences were acquired across seven experimental runs to generate twenty-two channel temperature gradient measurements. In many instances, two normalizing image sequences were taken for a single experimental series. For each data point in those experimental series with two normalizing image sequences, the normalizing image sequence that demonstrated greater similarity to the data point was utilized. In this section, several images are presented that are representative of typical results. In addition, the twenty-two channel temperature gradient and mid-width temperature measurements will be compared to expected values.

C.3.1 Representative Results

Figure C.7 shows corrected and normalized images for the normalizing data point and for two data points with applied temperature gradients. The normalizing image sequence was taken with the 'hot' and 'cold' blocks at room temperature with a channel temperature of 24.9 ℃, as measured by the channel thermocouple. The hot and cold block temperatures and other experimental parameters for these three image sequences are summarized in table C.2.

To generate a quantitative estimate of the channel temperature gradient, it was necessary to estimate the direction of the channel centerline relative to the pixel axes and transform temperature estimates from a pixel-relative coordinate system $(x - y)$ to a channel-relative coordinate system $(r - s)$. Once temperature estimates are transformed into a the $(r - s)$ coordinate system, the temperature gradient can be estimated by fitting the relationship between T and r to a first-order polynomial.

$$T(r) = p_1 \cdot r + p_2 \tag{C.5}$$

where T is the measured temperature, r is the distance from the channel centerline and p_1 and p_2 are fit parameters. The channel temperature gradient can be estimated

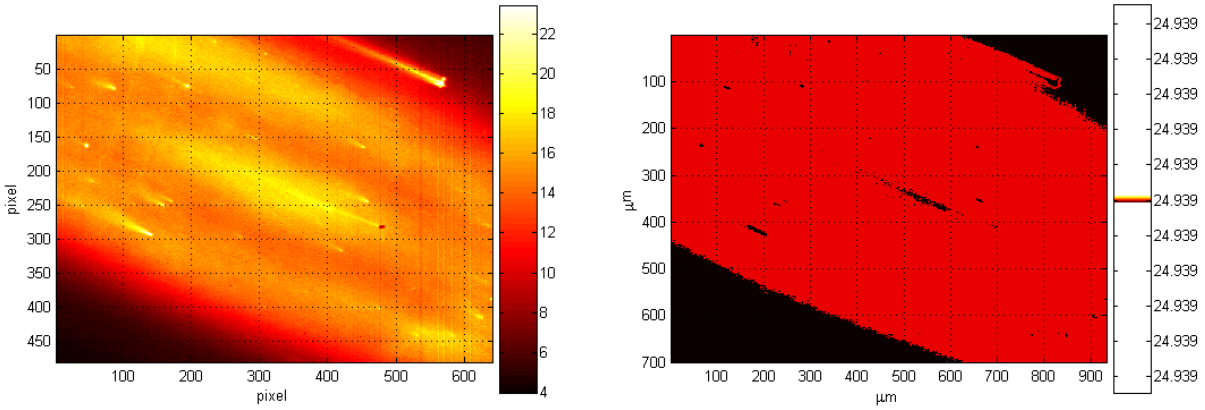

(a) $T_H \approx T_L \approx 25$**°C**

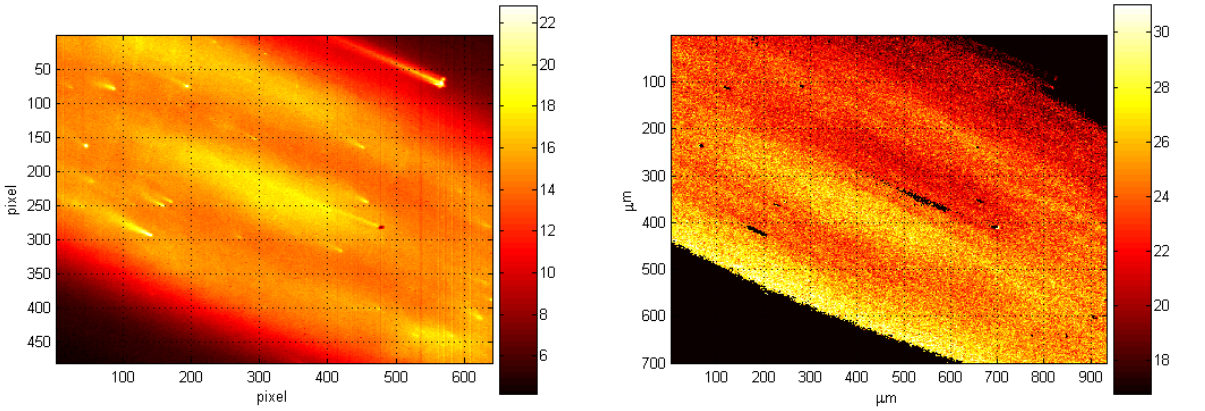

(b) $T_H \approx 50$**°C**, $T_L \approx 3$**°C**

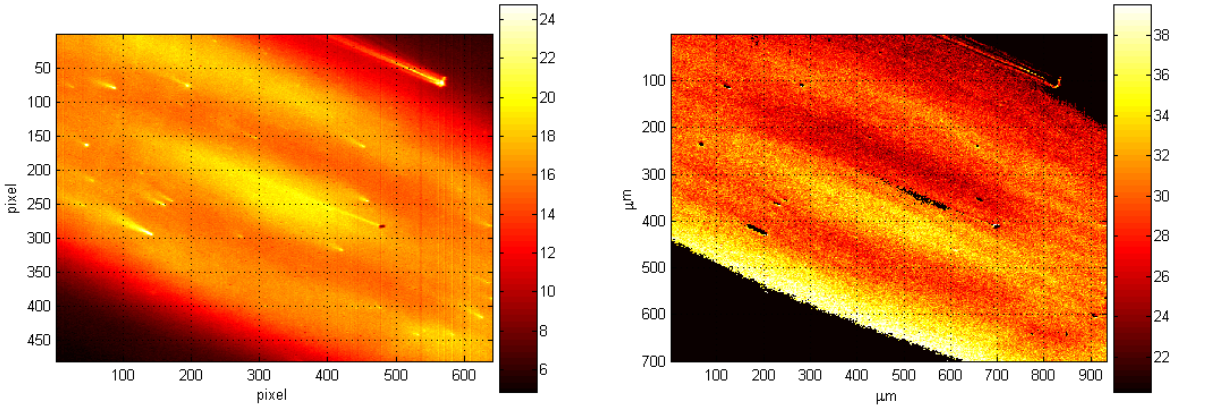

(c) $T_H \approx 65$**°C**, $T_L \approx 3$**°C**

Figure C.7: Corrected grayscale (left column) and normalized (right column) representative images. Experimental parameters for three image pairs are given in table C.2 Corrected images are false colored according to corrected grayscale value (scale:0-100), while normalized images are false colored according to temperature ([°C]).

Table C.2: Experimental parameters of experimental results shown in Figures C.7 and C.8. All temperatures are in units of [℃] and temperature gradients are in units of [℃/mm]. T_{TC} is the channel thermocouple measurment, and (dT/dr) is the channel temperature gradient predicted by FLUENT model.

Fig.	T_H	T_L	T_{TC}	$T_{1/2}$	$\frac{\Delta T}{\Delta r}$	$\left(\frac{dT}{dr}\right)$	p_1	p_2
C.7(a)	24.5	24.5	24.9	24.5	0.0	0.0	0.0	24.9
C.7(b)	49.4	2.9	28.9	26.1	4.6	7.1	7.7	24.4
C.7(c)	65.7	3.4	37.9	34.6	6.2	9.47	10.1	30.5

by the parameter p_1 and the mid-width channel temperature $T_{1/2}$ can be estimated by the parameter p_2:

$$p_1 \approx \frac{dT}{dr} \qquad \text{and} \qquad p_2 \approx T_{1/2} \tag{C.6}$$

The original normalized image, rotated normalized image, and temperature profile are shown in Figure C.8 for the image sequence with $T_H \approx 65$℃ and $T_L \approx 3$℃ (i.e. Figure C.7c).

The sinusoidal oscillation in Figure C.8c about the linear fit is typical of temperature gradient estimations found in this investigation. This oscillation can be seen in the images Figure C.8b-c as a bright and dark region pair. The pairs of bright and dark regions are artifacts that can be attributed to movement of the evanescent-wave illumination that spatially bias the normalized image.

C.3.2 Comparison to Predictions

For each data point, the magnitude of the channel temperature gradient and the mid-width channel temperature were estimated using the TIR-FMT technique. The temperature gradient estimates were compared to predictions from FLUENT simulations and the mid-width channel temperature was compared to the temperature inside the channel as directly measured by the channel thermocouple, T_{TC}.

The estimated channel temperature gradients using TIR-FMT are plotted against external temperature gradient in Figure C.9. The predicted relationship between

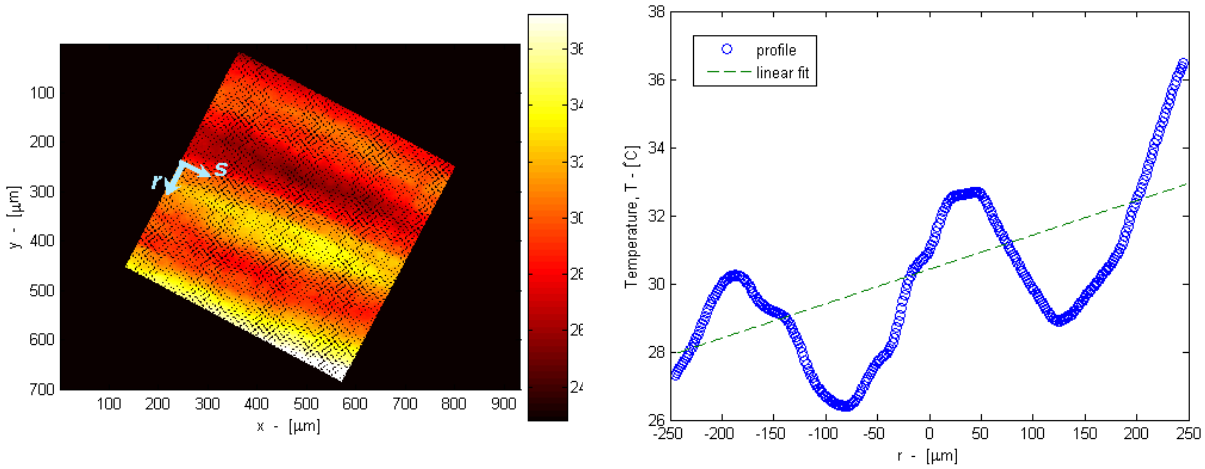

(a) (c)

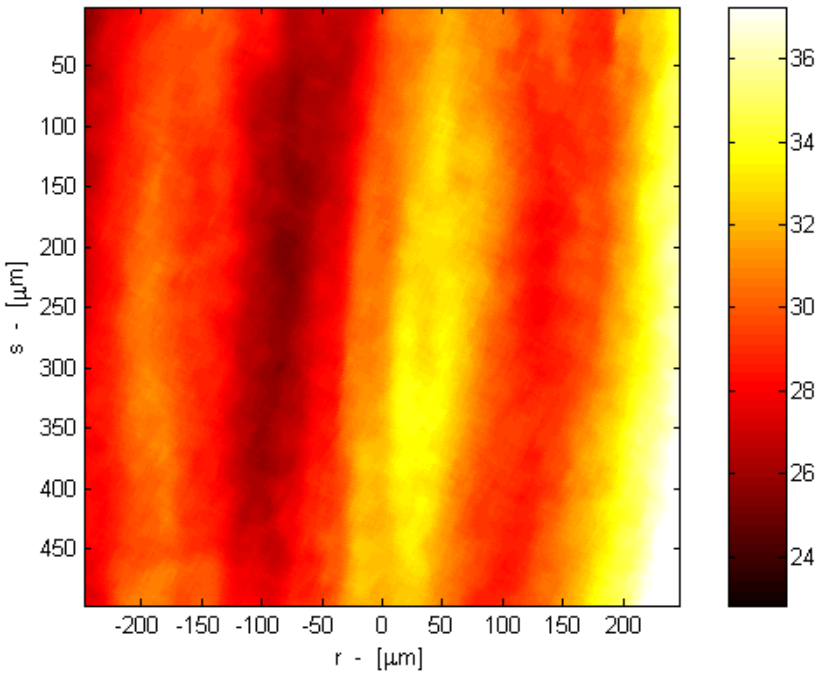

(b)

Figure C.8: Representative images of temperature profile generation: (a) temperature estimates in $x - y$ coordinate system after median pass filter; (b) temperature estimates in $r - s$ coordinate system; (c) average temperature profile with fit. Images are false colored by temperature ([℃]).

external temperature gradient and channel temperature gradient is also shown. There is a relatively weak correlation between temperature gradient values as predicted by FLUENT and those estimated using TIR-FMT. There is considerable scatter in gradient estimates, for instance for an external temperature gradient of approximately 4.5 ℃/mm, TIR-FMT estimates range from 0.67-7.67 ℃/mm—an order of magnitude difference.

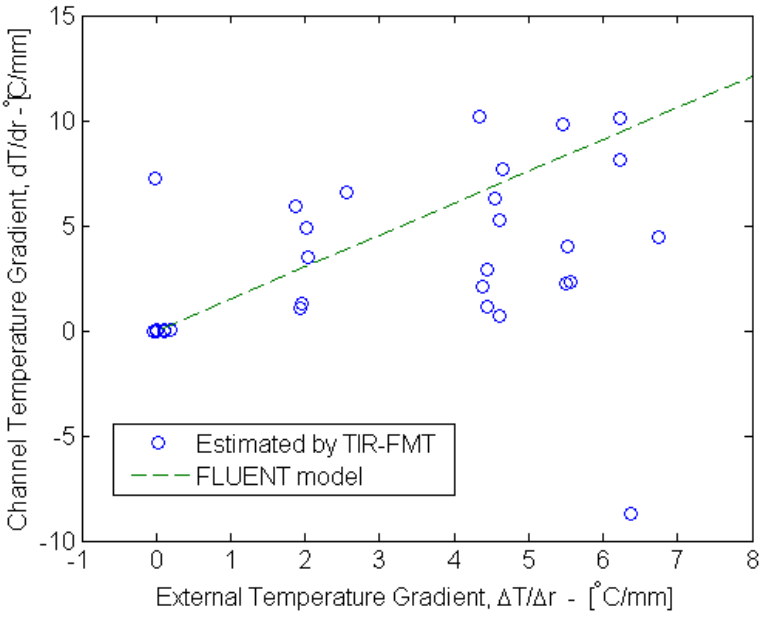

Figure C.9: Estimated channel temperature gradients from TIR-FMT measurements plotted against external temperature gradient.

The mid-width channel temperatures estimated by TIR-FMT and measured by the channel thermocouple are plotted against average block temperature in Figure C.10. Once again, there is a weak correlation between TIR-FMT estimates and the mid-width channel temperature measured by the channel thermocouple. The r.m.s. difference between thermocouple and TIR-FMT measurements of the mid-width channel temperature is 8.8℃.

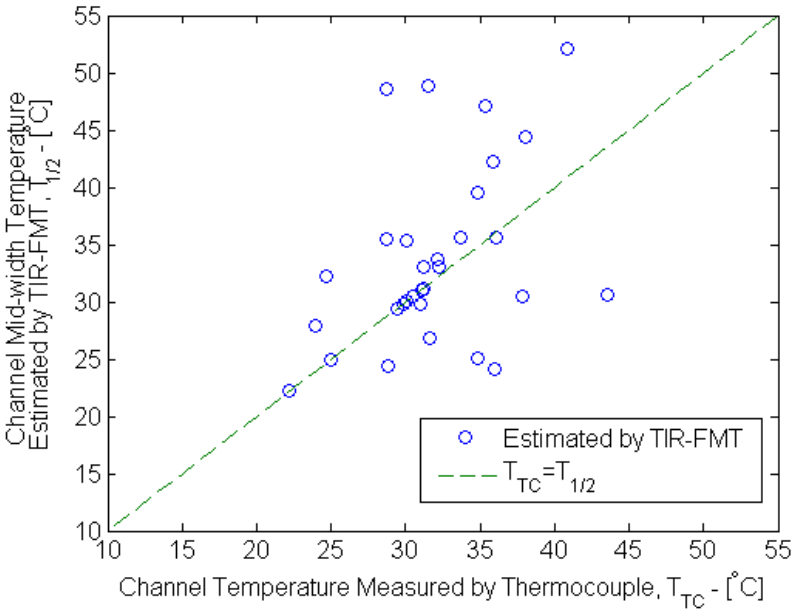

Figure C.10: Mid-width channel temperature estimated from TIR-FMT and measured by channel thermocouple plotted against average block temperature.

C.3.3 Normalization Error

The greatest source of error was due to the sensitivity of the normalization to variations in the fluorescence intensity. These variations in fluorescence intensity can be better understood by considering equation I.22

$$\mathscr{F} = \alpha I_0 \Phi \varepsilon \ell c \tag{I.22}$$

This equation indicates that fluorescence intensity will vary with changes in illumination I_0, concentration c, and path length through the solution ℓ. The fluorescence intensity will also change with variations in temperature due to the temperature dependence of quantum yield Φ and extinction coefficient ε. The path length through the solution does not change significantly. Therefore, variations in fluorescence intensity are due to variations in illumination, concentration and temperature.

The TIR-FMT technique presented here corrects for spatial variations in illumination and concentration by normalizing the measured fluorescence intensity by the fluorescence intensity measured with a uniform, known temperature field. The

technique relies upon the assumption that the illumination and concentration do not vary with time. However, experimental observations show that that the illumination and/or concentration vary with time.

The error associated with variations in illumination and concentration can be estimated from four cases where, for a single experimental series, two normalizing image sequences were taken under similar experimental conditions—one at the beginning and one at the end of the experimental series. For each normalizing image pair, the temperature was maintained at approximately the same temperature and the external temperature gradient was negligible. Therefore, variations between the normalizing image pairs was primarily due to variations in illumination and concentration. These errors, were considerable: between between 3 and 49 ℃/mm for channel temperature gradient measurements and between 2 and 15 ℃ for channel mid-width temperature measurements.

An example of a normalizing image pair is shown in Figure C.11. Although both image sequences were taken under similar experimental conditions with no temperature gradient, the fluorescence intensity is clearly different. Of further interest, the location of the primary illumination peak does not significantly change between the two normalizing image pairs. This implies that the variation in fluorescence intensity is not due to slight variations in the alignment of optical components. For this pair of normalizing images, the TIR-FMT estimates that the two images were taken at temperatures separated by approximately 14℃ and in the presence of a temperature gradient of approximately 40℃/mm. The pair of images were acquired at the same temperature with no temperature gradient, suggesting measurement errors of 14℃ and 40℃/mm.

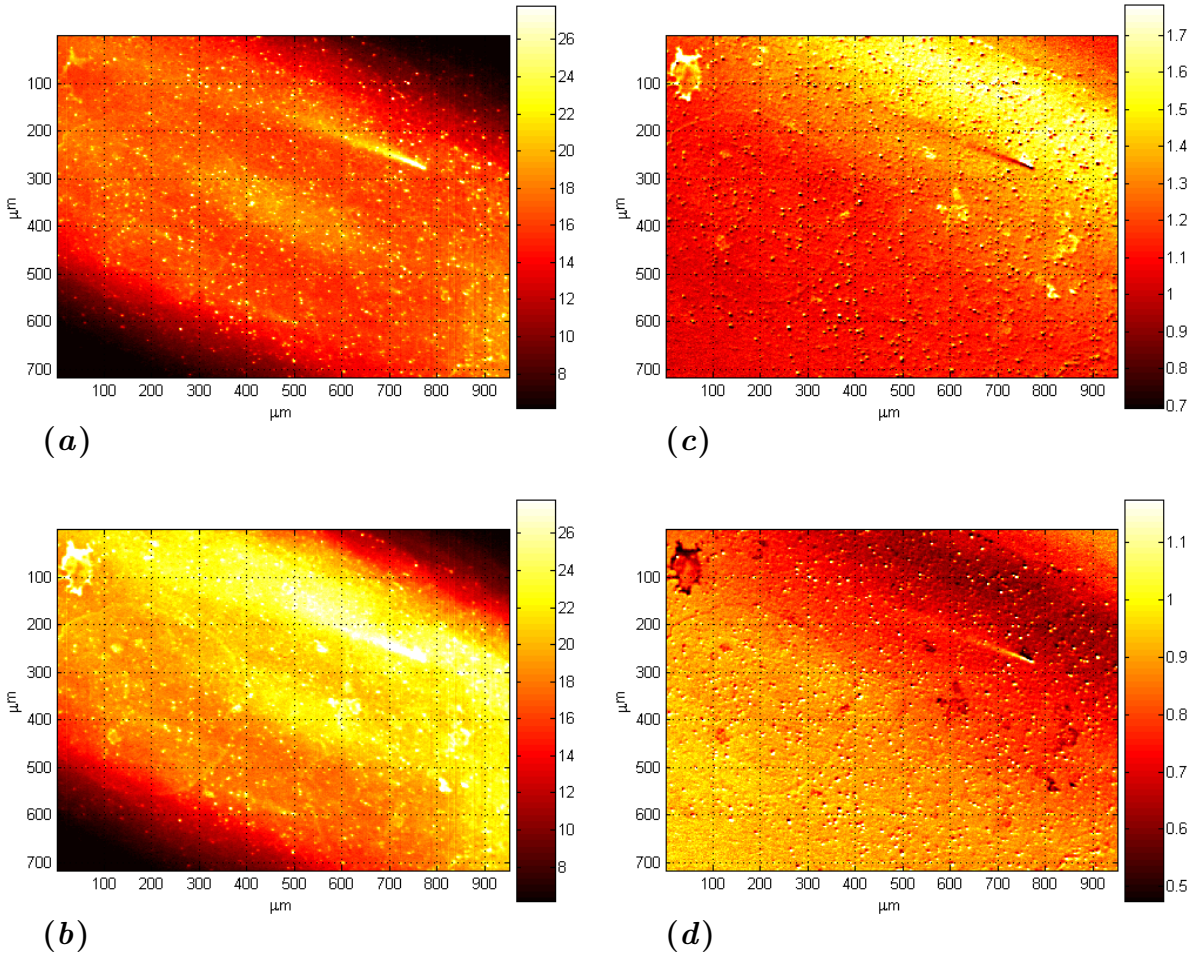

Figure C.11: Example of variations in fluorescence intensity for different normalizing image sequences in same experimental series. Corrected image are shown in left column: (a) first image sequence $\mathscr{C}$ and (b) last image sequence $\mathscr{C}'$ of experimental series. Normalized images are shown in right column: (c) $\mathscr{N} = \mathscr{C}'/\mathscr{C}$ and (d) $\mathscr{N} = \mathscr{C}/\mathscr{C}'$

C.4 Temperature Gradient Discussion

The uncertainty of channel temperature gradient and channel mid-width temperature measurements are significant and seriously limit the utility of the TIR-FMT technique. The uncertainty was likely caused by a combination of the following:

1. Variations in Illumination
2. Variations in Fluorophore Concentration
3. Experimental Design

The first two sources of experimental error are directly related to the TIR-FMT technique and will strongly influence fluorescence intensity measurements. Temperature and temperature gradient estimates are particularly sensitive to these fluctuations due to normalization during image processing. Reducing the variations in illumination and fluorophore concentration would greatly improve accuracy. The final source of experimental error is indirectly related to TIR-FMT. Therefore, any improvements in experimental design will only yield incremental improvements in accuracy.

Unfortunately, it is not possible to quantitatively decouple the influence of each of these four components. It is however, worthwhile to qualitatively discuss the relative contributions of these components to experimental scatter. In this section, these four sources of experimental fluctuations are discussed with particular emphasis on addressing two questions: 1) how could these sources contribute to experimental scatter? and 2) would this contribution to experimental scatter during temperature gradient experiments be considerably greater than that during calibration experiments?

C.4.1 Illumination

One of the key assumptions made in developing the theoretical basis of the TIR-FMT technique was that illumination remained temporally invariant across an experimental run. However, variations in illuminations were observed during experiments. These

variations in illumination contributed to the uncertainty of the normalized image. Furthermore, because of the low sensitivity of fluorescein to temperature (dF/dT) and the Gaussian distribution of the illumination,the TIR-FMT technique is particularly sensitive to temporal variations in illumination. The variations in illumination can be classified into two categories: thermal gradient lensing, and random variations.

C.4.1.1 Evanescent-Wave Illumination Movement: Thermal Gradient Lensing

During calibration experiments shifting of the evanescent-wave illumination was observed, which was attributed to the changes in the index of refraction of the fused silica prism as the temperature of the prism changed, resulting in a time-varying angle of refraction. During calibration, shifts in the illumination were typically in the direction of beam propagation. Such illumination shifts were also observed in the experiments conducted to measure the temperature gradient in the channel, however illumination shifts were also observed in the direction perpendicular to beam propagation.

Due to the spatially-varying profile of the evanescent-wave illumination these shifts resulted in a false temperature gradient. As an example, normalizing a Gaussian profile by the same profile that has been shifted by only 2% of the e^{-2} beam radius results in a temperature difference of 10 ℃ across the beam diameter (Figure C.12). In this investigation, the beam radius has been esimated to be $a = 300\mu$m, suggesting a shift of 6 μm produces a false gradient of 18℃/mm.

During calibration experiments the optical path through the fused silica would change slightly due to changes in the index of refraction at the beam entrance. During temperature gradient measurements, a strong temperature gradient also existed inside the fused silica substrate, resulting in thermal lensing and a displacement in evanescent-wave illumination toward the region of higher temperature. The representative images in Figure C.7 demonstrate this type of displacement.

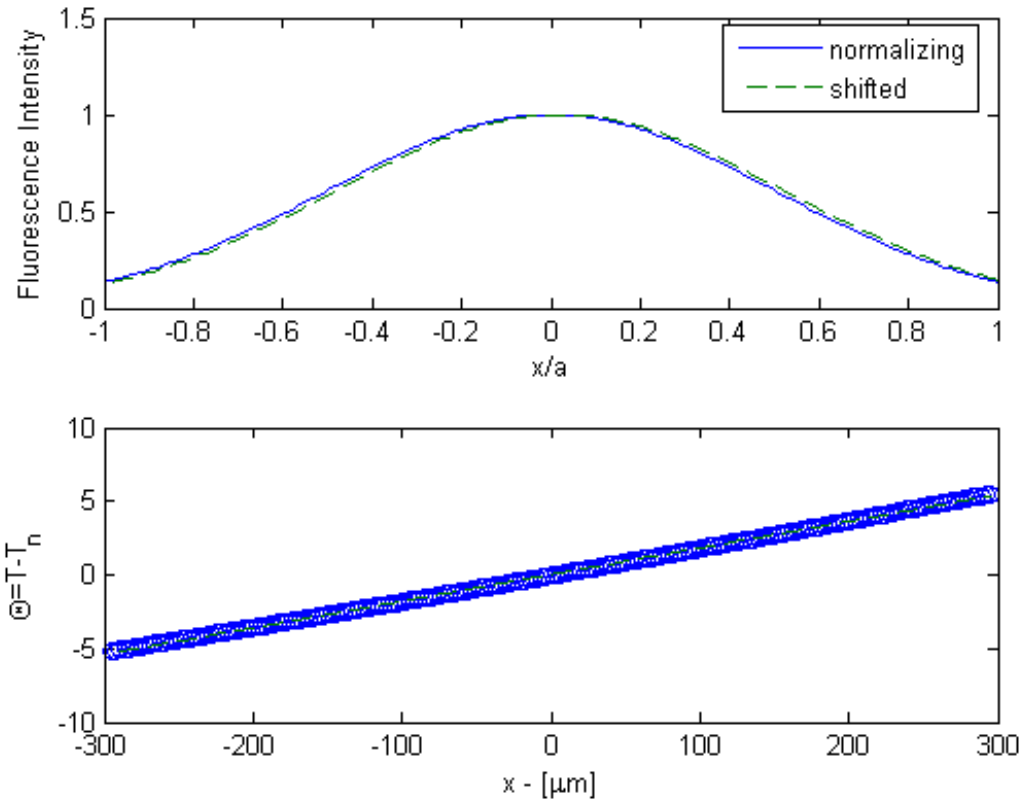

Figure C.12: Simulation of false temperature gradient generated by displacement of a Gaussian profile. Above: normalizing intensity and normalizing intensity shifted by $0.02a = 6\mu$m; below: false temperature gradient.

As the index of refraction of fused silica changes with temperature, an index of refraction gradient also develops:

$$\frac{dn}{d\vec{x}} = \frac{dn}{dT} \cdot \frac{dT}{d\vec{x}} \tag{C.7}$$

where n is the index of refraction of fused silica. This refractive gradient can act as a thermal lens and cause light propagating through the fused silica to curve toward the region of higher temperature. For light propagating perpendicular to the thermal and refractive gradients, the radius of curvature R_c of the light is described by [57]:

$$R_c = n\frac{1}{\left(\frac{dn}{dr}\right)} = n\frac{dr}{dn} \tag{C.8}$$

In the range of 0-100℃, fused silica has a constant $dn/dT = 12.5 \times 10^{-6}$, which for a temperature gradient of $dT/dr = 5$℃/mm would result in a radius of curvature of $R = 23.4$m. The optical path length through the fused silica substrate to the measurement region is approximately 23.4 mm. From trigonometry, the displacement of the beam under a 5℃/mm can be calculated to be $\Delta r = 11.7\mu$m. This shift is in the cross-channel direction toward the hot block. For a wide-range of temperature gradients, the beam shift follows a linear relationship with temperature gradient: $\Delta r/(dT/dr) = 2.34\mu$m·mm/℃.

The false gradient generated by displacement of the evanescent-wave illumination can be simulated using actual normalization images. The corrected images are shifted one pixel at a time in the cross-channel direction. Simulations on five normalizing image sequences (Figure C.13) show a near-linear relationship between displacement and false temperature gradient. The slope differs slightly for each normalizing image sequence due to the specifics of the illumination, ranging from .20 to .35℃/[μm·mm]. Combining the relationship for false temperature gradient and displacement with the relationship for displacement versus real temperature gradient, gives a relationship between the false and real temperature gradients. The false temperature gradient

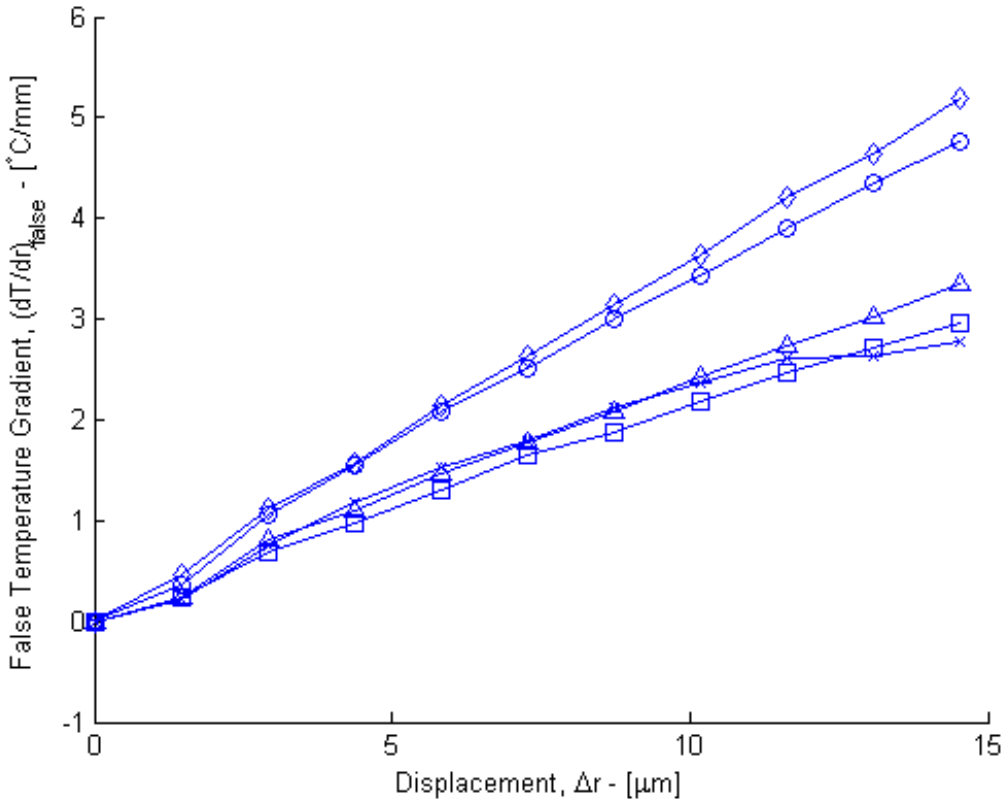

Figure C.13: Estimated false temperature gradient generated by real temperature gradient due to displacement of evanescent-wave illumination. Estimations are based upon five different normalizing images.

will act in the same direction as the real temperature gradient, and if acting independent of other sources of error would result in an over-estimation of the true channel temperature gradient by 40-70%.

C.4.1.2 Evanescent-Wave Illumination Movement: Secondary Effect of Illumination Movement

A secondary effect of the movement of the evanescent-wave illumination was can be attributed to slight changes in the optical path of the TIR laser beam propagating through the fused silica substrate. Although the fused silica is optical grade, imperfections such as bubbles, inclusions, and striae still exist. As the optical path changes slightly, the imperfections encountered and the scattering from these imperfections

will change as well.

These variations were present in calibration experiments (section 3.2.2.2), but the detrimental effect on measurements was considerably stronger in temperature gradient experiments. The increase in these variations in illumination in temperature gradient experiments can be attributed to two causes: 1) increased movement of the optical path of the TIR laser beam due to thermal gradient lensing; and 2) propagation of refracted and scattered light in the channel.

The three-dimensional temperature gradients in the fused silica substrate result in increased movement of the optical path of the propagating TIR laser beam through the fused silica. This increases the probability that refraction or scattering by imperfections along the optical path will occur.

If an imperfection is encountered by the propagating beam, the refracted and scattered light can also propagate more readily in the channel by reflecting off the channels side walls. During calibration experiments, scattered light would enter the bulk of the solution and be absorbed and emit fluorescence from a distance far away from the interrogation region. Therefore, during calibration experiments, background illumination was spatially uniform. However, light scattered in the channel was partially absorbed and partially reflected by the channel walls. Although much of the scattered light was absorbed, the light that was reflected was localized and would induce a spatial bias in the normalize fluorescence intensity.

An example of an image sequence where the fluorescence intensity was strongly biased by random fluctuations in illumination is shown in Figure C.14. Figure C.14(a) shows the corrected image taken with an 'external' temperature gradient of 4.3℃/mm and a predicted channel gradient of 6.6℃. The normalized image (Figure C.14(c)) corresponds to a cross-channel temperature gradient of 7.7℃/mm, slightly above expected values. However, the streamwise temperature gradient measured was 5.8℃/mm compared to a theoretical gradient of 0℃/mm.

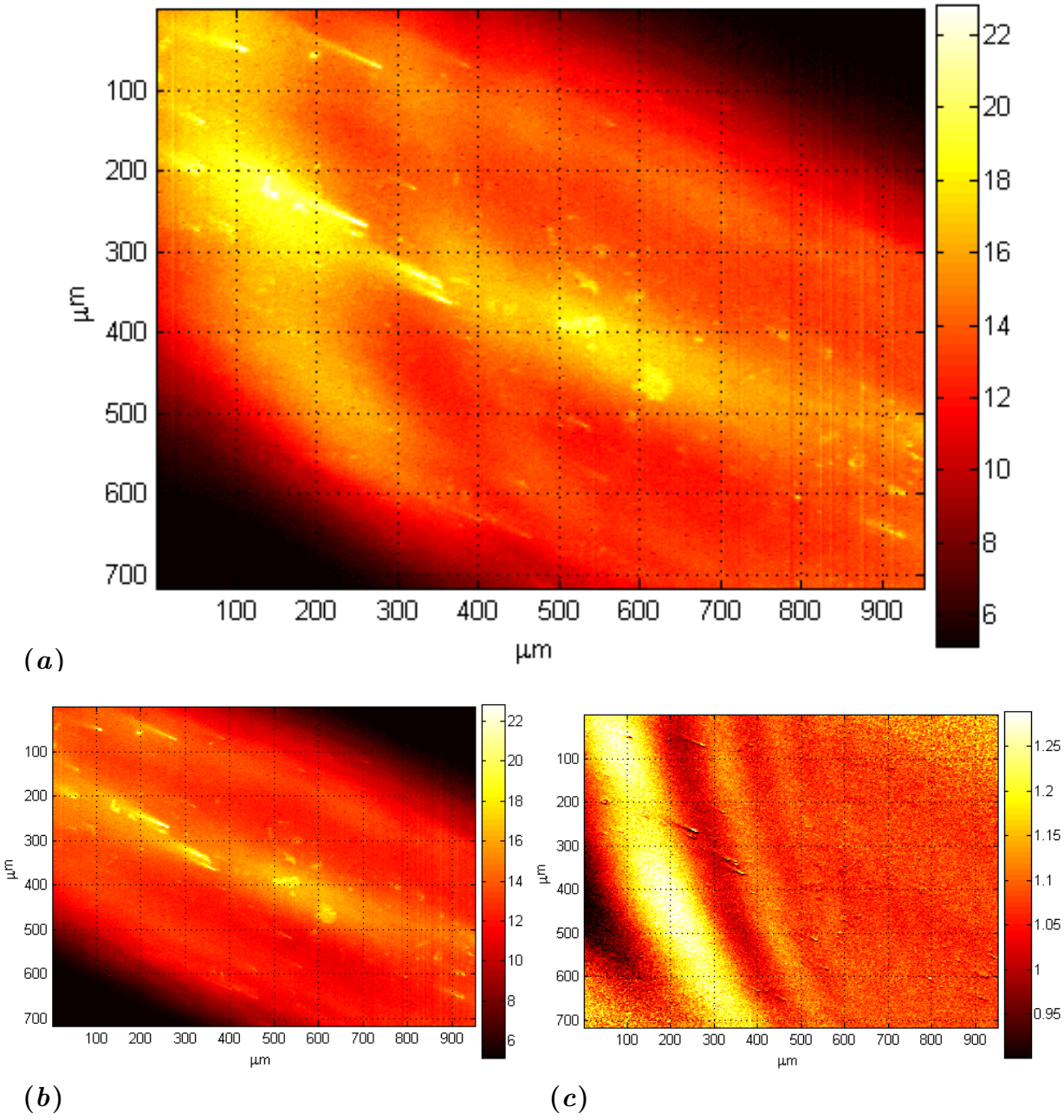

Figure C.14: Images with random variations in fluorescent intensity caused by random fluctuation in illuminating intensity. (a) Averaged and corrected image ($\mathscr{C}^{\phi}$) with abnormal fluorescent intensity; (b) Averaged and corrected normalizing ($\mathscr{C}^{n}$) image used for image (a); (c) normalized image of $\mathscr{C}^{\phi}$ by $\mathscr{C}^{n}$: $\mathscr{N}^{\phi} = \mathscr{C}^{\phi}/\mathscr{C}^{n}$.

C.4.2 Fluorophore Concentration

Another key assumptions made in developing the theoretical basis of the TIR-FMT technique was that fluorophore concentration remained constant with respect to time. In theory, spatial variation in fluorophore concentration would be corrected for by normalization. However in reality, spatial variations in fluorophore concentration would likely result in temporal variations in concentration.

Variations in fluorophore concentration could be caused by: 1) local adsorption of fluorophore at the fused silica-solution interface; and 2) contamination of the fluorophore solution.

C.4.2.1 Adsorption

For these temperature gradient experiments, un-buffered fluorescein solution was used. Fluorescein has been shown to adsorb to fused silica unless buffered to a pH above 9. As such, adsorption did occur and could have varied spatially due to local temperature.

C.4.2.2 Contamination

Contamination of the solution could have reduced the fluorophore concentration present in the interrogation region during some image sequences. Such contamination would affect the bulk solution concentration and would therefore affect fluorescence intensity in a spatially uniform manner. As the concentration varies between data points, the fluorescence intensity, temperature measurement and temperature gradient measurement will also vary linearly. For instance, a 15% reduction in fluorophore concentration would result in an approximate temperature decrese of 10℃ and a 15% reduction in the magnitude of the measured tempearture gradient.

Contamination could occur due to pockets of water left in the channel. Although efforts were made to remove all water from the channel before injecting fluorophore solution, it is likely that some pockets still remained. Due to the low flow rate

($Q = 2.8 \times 10^{-4}$ to 5.6×10^{-4} mL/sec), it is possible that water pockets were not cleared by flushing the channel with fluorescein. In particular, water pockets could persist in the thin gaps on either side of the channel between the fused silica and stainless steel.

Contamination could also occur due to sorption of fluorophore to exposed surfaces along the flow loop. Such exposed surfaces include the syringe interior, the interior of plastic tubing, the stainless steel channel apparatus, and the fused silica. As the fluorophore solution flows, if fluorophore is sorbed, then the bulk solution concentration is reduced.

Eventually, such sorption will reach steady state, and the bulk concentration will remain constant. The time necessary for sorption steady state to be reached will depend upon the solution flow rate, the distance along the flow loop, and the ratio of volume to surface area. The volume to surface area ratio in the channel is

$$\frac{V}{SA} = \frac{dwl_c}{2(w+d)l_c} = \frac{0.0629\text{cm}^3}{2.4\text{cm}^2} \approx \frac{1}{38}\text{cm} \tag{C.9}$$

The relatively low flow rate, low volume to surface ratio, and length of tubing and channel (≈ 100 cm) suggest that a much longer period of time is needed for sorption to reach steady state in the channel than in the calibration cell.

C.4.3 Experimental Design

Potential sources of error existed in the design of the experimental apparatus and procedure. These sources of error could have effected both the actual temperature gradient being measured inside the channel and the external temperature gradient being measured.

C.4.3.1 Orientation of Hot and Cold Blocks

The hot and cold aluminum blocks were placed in contact with the top of the stainless steel channel apparatus, and rotated such that the length of the blocks was parallel

to the channel length. Further, the hot and cold blocks were aligned with the channel such that the center of the channel was coincident with the middle of the hot and cold blocks. These alignments were performed visually and by hand and were subject to a considerable error conservatively estimated to be $\pm 10^\circ$ and ± 2 mm for angle and offset, respectively.

The temperature gradient induced in the channel should be influenced by the uncertainty of the angle, but should be independent of the offset. This error is the projection of the actual temperature gradient onto a line perpendicular to the channel, which can be estimated by $1 - \cos\beta_1$ where β_1 is the angle of misalignment. A misalignment of 10° will result in an error of only 1.6%.

The temperature in the middle of the channel was biased by the offset $\Delta r'$, but independent of angle. If the temperature gradient device were offset, then the temperature in the middle of the channel would be biased by approximately:

$$\Delta T_{1/2} = \frac{\Delta T}{\Delta r} \Delta r' \tag{C.10}$$

The external temperature gradients in this investigation were typically on the order of 5℃/mm; therefore, a 2 mm offset would result in an error of approximately 10℃.

Uncertainties in the alignment of the temperature gradient device could not greatly influence the channel temperature gradient, but could greatly influence the temperature in the middle of the channel. However, such variations in the temperature in the middle of the channel should be reflected in the temperature measured by the channel thermocouple.

C.4.3.2 Thermocouple Placement in Channel

The thermocouple inside the channel was placed such that the thermocouple sheath was in physical contact with the fused silica substrate. Ideally, the thermocouple could be placed such that it was perfectly centered in the channel; however, observation under the microscope showed that the thermocouple could be slightly offset

from the channel center by as much as $\pm 250\,\mu$m. In the presence of a 5℃/mm external temperature gradient, equivalent to a modeled channel temperature gradient of 7.6℃/mm, a $\pm 250\,\mu$m offset could result in a mid-width channel temperature bias of ±1.9℃.

C.4.3.3 Thermocouple Placement in Hot and Cold Blocks

The temperatures of the hot and cold blocks were used to determine the external temperature gradient, so any uncertainty in these temperature measurements could influence the accuracy of the modeled temperature gradient. The uncertainty of the these thermocouple measurements was estimated from manufacturer specifications to be approximately ±1℃.

An additional source of uncertainty comes from the thermal contact resistance between the aluminum blocks and the stainless steel apparatus. The thermal paste placed between the blocks and stainless steel apparatus has a thermal conductivity of 2.3 W/mK. To ensure good thermal contact without any 'dry' areas, a layer of the thermal paste between 0.5-2 mm thick was used. The quality of the thermal contact could effect the temperature gradient in the channel. When there is good thermal contact, heat is effectively transfered to the stainless steel apparatus so more heat is needed from the cartridge heater to raise the aluminum block to the desired set temperature. The enhanced heat transfer through the stainless steel channel results in a greater channel temperature gradient. When there is poor thermal contact, heat is poorly transfered to the stainless steel apparatus so less heat is needed to raise the aluminum block to the desired set temperature. Less heat is transfered through the stainless steel channel resulting in a lower channel temperature gradient.

It is believed that the thermal paste does a sufficient job of reducing the contact resistance between the aluminum block and stainless steel channel apparatus. However, the uncertainty associated with the thermal contact can be eliminated by placing

the thermocouples in the stainless steel channel apparatus instead of in the aluminum block. With this design, the thermocouple measurements will provide a better estimate of the external temperature gradient. The external temperature gradient will not be influenced by the thermal contact resistance or any offset in placement of the temperature gradient device.

REFERENCES

[1] Adams, T., Ghiaasiaan, S., and Abdel-Khalik, S., "Effect of dissolved noncondensables on hydrodynamics of microchannels subject to liquid forced convection," *Journal of Enhanced Heat Transfer*, vol. 6, no. 6, pp. 395 – 403, 1999.

[2] Adams, T., Ghiaasiaan, S., and Abdel-Khalik, S., "Enhancement of liquid forced convection heat transfer in microchannels due to the release of dissolved noncondensables," *International Journal of Heat and Mass Transfer*, vol. 42, no. 19, pp. 3563 – 3573, 1999.

[3] Allen, P. B., Rodriguez, I., Kuyper, C. L., Lorenz, R. M., Spicar-Mihalic, P., Kuo, J. S., and Chiu, D. T., "Selective electroless and electrolytic deposition of metal for applications in microfluidics: Fabrication of a microthermocouple," *Analytical Chemistry*, vol. 75, no. 7, pp. 1578 – 1583, 2003.

[4] Allison, S., Gillies, G., Rondinone, A., and Cates, M., "Nanoscale thermometry via the fluorescence of YAG:Ce phosphor particles: Measurements from 7 to 77 ℃," *Nanotechnology*, vol. 14, no. 8, pp. 859 – 863, 2003.

[5] Asheghi, M. and Yang, Y., "Micro- and nano-scale diagnostic techniques for thermometry and thermal imaging of microelectronic and data storage devices," in *Microscale Diagnostic Techniques* (Breuer, K. S., ed.), ch. 4, Springer, 2005.

[6] Atluri, V. P., Mahajan, R. V., Patel, P. R., Mallik, D., Tang, J., Wakharkar, V. S., Chrysler, G. M., Chiu, C.-P., Choksi, G. N., and Viswanath, R. S., "Critical aspects of high-performance microprocessor packaging," *MRS Bulletin*, vol. 28, no. 1, pp. 21 – 34, 2003.

[7] Axelrod, D., Burghardt, T. P., and Thompson, N. L., "Total internal reflection fluorescence," *Annual Review of Biophysics and Bioengineering*, vol. 13, no. 1, pp. 247–268, 1984.

[8] Axelrod, D., Hellen, E. H., and Fulbirght, R. M., "Total internal reflection fluorescence," in *Topics in Fluorescence Spectroscopy, Volume 3: Biochemical Applications* (Lakowicz, J. R., ed.), ch. 7, pp. 289–343, Plenum Press, 1992.

[9] Barnes, G. and Gentle, I., *Inerfacial Science: an Introduction*. Oxford University Press, first ed., 2005.

[10] Barrat, J.-L. and Bocquet, L., "Large slip effect at a nonwetting fluid-solid interface," *Phys. Rev. Lett.*, vol. 82, pp. 4671–4674, Jun 1999.

[11] Beckman, P., Roy, R. P., Whitfield, K., and Hasan, A., "A fast-response microthermocouple," *Review of Scientific Instruments*, vol. 64, no. 10, pp. 2947–2951, 1993.

[12] Cahill, D., Goodson, K., and Majumdar, A., "Thermometry and thermal transport in micro/nanoscale solid-state devices and structures," *Transactions of the ASME. Journal of Heat Transfer*, vol. 124, no. 2, pp. 223 – 41, 2002.

[13] Chaudhari, A. M., Woudenberg, T. M., Albin, M., and Goodson, K. E., "Transient liquid crystal thermometry of microfabricated PCR vessel arrays," *Journal of Microelectromechanical Systems*, vol. 7, no. 4, pp. 345 – 355, 1998.

[14] Coolen, M., Kieft, R., Rindt, C., and Van Steenhoven, A., "Application of 2-d lif temperature measurements in water using a nd:yag laser," *Experiments in Fluids*, vol. 27, no. 5, pp. 420 – 6, 1999.

[15] Coppeta, J. and Rogers, C., "Dual emission laser induced fluorescence for direct planar scalar behavior measurements," *Experiments in Fluids*, vol. 25, no. 1, pp. 1 – 15, 1998/06/.

[16] Crimaldi, J., "The effect of photobleaching and velocity fluctuations on single-point LIF measurements," *Experiments in Fluids*, vol. 23, no. 4, pp. 325 – 30, 1997.

[17] Dahm, W. J. A., *Experiments on entrainment, mixing and chemical reactions in turbulent jets at large Schmidt number*. PhD thesis, California Institute of Technology, 1985.

[18] Davidson, M. W., "Molecular expressions." http://www.microscopy.fsu.edu/.

[19] Drexhage, K. H., "Structure and properties of laser dyes," in *Topics in Applied Physics: Dye Lasers* (Schafer, F. P., ed.), ch. 5, Springer-Verlag, 1990.

[20] Einstein, A., "Über die von der molekularkinetischen Theorie der Wärme geforderte Bewegung von in ruhenden Flüssigkeiten suspendierten Teilchen," *Ann Phys*, vol. 17, 1905.

[21] Fleming, J.W., J. and Shiever, J., "Thermal history dependence of refractive index dispersion of fused silica," *Journal of the American Ceramic Society*, vol. 62, no. 9-10, p. 526, Sept.-Oct. 1979.

[22] Fujisawa, N., Funatani, S., and Katoh, N., "Scanning liquid-crystal thermometry and stereo velocimetry for simultaneous three-dimensional measurement of temperature and velocity field in a turbulent Rayleigh-Bernard convection," *Experiments in Fluids*, vol. 38, no. 3, pp. 291 – 303, 2005.

[23] Gad-el Hak, M., "Comments on 'critical view on new results in micro-fluid mechanics'," *International Journal of Heat and Mass Transfer*, vol. 46, no. 20, pp. 3941 – 5, 2003.

[24] Gad-el Hak, M., "Liquids: The holy grail of microfluidic modeling," *Physics of Fluids*, vol. 17, no. 10, p. 100612, 2005.

[25] Garimella, S. V., "Transport in microchannels - a critical review," *Annual Review of Heat Transfer*, vol. 13, pp. 1–46, 2003.

[26] Gendrich, C., Koochesfahani, M., and Nocera, D., "Molecular tagging velocimetry and other novel applications of a new phosphorescent supramolecule," *Experiments in Fluids*, vol. 23, no. 5, pp. 361 – 72, 1997.

[27] Ghiaasiaan, M. S., "ME 6302: Convection heat transfer." Class Notes, Georgia Institute of Technology, Spring 2005.

[28] Grattan, K. T. V., Palmer, A. W., and Zhang, Z., "Development of a high-temperature fiber-optic thermometer probe using fluorescent decay," *Review of Scientific Instruments*, vol. 62, no. 5, pp. 1210–1213, 1991.

[29] Grober, R., Schoelkopf, R., and Prober, D., "Optical antenna: towards a unity efficiency near-field optical probe," *Applied Physics Letters*, vol. 70, no. 11, pp. 1354 – 6, 1997/03/17.

[30] Guilbault, G. G., *Practical Fluorescence: Theory, Methods, and Techniques*. Marcel Dekker, Inc., 1973.

[31] Harvey, A., Gallagher, J., and Sengers, J., "Revised formulation for the refractive index of water and steam as a function of wavelength, temperature and density," *Journal of Physical and Chemical Reference Data*, vol. 27, no. 4, pp. 761 – 74, 1998/07/.

[32] Haugland, R. P., *Handbook of Fluorescent Probes and Research Products*. Molecular Probes Inc, ninth ed., 2002.

[33] Herwig, H. and Hausner, O., "Critical view on 'new results in micro-fluid mechanics': An example," *International Journal of Heat and Mass Transfer*, vol. 46, no. 5, pp. 935 – 7, 2003.

[34] Hohreiter, V., Wereley, S., Olsen, M., and Chung, J., "Cross-correlation analysis for temperature measurement," *Measurement Science and Technology*, vol. 13, no. 7, pp. 1072 – 8, 2002/07/.

[35] Hu, H., Koochesfahani, M., and Lum, C., "Molecular tagging thermometry with adjustable temperature sensitivity," *Experiments in Fluids*, vol. 40, no. 5, pp. 753 – 63, 2006.

[36] Icenhower, J. P. and Dove, P. M., "Water behavior at silica surfaces," in *Adsorption On Silica Surfaces; Surfactant Science Series; Vol. 90* (Papirer, E., ed.), ch. 9, New York Marcel Dekker, Inc, 2000.

[37] Imamura, M. and Koizumi, M., "Irreversible photobleaching of the solution of fluorescent dues. I. kinetic studies of the primary process," *Bulletin of the Chemical Society of Japan*, vol. 28, pp. 117–124, 1955.

[38] "International Technology Roadmap for Semiconductors," tech. rep., International Technology Roadmap for Semiconductors, 2005. http://www.itrs.net.

[39] International Union of Pure and Applied Chemistry, *IUPAC Compendium of Chemical Terminology*, second ed., 1997.

[40] Ippen, E., Shank, C., and Diennes, A., "Rapid photobleaching of organic laser dyes in continuously operated devices," *IEEE Journal of Quantum Electronics*, vol. QE-7, no. 4, pp. 178 – 179, 1971/04/.

[41] Jiang, L., Wong, M., and Zohar, Y., "Transient temperature performance of an integrated micro-thermal system," *Journal of Micromechanics and Microengineering*, vol. 10, no. 3, pp. 466 – 476, 2000.

[42] Kasnavia, T., Vu, D., and Sabatini, D. A., "Fluorescent dye and media properties affecting sorption and tracer selection," *Ground Water*, vol. 37, no. 3, pp. 376 – 381, 1999.

[43] Kim, H., Kihm, K., and Allen, J., "Examination of ratiometric laser induced fluorescence thermometry for microscale spatial measurement resolution," *International Journal of Heat and Mass Transfer*, vol. 46, no. 21, pp. 3967 – 74, 2003.

[44] Koochesfahani, M., *Experiments on turbulent mixing and chemical reactions in a liquid mixing layer*. PhD thesis, California Institute of Technology, 1984.

[45] Kosmulski, M., "Surface charge and zeta potential of silica in mixtures of organic solvents and water," in *Adsorption on Silica Surfaces; Surfactant Science Series; Vol. 90* (Papirer, E., ed.), ch. 11, New York Marcel Dekker Inc, 2000.

[46] Larsen, L. and Crimaldi, J., "The effect of photobleaching on PLIF," *Experiments in Fluids*, 2006.

[47] Lavieille, P., Delconte, A., Blondel, D., Lebouche, M., and Lemoine, F., "Non-intrusive temperature measurements using three-color laser-induced fluorescence," *Experiments in Fluids*, vol. 36, no. 5, pp. 706 – 16, 2004.

[48] Lavieille, P., Lemoine, F., Lavergne, G., and Lebouche, M., "Evaporating and combusting droplet temperature measurements using two-color laser-induced fluorescence," *Experiments in Fluids*, vol. 31, no. 1, pp. 45 – 55, 2001.

[49] Lavieille, P., Lemoine, F., and Lebouche, M., "Investigation on temperature of evaporating droplets in linear stream using two-color laser-induced fluorescence," *Combustion Science and Technology*, vol. 174, no. 4, pp. 117 – 142, 2002.

[50] Lichter, S., Roxin, A., and Mandre, S., "Mechanisms for liquid slip at solid surfaces," *Physical Review Letters*, vol. 93, no. 8, 2004.

[51] Lout, J., Finegan, T. M., Mohsen, P., Hatton, T. A., and Laibinis, P. E., "Fluorescence-based thermometry principles and applications," *Reviews in Analytical Chemistry*, vol. 18, no. 4, 1999.

[52] Mala, G. M. and Li, D., "Flow characteristics of water in microtubes," *International Journal of Heat and Fluid Flow*, vol. 20, pp. 142–148, 1999.

[53] Mao, H., Holden, M. A., You, M., and Cremer, P. S., "Reusable platforms for high-throughput on-chip temperature gradient assays," *Analytical Chemistry*, vol. 74, no. 19, pp. 5071 – 5075, 2002.

[54] Mao, H., Yang, T., and Cremer, P. S., "A microfluidic device with a linear temperature gradient for parallel and combinatorial measurements," *Journal of the American Chemical Society*, vol. 124, no. 16, pp. 4432 – 4435, 2002.

[55] Matarredona, O., Rhoads, H., Li, Z., Harwell, J. H., Balzano, L., and Resasco, D. E., "Dispersion of single-walled carbon nanotubes in aqueous solutions of the anionic surfactant naddbs," *Journal of Physical Chemistry B*, vol. 107, no. 48, pp. 13357 – 13367, 2003.

[56] Mchedlov-Petrossyan, N., Vodolazkaya, N., and Doroshenko, A., "Ionic equilibria of in organized solutions: the influence of micellar microenvironment on protolytic and photophysical properties of rhodamine B," *Journal of Fluorescence*, vol. 13, no. 3, pp. 235 – 48, 2003.

[57] Morton, N., "Gradient refractive index lenses," *Physics Education*, vol. 19, no. 2, pp. 86 – 90, 1984.

[58] "National bureau of standards certificate, srm 187a: Borax (ph standard)," 1960.

[59] Olsen, M. G. and Adrian, R. J., "Brownian motion and correlation in particle image velocimetry," *Optics and Laser Technology*, vol. 32, no. 7-8, pp. 621 – 627, 2000.

[60] *OMEGA Complete Temperature Measurement Handbook and Encyclopedia*, fifth ed.

[61] Panton, R. L., *Incompressible Flow*. John Wiley and Sons, Inc, third ed., 2005.

[62] Park, H., Dabiri, D., and Gharib, M., "Digital particle image velocimetry/thermometry and application to the wake of a heated circular cylinder," *Experiments in Fluids*, vol. 30, no. 3, pp. 327 – 338, 2001.

[63] Park, J.-J. and Taya, M., "Design of micro-temperature sensor array with thin film thermocouples," *Journal of Electronic Packaging*, vol. 127, no. 3, pp. 286–289, 2005.

[64] Peng, X. and Wang, B.-X., "Forced convection and flow boiling heat transfer for liquid flowing through microchannels," *International Journal of Heat and Mass Transfer*, vol. 36, no. 14, pp. 3421 – 7, 1993.

[65] Press, W. H., Teukolsky, S. A., Vetterling, W. T., and Flannery, B. P., *Numerical Recipes in C++*. Cambridge University Press, second ed., 2002.

[66] Qu, W., Mala, M., and Li, D., "Heat transfer for water flow in trapezoidal silicon microchannels," *International Journal of Heat and Mass Transfer*, vol. 43, no. 21, pp. 3925 – 36, 2000.

[67] Rajniak, P. and Yang, R. T., "Hysteresis-dependent adsorption-desorption cycles: Generalization for isothermal conditions," *AIChE Journal*, vol. 40, no. 6, pp. 913–924, 1994.

[68] Ross, D., Gaitan, M., and Locascio, L., "Temperature measurement in microfluidic systems using a temperature-dependent fluorescent dye," *Analytical Chemistry*, vol. 73, no. 17, pp. 4117 – 4123, 2001.

[69] Sakakibara, J. and Adrian, R., "Whole field measurement of temperature in water using two-color laser induced fluorescence," *Experiments in Fluids*, vol. 26, no. 1-2, pp. 7 – 15, 1999.

[70] Sakakibara, J. and Adrian, R., "Measurement of temperature field of a rayleigh-benard convection using two-color laser-induced fluorescence," *Experiments in Fluids*, vol. 37, no. 3, pp. 331 – 40, 2004.

[71] Santiago, J., Wereley, S., Meinhart, C., Beebe, D., and Adrian, R., "Particle image velocimetry system for microfluidics," *Experiments in Fluids*, vol. 25, no. 4, pp. 316 – 319, 1998.

[72] Saylor, J., "Photobleaching of disodium fluorescein in water," *Experiments in Fluids*, vol. 18, no. 6, pp. 445 – 447, 1995.

[73] Schafer, F. P., "Principles of dye laser operation," in *Topics in Applied Physics: Dye Lasers* (Schafer, F. P., ed.), ch. 1, Springer-Verlag, 1990.

[74] Seuntiens, H., Kieft, R., Rindt, C., and Van Steenhoven, A., "2D temperature measurements in the wake of a heated cylinder using lif," *Experiments in Fluids*, vol. 31, no. 5, pp. 588 – 595, 2001.

[75] Shi, L., Kwon, O., Miner, A., and Majumdar, A., "Design and batch fabrication of probes for sub-100 nm scanning thermal microscopy," *Journal of Microelectromechanical Systems*, vol. 10, no. 3, pp. 370 – 378, 2001.

[76] Sholes, R. R. and Small, J. G., "Fluorescent decay thermometer with biological applications," *Review of Scientific Instruments*, vol. 51, no. 7, pp. 882–884, 1980.

[77] Sinha, S., Ray, A., Kundu, S., Sasikumar, S., and Dasgupta, K., "Heavy-water-based solutions of rhodamine dyes: photophysical properties and laser operation," *Applied Physics B (Lasers and Optics)*, vol. B75, no. 1, pp. 85 – 90, 2002.

[78] Song, L., Hennink, E., Young, I., and Tanke, H., "Photobleaching kinetics of fluorescein in quantitative fluorescence microscopy," *Biophysical Journal*, vol. 68, no. 6, pp. 2588 – 600, 1995.

[79] Song, L., Varma, C., Verhoeven, J., and Tanke, H., "Influence of the triplet excited state on the photobleaching kinetics of fluorescein in microscopy," *Biophysical Journal*, vol. 70, no. 6, pp. 2959 – 68, 1996.

[80] Thompson, P. and Troian, S., "A general boundary condition for liquid flow at solid surfaces," *Nature*, vol. 389, no. 6649, pp. 360 – 2, 25 Sept. 1997.

[81] Thompson, P. A. and Robbins, M. O., "Shear flow near solids: Epitaxial order and flow boundary conditions," *Phys. Rev. A*, vol. 41, pp. 6830–6837, Jun 1990.

[82] Thomson, S. and Maynes, D., "Spatially resolved temperature measurements in a liquid using laser induced phosphorescence," *Transactions of the ASME. Journal of Fluids Engineering*, vol. 123, no. 2, pp. 293 – 310, 2001.

[83] Tiselj, I., Hetsroni, G., Mavko, B., Mosyak, A., Pogrebnyak, E., and Segal, Z., "Effect of axial conduction on the heat transfer in micro-channels," *International Journal of Heat and Mass Transfer*, vol. 47, no. 12-13, pp. 2551 – 2565, 2004.

[84] Toyoda, T. and Yabe, M., "Temperature dependence of the refractive indices of fused silica and crystal quartz.," *Journal of Physics D: Applied Physics*, vol. 16, no. 5, pp. 97–100 –, 1983.

[85] Tuckerman, D. and Pease, R., "High-performance heat sinking for vlsi," *IEEE Electron Device Letters*, vol. 2, no. 5, pp. 126–129, 1981.

[86] van der Heyden, F., Stein, D., Besteman, K., Lemay, S., and Dekker, C., "Charge inversion at high ionic strength studied by streaming currents," *Physical Review Letters*, vol. 96, no. 22, pp. 224502 – 1, 2006/06/09.

[87] van Der Heyden, F. H. J., Stein, D., and Dekker, C., "Streaming currents in a single nanofluidic channel," *Physical Review Letters*, vol. 95, no. 11, pp. 116104 – 1, 2005.

[88] Viswanath, R., Wakharkar, V., Watwe, A., and Lebonheur, V., "Thermal performance challenges from silicon to systems," *Intel Technology Journal*, no. Q3, p. 16, 2000.

[89] Wiberg, R. and Lior, N., "Errors in thermochromic liquid crystal thermometry," *Review of Scientific Instruments*, vol. 75, no. 9, pp. 2985 – 94, Sept. 2004.

[90] Yoda, M. and Sadr, R., "Nano-particle image velocimetry (nPIV): A new technique for measuring near-wall velocity fields with submicron spatial resolution," *AIAA Paper*, pp. 8686 – 8693, 2004.

[91] Zhang, Z., Grattan, K. T. V., and Palmer, A. W., "A novel signal processing scheme for a fluorescence based fiber-optic temperature sensor," *Review of Scientific Instruments*, vol. 62, no. 7, pp. 1735–1742, 1991.

[92] Zhang, Z. M., "Surface temperature measurment using optical techniques," *Annual Review of Heat Transfer*, vol. 11, pp. 351 – 411, 2000.